Probing Strongly Correlated States of Ultracold Atoms in Optical Lattices

Dissertation

zur Erlangung des Grades

"Doktor

der Naturwissenschaften"

am Fachbereich Physik

der Johannes Gutenberg-Universität

in Mainz

Simon Fölling

geboren in Münster

Mainz, den 16.10.2008

Datum der mündlichen Prüfung: 16. Oktober 2008

Abstract

This thesis describes experiments which investigate ultracold atom ensembles in an optical lattice. Such quantum gases are powerful models for solid state physics. Several novel methods are demonstrated that probe the special properties of strongly correlated states in lattice potentials. Of these, quantum noise spectroscopy reveals spatial correlations in such states, which are hidden when using the usual methods of probing atomic gases. Another spectroscopic technique makes it possible to demonstrate the existence of a shell structure of regions with constant densities. Such coexisting phases separated by sharp boundaries had been theoretically predicted for the Mott insulating state. The tunneling processes in the optical lattice in the strongly correlated regime are probed by preparing the ensemble in an optical superlattice potential. This allows the time-resolved observation of the tunneling dynamics, and makes it possible to directly identify correlated tunneling processes.

Zusammenfassung

In dieser Arbeit werden Experimente vorgestellt, in denen die Eigenschaften eines ultrakalten atomaren Gases in einem optischen Gitterpotential untersucht werden. Solche Quantengase sind sehr vielseitige Modellsysteme für Phänomene der Festkörperphysik. Um die besonderen Eigenschaften stark korrelierter Zustände in optischen Gittern zu untersuchen, werden neuartige Methoden realisiert, die in dieser Form erstmalig zum Einsatz kommen. So erlaubt es die Spektroskopie des Quantenrauschens in atomaren Ensembles erstmals, die Korrelationen in der räumlichen Dichte eines solchen Zustands sichtbar zu machen. Mittels einer anderen spektroskopischen Technik gelingt es ausserdem, die Existenz getrennter Phasen konstanter Dichte, die sogenannte Schalenstruktur des Mott Isolators, direkt nachzuweisen. Die komplexe Dynamik von Tunnelprozessen im optischen Gitter im stark korrelierten Regime wird durch Einsatz eines optischen Übergitters untersucht. Dadurch ist es möglich, die Tunneldynamik zeitaufgelöst zu erfassen und korrelierte Tunnelprozesse direkt zu beobachten.

Contents

1 Introduction

Ultracold quantum gases – already enjoying much attention due to the spectacular experimental progress made in recent years – are now increasingly becoming a popular topic of condensed matter physics. One important contribution to this surge in interest was the proposal [1] and subsequent realization [2] of the idea that such gases can be used to almost perfectly implement the Hubbard model. This fundamental model was developed in condensed matter physics to describe the behavior of interacting electrons [3] or bosonic particles (Bose-Hubbard model, [4]) in a crystal lattice. In the cold atom implementation of the model, this is realized by subjecting the ultracold atoms to a crystal potential created by laser light.

The strong interest in such systems does not just originate from the geometrical resemblance of the configuration with real crystal lattices. More importantly, they provide a an almost idealized realization of a system in a regime that is notoriously hard to handle theoretically. This regime is characterized by the fact that interactions within the ensemble lead to strong particle-particle correlations. In this respect, these new experiments differ strongly from most earlier ultracold atom experiments in the regime of weakly interacting gases, which focused on single-particle coherence effects. This new aspect poses new challenges for the way these ensembles are probed and analyzed, and novel methods developed to address this are the focus of this thesis.

Regarding ultracold or degenerate quantum gases as model implementations for other systems started already before the application to strongly correlated systems. In fact, experiments with such gases were seen as analogs to the physics of quantum systems from some very different fields almost since their first realization. One reason for this is that the description of the particles can be reduced to a few key properties at the ultra-low energy scales involved. These properties then completely define the behavior of the entire system.

The initial experiments on degenerate bosonic ensembles focused on the macroscopic wave nature of the Bose-Einstein condensate (BEC) [5, 6]. In a BEC, many particles – up to several million – occupy the same quantum state if interactions between them are sufficiently weak. Among these experiments are the atom optics equivalents of optical wave phenomena such as double slit interference [7]. Similarly, atom lasers [8–11] were realized with matter waves. In analogy to the macroscopic wave functions present in superfluids and superconductors, quantized vortices and vortex lattices [12–15] and Josephson junction physics [16, 17] were demonstrated.

Eventually, and as a major step forward for the role as a model system, the single particle wave function paradigm was left toward the regime of strong particle-

particle correlations in a wide range of implementations [18]. One way of achieving this is by increasing the interaction strength [19–21], until the weakly interacting regime is left. For bosons, however, this approach is typically limited by strong collisional losses. More recently, this method has enabled spectacular progress with strongly interacting Fermi gases [22–26], which can then exhibit close analogies to the interacting electron gases in metals and semiconductors.

The connection between solid state physics and ultracold atom phenomena was started much earlier, almost as soon as light fields were used for cooling of atoms: Band structure calculations for atoms in standing light waves explained unexpected characteristics of laser cooling in these systems [27] and crystal-like ordering of the atoms could be observed [28, 29]. The first dynamical phenomena with direct analogs in solid state physics, Bloch oscillations and Wannier-Stark ladders, were observed with cold atoms in optical potentials created by standing waves [30, 31].

Due to the narrow energy band structure arising in periodic optical potentials, the kinetic energy scales are strongly reduced. At the same time, the interactions increase due to the confinement provided. Therefore, optical lattices also provide a method of reaching a regime in which interaction effects dominate the ensemble behavior. By using a single one-dimensional lattice potential, such an increase of the interaction strength was used to observe effects of particle number squeezing in lattice sites [32]. Finally, inside a three-dimensional, crystal-like optical lattice potential, the strength of interactions in a degenerate gas can become much stronger than the kinetic energies. In this case the macroscopic occupation of the single particle ground state is completely lifted, leading to the Mott insulating regime for bosons [2].

Since this first novel quantum state, an ever-increasing variety of phases with widely varying properties and increasing complexity has been realized with atoms in periodic potentials. Among those are 1D and 2D Mott phases [33, 34], the Tonks-Girardeau gas [35, 36], band insulators for fermions [37] as well as strongly paired fermions in lattice potentials [38].

Most of these experiments used the same measurement schemes as introduced for probing weakly interacting gases. The most important tool is the ballistic expansion out of the trap followed by imaging the resulting density distribution. It was developed for probing the in-trap momentum distribution and the coherence properties of the ensemble. In the strongly correlated regime, however, these typically contain little information as there is usually no macroscopic single-particle phase relation and all momentum states have identical populations. In fact, one popular indicator used to identify the strongly correlated regime is actually the loss of coherence effects.

Other strategies were adapted from experimental solid-state physics such as the probing of excitation spectra by applying static or modulated external fields [2, 33]. These methods need to be modified to be applicable to ultracold atom ensembles due to the specifics of most of todays implementations. Coupling to reservoirs, for example, is usually not possible with atom ensembles. Typical schemes from condensed matter experiments such as steady-state transport measurements can therefore not be

implemented in the same way as for traditional solid state systems.

Recently, new methods of probing strongly correlated quantum gases were proposed and applied. They specifically address the special properties of these systems as opposed to those of weakly interacting quantum gases. In addition, they take advantage of experimental possibilities that do not exist for condensed matter systems. In this way, they can provide information about the many-body state which is not readily available for typical condensed matter systems. The methods demonstrated in this thesis, which will be outlined in the following, range from probing the macroscopic structure of the quantum gas within the trap – its overall density distribution – to the determination of the microscopic properties: The statistics, tunneling dynamics and the interaction properties of atoms inside the lattice potential.

Probing the Mott insulator shell structure The bosonic Mott insulator is still the benchmark system for ultracold atoms in optical lattices. The defining thermodynamical property of this quantum state is its lack of conductivity and compressibility due to a gap in the excitation spectrum [4]. One important consequence of this was already pointed out in the theoretical proposal which discussed its creation using BEC in optical lattices [1]: Due to the incompressibility, a spatially extended Mott phase has to be constant in density, regardless of the shape of any external potential. It can only exist at densities corresponding to integer occupation numbers of the lattice sites. In the inhomogeneous, parabolic confinement of the trap used to hold the atoms, it was predicted that a shell structure would develop. It consists of concentric, spherical shells with integer site occupation which are separated by thin spherical layers in the superfluid phase. This very special structure of the local density, however, has eluded direct observation for a long time. Experiments on Mott insulators so far have typically probed global properties such as excitation spectra or the average single-particle coherence in close analogy to condensed matter and BEC experiments, respectively.

Here, the detection of the shell structure is demonstrated by using the special interaction properties of atoms in the lattice in combination with a non-optical imaging technique similar to nuclear magnetic resonance imaging (NMRI). For this, the areas of different occupation numbers are distinguished by using number-state selective collisional interactions which change the internal spin of the atoms. This can be done either globally, or the number-state distribution in different parts of the cloud can be determined locally. With the local probing, the separation of the ensemble into the individual shells becomes visible. As this shell structure is very sensitive to thermal excitations, it is also possible to give upper limits on the temperature of the quantum gas within the lattice. This important parameter is very hard to access experimentally in the very low temperature regime.

Atom-atom correlations for probing complex quantum states In the strongly correlated regime of a 3D lattice, the underlying spatial structure – the fact that the atoms are confined to the periodic pattern created by the lattice sites – is "invisible" in the momentum distribution of the ensemble. Once the tunneling of atoms between lattice sites is suppressed such as in the bosonic Mott insulating state, no phase coherence exists between the lattice sites. In this case, all individual atoms independently leave the trap during the ballistic expansion and no interference occurs. The observed overall momentum distribution is merely determined by the wave function of a single atom in a well, without any information about the spatial structure of the gas. Similarly, in a fermionic band insulator all quasimomentum states are evenly occupied, resulting in a structureless momentum distribution.

The quantum statistics of indistinguishable particles provides a remarkable way to gain information about in-trap correlations even in this case. Due to these statistics, even atoms emitted independently from separate sources can exhibit correlations on detection, which was first described in the form of Hanbury Brown-Twiss correlations for bosons [39]. Information about the spatial correlations of the gas inside the trap can thus be extracted by analyzing statistical correlations between individual atoms after their release and ballistic expansion.

This is demonstrated by extracting the spatial correlations of the fundamental lattice structure from the quantum noise of the expanded distribution, in an approach motivated by recent theoretical proposals [40]. In the same way, the detection of states with density correlations which differ from those of the basic lattice structure is shown. This demonstrates that the noise correlation analysis provides a tool for probing more complex many-body states such as for example Néel-ordered phases [41], whose in-trap structure is not reflected at all in the averaged momentum distribution.

Dynamics and interactions in superlattices One new ability offered by optical lattices as opposed to solid state crystals is the possibility to dynamically change the lattice properties. The depth of the potential, for example, can usually be changed very easily for optical lattices. By combining potentials with different periodicities, even the implementation of lattices with dynamically variable structure and symmetry is possible. This was used to efficiently control and prepare atoms in an array of double well potentials in the strongly interacting regime. These double wells can be seen as microscopic lattices with only two sites, for which it is possible – again by exploiting the ability to dynamically change the lattice structure – to directly observe the underlying microscopic tunneling and interaction processes which govern the full many-body system.

For individual or weakly interacting atoms, the tunnel motion can be directly observed. In the strongly correlated regime, which is characterized by the suppression of tunneling of individual atoms, higher-order tunneling processes become the dominant dynamical effects. The direct observation of these processes in the two-well

"lattice" with high accuracy is demonstrated. Higher-order tunnel couplings are an important aspect of strongly correlated systems in optical lattices, as they create effective interactions between lattice sites, which in turn define the spin ground state of the ensemble.

Outline

This thesis is organized as follows: Chapter 2 gives a short overview of the description and properties of cold atoms in optical lattice potentials. Chapter 3 introduces the experimental setup as well as basic experiments and methods employed throughout this thesis. Chapter 4 is centered on the analysis of the global shell structure of the Mott insulator, and on probing the quantum many-body state inside the lattice using atom-atom correlations is described in chapter 5. In chapter 6, the control and direct observation of tunnel processes in optical lattices with the help of a double well potential is shown. Chapter 7 concludes the thesis and gives an outlook on possible further experiments and applications of the techniques described in this work.

Publications in the context of this thesis

Several papers have been published in refereed journals in the context of this thesis. In the following, these are listed in the order in which they were published. The most relevant ones for the content described in this thesis are provided as reprints in the appendix.

- *Tonks-Girardeau gas of ultracold atoms in an optical lattice*
  B. Paredes, A. Widera, V. Murg, O. Mandel, S. Fölling, I. Cirac, G. V. Shlyapnikov, T. W. Hänsch and I. Bloch
  Nature **429**, 277-281 2004

- *Spatial quantum noise interferometry in expanding ultracold atom clouds*
  S. Fölling, F. Gerbier, A. Widera, O. Mandel, T. Gericke and I. Bloch
  Nature **434**, 481-484 (2005)

- *Phase coherence of an atomic Mott insulator*
  F. Gerbier, A. Widera, S. Fölling, O. Mandel, T. Gericke, I. Bloch
  Phys. Rev. Lett. **95**, 050404 (2005)

- *Coherent collisional spin dynamics in optical lattices*
  A. Widera, F. Gerbier, S. Fölling, T. Gericke, O. Mandel, I. Bloch
  Phys. Rev. Lett. **95**, 190405 (2005)

- *Interference pattern and visibility of a Mott insulator*
  F. Gerbier, A. Widera, S. Fölling, O. Mandel, T. Gericke, I. Bloch
  Phys. Rev. A **72**, 053606 (2005)

- *Probing Number squeezing of Ultracold Atoms across the Superfluid-Mott Insulator Transition*
  F. Gerbier, S. Fölling, A. Widera, O. Mandel, I. Bloch
  Phys. Rev. Lett. **96**, 090401 (2006)

- *Resonant control of spin dynamics in ultracold quantum gases by microwave dressing*
  F. Gerbier, A. Widera, S. Fölling, O. Mandel, I. Bloch
  Phys. Rev. A **73**, 041602(R) (2006)

- *Adiabatic loading of a Bose-Einstein condensate in a 3D optical lattice*
  T. Gericke, F. Gerbier, A. Widera, S. Fölling, O. Mandel, I. Bloch
  J. Mod. Opt. **54**, 735 (2007)

- *Precision measurement of spin-dependent interaction strengths for spin-1 and spin-2 ^{87}Rb atoms*
  A. Widera, F. Gerbier, S. Fölling, T. Gericke, O. Mandel, I. Bloch
  New J. Phys. **8**, 152 (2006)

- *Formation of spatial shell structures in the superfluid to Mott insulator transition*
  S. Fölling, A. Widera, T. Müller, F. Gerbier, I. Bloch
  Phys. Rev. Lett. **97**, 060403 (2006)

- *Free fermion antibunching in a degenerate atomic Fermi gas released from an optical lattice*
  T. Rom, Th. Best, D. van Oosten, U. Schneider, S. Fölling, B. Paredes and I. Bloch
  Nature **444**, 733-736 (2006)

- *State preparation and dynamics of ultracold atoms in higher lattice orbitals*
  T. Müller, S. Fölling, A. Widera, I. Bloch
  Phys. Rev. Lett. **99**, 200405 (2007)

- *Direct Observation of Second Order Atom Tunnelling*
  S. Fölling, S. Trotzky, P. Cheinet, M. Feld, R. Saers, A. Widera, T. Müller, I. Bloch
  Nature **448**, 1029-1032 (2007)

- *Time-resolved Observation and Control of Superexchange Interactions with Ultracold Atoms in Optical Lattices*
  S. Trotzky, P. Cheinet, S. Fölling, M. Feld, U. Schnorrberger, A. M. Rey, A. Polkovnikov, E. A. Demler, M. D. Lukin, I. Bloch
  Science **319**, 295 (2008)

- *Quantum spin dynamics of squeezed Luttinger liquids in two-component atomic gases*
  A. Widera, S. Trotzky, P. Cheinet, S. Fölling, F. Gerbier, I. Bloch, V. Gritsev, M. D. Lukin, E. Demler
  Phys. Rev. Lett. **100**, 140401 (2008)

2 Ultracold atoms in optical lattice potentials

The experiments described in this thesis focus on the properties of several specific quantum phases of ultracold atom ensembles, and on methods to probe them experimentally. These states are governed by three fundamental properties of the atoms. They are indistinguishable, obey bosonic quantum statistics, and they interact only via a repulsive contact interaction. As an additional requirement the temperature has to be low compared to all other relevant energy scales.

The three most important quantum states for the experiments described are the Bose-Einstein condensate (BEC) in the pure harmonic trap as well as in the deep lattice potential ("superfluid state"), and the bosonic Mott insulator. They have in common that the temperature in each case has to be lower than the defining energy scales of the state. Transitions between these regimes are induced by changing the shape of the trapping potential, as this influences the mobility and the interaction strength of the particles.

The first of these states, the Bose-Einstein condensate, is also the starting point for all experiments shown. It occurs for three-dimensionally confined bosons when they condense into the lowest quantum state of the trap below a critical temperature T_c. The weak repulsive interactions between the atoms then govern the shape of this quantum state within the trap, leading to the density distribution depicted in figure 2.1a.

In a typical periodic lattice potential, the atoms are no longer confined by a single trapping potential, but the potential now has a substructure of many minima separated by barriers as shown in figure 2.1b. These barriers are so high that atoms can only travel between the wells by tunneling. If this tunnel mobility is high enough, then this ensemble is still a BEC. All atoms are condensed into the lowest quantum state of this configuration, which locally is given by the lowest energy bound state of each well. Globally, the lowest single-particle state spreads over many of the wells which are connected by tunneling. The density distribution of this superfluid phase is again the result of the balance between the confining potential and the repulsive interaction between the atoms.

The fact that the atoms are fully delocalized means that locally, only the expectation value of the atom number is defined for each site, around which the measured value fluctuates. If the repulsive interaction is very large or the tunnel coupling very small, the tunneling process of an individual atom to a neighboring site competes with the repulsive interaction between the atoms on the sites. This interaction leads to a suppression of the density fluctuations for the ensemble and a reduction of the condensed fraction. Eventually the system evolves to a locally constant density dis-

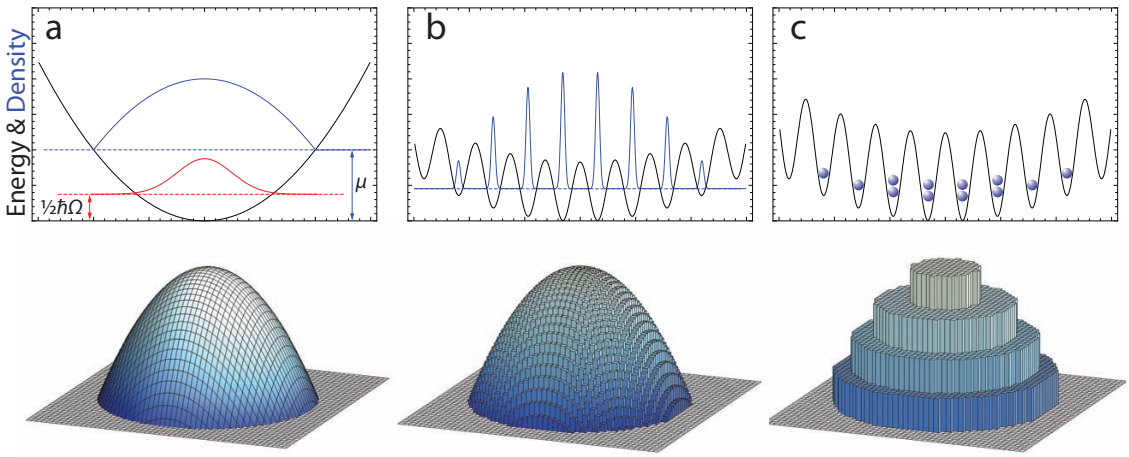

Figure 2.1: Three phases of interacting bosons at zero temperature in different potentials (black lines in top graphs). In (a), the confinement is purely parabolic. The single atom ground state is indicated in red. Interactions deform this wave function to the Thomas-Fermi (TF) distribution (blue line and surface plot). In (b), a periodic modulation generates an array of wells, with all well ground states connected by tunneling to one large wave function, into which all atoms are condensed. The 3D plot shows the average density on each site for a 2D array, which has the TF shape. For strong interactions (c), tunneling is suppressed, and the atoms are localized to one well. Here, only discrete integer occupation numbers exist. This leads to a density pattern consisting of concentric shells with constant density.

tribution with an integer number of atoms per site. At this point, the wave function of each atom is localized to one of the lattice wells, and the ensemble no longer occupies a single common quantum state. As the density is pinned to integer occupation per site, the overall density increases in discrete steps even in a smooth confining potential. In a spherical parabolic confinement, this leads to a structure of concentric spherical density shells as shown in figure 2.1c.

To achieve these states in the experiment, a Bose-Einstein condensate (BEC) is first prepared in a smooth parabolic potential. The trap is then converted into the periodic lattice potential. By increasing the modulation depth, the system crosses the superfluid regime, and finally enters the Mott insulating regime for very low tunneling rates. By doing the transformations of the potential slowly to reach adiabaticity, the new trap configuration is obtained with an ensemble as close to the ground state as possible.

In the following, an introduction to the physics of each of the regimes is given. This will include the essentials of Bose-Einstein condensates of weakly interacting atomic gases as well as the creation of optical lattice potentials and provide an introduction to the quantum mechanics of particles in such potentials. The most relevant properties of the superfluid and the Mott insulating state will be introduced and the effect of finite temperatures will be discussed. Much more detailed descriptions are available

in the literature, and many publications exist which are dedicated to specific aspects of these systems. For an overview, a number of monographs and review papers describe some of these aspects and provide detailed references [18, 42–48].

2.1 Bose-Einstein condensates with repulsive interactions

The Bose-Einstein condensation of atoms is based on the statistical properties of indistinguishable bosonic particles. It was predicted by A. Einstein in 1925 [49] for noninteracting gases, expanding ideas by S. N. Bose on the statistical properties of photons [50]. The first realization for a dilute gas of atoms succeeded in 1995 [5, 6].

The onset of this condensation when cooling a gas of bosonic atoms can be described as taking place when the phase space density becomes so high that the wave functions of the individual particles start to overlap [43]. For non-interacting particles confined in space by an external potential, a consequence is the macroscopic occupation of the lowest quantum state of the system. At temperature $T = 0$, all particles are in this state, representing a pure BEC.

As all atoms in the condensate are known to occupy the lowest quantum state, the whole ensemble can be described in terms of a macroscopic wave function:

$$\Psi(\boldsymbol{x}) = \sqrt{N}\Psi_0(\boldsymbol{x})$$

where Ψ_0 is the single-particle ground state wave function. The macroscopic wave function is therefore normalized to the number of atoms. It is sometimes described as an order parameter determining the local density and phase of particles in the condensed state [51].

The interactions present in typical Bose Einstein condensates are typically dominated by direct elastic atom-atom scattering processes. In the most general case these scattering properties are very complicated and highly dependent on the collisional energy. Using quantum mechanical scattering theory, they can in principle be calculated from the interatomic interaction potentials. For realistic atoms, however, this is usually not possible and also not necessarily useful due to the complexity of the description.

Because only very low energies are present in ultracold quantum gases, luckily the situation is considerably simplified: In most cases only the lowest energy s-wave scattering channel has to be taken into account. When the collision energy approaches zero, it can be shown that scattering is isotropic, energy-independent and characterized by a single parameter, the s-wave scattering length a_s. Therefore, the details of the molecular potential can be neglected and the many-body description greatly simplified by replacing the true interatomic potential by a much simpler model potential with the same scattering length. Often these are then treated as a contact interaction of the form

$$V_{atom-atom}(\boldsymbol{x}) = \frac{4\pi\hbar^2 a_s}{m} \cdot \delta(\boldsymbol{x}) = g \cdot \delta(\boldsymbol{x}).$$

Here, m is the mass of the atoms, and $\boldsymbol{x}$ their relative position. The interaction is fully characterized by the effective scattering length a_s, or, alternatively, the interaction constant g [52, 53]. For ^{87}Rb, $a_s \approx 100 a_B$, with $a_B = 0.053\,\text{nm}$ denoting the Bohr radius.

In a gas of many atoms, this potential gives rise to an interaction energy term in the hamiltonian. In the typical regime where the interaction between individual particles is small compared to their kinetic energy, the δ-function interaction of the sum of all atoms can be "averaged" in a mean-field approximation. This results in a local interaction potential experienced by each individual atom. The mean-field energy is given by the density of atoms $g \cdot |\Psi(\boldsymbol{x})|^2$ at a given location $\boldsymbol{x}$ (see e.g. [43]). The energy density due to this interaction is

$$V_{int}(\boldsymbol{x}) = g \cdot |\Psi(\boldsymbol{x})|^4.$$

Including this term into the Schrödinger equation for the macroscopic wave function Ψ yields the Gross-Pitaevskii equation (GPE)

$$i\hbar \frac{\partial}{\partial t}\Psi(\boldsymbol{x},t) = \left(-\frac{\hbar^2}{2m}\nabla^2 + V_{ext}(\boldsymbol{x}) + g|\Psi(\boldsymbol{x},t)|^2\right)\Psi(\boldsymbol{x},t). \tag{2.1}$$

The atom-atom interaction has been introduced as a mean field giving rise to an effective potential in addition to any external potential V_{ext} being present [54, 55]. This equation is a non-linear Schrödinger equation for the macroscopic wave function describing the common state of N particles. In the weakly interacting regime, this description of the condensate is very successful and can be applied to a wide range of phenomena such as vortices [13, 56] or solitons [57, 58].

The atoms therefore no longer condense into the quantum mechanical single particle ground state of the external potential, but into a modified state which has to be found by self-consistently solving the stationary GPE [59]

$$\mu\Psi(\boldsymbol{x},t) = \left(-\frac{\hbar^2}{2m}\nabla^2 + V_{ext}(\boldsymbol{x}) + g|\Psi(\boldsymbol{x},t)|^2\right)\Psi(\boldsymbol{x},t). \tag{2.2}$$

The chemical potential μ fixes the overall atom number N and is determined by the condition

$$\int |\Psi(\boldsymbol{x})|^2 d\boldsymbol{x} = N.$$

For smooth potentials, the stationary GPE can be solved easily when neglecting the kinetic term compared to the overall interaction term. The solutions are then simply given by the the balance between the external potential and the interactions due to the local density

$$n(\boldsymbol{x}) = |\Psi(\boldsymbol{x})|^2 = \begin{cases} 0 & \text{if } V_{ext}(\boldsymbol{x}) \geq \mu \\ \frac{\mu - V_{ext}(\boldsymbol{x})}{g} & \text{if } V_{ext}(\boldsymbol{x}) < \mu. \end{cases} \tag{2.3}$$

For most realistic potentials, this approximation only fails at the very boundaries of the atom cloud. The resulting density distribution, shown in figure 2.1a, is often called *Thomas-Fermi distribution* [59], as the approximations made correspond to the approximations for fermions in atomic potentials [60, 61].

Another consequence of interactions is that it modifies the structure of the ground state such that there is a finite probability for an atom to be in excited states even at $T = 0$. This correction reduces the energy of the quantum mechanical ground state compared to a product state with all atoms occupying the same wave function. The reduction in the ground state occupation is referred to as quantum depletion [62], as opposed to the thermal depletion of the condensate population which occurs with an increase of the temperature. In the case of typical macroscopic condensates in parabolic trapping potentials, the quantum depleted fraction of the population is usually on the order of 0.01 and does not play a role in experiments [42, 63].

When interactions are increased, the quantum depletion increases. The assumptions made for the mean field averaging eventually break down. For the averaging to work, it was assumed that the interaction between two individual particles is low compared to the complete kinetic energy of the same atoms. We can estimate $\epsilon_{int} \approx gn$ and $\epsilon_{kin} \approx \hbar^2/2ml^2$, with $l \sim n^{-1/3}$ the typical interparticle distance. This yields the ratio

$$\zeta = \frac{\epsilon_{int}}{\epsilon_{kin}} = \frac{g \cdot n}{\hbar^2/m \cdot n^{2/3}} \approx 4\pi n^{1/3} a_s \ll 1 \tag{2.4}$$

In the opposite case $\epsilon_{int} \gg \epsilon_{kin}$ the population of the lowest momentum state vanishes as all states become populated. The ratio ζ can be increased by enhancing the interaction strength, for example by increasing the density or the scattering length a_0 close to atomic Feshbach resonances [21, 64]. Unfortunately, this approach is strongly affected by intrinsic loss mechanisms, which are also enhanced with both density and scattering length. The most important of these is the three-body recombination, in which three atoms collide to form a bound molecule of two atoms, leaving the third unbound. The energy released by forming the bound state is converted to kinetic energy of the molecule and the third atom, and is typically high enough to remove both from the trap. The rate of such recombinations is $\Gamma_{3B} \propto K_3 n^2$, with a rate constant K_3 which in turn scales as a_s^4 [65]. As the interaction energy only increases as $a_s \cdot n$, the three-body recombination will typically prevent the formation of a stable, strongly interacting ensemble. Note that this is not necessarily the case for a two-component ensemble of interacting fermionic particles. In this case, three-body collisions are effectively suppressed. This can be understood as a result of the Pauli blocking as two of the particles involved are necessarily identical. Strongly interacting Fermi gases can therefore be extremely long-lived.

For the correlated Bose gases discussed in this thesis, the strongly interacting regime is reached without changing the scattering length. Instead, the introduction of an optical lattice potential drastically quenches the kinetic energy ϵ_{kin} by restricting the

atomic motion to narrow energy bands, and also enhances the interaction by increasing the local density within the potential minima. At the typical low average occupation numbers per site (1 to 3), the probabilities for inelastic losses are nonetheless suppressed, and three-body losses vanish completely in the insulating state for $n < 3$ [66]. The typical lifetime of the atoms in the lattice is on the order of several seconds even for sites with three atoms, and is usually limited only by rest gas collisions and spontaneous light scattering for lower occupation numbers.

2.2 Optical lattice potentials

The optical lattice potentials used throughout this thesis are three-dimensional periodic potential landscapes. They are implemented using far detuned light fields which produce conservative dipole potentials, allowing to create potentials with the desired crystal-like structure [67].

2.2.1 Dipole potentials

Optical dipole potentials in general offer a powerful way of realizing trapping potentials for atoms. One big advantage of this method is the fact that the trap geometry is directly given by the spatial light pattern used, which allows for the generation of almost arbitrary potential shapes. In addition, in many cases the resulting potential is independent of the atoms hyperfine state. This can allow for the simultaneous trapping of multiple spin states in the same potential.

The optical potentials for atoms are caused by the light-induced electric dipole moment of the atom. It oscillates at a fixed phase to the light wave and experiences an energy shift due to the interaction of the dipole with the electric field of the light. The effect can be described both in terms of classical electromagnetic dipoles and as quantized atom-photon interactions [68, 69].

The induced dipole $\boldsymbol{d} = \alpha(\omega)$ in the electric field $\boldsymbol{E}$ gives rise to an energy

$$E_{dip}(t) = -\boldsymbol{d} \cdot \boldsymbol{E} = -\operatorname{Re}(\alpha(\omega))\boldsymbol{E}^2(t) \tag{2.5}$$

where $\alpha(\omega)$ denotes the complex polarizability at the frequency ω. In the time-average, the potential resulting from a light intensity I is

$$V_{dip} = -\operatorname{Re}(\alpha(\omega))\boldsymbol{E}_0^2(t) = -\frac{1}{2\epsilon_0 c}\operatorname{Re}(\alpha(\omega))I. \tag{2.6}$$

Due to the induced oscillating electric dipole, the atoms can also emit radiation. The rate at which photons are scattered out of the light field is given by the imaginary part of the polarizability in a similar way as the dipole potential itself:

$$\Gamma_{scat}(\omega) = -\frac{1}{\hbar\epsilon_0 c}\operatorname{Im}(\alpha(\omega))I \tag{2.7}$$

Assuming that only one optical transition of frequency ω_0 of the atom has to be taken into account, the polarizability for the two-level system can for example be calculated assuming a classical dipole oscillator with damping rate Γ as

$$\alpha(\omega) = \frac{6\pi\epsilon_0 c^3}{\omega_0^2} \times \frac{\Gamma}{\omega_0^2 - \omega^2 - i(\omega^3/\omega_0^2)\Gamma}, \tag{2.8}$$

where Γ is the decay rate of the excited level [68]. Entering this into eqs. 2.6 and 2.7 and approximating for a large detuning $\Delta = \omega - \omega_0$, we obtain

$$V_{dip} = \frac{3\pi c^2}{2\omega_0^3} \times \frac{\Gamma}{\Delta} I \tag{2.9}$$

$$\Gamma_{scat} = \frac{3\pi c^2}{2\hbar\omega_0^3} \times \frac{\Gamma^2}{\Delta^2} I \tag{2.10}$$

The scattering of photons has to be avoided, as the energy transferred by scattering a single photon is much larger than the average thermal energy. Therefore, the rate must be low enough that each atom emits on average much less than one photon during the experiment. As the scattering rate scales as Δ^{-2}, whereas the potential depth V_{dip} scales as Δ^{-1}, this rate can be decreased for a given constant potential depth by increasing both the detuning Δ and the intensity I. The sign of the dipole

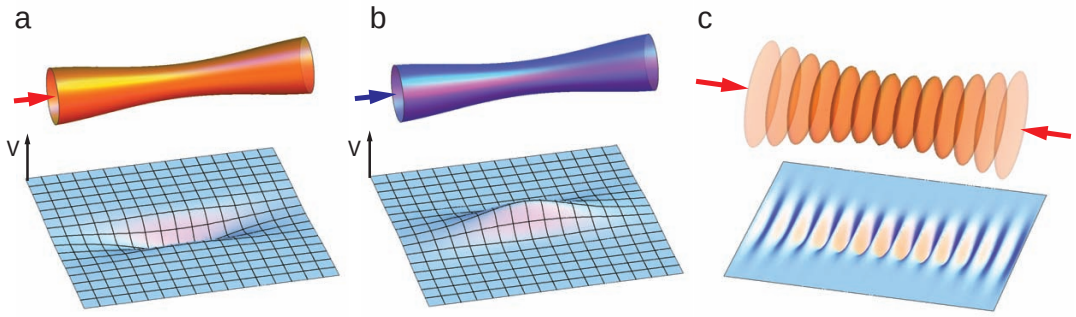

Figure 2.2: Optical dipole potentials: Light which is red detuned to the resonance of the atoms, creates an attractive potential V (**a**). Blue detuned light leads to a repulsive potential (**b**). By retro reflecting the light beam, an optical standing wave is formed, which creates a sinusoidal modulation of the potential along the axis of the beams (**c**).

potential U_{dip} depends only on the sign of the detuning Δ. If the light field has a negative detuning towards the resonance (red detuning), the potential is attractive and proportional to the light intensity as depicted in figure 2.2a. For $\Delta > 0$, the light creates a repulsive potential (Fig. 2.2b).

For all experiments discussed in this thesis the wavelength of the light is far detuned (typically tens of nanometers) from all optical resonances of the ^{87}Rb atom. As a consequence, the spontaneous scattering of light can be neglected. The detuning

is also large compared to the hyperfine splitting as well as the fine structure of the atoms. Together with the fact that all light beams discussed are linearly polarized, this results in potentials which can be treated as fully spin-insensitive.

2.2.2 Standing wave optical lattice

Periodic optical dipole potentials are often called optical lattices. The particular potentials used in the context of this thesis are formed by retro-reflecting a beam of light into itself. The resulting standing wave creates a potential which is sinusoidal with a periodicity of $a_{lat} = \lambda_{lat}/2$, as depicted in figure 2.2c. For red detuned light, it forms a series of potential minima with a flat "pancake" symmetry along the lattice beam.

Most lattice potentials discussed in the following have a simple cubic symmetry, which means they are periodic along all coordinate axes of a cartesian reference frame. For this, three independent standing waves are used to create three independent and orthogonal periodic potentials along each of the main coordinate axes of the trap. By choosing mutually orthogonal polarizations wherever possible and detuning the lattice beams by at least 20 MHz from each other, cross-interference between the beams vanishes in the time average. The resulting total potential is then simply the sum of all three periodic potentials. Its geometry is such that the potential min-

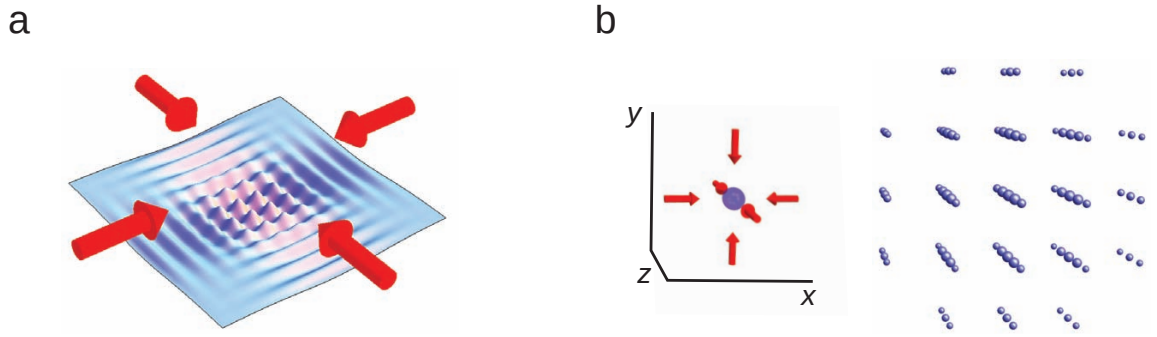

Figure 2.3: Optical lattices formed by orthogonal sinusoidal potentials. Counterpropagating laser beams along the principal coordinate axes create standing waves, and overlapping two (a) or three (b) of such potentials in a mutually orthogonal way creates a two-dimensional (a) or three-dimensional (b) optical lattice. The resulting geometry of the potential minima is that of a simple cubic crystal structure.

ima are aligned in a simple cubic lattice structure (figure 2.3). For most experiments, the depth of the potential along each of these axes is chosen to be the same, resulting in a uniform tunnel coupling strength to neighboring sites. Tunneling between sites which are not immediate neighbors along one of the lattice axes can usually be neglected, as will be discussed shortly.

2.3 Quantum mechanics of particles in periodic potentials

The quantum mechanics of particles in periodic potentials has a number of remarkable universal properties which are independent of the detailed shape of the potential. The most striking one is the energy spectrum of these systems, which typically consists of energy bands separated by energy gaps. While this happens almost independently of the specific potential, the exact shape has to be taken into account in order to determine the specific structure of these bands as well as the density of states within them. These calculations are described in most condensed matter physics textbooks [70, 71], therefore in the following we will shortly discuss the results for the specific band structure of ^{87}Rb in a sinusoidal potential with cubic symmetry.

2.3.1 Band structure

Since the 3D potential consists of a sum of three independent sinusoidal standing waves, the hamiltonian is separable into a sum of three independent one-dimensional hamiltonians, which can be evaluated separately. The solutions for these potentials with periodicity a are Bloch waves, which have the structure of a plane wave with a quasimomentum $|q| < \pi/a \cdot \hbar$ multiplied with a function u which has the same periodicity as the lattice potential (see e.g. [70, 71]):

$$\phi_q^n(x) = e^{iqx/\hbar} \cdot u_q^n(x) \tag{2.11}$$

For each quasimomentum q, many solutions are possible, which are identified by their band index n.

The natural energy scale for phenomena in periodic potentials is proportional to the kinetic energy of a particle with the maximum quasimomentum $q = \hbar\pi/a$ in free space, for example after sudden removal of the potential. This energy is

$$E_{q_{max}} = \frac{q_{max}^2}{2m} = \frac{h^2}{2ma^2}, \tag{2.12}$$

where m is the mass of the atom. In the context of optical lattices, the commonly used energy scale is the recoil energy, which corresponds to the kinetic energy an atom acquires due to the recoil motion from emitting a single photon of light at rest. It is given by

$$E_{\mathrm{R}}(\lambda) = \frac{p_{phot}^2}{2m} = \frac{h^2}{2m\lambda^2}, \tag{2.13}$$

with λ being the wavelength of the light. For an optical lattice produced by light with wavelength λ_{lat}, the lattice constant $a = \lambda_{lat}/2$, yielding $E_{\mathrm{R}} = \frac{1}{4}E_{q_{max}}$. Unless explicitly given, the E_{R} energy scale used in conjunction with a specific optical lattice with wavelength λ_{lat} is always $E_{\mathrm{R}}(\lambda_{lat})$.

The energy spectra for optical lattice potentials are shown in figure 2.4. Here, the

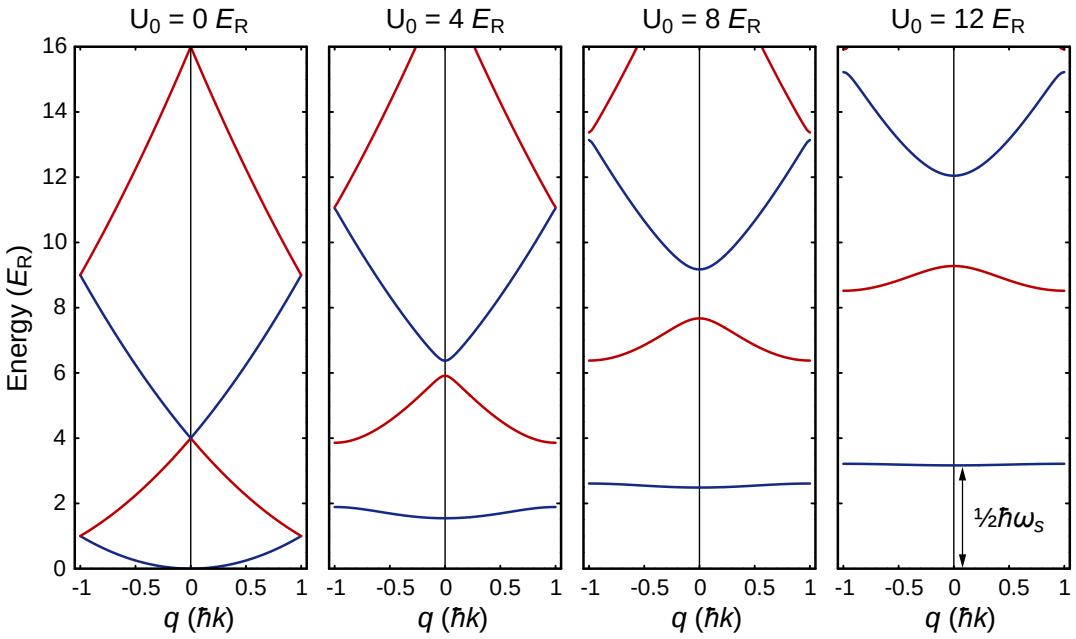

Figure 2.4: Band structure of a one-dimensional sinusoidal lattice with increasing lattice depth. The energy of each Bloch wave is plotted against the quasimomentum q, which can take any value between $-\hbar k$ and $\hbar k = \pi\hbar/a$. The solutions corresponding to bands with even band index are plotted in blue, those with odd band indices are plotted in red. For very deep lattices, the lowest bands are flat and tunneling is suppressed. The lowest band energy then corresponds to the lowest energy level of the on-site harmonic oscillator with frequency ω_s.

energies of all Bloch waves are plotted against their quasimomentum q. The band gaps first become visible between the lower bands. For deeper lattices, the bands become flatter and converge toward energy levels which are independent of q and separated by the band gaps. In the limit of very deep lattices, these correspond to the harmonic oscillator levels spaced according to the oscillator frequency ω_s as determined from the quadratic approximation of the potential around each minimum.

Wannier functions

While the Bloch wave functions are the eigenfunctions of the periodic potential, they are not a straightforward way to describe local phenomena which are restricted to individual lattice sites. For this, a representation using wave functions localized to the sites is preferable. All Bloch waves can be expanded in terms of Wannier functions, which are the wave functions within a given energy band which are maximally localized to one specific lattice site [70]. This makes them the natural choice for the on-site representation.

The Wannier functions $w_j^{(n)}(\boldsymbol{x}) = w^{(n)}(\boldsymbol{x} - \boldsymbol{x}_j)$ for band n and site j at position x_j

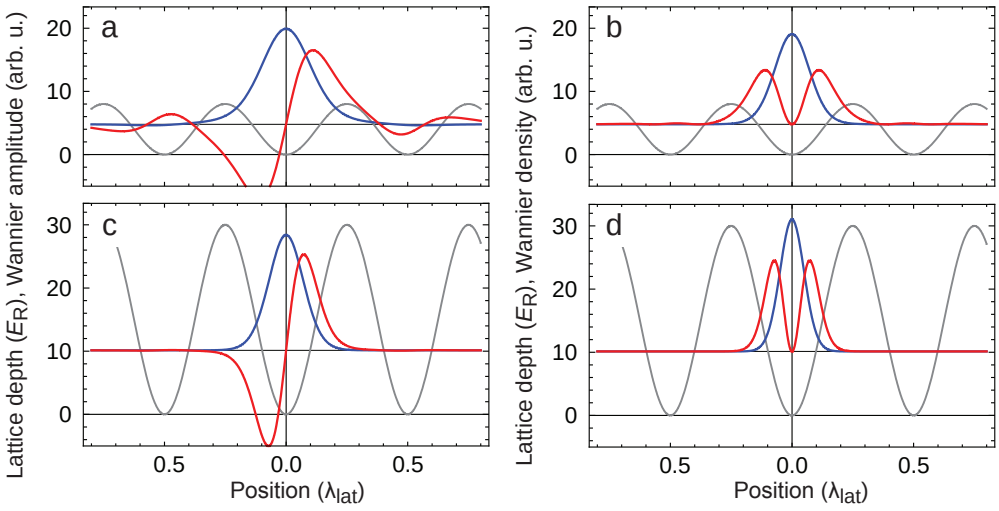

Figure 2.5: Wannier functions and the tight-binding limit: **a** and **b** show the Wannier function amplitude and density, respectively, for a lattice depth of $8\,E_R$. The blue curves correspond the the lowest (first) band Wannier functions, the red curves to those of the second band. For deeper lattices, as shown in the corresponding plots **c** and **d** for a lattice of $30\,E_R$ depth, the Wannier functions are more strongly localized to the potential minima and the overlap with neighboring sites is reduced. The lattice potential is shown in gray. The wave functions have been offset for clarity.

are formally defined from the set of Bloch waves $\phi^n_{\boldsymbol{q}}$ such that

$$\phi^n_{\boldsymbol{q}}(\boldsymbol{x}) = \sum_j w_j^{(n)}(\boldsymbol{x} - \boldsymbol{x}_j) e^{j\boldsymbol{q}\boldsymbol{x}}, \tag{2.14}$$

where q denotes the quasimomentum of the Bloch wave. The resulting functions for lattice depths of $8\,E_R$ and $30\,E_R$ are shown in figure 2.5. They form an orthonormal basis for the wave functions in a periodic potential, therefore the hamiltonian can be expressed in terms of the these functions as an alternative to the Bloch functions in order to obtain a description based on local properties.

Tight-binding limit

For shallow lattices, Wannier functions are not very localized and have significant overlap with many of their neighbors. In this case the localized Wannier basis is of little use, and it is usually easier to work in the Bloch basis. The situation is opposite for deep lattices, where the Wannier functions are tightly localized and usually only the coupling to the nearest neighbors is important. This is obtained by writing the

hamiltonian in the Wannier basis as

$$H = -\sum_{i,j,m,n} J_{i,j}^{(m,n)} \hat{a}_i^{(m)\dagger} \hat{a}_j^{(n)} \tag{2.15}$$

Here, $J_{ij}^{(n,m)}$ denotes the exchange integrals

$$J_{ij}^{(m,n)} = \int w_m^*(\boldsymbol{x} - \boldsymbol{x}_i) \left(\frac{-\hbar^2}{2m} \nabla^2 + V_{lat}(x) \right) w_n(\boldsymbol{x} - \boldsymbol{x}_j) d\boldsymbol{x} \tag{2.16}$$

and $\hat{a}_i^{(n)\dagger}$ is the operator creating a particle in the Wannier function localized at site i for the band n.

We will assume from now on that the system is cold enough that only the lowest band is significantly occupied, and therefore drop the band indices. By inserting the Bloch eigenstate basis, the hamiltonian is diagonalized and one obtains that $2J_{ij}$ corresponds to the $(i-j)$th Fourier component of the dispersion relation $\epsilon(q)$ [18].

For increasing lattice depths, the situation can be drastically simplified as the overlap integrals J_{ij} drop very fast with the distance of the sites i and j, and the dispersion relation $\epsilon(q)$ approaches a sinusoidal function. Neglecting an overall energy offset, one now can assume that $J_{i,j} = J$ if i and j denote neighboring sites, and $J_{i,j} = 0$ otherwise. J is value of the corresponding exchange integrals (usually termed "tunnel coupling"). In this tight binding approximation, the hamiltonian simplifies to

$$H = -\sum_{\langle i,j \rangle} J \hat{a}_i^\dagger \hat{a}_j, \tag{2.17}$$

where $\langle i, j \rangle$ denotes pairs of nearest neighbors i, j. It has an energy spectrum of

$$\epsilon(q) = -2J(1 - \cos(q \cdot a)), \tag{2.18}$$

so that the tunnel coupling J between neighboring sites in this approximation is directly related to the band width of the energy spectrum [72]

$$|J| \approx \frac{\epsilon(q)_{max} - \epsilon(q)_{min}}{4}.$$

2.3.2 Bose-Hubbard description for deep potentials

In the regime of deep lattices where the wave functions are strongly localized and the dynamics is restricted to tunnel processes between neighboring wells, it is straightforward to describe the system completely in terms of local properties and processes, including the interactions. This approach is followed in the Hubbard model [3], originally developed for electrons and therefore fermionic particles. Its bosonic variant,

the Bose-Hubbard model, uses the same approach but employs bosonic instead of fermionic operators [4].

The Bose-Hubbard hamiltonian is written in terms of the annihilation and creation operators $\hat{a}_i$ and $\hat{a}_i^\dagger$ for particles in a lattice site i to describe the local on-site interaction and nearest neighbor tunneling:

$$\hat{H} = -\sum_{<i,j>} J\hat{a}_i^\dagger \hat{a}_j + \sum_i E_i \hat{n}_i - \mu \hat{n}_i + \frac{1}{2}U(\hat{n}_i(\hat{n}_i - 1)) \tag{2.19}$$

Here, $\hat{n}_i = \hat{a}_i^\dagger \hat{a}_i$ is the number operator which determines the occupation of site i. The meaning of the four terms can be described as follows:

The first term corresponds to the kinetic energy of the particles in the tight-binding approximation as introduced in the previous section. It describes the dynamics in terms of the tunneling matrix element J, the tunneling rate between neighboring sites, neglecting direct tunneling over several sites. Usually only the lowest band is included, but the model can in principle also be used with higher bands, and the hamiltonian can be extended to a multi-band description. Values of J for typical experimental parameters are shown in figure 2.6. In the second term, the effect of an external potential is taken into account, which creates an energy offset E_i at site i. Usually, these offsets will be given by the external confining potential.

The next term introduces a chemical potential μ, creating a grand canonical description where the particle number is not fixed. For a given set of parameters, the atom number is set by the chemical potential. Finally, the last term of the hamiltonian describes the interaction between the particles. It includes only interactions between particles on the same lattice site and neglects all others. However, non-local interactions could be introduced by adding an additional interaction term. For atoms like ^{87}Rb, where the collisional point-contact interaction is by far the dominating mechanism, this is typically neglected.

The on-site interaction parameter U, also shown in figure 2.6, describes the energy shift due to the collisional interaction between two atoms localized on the same site. For a point-contact interaction and assuming a known on-site wave function $w(\boldsymbol{x})$, this energy is evaluated in the same way as the interaction integral in the mean field case discussed in section 2.1:

$$U = g \cdot \int |w(\boldsymbol{x})|^4 d\boldsymbol{x} \tag{2.20}$$

This makes the assumption that the on-site wave function of each of the two atoms is the same as that of a single atom. It neglects any changes to the wave function that the interactions can induce. Taking the repulsive interaction into account leads to a broadened wave function and modified particle-particle correlations. For low occupation numbers n this effect is relatively small in the case of ^{87}Rb, but can become significant for $n \geq 4$ [73]. Such modifications to the wave functions also affect the

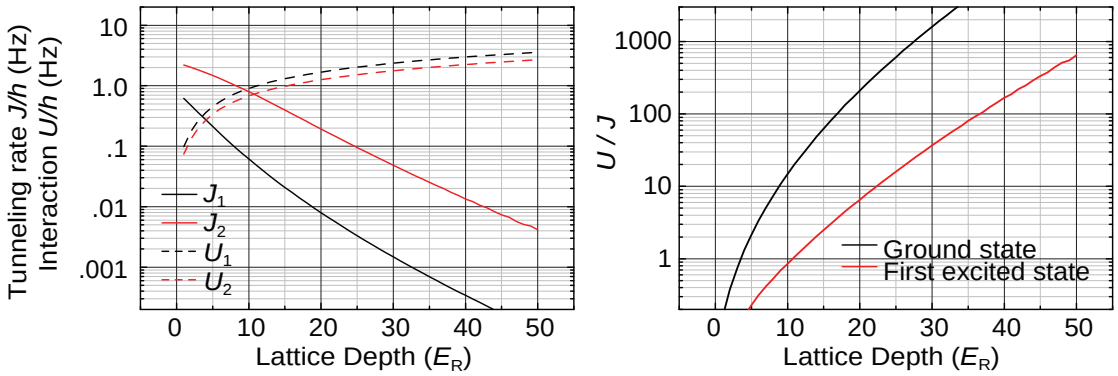

Figure 2.6: Tunnel coupling J and interaction energy U for different lattice depths. Increasing the lattice modulation leads to an increase in U (dashed) and an exponential decrease in J (solid, a). The ratio between the two varies over many orders of magnitude for typical experimental parameters (b). In both plots, the black line corresponds to the parameters for the lowest band, red lines to the values relevant for the first excited band.

tunneling parameter J. Calculations which do take modifications of the wave functions into account result in corrections to the parameters U and J on the order of 3-5% for strongly localized ^{87}Rb atom pairs in a lattice with typical parameters [74–76].

2.3.3 Superfluid to Mott insulator transition

In order to illustrate the properties of systems described by the Bose-Hubbard hamiltonian eq. 2.19, we will discuss the important limiting cases. We first assume a homogeneous system without any potential apart from the periodic lattice (i.e. $E_i = 0$). Therefore, for a given mean atom number per site $\bar{n}$, the ground state properties of the hamiltonian are completely determined by the parameters J and U.

Superfluid state

In the weak interaction limit $U \approx 0$, the system can be described as a Bose-Einstein condensed state in an optical lattice potential — all atoms are in the lowest energy single-particle state of this potential. This is the Bloch wave with zero momentum in the lowest band. To analyze this in terms of the Bose-Hubbard hamiltonian, we describe the wave function in terms of the states of the lattice sites.

The ground state wave function, given by the zero momentum Bloch wave, is the sum of the Wannier wave functions (eq. 2.14) at each lattice site i with constant phase

$$|\Psi\rangle = \alpha \sum_i \hat{a}_i^\dagger |0\rangle,$$

with the normalization factor α. This yields the ground state for N particles on M

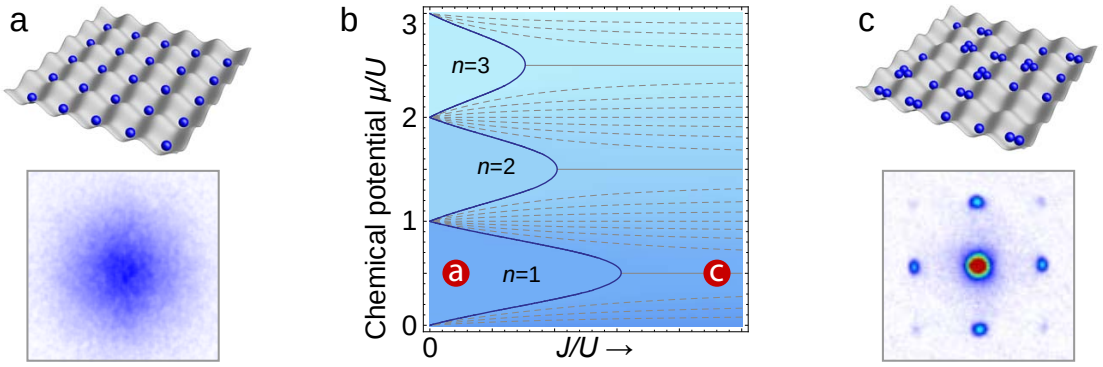

Figure 2.7: The Bose-Hubbard model has two very distinct phases for $T = 0$. The Mott insulator state for low J has a well-defined occupation number on each site, but no global phase coherence, so no interference can occur for the matter wave (a). The schematic phase diagram (b) shows the phase boundaries as blue lines as well as the two states shown marked in red. The color shading from blue to white in (b) indicates increasing on-site density. In the superfluid state, the phase is well-defined for all sites, resulting in an interference pattern in the matter wave created when releasing the atoms to free space (c). The on-site atom numbers in this state are Poisson distributed.

lattice sites

$$|\Psi\rangle^N \propto \frac{1}{\sqrt{M}} \left(\sum_{i=1}^{M} \hat{a}_i^\dagger \right)^N |0\rangle.$$

In the limit of a large system size $M, N \to \infty$ with constant average occupation $\bar{n} = N/M$, this state becomes separable into a product of single site states. At each site i, a superposition of Fock states $|k\rangle_i = (\hat{a}_i^\dagger)^k |0\rangle$ with all possible occupations k is present. This is illustrated in figure 2.7c — while the average density is well defined and constant over the lattice, the atom number determined by measuring each individual site is randomly distributed.

In this situation the ground state is the state $|\Psi\rangle$ for a given average on-site particle number $\bar{n}$ which maximizes $\langle\Psi| \sum_{<i,j>} \hat{a}_i^\dagger \hat{a}_j |\Psi\rangle$ for neighboring sites i and j. For a state $|\Psi\rangle = \prod_i |\Psi\rangle_i$ consisting of a product of states $|\Psi\rangle_i$ for each site i this is the case for $|\Psi\rangle_i$ which are eigenstates of the operators $\hat{a}_i^\dagger$ and $\hat{a}_i$. An appropriate basis for this is given by the coherent states or Glauber states [4, 77]

$$|\Psi(\bar{n})\rangle_i = \mathrm{e}^{-|\alpha_i|^2/2} \sum_{n=0}^{\infty} \frac{{\alpha_i}^n}{\sqrt{n!}} |n\rangle_i, \tag{2.21}$$

where α_i denotes the wave function phase and the expectation value of the atom number $\bar{n} = |\alpha_i|^2$ at site i. The ground state has constant phase and constant density throughout the lattice:

$$|\Psi(\bar{n})\rangle = \prod_i \mathrm{e}^{-|\alpha|^2/2} \sum_{n=0}^{\infty} \frac{\alpha^n}{\sqrt{n!}} (\hat{a}_i^\dagger)^n |0\rangle \tag{2.22}$$

This ground state of the system when the on-site interaction U is small compared to the tunneling strength J is commonly named the superfluid state, as there is no resistance to mass flow.

Mott insulator state

When increasing the interaction relative to the tunneling strength, the properties of the system change drastically. With increasing U, the system reaches a quantum critical point which marks the transition from the superfluid to the Mott insulator. The position of this point varies with the filling of the sites. For a filling of $n = 1$, mean-field theory predicts it at $U/J = 5.8 \cdot z$, where z is the number of nearest neighbors of a given site [4, 78–80]. Newer calculations taking corrections to the mean-field approach into account report different values. Recently, a critical ratio of $U/J = 4.89 \cdot z$ has been obtained by three-dimensional lattice Quantum Monte Carlo calculations (see [81] and references therein). For large occupation numbers, the critical ratio approaches $U/J = z \cdot 4n$ [82]. At sufficiently low temperatures, the transition itself is a quantum phase transition, which is not driven by thermal fluctuations [83].

Figure 2.7b schematically shows the phase diagram of the $T = 0$ Bose gas in the μ–J plane. For large J the system is superfluid, whereas for low J there exist a number of distinct areas ("Mott lobes") in which the system is insulating [4]. The density in each of these Mott lobes is an integer number of particles per site, determined by the chemical potential. For $J = 0$, the Mott lobes are not separated by a superfluid phase, and the density undergoes discrete steps when increasing the chemical potential.

This limiting case can be easily understood. Since the interaction energy for a given site scales quadratically with site occupation, fluctuating site occupations increase the total interaction energy, and the ground state of a system with an integer average filling n is given by a product of identical Fock states

$$|\Psi\rangle \propto \prod_i |n\rangle_i,$$

where the atom number on each site i is exactly n (fig. 2.7a).

In homogeneous systems, the average filling $\bar{n}$ could also be non-integer, in which case the ground state is more complicated, but can be described as a Mott insulator with an occupation $\lfloor \bar{n} \rfloor$ coexisting with a hard core gas of strongly interacting bosons with an average density of $\bar{n} - \lfloor \bar{n} \rfloor < 1$. Here, $\lfloor x \rfloor$ denotes the largest integer value y such that $y \leq x$.

With a fixed atom number on each site in the Mott insulator state, the conjugate variable which is the phase of the wave function on each site has the maximum uncertainty. It is completely undefined, so no interference can occur between the matter waves released from these sites (fig. 2.7a). This is in strong contrast to the superfluid case where the phase is well-defined throughout the whole ensemble.

While the global phase coherence is completely lost in the Mott insulator due to the localization of the atoms, locally this is not entirely the case. Due to the fact that J is small compared to U, but necessarily finite in order to obtain equilibrium, corrections to the ground state beyond leading order create a small admixture of particle/hole pairs. For weak tunneling these pairs are very localized such that the hole and particle admixtures are on neighboring sites. This local coherence can be detected by analyzing the corresponding weak interference between atoms released from the lattice (see section 3.2.1) which persists even in the Mott insulating regime. Deep in the insulating regime, interference pattern is further suppressed proportionally to J/U as $J/U \to 0$ [84, 85].

2.3.4 The influence of the confining potential

In the real lattice potential, the system is not homogeneous but has a finite size. It is confined by the parabolic magnetic trap as well as the overall profile of the laser beams which produce the lattice potential. This latter confinement is created by the attractive potential of each red-detuned beam along the two axes orthogonal to its propagation direction. As the size of the beams is typically much larger than the size of the atom cloud, the potential can usually be described as a homogeneous periodic lattice potential with an additional harmonic confinement. Locally, on each site the chemical potential is therefore reduced by the potential energy shift of that specific site. It consists of two parts, one being the external confining potentials such as from the superimposed magnetic trap, and the other from the local zero point energy of the lattice site ($1/2\hbar\omega_s$). Close to the center of the trap, these can typically be combined to a parabolic confinement. This results in a total potential energy E_i of site i at position (x_i, y_i, z_i) as

$$E_i = \frac{1}{2} m(\Omega_x^2 x_i^2 + \Omega_y^2 y_i^2 + \Omega_z^2 z_i^2),$$

for a harmonic confinement with trap frequencies $\Omega_{\{x,y,z\}}$ along the x, y and z axes.

Superfluid Case

In the weakly interacting case, the situation is comparable to the situation without the periodic potential: Within the given band, the kinetic energy is reduced compared to the case without the lattice, due to the reduced curvature of the dispersion relation[1]. The external potential then reduces the local chemical potential in the same way as in the Gross-Pitaevskii equation, and we arrive again at the Thomas-Fermi distribution in the weakly interacting limit. The on-site wave function is described by the coherent states which minimize the dominating tunneling term. The average occupation

[1] The very large kinetic energy component due to the zero-point on-site energy can be subtracted as it is only a constant offset.

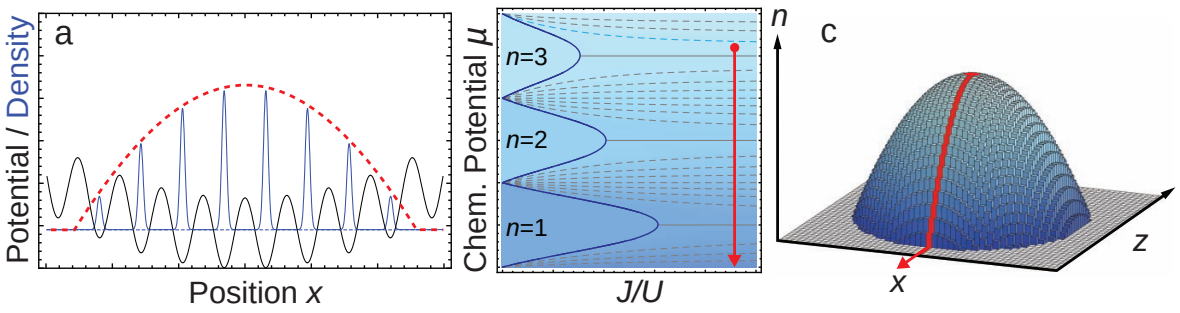

Figure 2.8: Geometry of the superfluid phase in the lattice with confinement (black line in a). The atoms are delocalized over the lattice, with the local density of the wave function shown in dark blue. Its global shape is given by the Thomas-Fermi distribution (red dashed line). The ensemble occupies a range of points in the schematic phase diagram (red line), as the chemical potential changes with the distance from the center of the trap (red circle). The resulting density distribution in a 2D plane of the cloud is the Thomas-Fermi distribution (c).

number is determined by minimizing the local potential energy and chemical potential terms. For a given chemical potential μ, minimizing each site individually then yields

$$\bar{n}_i^{\mathrm{TF}} = \frac{\mu - E_i}{U} \tag{2.23}$$

for all sites with $\mu \geq E_i$. For sites with $\mu < E_i$, $\bar{n} = 0$ to exclude negative densities. For $\Omega_{\{x,y,z\}} = \Omega$, this results in the Thomas-Fermi distribution

$$\bar{n}_i^{\mathrm{TF}} = n_0 \max(0, 1 - (x^2 + y^2 + z^2)/R_{\mathrm{TF}}^2). \tag{2.24}$$

Here R_{TF} is the Thomas-Fermi radius such that the potential energy at this radius equals the global chemical potential, and $n_0 = \mu/U$ is the central density.

2.3.5 Mott insulator in confining potential: the shell structure

In the limit of $U \gg J$, the tunnel coupling can be neglected even for the determination of the on-site states. Now the complete distribution is determined solely according to the interactions and the potential energy terms. Like in the homogeneous case, fluctuations of the on-site occupation are suppressed due to the quadratic term in the interaction energy. In contrast to the homogeneous case with a fixed average site occupation, however, the ensemble in the trap, where only the global chemical potential is fixed, is not forced to non-integer occupation numbers. The hamiltonian with neglected tunneling term

$$H = \sum_i E_i \hat{n}_i - \mu \hat{n}_i + \frac{1}{2} U(\hat{n}_i(\hat{n}_i - 1))$$

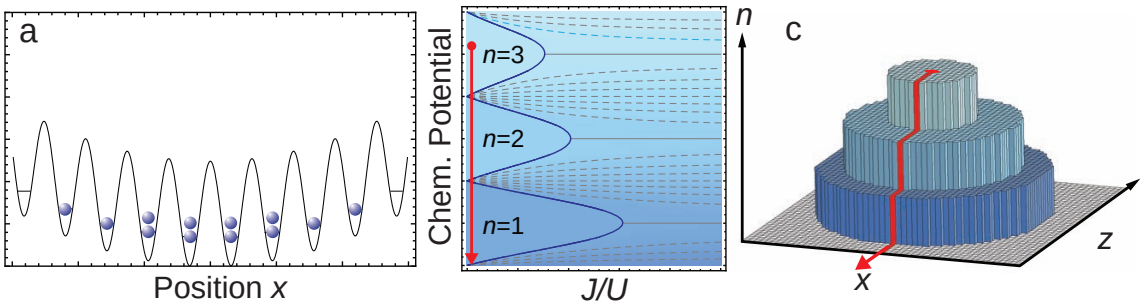

Figure 2.9: Mott insulator in a confining potential. Each atom is confined to a single site of the potential (a), with the energetically lowest lying sites occupied first. The chemical potential changes with the distance from the trap center, and different parts of the ensemble can be in different phases of the schematic phase diagram (b). The result is a shell structure of regions with constant density phases (c).

is then minimized for a filling

$$n_i = \left\lfloor \frac{\mu - E_i}{U} + 1 \right\rfloor,$$

for $\mu > E_i$ and $n_i = 0$ otherwise. In the case of a parabolic and spherically symmetric confinement, the density therefore decreases in discrete steps from the center to the edge of the cloud. The outer edge of the distribution is defined by $\mu = E_i$. For a parabolic confinement with trap frequency Ω_t, $E_i = \frac{1}{2}m\Omega_t^2 r_i^2$, where r_i is the distance of the site i from the trap center. The cloud therefore has an overall radius

$$R = \sqrt{2\mu/m}/\Omega_t.$$

Outside the sphere of radius R, there are no atoms. Inside the sphere, all sites are occupied by at least one atom. The condition for occupation of a site with more than n atoms is $\mu > (n-1)U - E_i$. These regions are again spherical with an outer radius $R_n = \sqrt{2(\mu - n \cdot U)/m}/\Omega_t$. The density distribution is therefore a series of concentric shells around the trap center, with an occupation n within the interval R_{n-1} to R_n.

The density as a function of the distance from the center of the parabolic trap and within a two-dimensional plane through the center is shown in figure 2.9. Due to the shape in the 2D plane, this distribution is often described as the "wedding cake structure". For small but finite J, the Mott shells are separated by regions with superfluid properties.

2.4 Shell structure at non-zero temperatures

The temperature of a quantum gas in the strongly correlated state is a very important parameter for the correct description of the state of the ensemble. Unfortunately, for

systems in interesting parameter ranges, it is notoriously hard to measure. For weakly interacting quantum gases, the temperature is typically determined by measuring the momentum distribution by a ballistic expansion. The temperature is derived from the wings of the distribution, outside the Thomas-Fermi part of the cloud. For the very low temperatures discussed here this is already hard, due to the very small fraction of atoms in this "thermal part" of the distribution. It is not possible in the strongly correlated regime in the optical lattice, since the momentum spectrum in the lowest band is flat, and the interactions lead to a momentum spread over the full Brillouin zone even at zero temperature.

The finite temperature state of the ensemble for very low temperatures can usually described in terms of the ground state with a small fraction of excitations. In the following we will analyze the thermodynamics of fully localized bosons in the deep optical lattice, showing the effect of the dominant excitations in that regime [86]. In reverse, this highlights a way to measure the temperature without relying on the momentum distribution.

In the limit of negligible J, we can describe the ensemble of particles purely in terms of the chemical potential μ, the interaction energy U and the external potential E_i at position i. Particle exchange between the sites is allowed, but since we assume a negligible energy scale for tunnel coupling, the thermodynamical partition function of the ensemble can be separated into individual single site partition functions:

$$z_i = \sum_{n_i=0}^{\infty} \exp\left(-\beta\left(U \cdot n_i(n_i-1)/2 - (\mu - E_i)n_i\right)\right) \tag{2.25}$$

Here, $U \cdot n_i(n_i-1)/2$ is the total interaction energy in the site i, $\beta = 1/(k_B T)$, and the summation is over all occupation numbers n_i on this site.

The probability of the number state $|n\rangle_i$ is then given by

$$P_i(n_i) = \frac{1}{z_i} \exp\left(-\beta\left(U \cdot n_i(n_i-1)/2 - (\mu - E_i)n_i\right)\right) \tag{2.26}$$

And the average occupation is $\sum_{n_i} n_i \cdot P_i(n_i)$.

The result of such a calculation for trap geometries analog to those in the experiment is shown in figures 2.10 and 2.11 for atom numbers $N_{tot} = 1.0 \cdot 10^5$and $N_{tot} = 10 \cdot 10^5$, respectively. The four columns represent the results for four different temperatures. The rows of graphs show some specific resulting observables which can be measured experimentally. In the experiments presented in this thesis, only density distributions which are integrated along one or more coordinate axes can be obtained. Therefore, the top row of graphs shows the 3D distribution, whereas in the other rows, each distribution shown is derived from the previous one by integrating along one of the remaining coordinate axes. In the last row only total populations integrated of the full ensemble are given.

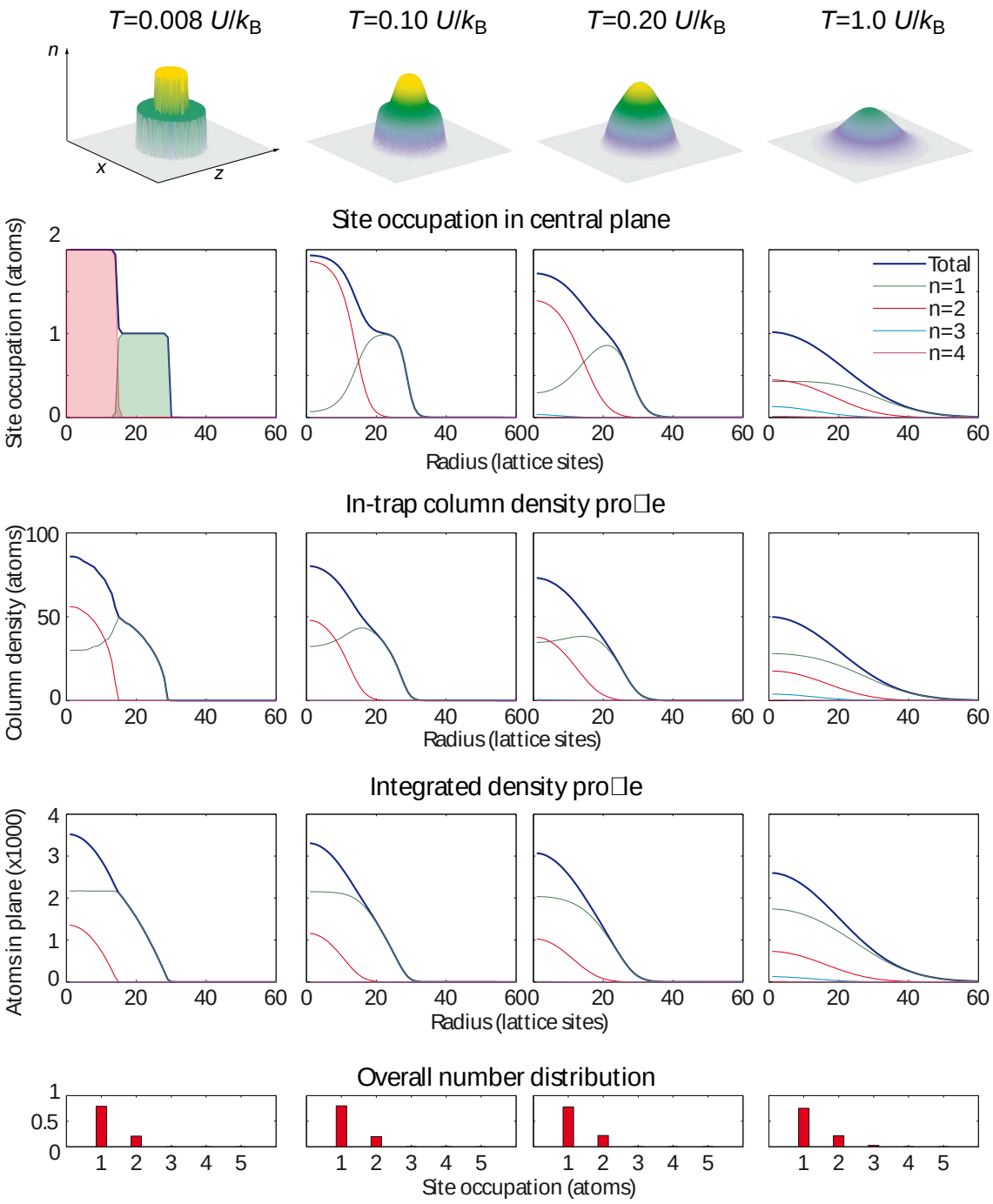

Figure 2.10: Calculated Mott shell structure for different temperatures T and approximately 10^5 atoms in a trap corresponding to the one used in the experiment. The top two rows show the on-site density both in the central plane and along one line through the center. The third row shows the column densities obtained by integrating along the z-axis, and the fourth row the number of atoms in each lattice plane, obtained by integrating along x and z. The lowest row shows the total population of atoms in each fock state. The contributions by each of these number states to the total profiles shown above are shown in color.

Density (atoms per site)

At the top of the page, the density distribution in the central plane of the cloud is shown for the full plane. The second row gives the same information along one line from the center to the edge of the cloud. In addition, the contributions to this density from each of the number states are shown separately. For zero temperature, this shows the well-known "wedding cake" structure of the Mott insulator shells, with up to five layers or shells for large atom numbers (fig. 2.11). These shells do not overlap and the density is constant within their volume. For the low atom numbers shown in figure 2.10 the density in a core with a radius of 15 lattice sites is due to doubly occupied sites ($n = 2$), whereas all sites outside of this radius and up to $r = 28$ are occupied by exactly one atom. Increasing the temperature "melts" this shell structure: Already at $k_B T = 0.1\,U$, the steps are significantly washed out due to particle-hole excitations close to the shell edges. At a temperature of $k_B T = 0.2\,U$, the shells start to disappear completely and the local density is strongly smoothed.

At this temperature the system is still far from being described as a non-interacting classical gas. For this, the temperature has to be larger than the interaction energies present. For the low densities this transition happens around $k_B T = 1.0\,U$, which is the point where the minimum in the center of the $n = 1$ site distribution completely disappears.

For higher atom numbers (fig. 2.11), the low n distributions do not lose this minimum even further into the fully thermal regime due to the Poisson on-site statistics and the increased interaction energy scales. The outermost ($n = 1$) distribution even has a minimum at $k_B T = 3\,U$, where the cloud is already reasonably well described by a classical Boltzmann gas. The influence of the heating is strong for the innermost shells, however, with the overlap between the $n = 1$ and $n = 2$ shells increasing first. The shell structure itself melts at a similar temperature as for low densities and is strongly smoothed by $k_B T = 0.15\,U$.

Integrated (column) density

The density of atoms at a given point in three-dimensional space is often not experimentally accessible. Typically, methods for probing the density distribution integrate over parts of the cloud. The standard method for recording the density distributions is absorption imaging (see sec. 3.2) in the trap, which yields the column density of the cloud integrated along the line of sight of the camera. The second row of figures shows this column density integrated along the z-axis plotted against distance from the center of the cloud along the y-axis. Similar to the first row, the density components from each of the number states are also given, which can be probed if in-trap absorption imaging is combined with a number-state selective process [73]. Due to the integration, the constant density in the shells does not show directly anymore, but the outer ($n \leq n_{max}$) density components still have a ring shape in 2D. The column

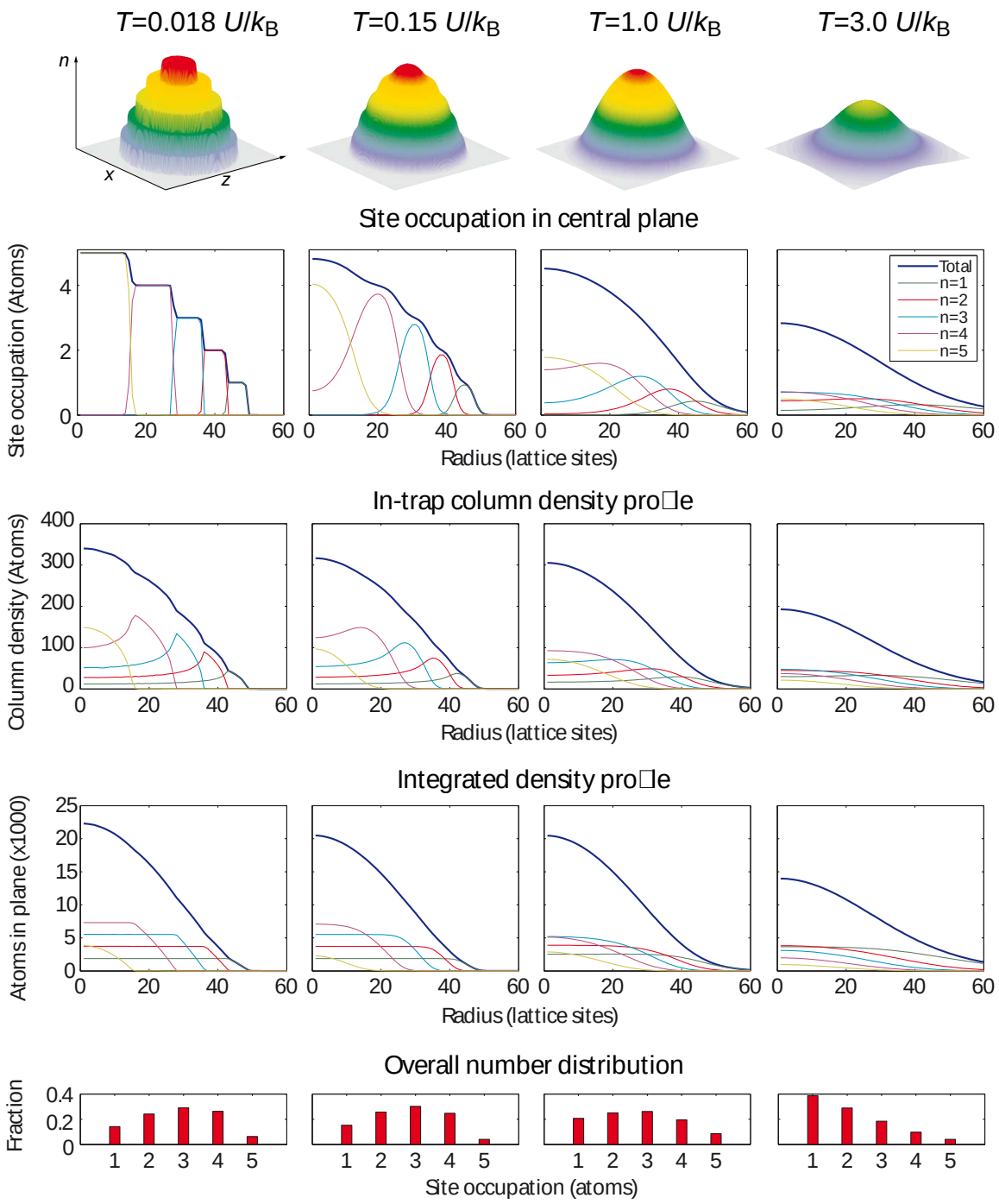

Figure 2.11: Predicted Mott shell structure for larger average filling due to a larger atom number (1.0×10^6) in a strongly confining trap. In this configuration, five concentric shells exist for $T = 0$ The shell structure melts around $k_B T = 0.15\,U$ and the system becomes fully thermal for $k_B T \geq 3\,U$.

density of this component, however, is not constant within this ring shape and is low but does not vanish in the interior of the ring. This ring-like shape with a minimum of the column density disappears completely only at $k_B T \approx U$ or even larger. The exact shape of the rings for low temperatures with the two sharp edges is, however, characteristic for the constant density outer shells.

1D density profile

By integrating over a whole plane which is displaced by a distance x from the center of the trap, a linear density profile of the cloud is obtained. This type of profile corresponds to the observable measured in the experiments presented in section 4.2 [87]. Here, all atoms in a horizontal plane are addressed and collectively counted, leading to an integrated one-dimensional density profile. In this case, no minima are recorded in the center of the trap, and the signature of the shell structure is visible in the total profile as a sharp outer edge as well as a kink at every position corresponding to a shell boundary. Between these, the shape is given by inverted parabola functions.

The profiles from each of the individual number state components in the $T = 0$ Mott insulator case are characterized by a sharp edge at the outer boundary of the shell and a kink at the inner edge. The shape between the inner and outer radius of the respective shell is given by an inverted parabola, which is "truncated" at the inner shell boundary. This can be shown by integrating a constant density spherical shell with the inner and outer radius r_i and r_o over a full plane. This profile can be evaluated as the difference between the profile of a sphere with radius r_o and that of a sphere with radius r_i:

$$n_{tot}(y) = \int_x \int_z n_0 \frac{1}{2} \left(h(r_o^2 - x^2 - y^2 - z^2) - h(r_i^2 - x^2 - y^2 - z^2) \right) dx, dz$$

Where $h(x)$ is the Heaviside function with $h(x) = -1$ for $x < 0$, $h(0) = 0$ and $h(x) = 1$ for $x > 0$.

This leads to the truncated parabola profile

$$n_{tot}(y) = \begin{cases} n_0 \pi (r_o^2 - r_i^2) & y < r_i \\ n_0 \pi (r_o - y^2) & r_i \leq y \leq r_o \\ 0 & y > r_o \end{cases} \tag{2.27}$$

This structure is lost when the temperature is increased: At a temperature of $k_B T = 0.1\,U$, the edges of the density distribution for low atom numbers start to be significantly washed out on the scale of a few lattice sites. For higher temperatures the edges and then the flat top of the parabola shape are quickly lost completely, and at $k_B T = 1.0\,U$, all profiles are closer to gaussian distributions than those obtained from a Mott insulator. For larger atom numbers the change is not so obvious for the profiles corresponding to low n. While all edges are strongly smoothed at $k_B T = 0.15\,U$,

a flat top remains in those shells even for very high temperatures. Only the innermost hollow shell (second largest n) does lose this flat top property almost simultaneously with the breakdown of the Mott shell structure.

Identifying the Mott shell distribution therefore gives an effective upper estimate on the temperature of the gas in the lattice with parameters corresponding to the ones shown. If a succession of sharply separated shells is present, the temperature must be smaller than $k_B T \approx 0.2\,U$ in such a lattice.

Overall number state populations

Finally, when integrating all number state components over the last remaining coordinate axis, we obtain the global number state distributions of all sites in the trap. The last row of plots shows the fraction of the overall atom population residing in sites with a given occupation number. These observables correspond to the measurements which will be described in section 4.1 of this thesis [88]. For most configurations, the distribution is only changed when particle-hole pair excitations are created in the bulk of the Mott shells. These excitations have an energy scale of U, therefore the distribution as shown here is largely unaffected until $k_B T \approx U$, and it is only suitable for measuring temperatures larger than the U/k_B scale.

The distribution is, however, very sensitive to the changes of the tunnel coupling J even in the regime of very low temperatures. Also, since larger populations are counted when determining these fractions experimentally, the dependence of the relative populations can be measured efficiently for many different sizes of the ensemble with a good signal to noise ratio. This allows for the direct observation of number squeezing without spatial resolution, and of the critical atom numbers which mark the boundary for the formation of additional shells. These important properties of the transition from the superfluid to the Mott insulating regime will be investigated experimentally in the following section.

3 Experimental setup and techniques

The experimental setup used for the projects presented in this thesis was originally developed in Munich [89, 90], and was taken apart and the parts transported to Mainz with only the vacuum chamber kept assembled. Subsequently, the setup was rebuilt in the course of the following year. While some parts were redesigned in the process and many components were exchanged, the basic setup has stayed the same and as such has been described in several publications [89–94]. In the following therefore only a brief introduction of the operating principle and the key properties will be given. The description will be detailed only in those aspects with special relevance for the experiments discussed in the later chapters. Some very specific parts of the setup, such as the additional laser setup for the superlattice potentials, will be introduced in the chapter describing the corresponding experiments.

Typically, the experiments are conducted in cycles, each lasting approximately one minute. Each cycle consists of a number of steps to prepare the quantum gas, conduct the actual experiment and then measure the result. In the first step, a magneto-optical trap (MOT) is used to collect atoms from a room temperature gas within 15 s. This trap also cools the atoms, especially in the last phase which employs an optical molasses. In the next step the atoms are confined by a magnetic quadrupole trap and then transported from the MOT chamber to a second chamber with very low background pressure. In the third step, the pure quadrupole trap is modified to a tightly confining quadrupole-Ioffe configuration (QUIC), and the cloud is cooled further for up to 30 s evaporative cooling until a BEC is formed. The QUIC trap current configuration is then changed to achieve a spherical BEC in a weakly confining trap.

At this point, the optical lattice potential is introduced by adding mutually orthogonal standing waves which intersect at the BEC position. This starts the actual experiment which typically involves manipulating the atoms in the lattice by laser potentials, radiofrequency waves and magnetic fields. At the end of the cycle, the trap is typically switched off quickly, and the atom ensemble ballistically expands in free space. After a short time of free flight, the spatial distribution of the expanded cloud is recorded by an imaging system. The image is then downloaded into a computer for analysis, and the next experiment cycle is initialized.

3.1 Implementation of the experiment

All of the steps outlined above can only be realized in an ultra-high vacuum (UHV). Characteristic for for vacuum setup used (shown in figure 3.1) is the spatial separation of the chamber used for the magneto-optical trap (MOT) from the main vacuum

chamber in which the Bose-Einstein condensation is achieved and the subsequent experiments are conducted.

3.1.1 BEC preparation

Magneto-optical trap and magnetic transport

The MOT collects ^{87}Rb atoms from the room-temperature vapor inside the chamber and cools them to temperatures in the millikelvin range [69, 95]. Furthermore, the cloud is compressed toward the center of a magnetic quadrupole field. The MOT is followed by an additional optical molasses phase [96] for further cooling into the microkelvin range before loading the atoms into a magnetic trapping potential [97, 98]. The magnetic trap consists of a quadrupole field of the same geometry as the MOT field, but with a much stronger gradient. Since the atoms are actively pumped into the $F = 1, m_F = -1$ hyperfine state after the molasses stage, they are low-field seekers and are trapped by the field minimum in the center of the quadrupole. The two chambers are connected by a series of additional quadrupole coils which can be switched in sequence [90]. In this way, the atoms are "handed over" from one quadrupole field center to the next, first along the x-axis and then the z-axis (yellow arrow in figure 3.1), over a total distance of $\approx$ 40 cm. One big advantage of this transport design is the possibility to use a simple MOT implementation which directly loads from a background vapor of ^{87}Rbat a relatively high pressure (typically several 10^{-9} mbar) without the need of an additional cold atom source such as a 2D-MOT or Zeeman slower. The rubidium vapor is injected into the MOT chamber from a small oven section which can be heated to increase the vapor pressure. The BEC chamber into which the atoms are transported is a glass cell with a much lower pressure (below 10^{-10} mbar). Here, the rate of atom loss and heating through background gas collisions is low enough to enable Bose-Einstein condensation. Another advantage of the transport scheme is the good optical access to the BEC along all axes since no MOT optics have to be placed around this chamber.

Magnetic trap and Bose-Einstein condensation

While a quadrupole field is a very simple and effective way to trap large amounts of atoms in low-field seeking states, it is generally unsuitable for Bose-Einstein condensation. The reason for this is the field geometry in the trap potential minimum. Here the field strength vanishes, and its direction changes rapidly around this point. This means that for atoms passing the trap center at a close distance, the Larmor precession frequency is low enough that their spin does not adiabatically follow the rapidly changing field direction. This leads to spin-flips, and a subsequent loss of these atoms from the trap, since in the $F = 1$ manifold only the $m_F = -1$ state is low-field seeking. These so-called Majorana losses become a problem when the density

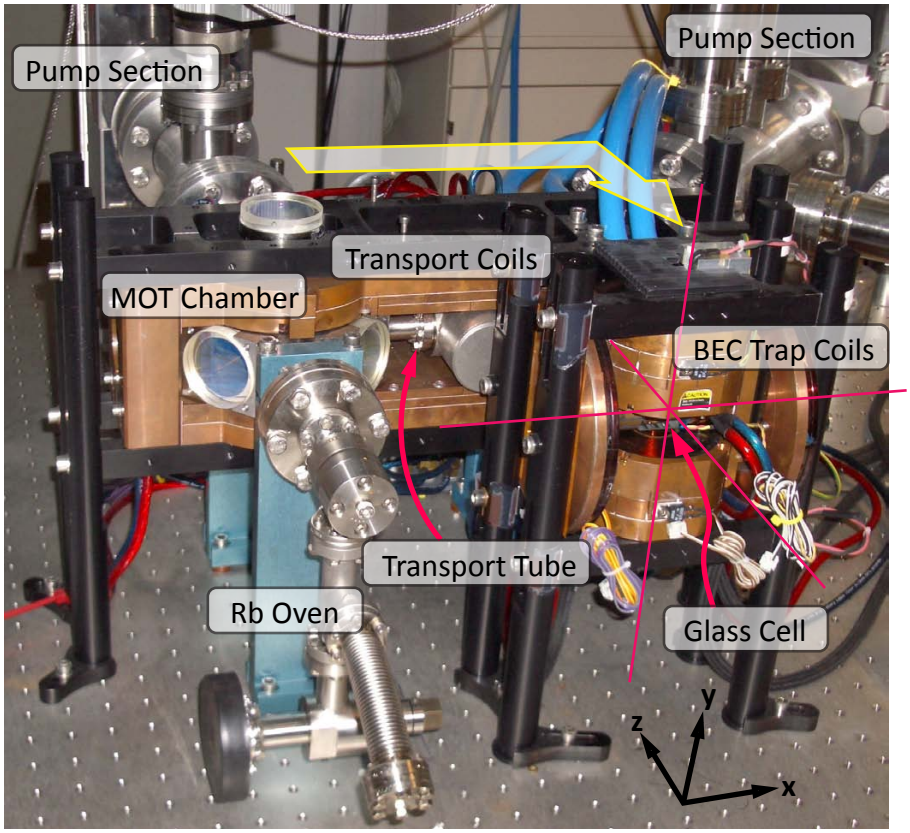

Figure 3.1: Image of the experimental setup before the addition of the optical components. The experiment is separated into two sections, the MOT chamber and the BEC chamber. The large yellow arrow indicates the transport between the two through the transport tube. The red lines illustrate the orientation of the three lattice beams intersecting in the BEC position.

of the atoms close to the center of the trap increases. This occurs when approaching quantum degeneracy, and prevents the onset of Bose condensation in such a magnetic field geometry.

Numerous solutions exist to circumvent this problem by creating trapping potentials in which the overall potential has a minimum with non-vanishing field strength. For the experiment presented here, a static magnetic trapping field created by magnetic coils in the so-called Quadrupole-Ioffe Configuration (QUIC) is used [99]. After the transport, the trap is therefore changed from the quadrupole to the QUIC geometry by increasing the current in the Ioffe coil, an additional coil oriented perpendicularly to the quadrupole pair (see figure 3.2). The resulting magnetic field configuration has a minimum on the Ioffe coil axis in between the quadrupole field center and the Ioffe coil. This leads to a displacement of the cloud by several mm toward the QUIC coil. In the new trap minimum, the magnetic field has a strength of several Gauss, which prevents the occurrence of Majorana losses. Close to the minimum,

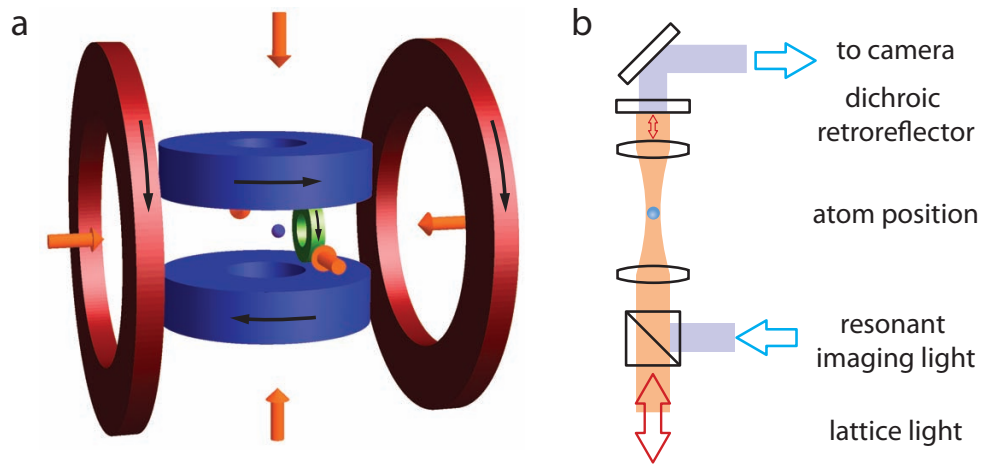

Figure 3.2: Schematic drawings of the magnetic trap components (**a**) and the optical lattice setup (**b**). The primary trapping coils (blue) are operated in a quadrupole configuration. The glass cell (not shown) is located between these coils. A third coil (green) allows the transformation from a quadrupole to a quadrupole-Ioffe configuration (QUIC), displacing the atom cloud (blue sphere) slightly to the right. To change the trap to a more spherical geometry, two offset coils (red) close to Helmholtz configuration provide a 150 G offset field. **b** A red-detuned (typical wavelength 840 nm) lattice beam is retroreflected by a dichroic mirror, forming a standing wave potential. The atoms are located in the beam waist formed by two lenses outside of the vacuum setup. A resonant imaging beam is superimposed onto the same beam path. The retroreflector is transparent for this wavelength, allowing for imaging directly along the lattice axis.

the trap can be approximated by a 3D parabolic potential with the trap frequencies $\omega_x = 2\pi \times 15$ Hz, $\omega_y = 2\pi \times 120$ Hz and $\omega_z = 2\pi \times 120$ Hz.

In this trap configuration, the temperature of the cloud is further reduced by radiofrequency (RF) evaporation (see e.g. [43, 69]). This method exploits the fact that only one m_F-state in the $F = 1$ manifold is magnetically trapped. Transitions between the Zeeman sublevels can be driven by a radiofrequency field, the resonance frequency of which strongly depends on the magnetic field present. The transition frequency in the potential minimum is typically 2.5 MHz for the trap described above. If an RF field with a higher frequency is present, atoms at certain distances from the trap center are in resonance. Such fields are therefore a way to selectively change the m_F state of atoms in the outer regions of the cloud. Since these atoms are then no longer trapped, they are efficiently removed from the ensemble. By selectively removing only the outermost atoms of the cloud, which have the highest energy, the average energy of the sample reduces and the cloud equilibrates at a lower temperature. By slowly decreasing the RF frequency, the temperature is reduced by several orders of magnitude until quantum degeneracy is reached at a critical temperature of approximately 0.5 μK and a Bose-Einstein condensate is formed.

Quasi-pure BECs, which show no significant residual thermal component with up to 5×10^5 atoms can be routinely produced with an evaporation time of 30 s.

High Offset Trap

The strong anisotropy of the magnetic trap – the trapping frequencies along the main axes differ by almost an order of magnitude – is not optimal for transferring the atoms into an optical lattice potential. The preferred aspect ratio of the optical trap is spherical, so the shape of the cloud would have to change strongly during the transfer. To make this transition more adiabatic, an additional transformation is executed to transform the magnetic trap to a spherical shape. For this, an additional set of coils close to Helmholtz configuration around the previously described setup creates a homogeneous offset field at the position of the atoms (red coils in figure 3.2). This field is again oriented along the x-axis, in parallel with the field in the trap minimum, and increased to approximately 150 G. The main effect of this is a reduction of all trap frequencies, which now lie between $2\pi \times 12$ Hz and $2\pi \times 18$ Hz.

As the vertical confinement of the magnetic potential has been strongly reduced, the gravitational force becomes very significant. In order to determine the resulting total trapping potential, both the magnetic and the gravitational potential therefore have to be taken into account. The minimum of this combined potential is approximately 2 mm lower than the center of the original QUIC trap. This displacement of the equilibrium position is called gravitational sag. The combined potential can again be approximated by a 3D parabolic configuration with the same trap frequencies around this new overall minimum, but with a magnetic field gradient present at the position of the atoms to counteract gravity. This gradient will be used as an experimental tool in chapter 4.

3.1.2 Optical lattice setup

The previously described coil configuration allows optical access through all magnet coils (see figures 3.1 and 3.2). The three lattice axes are along the vertical (y-axis) direction, through the QUIC coil along the x-axis, and along the second transport axis (z-axis). Due to the absence of MOT optics around the main chamber of the apparatus, all of these paths are free for lattice and imaging beams. As outlined in section 2.2.2, the optical lattice is created by three independent optical standing waves, one along each of the three main axes. The setup of the main optical components of each of these is schematically shown in figure 3.2. Laser light from an optical fiber is collimated and then directed to the BEC through a focusing lens. The atoms are at the focus of the beam, which has a waist of typically 140 μm. A resonant laser beam for absorption imaging (described in the next section) is overlapped on the same path, but is switched separately.

The optical lattices used for this study are ideally pure conservative potentials and do not contribute to heating by photon scattering (see section 2.2.1). Therefore, they have to be far detuned to any optical resonance of the ^{87}Rb atoms. The main trapping light source is a Coherent MBR 110E titanium-sapphire laser operated at a wavelength of typically 844 nm and up to 4.5 W of output power. This light is split into three separate beams, each of which first passes an acousto-optical modulator (AOM) for controlling the beam intensity and is then coupled into a single mode, polarization maintaining (PM) optical fiber. The fiber coupling is susceptible to thermal drifts and mechanical vibrations, therefore the power output of the fiber is continuously monitored by an amplified photodiode. A feedback circuit stabilizes this power by acting on the AOM driver. The feedback circuits for the individual beams are controlled by independent arbitrary waveform generators to dynamically change the potential depths. Each of the intensity wave forms of the lattice axes can therefore be independently chosen.

To avoid interference between the beams, the light forming the three lattice axes is frequency shifted such as to be mutually detuned by at least 20 MHz. The light polarizations are also chosen orthogonal to each other. In this way, cross-interference between the beams can be completely neglected in the time averaged potentials.

3.2 Absorption imaging

Since the atoms absorb resonant light, they can quite literally be "photographed". This is the most common way to extract data from the atom ensemble in cold atom experiments. In the following, this method and typical shapes of the resulting images will be explained.

For the imaging conducted in this experiment, a resonant light beam with a large cross section is illuminating the cloud and the shadow produced by the atoms on the other side is recorded by a CCD array (camera) as shown in figure 3.3. While passing through the cloud, the beam is attenuated due to the absorption from the atoms, which at a given position is proportional to the 3D density of atoms. For a light beam propagating along the z-axis of a coordinate system, the overall absorption along the path of one light ray is thus given by the Lambert-Beer law as

$$I(x,y) = I_0(x,y) \cdot e^{-\int \rho(x,y,z)\sigma dz} = I_0 e^{-D(x,y)},$$

where $I_0(x,y)$ is the initial intensity of the light and $\rho(x,y,z)$ is the local density of atoms at position (x,y,z) in space. The absorption cross section of one atom is given by σ and D is the resulting integrated optical density of the light. This approach assumes that the initial intensity of the light is small compared to the saturation intensity of the atomic transition used for the imaging. In the image from the CCD camera, the attenuation of the light recorded by an individual pixel therefore encodes

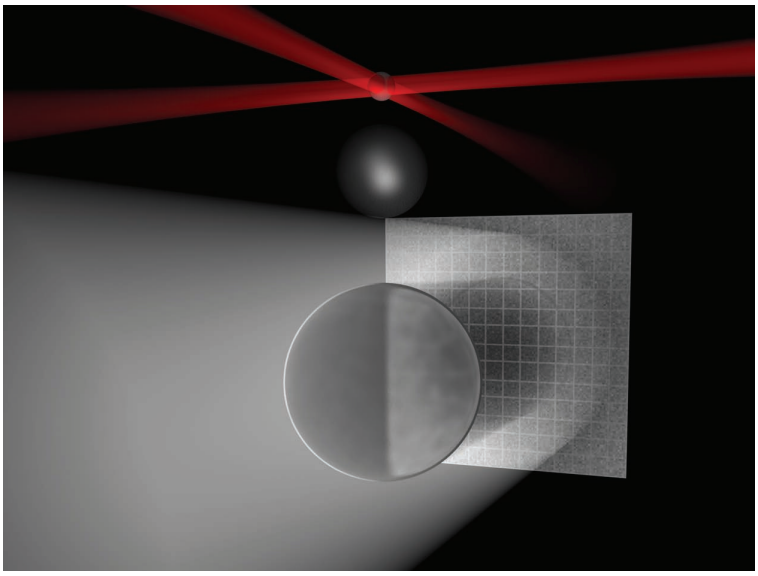

Figure 3.3: Simplified view of the expansion and imaging sequence. The atoms are released from the lattice trap created by intersecting laser beams (red). The cloud expands while falling, and is eventually illuminated by a flash of laser light. The shadow cast by the atom ensemble is projected to a CCD array and contains the 2D integrated density distribution in the CCD plane.

the optical density of the atom cloud along the path of the light ray that illuminates this particular pixel.

Since the illumination beam typically is not uniform, the optical density is usually determined by a two-step procedure: First, one image is taken which contains the shadow of the atom cloud. Then, the atoms are removed from the field of view, typically by waiting until they have dropped far enough to not be visible on the images. Now, a reference image is taken which records the profile of the illuminating beam and therefore yields $I_0(x, y)$ for each pixel.

To account for a constant offset of each pixel which is present even when no light hits the camera, an additional image is taken without any illumination beam. This so-called dark image is then subtracted from both the shadow image and the reference image to cancel the bias. To reconstruct the integrated density, both images are then divided and the logarithm is taken:

$$\int \rho(x, y, z)dz = D(x, y)/\sigma = \frac{1}{\sigma} \ln\left(\frac{I(x, y) - I_{dark}(x, y)}{I_0(x, y) - I_{dark}(x, y)}\right) \tag{3.1}$$

Here, the division of the optical density D by the absorption cross section σ yields the column integrated atom density for each pixel.

3.2.1 Time of flight imaging of atoms from deep lattices

For the experiments presented in this thesis, the atom clouds being imaged are released from an optical lattice potential. In the following, the shape of the typical density distributions recorded in this way after ballistic expansion will be discussed. The lattices are usually deep enough that the system is best described in the tight-binding picture, using localized on-site wave functions. The shape of each of these wave functions is mostly determined by the local shape of the potential at the lattice site, and the phase is constant within the site. In most cases, the atoms are in the single-well ground state, and the Wannier function can be approximated by a gaussian.

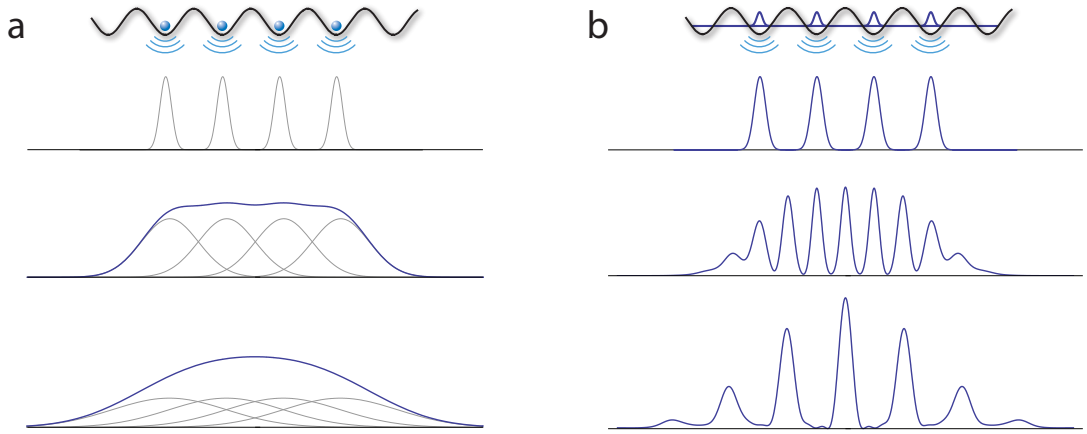

Figure 3.4: Evolution of the density distribution after release from a deep lattice trap. Each of the gaussian on-site wave functions expands independently (thin gray lines in **a**). For localized atoms that have no defined phase relation, the expectation value for the total density is the sum of the expectation values (blue lines in **a**). **b** In the case of a well-defined constant phase, the wave functions interfere and a diffraction pattern develops.

The density distribution in space after the time of flight period t_{exp} can be written as the expectation value of the density operator n,

$$\langle \hat{n}(\boldsymbol{x}, t_{exp}) \rangle = \langle \hat{a}^\dagger(\boldsymbol{x}, t_{exp}) \hat{a}(\boldsymbol{x}, t_{exp}) \rangle = \left\langle \sum_j \hat{a}_j^\dagger(\boldsymbol{x}, t_{exp}) \sum_k \hat{a}_k(\boldsymbol{x}, t_{exp}) \right\rangle , \tag{3.2}$$

where $\hat{a}^\dagger(\boldsymbol{x}, t)$ is the creation operator for an atom at position $\boldsymbol{x}$ at time t, which is then expressed in terms of the operators $\hat{a}_j^\dagger(\boldsymbol{x}, t)$ which describe the contributions to the field (at time t) from atoms released at $t = 0$ from lattice site j. Assuming gaussian initial (on-site) wave functions, the operator at time t can be derived from the on-site operator by the evolution of the gaussian wave packet with initial width σ_0 in free space:

$$\hat{a}_j^\dagger(\boldsymbol{x}, t_{exp}) = W(\boldsymbol{x} - \boldsymbol{x}_j, t) e^{\frac{i\hbar t}{2m^2\sigma_0^2\sigma(t)^2}\boldsymbol{x}^2} \hat{a}_j^\dagger \tag{3.3}$$

Here,

$$W(\boldsymbol{x},t) = \frac{2\pi^{3/4}}{\sqrt{\sigma_0 + \frac{i\hbar t}{m\sigma_0}}} e^{-\frac{\boldsymbol{x}^2}{2\sigma(t)^2}}$$

is the gaussian envelope with

$$\sigma(t) = \sqrt{\sigma_0^2 + \frac{\hbar^2 t^2}{\sigma_0^2 m^2}}$$

the width of the expanding gaussian at time t. $\hat{a}_j^\dagger$ is the usual field operator for a particle in the lattice site j. For situations where the on-site wave function is not well approximated by a gaussian, such as in the case of atoms in higher-lying bands, this expression has to be replaced by the appropriate momentum space Wannier function.

Using the wave function 3.3 to evaluate the density distribution from eq. 3.2, we obtain

$$n(\boldsymbol{x},t_{exp}) \;=\; \sum_{j,k} W^*(\boldsymbol{x}-\boldsymbol{x}_j)W(\boldsymbol{x}-\boldsymbol{x}_k) e^{\frac{i\hbar t_{exp}}{2m^2\sigma_0^2\sigma(t_{exp})^2}(2\boldsymbol{x}(\boldsymbol{x}_j-\boldsymbol{x}_k)+\boldsymbol{x}_k^2-\boldsymbol{x}_j^2)} \hat{a}_j^\dagger \hat{a}_k. \quad (3.4)$$

We now assume that the time of flight t_{exp} is chosen so long that the expanded cloud is much larger than the original distribution. This means that $\sigma(t_{exp}) \gg \boldsymbol{x}_j$ for all j. As $W(\boldsymbol{x},t_{exp})$ is a smooth gaussian with width $\sigma(t_{exp})$, this therefore leads to $W(\boldsymbol{x}+\boldsymbol{x}_j,t_{exp}) \approx W(\boldsymbol{x},t_{exp})$ for all j. We make the same approximation for the phase term, such that

$$2\boldsymbol{x}(\boldsymbol{x}_j-\boldsymbol{x}_k)+\boldsymbol{x}_k^2-\boldsymbol{x}_j^2 \approx 2\boldsymbol{x}(\boldsymbol{x}_j-\boldsymbol{x}_k). \quad (3.5)$$

This is, however, not as strict as the previous assumption, as the phase term is not as smooth as the envelope W, so it is generally not fully applicable for typical ballistic expansion times. It breaks down for high spatial frequency components corresponding to the largest values of $\boldsymbol{x}_j - \boldsymbol{x}_k$ becoming comparable to scales in the coordinate $\boldsymbol{x}$. Structures on the scale of maximal $\boldsymbol{x}_j - \boldsymbol{x}_k$ are therefore distorted first, which is the size of the initial distribution (before release). As a consequence, outside of the immediate near field, the minimum feature size is given by the initial distribution size.

Furthermore, long expansion from strongly localized sites also implies $\sigma_0 \ll \sigma(t_{exp})$ and we can approximate

$$\sigma(t_{exp}) \approx \frac{t\hbar}{\sigma_0 m}.$$

With these approximations, the density distribution after expansion from an array of lattice sites with strong confinement is

$$\langle \hat{n}(\boldsymbol{x},t_{exp})\rangle \;=\; |W(\boldsymbol{x})|^2 \sum_{j,k} e^{\frac{im\boldsymbol{x}}{\hbar t_{exp}}(\boldsymbol{x}_j-\boldsymbol{x}_k)} \left\langle \hat{a}_j^\dagger \hat{a}_k \right\rangle. \quad (3.6)$$

Single wave function case

As derived in the previous chapter, in the superfluid case $J \ll U$, all atoms are fully delocalized and occupy the same global wave function. The local wave functions are coherent states which follow the relation

$$a_j|\Psi\rangle = \alpha_j|\Psi\rangle = e^{i\phi_j}\sqrt{n_j}|\Psi\rangle,$$

with α_j the local wave function, ϕ_j the local phase and n the expectation value of the occupation at lattice site j. In the superfluid ground state, the phase is constant and can be chosen as $\phi = 0$. In the time of flight expansion, we therefore get

$$\langle n(\boldsymbol{x}, t_{exp})\rangle \quad = \quad |W(\boldsymbol{x})|^2 \left(\sum_j e^{\frac{im\boldsymbol{x}}{\hbar t_{exp}}(\boldsymbol{x}_j)} \sqrt{n_j} \cdot \sum_k e^{\frac{-im\boldsymbol{x}}{\hbar t_{exp}}(\boldsymbol{x}_k)} \sqrt{n_k} \right). \tag{3.7}$$

In the simple cubic optical lattice, the site positions $\boldsymbol{x}_j$, $\boldsymbol{x}_k$ form a regular lattice with a spacing of $a = \lambda_{lat}/2$, and the components of the position vectors $\boldsymbol{x}_j$ are integer multiples of a. Apart from the Wannier function envelope, the expanded density distribution is therefore the absolute square of a Fourier sum, the Fourier coefficients being the wave function amplitude $\sqrt{n_j}$. The periodicity of the Fourier sum is defined by the characteristic length in the argument of the exponential,

$$l = 2\pi\hbar t_{exp}/a/m = 4\pi\hbar t_{exp}/\lambda_{lat}/m = 2\hbar k_{lat} t_{exp}/m.$$

The periodic term is multiplied with the absolute square of the expanding on-site gaussian function $W(\boldsymbol{x}, t)$. This formula directly corresponds to the pattern of a wave which is diffracted by a grating: The gaussian corresponds to the single-slit transmission envelope, and the Fourier sum is the interference term between the waves emanating from each of the slits.

For a one-dimensional array of N_s sites spaced by a between $-(N_2-1)/2 \cdot a$ and $(N_s-1)/2 \cdot a$, the pattern evaluates as

$$n(x) = |W^*(\boldsymbol{x})|^2 \sum_{k=(N_s-1)/2}^{(N_s-1)/2} e^{i2\pi\frac{x}{l}k} \sum_{j=(N_s-1)/2}^{(N_s-1)/2} e^{-i2\pi\frac{x}{l}j} = |W^*(\boldsymbol{x})|^2 \frac{\sin(\pi N_s x/l)^2}{\sin(\pi x/l)^2}.$$

This function has the approximate shape of the one shown in figure 3.4b for an array of 4 sites. It represents a regular array of peaks spaced by the width of the Brillouin zone l which is multiplied with a (gaussian) envelope from the expanded on-site Wannier function. When increasing the number of sites N_s, the peaks become narrower as $1/N_s$ according to the Fourier transform. Due to the approximations made, however, the calculation only holds as long as the peak width is larger than the cloud size prior to expansion. The effect of the initial size of the cloud is a smoothing of the distribution on this scale. In addition, each of the peaks corresponds to a packet of

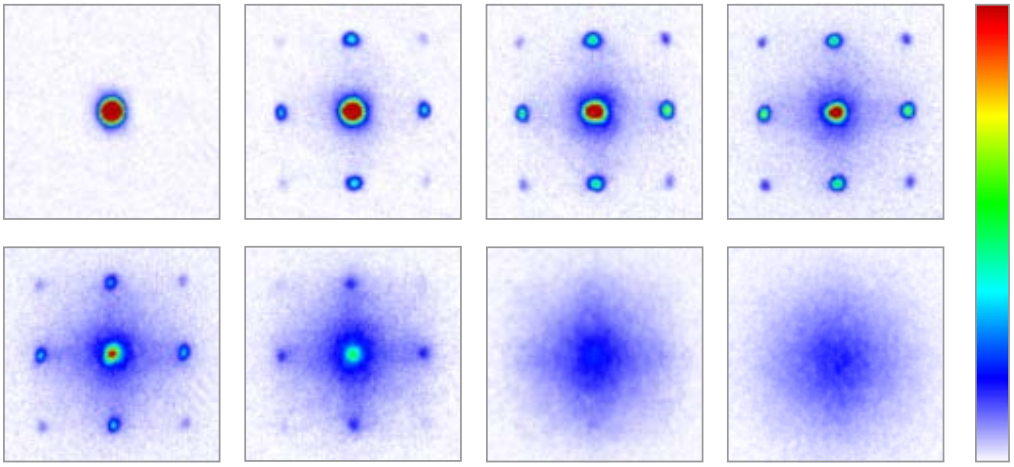

Figure 3.5: Momentum distribution of the atoms in the superfluid to Mott insulator transition. The cloud is imaged after a time of free expansion from the trap. The first image shows the expanded BEC without lattice. For the other images the lattice depth is progressively increased (3.5, 7, 10, 14, 15, 17.4 and 22 E_R, respectively) until the suppression of the superfluid component results in the loss of interference.

atoms moving close together, which means that they interact during the expansion as well as with the whole ensemble during the initial phase of the expansion. This can be modeled as a mean-field repulsive interaction which further broadens the discrete peaks, and for low lattice depths has to be taken into account when the absolute atom density after expansion is analyzed quantitatively [100, 101].

Figure 3.5 shows the expansion images obtained for different lattice depths. The first image shows the BEC emitted from a parabolic trap without any periodic potential. It expands as a compact cloud, and the size after expansion is completely dominated by the repulsive interaction of the atoms during the time of free flight. For shallow lattices, the interference pattern is clearly visible along the two dimensions shown. The number of occupied lattice sites along each direction is $N_S \approx 25$, such that the width of the peaks is dominated by the initial size of the cloud.

Incoherent case

In the Mott insulating state, the ensemble properties are very different. Here, the quantum state of each site j is a Fock state, which is not an eigenstate to the a_j operators. Instead, for these states it holds that

$$\langle \Psi | \hat{a}_j^\dagger \hat{a}_k | \Psi \rangle = \delta_{jk} n_j,$$

with n_j the occupation number of site j.

With this relation, we get for the expanded density distribution:

$$\begin{aligned}\langle n(\boldsymbol{x}, t_{exp})\rangle &= |W(\boldsymbol{x})|^2 \sum_{j,k} e^{\frac{im\boldsymbol{x}}{\hbar t_{exp}}(\boldsymbol{x}_j - \boldsymbol{x}_k)} \delta_{nj} n_j \\ &= |W(\boldsymbol{x})|^2 \sum_j n_j \\ &= N_{tot} |W(\boldsymbol{x})|^2 \end{aligned} \tag{3.8}$$

In the Mott insulating case, the expanded density distribution is therefore simply given by the gaussian envelope of the expanding on-site wave function, and no structure of the underlying lattice is visible. The transition from the superfluid to the Mott insulating regime is shown in figure 3.5. When loading the atoms into the deep lattice, the lattice depth is increased smoothly, leading to a larger and larger squeezing of the on-site number distribution and a disappearance of the interference term by the time the lattice depth reaches about $V_0 \approx 15\, E_\mathrm{R}$.

It should be noted that, while the interference term due to the global coherence of the superfluid phase vanishes completely, a weak sinusoidal interference pattern with the same periodicity persists even in the Mott phase for systems with finite J. This is visible in the images shown in figure 3.5 for the two deepest lattices. This broad interference is caused by the previously mentioned local coherence created by the admixture of particle-hole pairs in the ground state of a Mott insulator due to the finite tunnel coupling J and is discussed in detail in [84, 85].

3.2.2 Brillouin zone mapping

A variant of the time-of-flight scheme is the Brillouin zone mapping technique. This method is specific to optical lattices, and makes it possible to obtain the lattice quasi-momentum distribution as opposed to the distribution of free-space momenta in the trap [37, 102–104]. The difference to the normal ballistic expansion technique is that the trap is not switched off instantaneously. Instead, the lattice beams which constitute the trap are ramped down on a timescale which is fast only compared to the "macroscopic" dynamics inside the trap – dynamics which requires tunneling processes and takes place within individual bands of the band structure. At the same time the ramp is slow compared to the on-site dynamics which is given by the band gap scale as opposed to the band width. During this ramp, all atoms therefore adiabatically follow the band structure as illustrated in figure 3.6. In contrast to the non-adiabatic switch-off, where the Bloch state basis of the lattice is projected onto the plane wave basis of free space, this mapping technique adiabatically connects the Bloch basis with the free-space plane wave basis. Each band of Bloch states is projected to a specific subset of free space momenta which is a combination of Brillouin zones and is separate from the subsets corresponding to other bands. This method

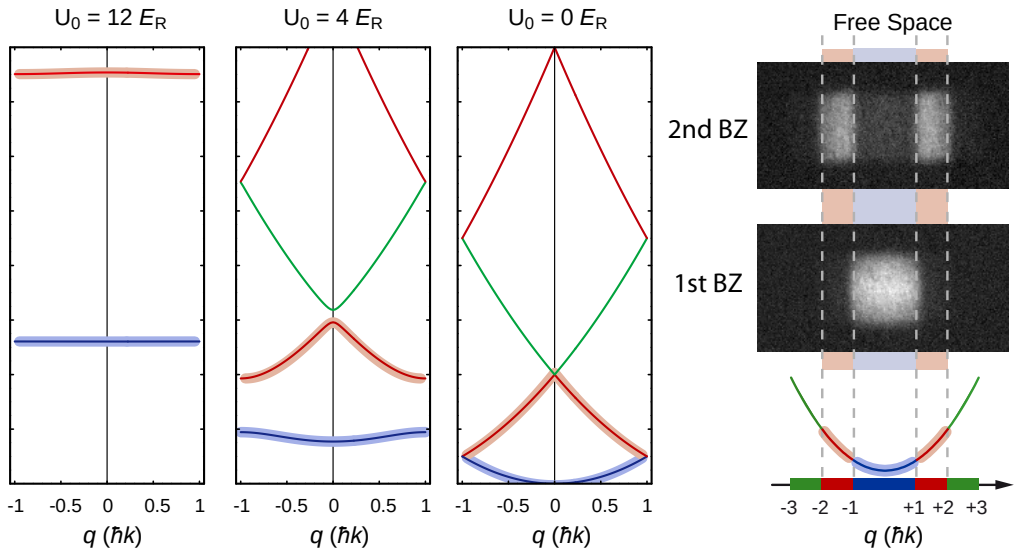

Figure 3.6: Schematic view of the Brillouin zone mapping process. During the ramp-down of the lattice, the populations of each of the bands are mapped to specific regions in momentum space. These are given by combinations of Brillouin zones and can be recorded after ballistic expansion. For the absorption images shown, the ensemble has been specifically prepared in the second (red shading) and the first (blue) Brillouin zones, respectively [105].

is therefore a very useful way of separately determining the atom populations in the individual bands of the lattice band structure.

3.3 Controlled spin-changing collisions

Atoms in a deep optical lattices are confined very tightly on the one hand, leading to strong mutual interactions between atoms on one site. On the other hand, individual atoms are separated very effectively from the particles in other lattice sites. For typical parameters, many sites of the lattice are occupied with one or two atoms each. The lattice potential wells therefore provide ideal "test tubes" for "reactions" between the atoms they contain. Several different types of such reactions between two atoms in one site have been studied in this way. These include controlled collisions between two atoms resulting in a collisional phase shift [106] and the dependence of the corresponding collision properties on the magnetic field close to a Feshbach resonance [107]. Also, two atoms can react to form a molecule in a very controlled way, driven either by photoassociation [108, 109] or through magnetic Feshbach resonances [110–113]. In all of these situations, the process can be extremely well controlled due to the fact that the state of the atoms is perfectly defined – all internal and external degrees of freedom are fixed by the preparation of the "samples" in the lattice.

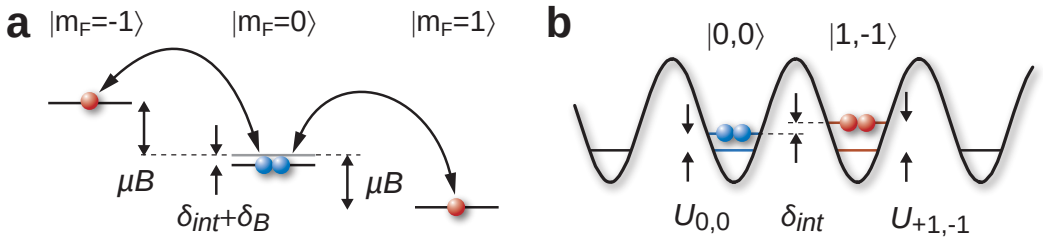

Figure 3.7: Spin changing collisions in the $F = 1$ hyperfine manifold. **a** Two atoms in the $m_F = 0$ state are converted to an $m_F = -1, m_F = 1$ pair during the collision. The initial and the final two-particle state are detuned by an energy δ_{tot}, which contains contributions from the quadratic Zeeman effect (δ_B) and the contact interaction (δ_{int}). **b** At very low magnetic fields, the Zeeman effect for the two atoms in $m_F = \pm 1$ cancels, and the detuning is dominated by the difference in interaction energy between the two states.

Another reaction which can take place when two atoms meet is the so-called spin-changing collision. This describes a process in which the collision products have different spins from the initial configuration. As for the effects described before, this process is especially well-defined for atoms in an optical lattice site, and as a result can serve as a tool to control the internal states of the atoms. In the following, only a brief introduction will be given to the subject, which has been studied in detail in several publications [94, 114–116]. The description will then focus on the microwave dressing method devised for actively controlling the spin-exchange process, which makes such collisions a powerful and robust tool for quantum state engineering.

3.3.1 The spin exchange process

When two atoms are confined to the ground state of a lattice site, the only degrees of freedom that can exhibit dynamics are the internal ones. As there is no coupling to the outside world and all potentials are static, no angular momentum can be added or removed. With static magnetic fields, the projection of the overall spin along the magnetic field direction therefore has to be conserved. For two atoms prepared in the $|\, F = 1, m_F = -1 \,\rangle$ state, this means that no transition to any other configuration is possible, as within the $F = 1$ hyperfine manifold of ^{87}Rb, no other combination of two states has a total projected angular momentum of $m_{F(tot)} = -2$.

The total projected angular momentum $m_{F(tot)} = 0$ however can be realized in two ways: With the two atoms in $|\, F = 1, m_F = 0 \,\rangle$, or one atom in $|\, F = 1, m_F = -1 \,\rangle$ and one in $|\, F = 1, m_F = 1 \,\rangle$ as illustrated in figure 3.7. Therefore, transitions between these two two-particle states are possible. Similarly, two identical atoms in the $F = 2$ hyperfine manifold can make transitions between different two-particle states unless both atoms are in a stretched state and $m_{F(tot)} = \pm 4$ (See [94, 114, 116]).

The rate of these transitions and the maximum transition efficiency depend on the coupling strengths and the energy differences between these different two-particle states. In the following, we will focus on the $F = 1$ hyperfine manifold, which is the one that can be applied more easily for quantum state engineering as the atoms in this state can not undergo hyperfine changing collisions. Such collisions change the state of at least one atom from $F = 2$ to $F = 1$, thus releasing $h \times 6.8\,\mathrm{GHz}$ of energy, which typically expels the atoms involved from the trap.

Spin-changing collisions can of course also occur in bulk ensembles without tight confinement to a lattice. In spinor BECs of more than one spin component, they provide a coupling between the spin states, which then show a complex dynamics according to the initial magnetization and the relative chemical potentials of the spin populations [117–119].

Low magnetic fields

In the following, we will use the state

$$\mid m_F = 0,\, m_F = 0 \,\rangle = |m_F = 0\rangle_L |m_F = 0\rangle_R$$

to designate the two-particle state with both atoms in $\mid F = -1,\, m_F = 0 \,\rangle$. The state

$$\mid m_F = 1,\, m_F = -1 \,\rangle = \frac{1}{\sqrt{2}}(|m_F = 1\rangle_L |m_F = -1\rangle_R + |m_F = -1\rangle_L |m_F = 1\rangle_R)$$

is the configuration corresponding to a spin triplet with one atom in $\mid F = 1,\, m_F = -1 \,\rangle$ and the other in $\mid F = 1,\, m_F = 1 \,\rangle$. These two two-particle states are not very sensitive to magnetic fields, as the total linear Zeeman shift for both is 0. When all magnetic field effects can be neglected and the external degrees of freedom are fixed and constant, the only difference in energy results from the interaction part of the hamiltonian.

For the two states described, a small difference between the scattering lengths of the respective states leads to slightly different on-site interaction energies. Within the $F = 1$ hyperfine manifold and for a total projected angular momentum of $m_{F(tot)} = 0$, the two interaction energies $U_{+1,-1}$ and $U_{0,0}$ differ by $\delta_{int} = h \times 11.8\,\mathrm{Hz}$.

The experimental sequence for the observation of spin-changing collisions is shown in figure 3.8. It begins by preparing the ensemble in an optical lattice trap with a depth $V_0 \geq 40\,E_R$ chosen such that all atoms are strongly confined to a single site and all tunneling is suppressed. For the rest of the experiment, the spatial distribution across the lattice is thus frozen. The parabolic magnetic trapping field can therefore be switched off, with a homogeneous bias field of 1.2 G remaining in order to preserve the quantization axis. After a hold time of $\approx 50\,\mathrm{ms}$ to allow for the fields to stabilize, two fast microwave π-pulses then transfer the atoms from the $\mid F = 1,\, m_F = -1 \,\rangle$ state to the $\mid F = 1,\, m_F = 0 \,\rangle$ state via $\mid F = 2,\, m_F = 0 \,\rangle$. Immediately after this, the

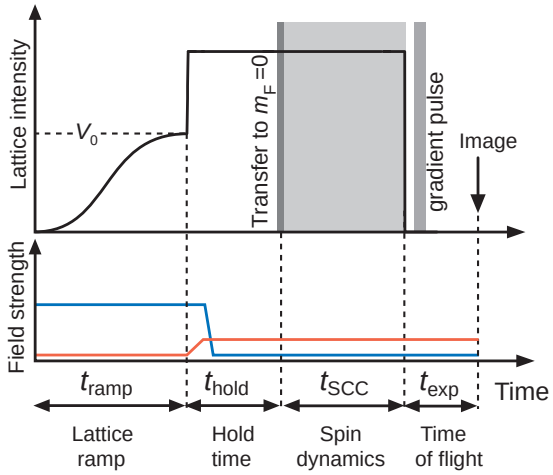

Figure 3.8: Experimental sequence for determining the fraction of doubly occupied sites in the ensemble. After the lattice ramp and magnetic trap switch-off, all atoms are transferred to $m_F = 0$ and subsequently undergo spin dynamics for a time t_{SCC}. Finally, the spin populations are separated by a gradient field and then recorded.

bias field is ramped to a small value, and the atoms are held in this condition for a variable time t_{SCC}, during which the spin-exchanging collisions can occur.

The cloud is then released from the trap and the spin components are separated during the ballistic expansion by the application of a magnetic gradient field ("Stern-Gerlach pulse") for 3.5 ms. Two resulting images are shown in figure 3.9a. The central cloud contains all atoms still in the $m_F = 0$ state. The left and right clouds consist of atoms in the $m_F = -1$ and $m_F = +1$ states, respectively, which become populated by the collisional process. The data is then analyzed by either directly counting the atoms through integrating rectangular regions as depicted in figure 3.9a or by fitting gaussians to the peaks in the vertically integrated profile (fig. 3.9b).

The resulting evolution of the $m_F = 0$ and the $m_F = \pm 1$ populations during the interaction time t_{SCC} is shown in figure 3.10. For low magnetic fields (black symbols), a clear sinusoidal evolution is visible, showing that a large fraction of the atoms oscillates between the two states. The oscillatory behavior shows that the spin-changing collision provides a coherent coupling between the two two-particle states. The oscillations can therefore be described as Rabi oscillations between the two states which are driven by the collisional coupling.

Influence of the magnetic field

Magnetic fields shift the energies of the Zeeman sublevels $m_F = -1, 0, 1$ according to their magnetic momenta. These shifts can influence the energies of the two-particle

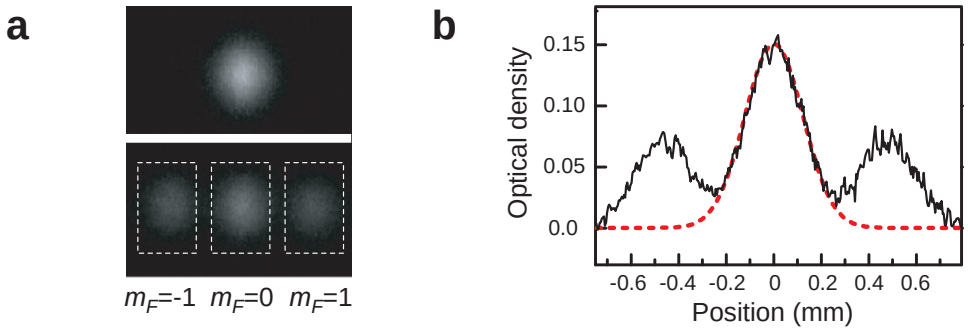

Figure 3.9: Absorption image after time of flight with Stern-Gerlach field for separating the spin states (a). The two images show the cloud after being prepared in $m_F = 0$, and before and after undergoing spin-changing collisions. (b) Vertical integration of the second image allows fitting three separate gaussians to determine the populations in the three m_F-states.

states, and therefore affect the resonance condition of the process.

To first order, the Zeeman shift of the atoms in the $\mid m_F = 1,\ m_F = -1 \rangle$ state is zero, and the effects on the two atoms of the $\mid m_F = 1,\ m_F = -1 \rangle$ cancel. However, the second order contributions are all positive and not identical, leading to an additional differential energy shift $\delta_B(B)$ between the two two-particle states. In the case of ^{87}Rb this contribution has the same sign as δ_{int} and therefore increases the total energy difference $\delta_{tot} = \delta_{int} + \delta_B(B)$ between the two states with increasing magnetic field.

As can be seen in the earlier data, the coupling between the $\mid m_F = 0,\ m_F = 0 \rangle$ and the $\mid m_F = 1,\ m_F = -1 \rangle$ state is very weak, and the energy mismatch created by the second order Zeeman effect can be easily large enough to bring the collisional coupling between the levels out of resonance. This is shown in figure 3.10, where an applied field of just 0.6 G (blue symbols) strongly reduces the oscillation amplitude.

The behavior can be most easily understood in terms of a two-level Rabi model, where the coupling with strength Ω_0 between the two levels is provided by the spin-exchange collisions. The transitions are detuned from resonance by the energy $\delta_{tot} = \delta_{int} + \delta_B(B)$. The contribution δ_B due to the second order Zeeman shift can be calculated using the Breit-Rabi formula [120]:

$$\delta_B(B) = \frac{\pi^2\hbar^2(g_i - g_J)\mu_B^2}{2E_{HFS}}B^2 \approx h \times 144\,\mathrm{Hz/G^2}$$

Here, g_i and g_J are the g-factors of the nucleus and the spin-orbit coupled electron, respectively, E_{HFS} is the hyperfine splitting and μ_B is the Bohr magneton. This detuning increases the bare Rabi frequency Ω_0 of the spin exchange coupling to the effective Rabi frequency Ω' according to $\Omega'(\delta_{tot}) = \sqrt{\Omega_0^2 + \delta_{tot}^2}$. At the same time, the amplitude decreases as $\Omega_0^2/\Omega'(\delta_{tot})^2$.

From fitting this Rabi model to the data as shown in figure 3.10, the bare coupling

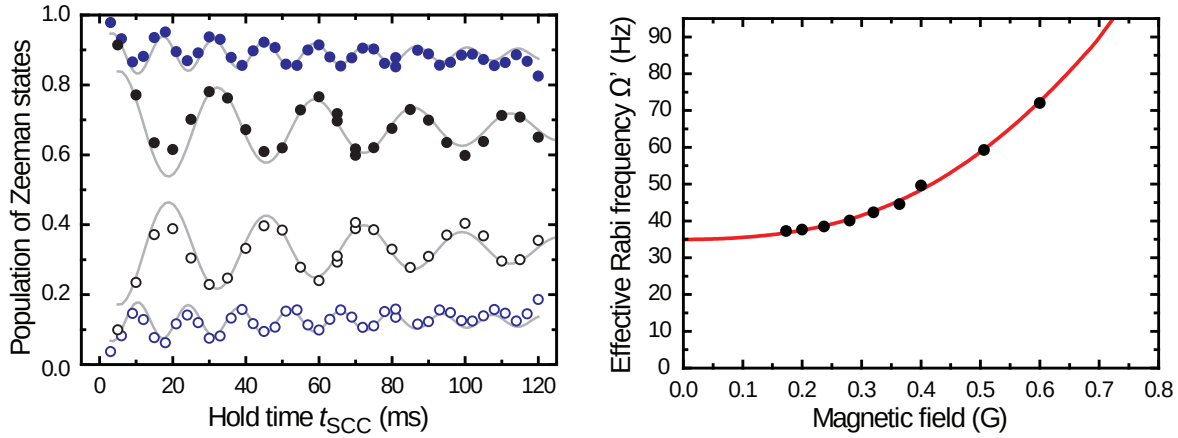

Figure 3.10: Coherent spin exchange oscillations and the influence of the magnetic field. The observed oscillations for 0.2 G (black) and 0.6 G (blue) are shown in (a). Solid points denote population in $|\, F = 1,\, m_F = \pm 1 \,\rangle$, hollow points that in $|\, F = 1,\, m_F = 0 \,\rangle$. Gray lines are fits with a damped sine function. The field dependence of the oscillation frequency is shown in (b), with the red line showing a fit with the two-level Rabi model to determine Ω_0 and δ_{int} (see text). The error bars are plotted, but smaller than the symbols.

strength Ω_0 and the interaction-induced detuning δ_{int} can be deduced. This is in fact the method by which the value of $\delta_{int} = h \times 11.8\,\mathrm{Hz}$ is determined. Both Ω_0 and δ_{int} only depend on the wave function overlap and the difference in the scattering lengths which apply to the two two-particle states. For a known wave function overlap, this scattering length difference is therefore the only fit parameter. This shows that the spin-changing collisions are a very capable probe for the interaction properties of the atoms. For more details on the scattering length analysis and the treatment of the spin-changing collisions in the $F = 2$ hyperfine manifold see [94, 114, 116].

3.3.2 Microwave control of spin-changing collisions

The quadratic Zeeman effect can be used effectively to increase the detuning of the coherent collisions and to bring them out of resonance. For very moderate magnetic fields on the order of 1 G, the collisional process is energetically far detuned, and therefore strongly suppressed. However, the detuning can not be reduced below δ_{int} using B-fields alone, since for ^{87}Rb the quadratic Zeeman shift and δ_{int} have the same sign. The quadratic Zeeman effect can not be inverted by inverting the field, and the detuning is therefore always increased in the presence of a field. In the following, a way to introduce an additional level shift will be demonstrated, which allows to bring the strongly detuned spin exchanging collisions back into resonance. The method is based on the introduction of a detuned microwave field, which induces different level shifts for the two two-particle states, allowing for a controlled relative shift.

The optical dipole potentials introduced in chapter 2.2.1 create an effective potential because the state of the atoms is energetically shifted due to the coupling to a second level. The coupling in that case is introduced by the electromagnetic field of the light, which is typically chosen far detuned from the resonance in order to avoid actual transitions to that state. To derive the energy shifts applicable in that case, the detailed level structure of the atom was not taken into account. This was possible since the detuning of the coupling field in the case of typical optical potentials is much larger than the energy splittings between the sublevels of the ground state and the excited state. In that case, all ground states experience the same energy shift from linearly polarized light, and the potential is therefore state-independent.

In this section, a microwave field with a frequency of $\omega \approx 6.8\,\mathrm{GHz}$ is introduced, which couples the states in the $F = 1$ hyperfine manifold to those with $F = 2$. As the microwave field couples to the magnetic moment of the atoms as opposed to the electric one, the level shift it produces is called AC Zeeman effect. The microwave radiation used has a much smaller detuning from the resonances than the light fields described earlier. Its detuning is comparable to the Zeeman splitting induced by the magnetic fields present (see figure 3.11). Therefore, the detunings from the different hyperfine resonances present for the individual Zeeman substates in the $F = 1$ hyperfine manifold can be very different. As a result, the strength of the coupling varies for the substates, resulting in m_F-state dependent energy shifts.

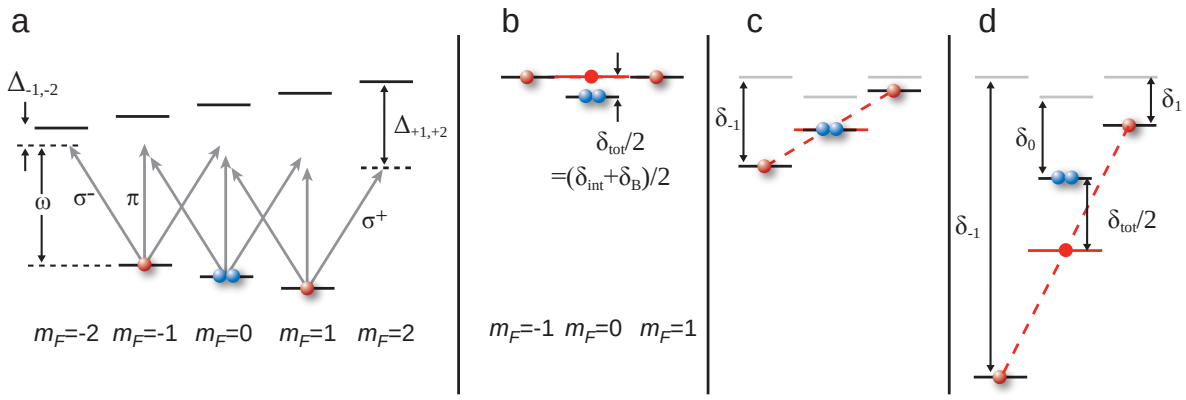

Figure 3.11: Microwave radiation can change the energy offset between the $|\, m_F = 0,\, m_F = 0\,\rangle$ and the $|\, m_F = 1,\, m_F = -1\,\rangle$ states. **a** The microwave fields used contain all three polarization components, therefore nine different transitions have to be taken into account to evaluate the $F = 1$ level shifts. The effect of the AC Zeeman shifts is shown in **b**-**d**, where the relative energies of the states are plotted along in the vertical axis. Here, the linear Zeeman shift is not included. In **b**, no AC field is present, and the detuning is due to interactions and the second-order Zeeman shift. In **c**, an AC field reduces all single-atom energies by different amounts δ_m, in this case bringing the combined $|\, m_F = 1,\, m_F = -1\,\rangle$ two-particle energy (red horizontal line) into resonance with $|\, m_F = 0,\, m_F = 0\,\rangle$. In **d**, the total shift is so large that the two two-particle states are off-resonant again, but with an inverted detuning δ_{tot}.

Figure 3.11a shows the structure of the hyperfine states involved. In the situation shown, each possible transition between two hyperfine states $|\, F = 1,\, m_F = m_1 \,\rangle$ and $|\, F = 2,\, m_F = m_2 \,\rangle$ is detuned by the amount Δ_{m_1,m_2}. Of these, $\Delta_{-1,-2}$ is the smallest in the chosen configuration, and this transition generally dominates the overall effect by reducing the energy of the $|\, F = 1,\, m_F = -1 \,\rangle$ level. The energy of the $|\, m_F = 1,\, m_F = -1 \,\rangle$ two-particle state will therefore be reduced with respect to the $|\, m_F = 0,\, m_F = 0 \,\rangle$ state, resulting in a negative energy shift δ_{UW}. Another way to create differential shifts for the different sublevels is through the use of strong polarization in detuned microwave or light fields [121–123].

The microwave frequency can be chosen far detuned from all single-particle resonances, and the field is weak enough to allow for weak coupling approximations. The total energy shift for the atomic state $|\, F = 1,\, m_F = m_1 \,\rangle$ can therefore be calculated as the sum of the individual shifts resulting from each of the possible couplings to the states in the $F = 2$ manifold:

$$\delta_{m1} = \frac{3}{4} \sum_{m2=-2}^{2} C_{\{m1,m2\}} \Omega^2_{(m2-m1)} \frac{h}{4\Delta_{m1,m2}}$$

Here, $C_{\{m1,m2\}}$ is the square modulus of the Clebsch-Gordan coefficient for the dipole transition from $|\, F = 1,\, m_F = m_1 \,\rangle$ to $|\, F = 2,\, m_F = m_2 \,\rangle$. Ω_p denotes the strength of the microwave coupling for each of the three polarization components. It corresponds to the σ^- polarization for $(p = -1)$, π for $(p = 0)$ and σ^+ for $(p = +1)$, and is 0 for all other p. These couplings are determined independently by measuring the Rabi frequency of resonantly driven microwave transitions for each of the components and normalizing with the Clebsch-Gordan coefficients. In this way, the relative intensities of the three microwave polarization components were determined to be

$$I_{\sigma^-} : I_\pi : I_{\sigma^+} = \Omega^2_{-1} : \Omega^2_0 : \Omega^2_{+1} = 0.33 : 1.0 : 0.02.$$

These ratios are fixed by the magnetic field direction and the microwave setup, and in the experiment only the total intensity is varied. At maximum intensity, coupling strengths up to 82 kHz are reached on the π-transition.

The total change of the detuning between the two two-particle states is then calculated as

$$\delta_{UW} = \delta_{-1} + \delta_{+1} - 2\delta_0.$$

This is illustrated schematically in figure 3.11b-d, for three situations without microwave field as well as with a coupling strength that shifts the spin collisions into resonance and with a strong field present which completely reverses the detuning.

In figure 3.12a, the shift of the total two-particle detuning $\Delta = \delta_{int} + \delta_B + \delta_{UW}$ in the presence of both a magnetic as well as a microwave field is shown in red for different microwave frequencies ω. The magnetic field is $B = 0.42\,\mathrm{G}$, and the microwave coupling strength $\Omega_\pi = 2\pi \times 23\,\mathrm{kHz}$. When increasing the frequency ω, the single-particle resonances cause a diverging shift whenever one of the detunings Δ_{m_1,m_2} is

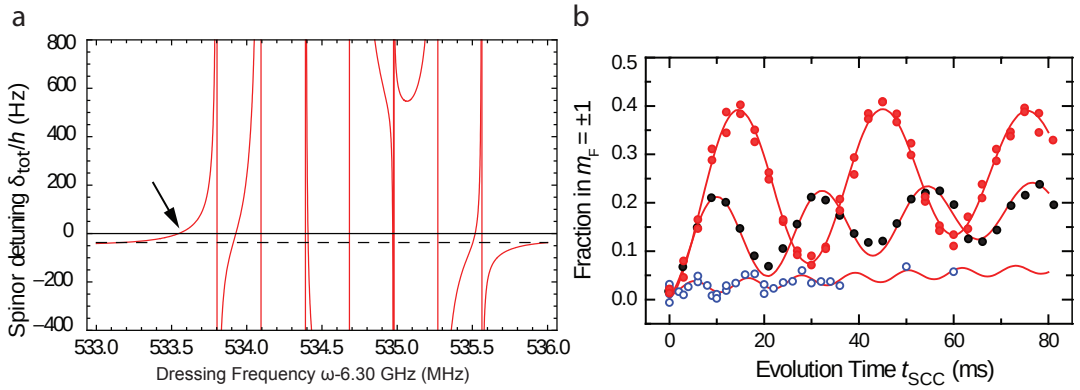

Figure 3.12: Controlling the spin changing collisions by using a microwave dressing field. **a** Calculated detuning of the spin exchange for a fixed drive field strength $\Omega_\pi = 2\pi \times 23\,\mathrm{kHz}$ of varying frequency ω and a magnetic field of 0.42 G (red). The dashed line shows the detuning without the microwave field. There are several resonances for the spin-exchange, where $\delta_{tot} = 0$, with the arrow marking the one that is chosen for the data in the right panel. **b** Spin oscillations in a bias field of 0.42 G, with no dressing field (black) and with the dressing field tuned to bring the spin exchange into resonance (red filled). The blue circles show the spin oscillation when the detuning is overcompensated and the spin exchange is no longer in resonance, corresponding to figure 3.11d.

zero such that two hyperfine levels are resonantly coupled by the microwave. The spin-exchange resonances occur whenever the overall two-particle state detuning δ_{tot} has a zero crossing. This is the case for several values of the microwave frequency outside of the single-particle resonances. The most robust one of these is denoted with an arrow. It is the one which is red-detuned to all of the single-particle resonances, as all of these resonances are maximally detuned in this case. By this, the rate of undesired microwave-driven transitions from the $F = 1$ to the $F = 2$ manifold is minimized to below the detection limit.

The measurements in figure 3.12b show the effect of the AC Zeeman shift applied during the full evolution period t_{SCC} for the three cases sketched in figure 3.12b-d. The microwave frequency corresponds to the value of 533.545 Mhz indicated in the left panel, which leads to a resonance at a coupling strength of $\Omega_\pi = 2\pi \times 23\,\mathrm{kHz}$. The spin oscillations without a control field are shown in black. With the microwave field tuned to bring the spin oscillations into resonance, their amplitude is strongly enhanced (red filled circles). By increasing the intensity even further, the spin oscillations become off-resonant again and can be strongly suppressed (blue circles), with the $|\, m_F = 0,\ m_F = 0 \,\rangle$ state now being higher in energy than $|\, m_F = 1,\ m_F = -1 \,\rangle$.

The maximum amplitude on resonance is smaller than one due to the fact that the distribution in the trap does not only consist of doubly occupied sites. Atoms without a collision partner can not change their hyperfine state and do not contribute to the signal. Even for sites with an occupation number $n > 2$ the process is suppressed,

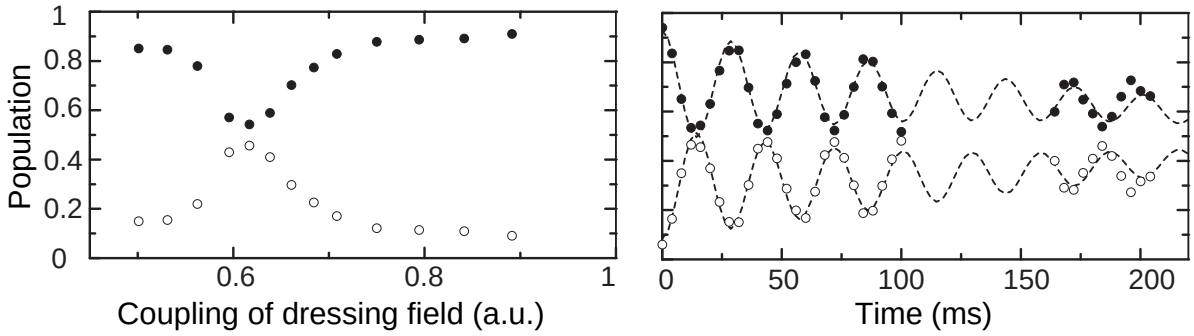

Figure 3.13: Transfer efficiency from $m_F = 0$ (black) to $m_F = \pm 1$ (hollow circles). **a** Oscillation amplitudes of the spin populations in a 1.2 G offset field plotted against increasing microwave coupling strength. A sharp resonance occurs with a maximum fraction of 45% of the atoms transferred to the $m_F = \pm 1$ states. **b** time evolution of the populations on resonance. The maximum transfer of 45% is reached after 15 ms.

as the presence of additional atoms results in a different value of δ_{int}, leading to a significantly modified resonance condition in the case of ^{87}Rb. This makes the collision process a very useful probe for the occupation number inside the lattice sites, which will be employed in the following chapters to probe the properties of the atom ensemble in the lattice.

By increasing the quadratic Zeeman shift via a stronger magnetic field, the detuning of the spin oscillations without the microwave field present is increased, and the spin oscillation can be brought completely out of resonance. Figure 3.13 shows the effect of the dressing field in this situation. Without the microwave, the spin oscillations are strongly suppressed, but can be made resonant using a dressing field, which now has to provide a much larger coupling than in the $B = 0.4\,G$ case. For the data shown, the magnetic field is $B = 1.2$ G. In this situation, the detuned microwave field ($\omega = 2\pi \cdot 6831.5$ MHz) can be conveniently used as a switch to control the coherent evolution between the two two-particle states, as the spin-exchange is completely suppressed for this magnetic field. The coherent coupling can be activated for a very precisely determined length of time. By choosing an evolution time τ_π which corresponds to one half oscillation – a "π-pulse" of the Rabi-like system – a controlled transfer of almost all pairs in the $|\, F = 1, m_F = 0 \,\rangle$ to the $|\, F = 1, m_F = \pm 1 \,\rangle$ states can be achieved. For the experiments presented in the following chapters, this process provides a very clean way to efficiently separate singly- from doubly occupied lattice sites, as the spin states only change in doubly occupied sites.

4 Number squeezing and the Mott shell structure

When the atom ensemble in the optical lattice is brought from the superfluid to the Mott insulating regime, the distribution of the particles over the lattice sites changes dramatically. This change of the distribution, discussed in chapter 2, is reflected both in the local on-site distribution of states as well as in the global structure of the cloud. Locally, the single site quantum state changes from a coherent state, corresponding to a superposition of number states $|j\rangle$ with different occupation numbers j, to a number squeezed state $|n\rangle$ with a well-defined, integer atom number. Globally, the cloud changes its structure from a smooth shape to a shell structure with spherical areas of constant density separated by narrow boundary layers. In the following, these drastic changes of the quantum state will be investigated experimentally.

4.1 Detection of number squeezing

To detect the change of the local atom distribution between the superfluid and the Mott insulator state, it is necessary to distinguish between the number squeezed states of the Mott insulator and the Poisson distribution of the superfluid. Therefore, a method is needed which can separate the different site occupation states. For this, the controlled spin-changing collisions introduced in section 3.3 are used. These collisions change the internal state of all atoms in doubly occupied sites from $m_F = 0$ to $m_F = \pm 1$, but do not affect sites with other occupation numbers. The populations in these different levels are then separated upon release from the trap by a magnetic gradient "Stern-Gerlach" field.

4.1.1 Experiment sequence

The experimental sequence is outlined in figure 4.1 for a Mott insulator with two shells. The magnetic field ramps and microwave pulse sequence used are equivalent to the ones used in section 3.3.2. After the BEC is prepared in the high-offset magnetic trap, the lattice is ramped up in 160 ms to the desired value V_0. After the final configuration has been reached, the lattice depth is increased very quickly (0.5 ms) in order to stop any tunneling, effectively freezing the occupation state of each site.

The magnetic trap is then switched off, and only a bias field of 1.2 G remains, which is sufficiently high to suppress any spin-changing collisions in the $F = 1$ manifold. After a hold time to allow the magnetic fields to settle, the atoms are transferred from the $|\, F = 1,\, m_F = -1 \,\rangle$ to the $|\, F = 1,\, m_F = 0 \,\rangle$ state via the $|\, F = 2,\, m_F = 0 \,\rangle$ state using two microwave π-pulses as discussed in section 3.3. The microwave dressing

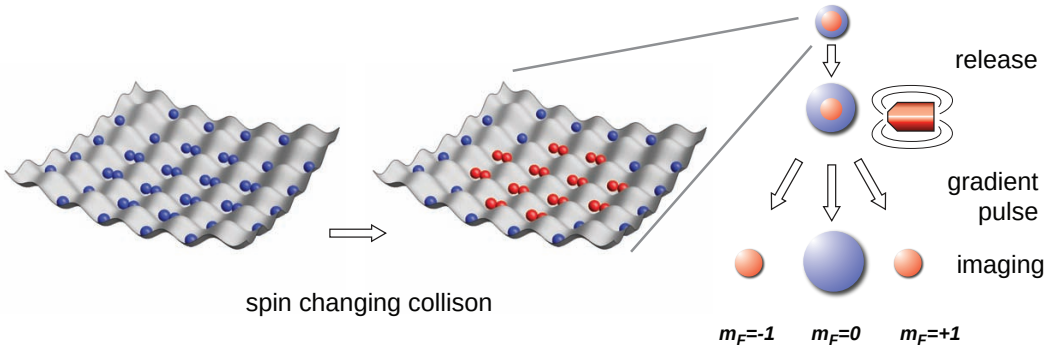

Figure 4.1: Experimental procedure to measure the number squeezing effect in the Mott insulator. A controlled spin changing collision is used to modify the hyperfine state of all atoms in the $n = 2$ shell. These are then separated from the rest of the cloud by a Stern-Gerlach gradient pulse during the ballistic expansion.

field at 531.5 MHz then enables the coherent collisions for $t_{SCC} = 15\,\text{ms}$. This pulse length corresponds to a collision-driven π-pulse. After this, the $|\, m_F = 0,\ m_F = 0\,\rangle$ atom pairs have been transferred to $|\, m_F = 1,\ m_F = -1\,\rangle$, while all atoms on singly occupied sites are still in $|\, F = 1,\ m_F = 0\,\rangle$. The atoms are then released from the trap, and a magnetic gradient field applied during the ballistic expansion separates the spin components. The three clouds corresponding to the three spin components are imaged with standard absorption imaging (see sec. 3.2).

By integrating over the three clouds on the image, the atom numbers in each spin component $N_{m_F=-1}$, $N_{m_F=0}$ and $N_{m_F=+1}$ are determined. These directly correspond to the numbers of atoms in singly and doubly occupied sites in the trap:

$$N_1 = N_{m_F=0} \tag{4.1}$$
$$N_2 = N_{m_F=-1} + N_{m_F=+1} \tag{4.2}$$

Small corrections (typically on the order of a few percent) are applied to these numbers since the transfer processes is not perfect, and a small fraction of atoms is transferred from $|\, F = 1,\ m_F = 0\,\rangle$ to the $|\, F = 1,\ m_F = \pm 1\,\rangle$ states when switching off the high offset magnetic trap. The necessary corrections are calibrated using sequences without dressing pulse as well as sequences without microwave transfer pulses (See section 4.6.1).

4.1.2 Pair fraction results

The experiment is repeated for many different atom numbers. To see the effects of number squeezing, the resulting fraction of doubly occupied sites $N_2/(N_1 + N_2)$ is plotted against the total atom number $N_1 + N_2$.

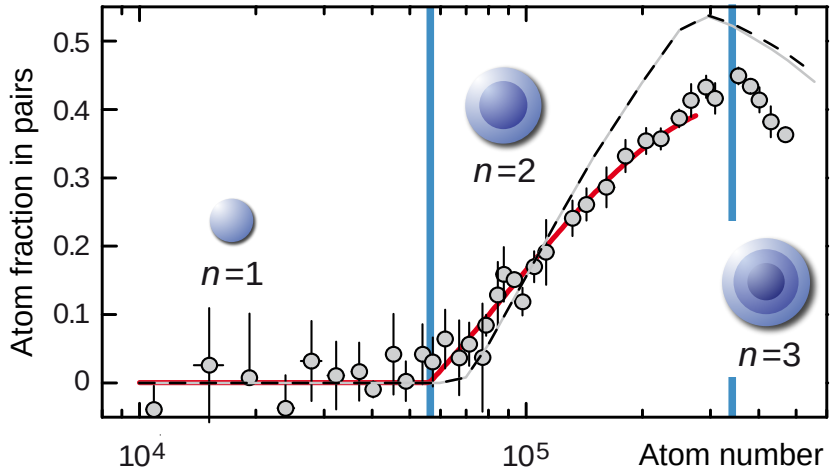

Figure 4.2: Fraction of atoms in doubly occupied sites in the Mott insulating state. For low atom numbers, no pairs exist in the cloud. For populations larger than a critical atom number, a doubly occupied shell occurs, leading to a sudden rise of the number of sites with two atoms. As a shell with three atoms per site forms, the fraction of doubly occupied sites starts to decrease. The red solid line is a fit function to capture the position of the onset of pair formation. The gray and black dashed lines correspond to the theoretically expected signal for $T = 0$ and $J = 0$, where the dashed graph contains the correction due to spin exchanges in the triply occupied sites.

Number squeezing in the Mott insulator

Figure 4.2 shows the results for a system deep in the Mott insulating regime ($V_0 = 40\,E_\mathrm{R}$). Here, we expect the atom cloud to distribute according to a shell structure as discussed in section 2.3.5. The number of shells increases for increasing atom number. Below a critical atom number the chemical potential μ in the center of the trap is lower than the interaction energy U. In this situation there is only one single spherical shell, which has a density of exactly one atom per site. At this atom number and below therefore no atom pairs are expected to exist, demonstrating that the on-site density is squeezed to single occupation. This can be seen in results shown figure 4.2, where the measured pair fraction is 0 up to a total population of $\approx 5.7 \cdot 10^4$, just below the expected threshold of $6.8 \cdot 10^4$. The uncertainty of $\approx 1 \cdot 10^4$ is dominated by the 15% uncertainty of the atom number calibration applied.

The region of doubly occupied sites which forms in the center of the trap above this threshold increases in size for rising atom number, resulting in an increase of the fraction of atoms in that shell. This holds until the next shell starts to form in the center of the trap, where each site is occupied by three atoms. As the spin exchange process is only resonant for pairs, atoms from triply occupied sites are included in N_1. This shell now grows rapidly with increasing atom number, resulting in a decrease of

the pair fraction as soon as the $n = 3$ shell forms.

The red line in the graph is an empirically determined fit function used as a guide to the eye and to determine the position of the kink at the critical atom number for $n = 2$ shell formation. The gray line shows the theoretically predicted $n = 2$ fraction, without taking trap anharmonicity, finite temperature effects or the small rate of spin exchanging collisions in $n = 3$ sites into account. The correction according to the expected 3% of triply occupied states undergoing spin exchange is shown as the dashed black line.

Transition from the superfluid to the Mott insulating regime

A very different behavior of the pair fraction is predicted in the superfluid regime, where each site is occupied by a superposition of many number states (see section 2.3.3). These are distributed according to Poisson statistics, therefore each site has a finite probability to be occupied by a pair of atoms even for very low overall densities.

Figure 4.3 shows the evolution of the number statistics when increasing the lattice depth from the superfluid to the Mott insulating regime. For low lattice depths, the distribution is smooth and there is always a finite fraction of doubly occupied sites, until a critical atom number for pair formation appears at the crossover to the Mott insulator.

Theoretically predicting the on-site number distribution in the transition regime is much harder than for the Mott insulator case. In the case of a perfect superfluid with U almost zero, the probability to find an atom pair in a given site is determined by the Poisson statistics according to the chemical potential at that location. However, even for weak lattices we are not deep enough in the superfluid regime to be able to make this assumption, so a partial squeezing still has to be taken into account. More importantly, the ramp-up of the lattice for freezing the on-site distribution can not be conducted arbitrarily fast. It must be slow enough to avoid the creation of vibrational excitations. In the superfluid regime the tunneling times are not negligible compared to this ramp time, and tunneling distorts the number distribution during the lattice depth increase.

The number distributions obtained from a mean field calculation through the transition regime [78, 80] are shown in grey, where the dashed lines again include the corrections due to the partially colliding atom triplets. This approach separates the ensemble into a superfluid and insulating fraction. In makes a very rough prediction for the expected pair fraction curves for our parameters in the superfluid to Mott insulator transition, with typically a somewhat lower number squeezing than observed.

The prediction of the correct number statistics including all correlations is a nontrivial calculation, especially when taking finite temperatures into account, and various analytical approximations as well as numerical approaches have been developed by theorists to this end [124–129].

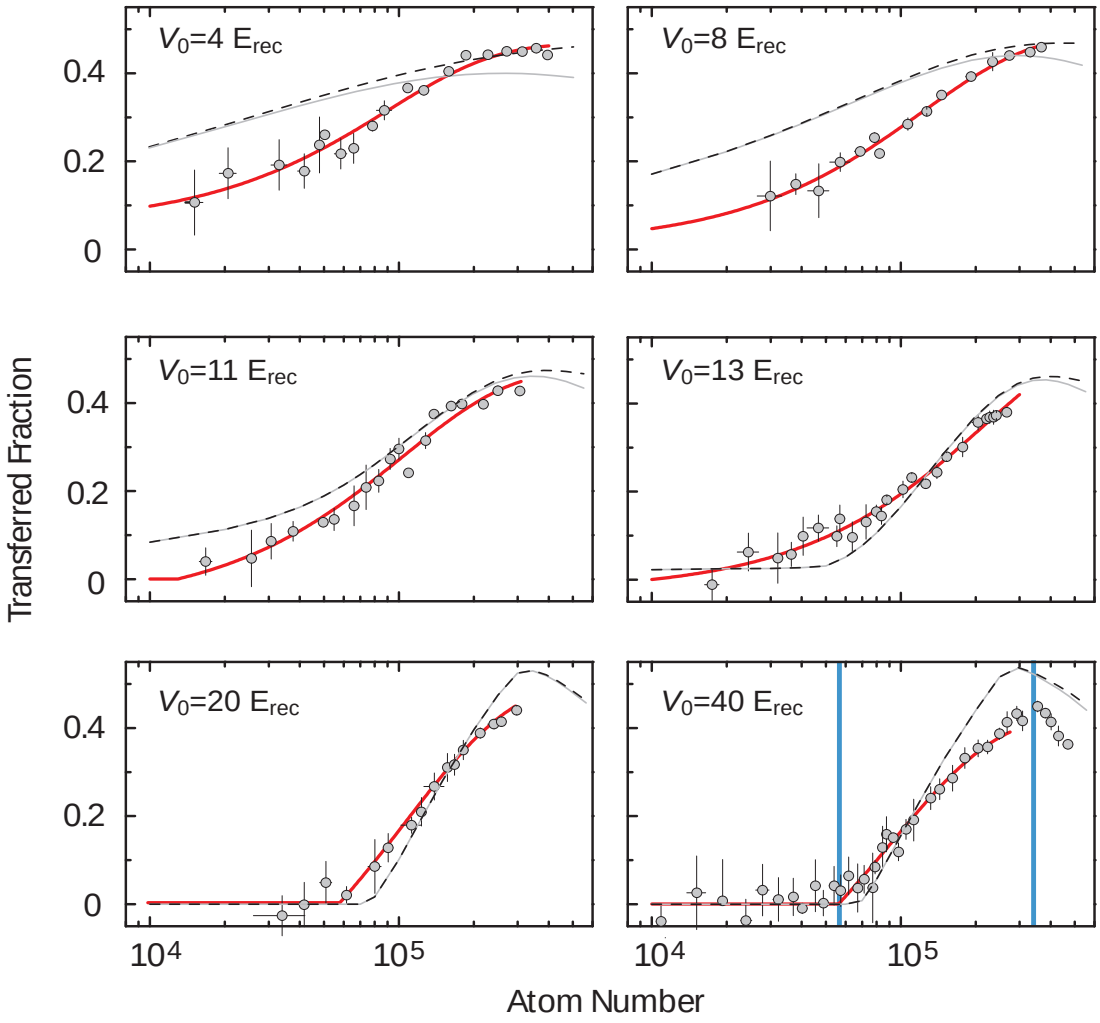

Figure 4.3: Fraction of doubly occupied sites in the transition from the superfluid to the Mott insulating regime (Gray filled circles). The red lines show a fit with an empirically determined function as a means to determine the critical atom number. The gray line shows the pair fraction expected from mean field calculations, where the dashed curve shows the signal expected with the corrections from triply occupied sites included.

4.2 Probing the density distribution in the trap

The perfect Mott insulator (for zero temperature and $J \ll U$) is incompressible and therefore forced to a locally constant density as outlined in chapter 2.3.5. This leads to the formation of a shell structure of concentric spherical layers with sharp boundaries. Since the thickness of these layers is expected to be on the order of only $5\,\mu$m for typical parameters, a very high spatial resolution in the 1μm range is required to identify the structure. For direct optical imaging into the vacuum cell this is usually achieved with dedicated high-resolution optics. This is unfortunately not available in current 3D optical lattice experiments, as these were typically not explicitly designed for high resolution imaging. To circumvent this problem, an indirect imaging technique was used. It bears some analogy to the nuclear magnetic resonance imaging (NMRI) technique widely used for medical imaging. The scheme applied here creates one-dimensional integrated profiles of the density distribution in the trap. The resolution is only limited by the shot-to-shot reproducibility of the atom cloud and the time available for accumulating data to achieve a reasonable signal to noise ratio.

The method can be outlined as follows: The atom distribution of interest is placed in a magnetic gradient field. As a result, the resonance frequency for field-sensitive microwave transitions is position-dependent over the cloud. For a homogeneous gradient field, it increases or decreases along the direction of the gradient. By choosing the appropriate microwave pulse frequency and shape, it is therefore possible to selectively transfer atoms in a narrow slice ("counting region") of the cloud to another internal state ("counting state"), as illustrated in figure 4.4. This method was previously discussed for spatially addressing atoms in an ensemble, for example in the context of quantum information [130, 131] or to probe the spatial structure of harmonic oscillator states in a 1D lattice [132].

After this transfer, the atoms in the original and final internal states can be separately counted, effectively determining the density of atoms in the counting region. By repeating the experiment many times with different frequencies, different locations along the gradient direction are probed and a one-dimensional integrated density profile is obtained. The spatial resolution using this method is no longer determined by the optical resolution of the imaging system, but instead by the width of the counting region. For a given strength of the field gradient, this width is the frequency range in which the microwave pulse transfers atoms to the counting state. Due to the long lifetime of the counting state, the microwave pulses used can be very long and use low coupling strengths. This translates directly to arbitrarily narrow counting regions. The resolution of the method is therefore only limited by the shot-to-shot repeatability of the experiment and the ability to detect the low number of atoms from the counting region reliably (see also section 4.4.1).

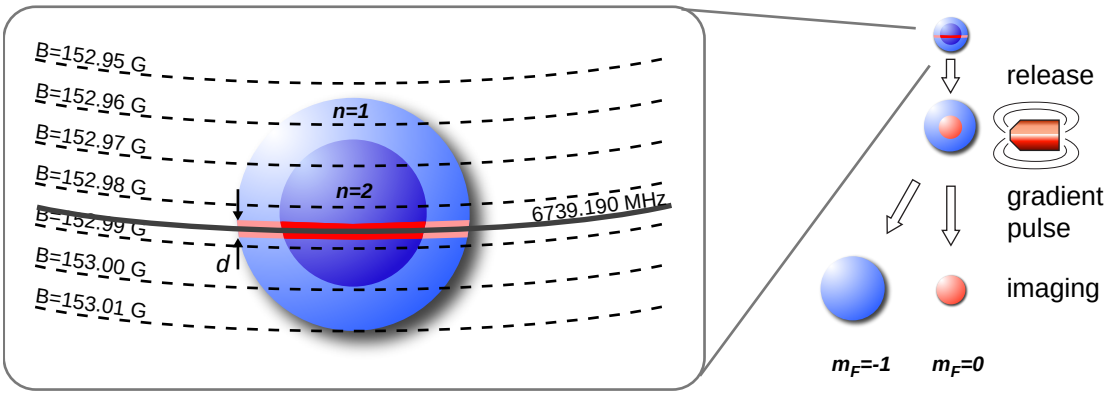

Figure 4.4: Sketch of the slicing technique: Atoms in a region of width d within cloud are transferred from the $|\, F = 1,\, m_F = -1 \,\rangle$ to the $|\, F = 2,\, m_F = 0 \,\rangle$ state. The microwave pulse of frequency f used for this transfer is resonant only in this particular region of the cloud. The cloud is then released and the two states spatially separated by a magnetic gradient during expansion.

4.3 Experimental sequence

After the preparation of the BEC in the high offset QUIC trap (see section 3.1.1), the atoms are shifted from the field minimum of the magnetic trap by the gravitational sag distance of approximately 2 mm. This equilibrium position is given by the condition that the potential due to the field gradient exactly compensates for gravity:

$$m_{Rb} \cdot g = \mu_M \frac{\mathrm{d}B}{\mathrm{d}y}$$

The magnetic dipole moment μ_M for ^{87}Rb in an offset field of $\approx 153\,\mathrm{G}$ can be calculated with the Breit-Rabi formula [120], yielding am equilibrium gradient of $\partial B/\partial z = 3.4\,\mathrm{G/mm}$ which provides the spatial selectivity of the microwave pulse. Translated into a frequency gradient for the $|\, F = 1,\, m_F = -1 \,\rangle \;\rightarrow\; |\, F = 2,\, m_F = 0 \,\rangle$ microwave transition this corresponds to a spatial selectivity of $0.54\,\mu\mathrm{m/kHz}$. The lateral confinement of the trap means that the surfaces of equal field strength are curved upward at the position of the atoms. Due to the large sag distance, this curvature is not significant for the shape of the integrated density profiles within our measurement accuracy.

The lattice beams are superimposed with the equilibrium position of the atoms and are subsequently ramped on to an arbitrary final value V_0 within typically 160 ms [133]. After reaching the desired configuration of the system, the lattice depth is rapidly increased to $40\,E_\mathrm{r}$ within $100\,\mu\mathrm{s}$ in order to freeze out the density distribution. For the slice transfer, typically two independent pulses to two different states

at separate positions of the cloud are employed. This serves to reduce the number of repetitions required for a full profile. The two transitions used are $|\, F = 1, m_F = -1\,\rangle \rightarrow |\, F = 2, m_F = -1\,\rangle$ and $|\, F = 1, m_F = -1\,\rangle \rightarrow |\, F = 2, m_F = 0\,\rangle$. The obvious third one-photon transition $|\, F = 1, m_F = -1\,\rangle \rightarrow |\, F = 2, m_F = -2\,\rangle$ is not used because the coupling strength of the σ^--transition in the high offset field is too low due to a weak σ^- polarization component of the microwave and a frequency cutoff in the amplifier setup.

4.4 Data analysis

To generate a full density profile, many data points are taken independently for different sampling positions. The recorded images which represent the density distribution after the Stern-Gerlach separation are saved and post-selected by removing all measurements with a total number of atoms outside the target range from the subsequent analysis.

The probing frequencies are then translated to magnetic field strengths using the Breit-Rabi formula. The field strength values are converted to positions using the known gradient. By integrating over the regions of the three separated clouds, or alternatively by fitting a gaussian to each cloud and determining the volume, the atom numbers in all m_F states are determined. These numbers are then corrected for the background which originates from unwanted hyperfine transfers during the magnetic field switching. The fraction in the two slices probed is then calculated and all measurements for the same position are binned together and averaged. The error bars of this average are computed by first determining the average scatter of the data points around the average for their respective position. This value is then used to compute the uncertainty of the mean value from the individual measurements for each position.

4.4.1 Spatial resolution

The resolution which can be achieved by the method used is in principle given by the thickness of the slices which are transferred to the counting state. For simplicity, we use rectangular pulses with a length τ_P and the coupling strength Ω chosen such that the atoms on resonance experience a π-pulse. For this situation, the transfer probability $PSF(\Delta)$ for atoms detuned by Δ from the resonance frequency of the two-level system can be calculated as

$$PSF(\Delta) = \frac{\Omega^2}{2|\Omega^2 + \Delta^2|}\left(1 - \cos(\sqrt{\Omega^2 + \Delta^2}\tau_p)\right), \tag{4.3}$$

with $\Omega = \pi/\tau_p$ (see e.g. [69]). The shape of this distribution corresponds to the point spread function (PSF) of the one-dimensional imaging process. It is similar to

the sinc-function ($\sin(x)^2/x^2$) which describes the spectral density of the pulse. The borders (first zero crossings) of the central peak are at $\Delta = \pm\sqrt{3}\Omega = \pm\sqrt{3}\pi/\tau_P$. Therefore, the width of this peak in frequency space is $2\pi\sqrt{3}/\tau_P$. It can be made arbitrarily small by increasing the time τ_P of the pulse and correspondingly adjusting the coupling strength Ω.

The width of the pulse in frequency space is directly related to the width in real space by the magnetic field gradient and the field sensitivity of the transition used. When two transitions are probed in a single iteration of the experiment, the lengths of the pulses are chosen such that the slice thicknesses in real space are identical. For the σ^+ and the π transition, typical pulse lengths are 521 μs and 225 μs, which yields a total pulse width of 3.3 kHz for the σ^+-transition. This corresponds to a spatial width of 1.8 μm and full width half maximum (FWHM) of 0.834 μm of the central peak of the PSF.

If the slicing areas can be made arbitrarily thin, then what is the resolution limit of the method? One obvious limit is the reproducibility of the density distribution which is being examined and of the magnetic gradient field which determines the position which is probed. As one consequence, the position of the cloud has to be very reproducible between experimental cycles. The confining potential is dominated by the gaussian profile of the lattice laser beams. The pointing stability of each of the lattice beams therefore has to be on the micrometer scale for the duration of the profile scan.

The resonance position along the gradient for a given microwave frequency is given by the magnetic field offset and gradient. The dominating contribution to the field at the position of the atoms is from the homogeneous offset field, with a strength of approximately 150 G. A deviation of 2 μm corresponds to a magnetic field stability of 60 mG or a relative stability of up to 4×10^{-7}. The power supply driving the 72 A current used for this offset field[1] has a specified relative stability of 1×10^{-7}. The current ramp for this field, which also controls the 2 mm movement of the BEC from close to the center of the magnetic trap to the sagged position, is optimized for minimized oscillations at the final position. The residual position fluctuations are always small compared to the effective pixel size of the optical imaging system (4.0 μm).

Originally, the simultaneous sampling of several positions in the distribution was introduced in order to be able to compensate for shot-to-shot fluctuations in cloud position and magnetic field offset. One way to achieve this is to keep one of the sampled slice positions stationary in a part of the profile with a known density gradient. Deviations of each individually measured density value from the average can then be used to correct the slice position of all other samples taken in the same cycle. In this way drifts occurring on a timescale longer than the combined sampling time (approximately 1 ms) can be canceled. For the measurements presented here, however, this drift compensation was usually not employed. Improvements on the experiment

[1] Danfysik, 150 A maximum current

eventually resulted in a reproducibility which was no longer limiting compared to the counting resolution discussed below. Therefore, the simultaneous sampling was utilized only to increase the rate of data taking.

4.4.2 Counting limit

One obvious consequence of increasing the profiling resolution by decreasing the slice thickness is the reduction of the number of atoms per slice. This number can only be reduced to a point where it is still feasible to count the atoms in a reliable way. This counting takes place by integrating the optical density in the part of the absorption images which correspond to the appropriate hyperfine state. One inherent limit is therefore due to the shot noise in the number of photons which can be registered in that area. In practice, however, small shot-to-shot fluctuations in the inhomogeneity of the image background limit our sensitivity to approximately 50 atoms. The counted atom number per slice should be much larger than this limit. This can be achieved in two ways: Either by choosing an appropriately large slice thickness, which includes a sufficiently large amount of atoms or by summing the counted signal for several independent images with the same parameters. With the latter method, the counting fluctuations also add up, therefore the relative sensitivity improves with the square root of the number of images only.

The uncertainty in the atom number in a given slice limits the resolution of the method in practice, since only those features in the density distribution can be identified which lead to a change in atom number in adjacent slices which is large enough to be identified against the noise. Under good conditions, this is on the order of only a few lattice spacings.

4.5 Experimental results

4.5.1 Density profile of a Mott insulator

The density profiles obtained with this method for a Mott insulator in the optical lattice trap at a lattice depth of $40\,E_R$, are shown in figure 4.5. The data is taken with a resolution of about $0.8\,\mu$m FWHM ($521\,\mu s$ pulse length for the σ^+ transition). It allows for a direct determination of the sizes of the clouds inside the trap, and the profiles have sharp outer edges. The gray curves shows the results of a fitting the data with a model which assumes a perfect insulator state consisting of two or three Mott shells with constant integer site occupation. Apart from a $1\,\mu$m drift toward higher frequencies that occurred for the highest atom number scan[2] and had to be included, the data is very consistent with this model. However, the expected shape

[2]Most likely caused by an increase of the rubidium oven temperature before the last measurement in order to increase the maximum atom number

for a superfluid cloud with the same width and the same atom number, shown as the dashed curve in **b**, is so similar that the two can not be distinguished very well (However, with data taken at this high resolution, the difference in fit residuals is significant in the low atom number regime). In addition to this, a best fit with a gaussian shape, corresponding to a fully thermal distribution without effects of interactions is plotted for reference.

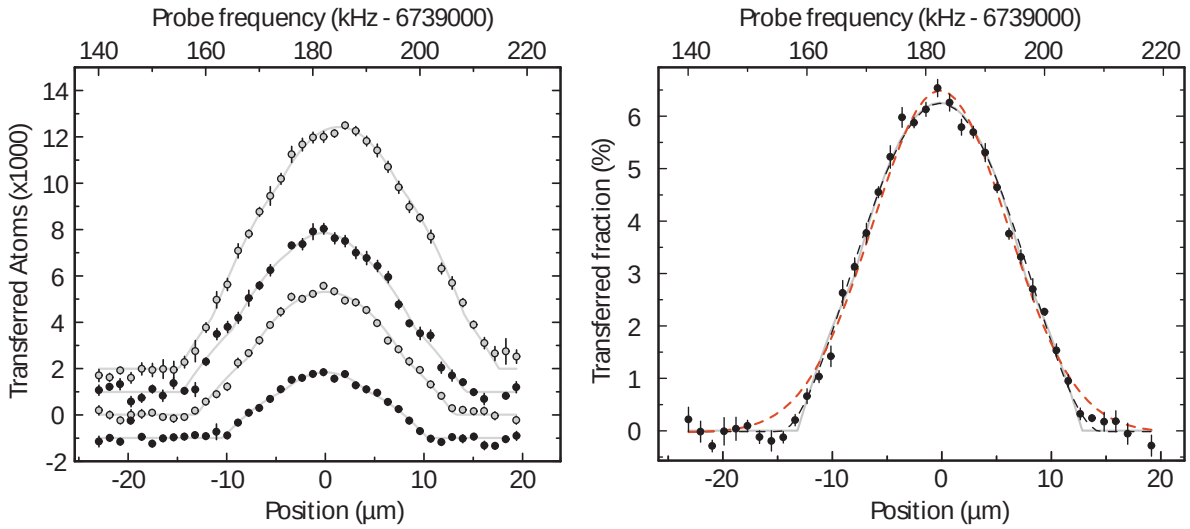

Figure 4.5: Density profiles of the Mott insulator distribution for different atom numbers (left panel). The density is plotted against the σ^+ probe frequency (top scale) as well as against position along the y-axis (bottom scale). The curves are offset along the vertical for clarity, and correspond to atom numbers of 1.1, 2.5, 3.6 and 7.1×10^5 atoms (bottom to top). Gray lines denote fits to the curves with a shell structure profile. The curves in the right panel, which correspond to 2.5×10^5 atoms, show the shapes of the profiles expected for the Mott insulator (gray) with the distinctive sharp edges and a kink around $\pm 8\,\mu$m. In addition, the profiles of a superfluid (black dashed) and a thermal cloud (red dashed) of the same atom number are plotted.

4.5.2 Spatially selective manipulation of atoms

While the slicing method described here is mostly employed as a scheme to measure density distributions, it inherently involves spatially manipulating the cloud of atoms by manipulating the internal state of the atoms locally. This can be shown directly by modifying the cloud in a defined way and recording the resulting change. It is demonstrated in figure 4.6, where the central slice of the distribution was transferred by a first microwave pulse ("manipulation pulse") to the $|\, F = 2, m_F = -1 \,\rangle$ state. A second pulse on the $|\, F = 1, m_F = -1 \,\rangle \;\rightarrow\; |\, F = 2, m_F = 0 \,\rangle$ transition with

the same spatial width is used as a probing pulse to obtain the resulting distribution. Since the second pulse does not couple to the $|\, F = 2,\, m_F = -1 \,\rangle$ state, the atoms are effectively removed from the density profile optained by the probing. In principle it is even possible to physically remove the atoms addressed by the first pulse using light resonant to $|\, F = 2,\, m_F = -1 \,\rangle$ state which could push those atoms out of the trap.

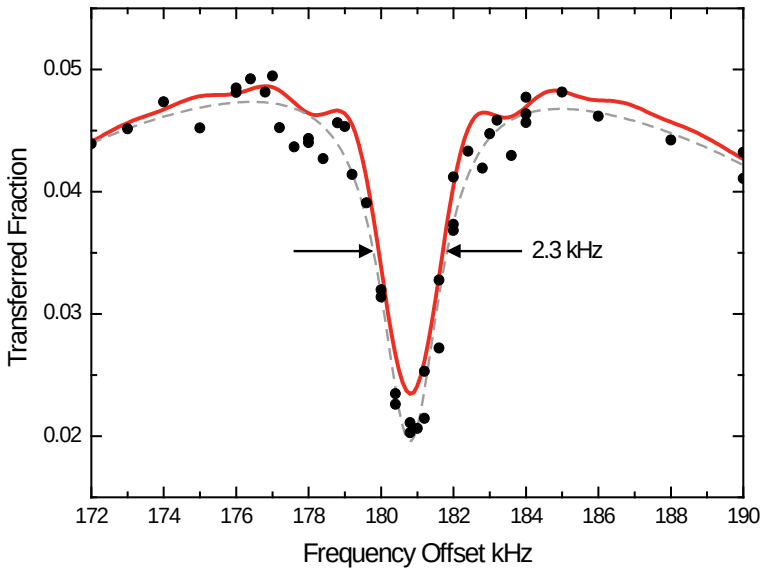

Figure 4.6: Resolution of the slicing technique: Atoms in the center of the cloud are removed by transferring one slice from $|\, F = 1,\, m_F = -1 \,\rangle$ to the $|\, F = 2,\, m_F = -1 \,\rangle$ state. The cloud is then probed by a second pulse with the same spatial width which transfers atoms to the $|\, F = 2,\, m_F = 0 \,\rangle$ state. The dashed line denotes a combined fit of the Mott shell structure to the unmodified cloud from which a gaussian peak was subtracted. The parameters of the gaussian were fitted to the data shown, resulting in a FWHM of 2.3 kHz. The solid red curve denotes the expected profile calculated directly from the known pulse parameters.

The obtained $m_F = -1$ density profile after removing the central slice is shown in figure 4.6. The pulse widths used are 225 μs on the $|\, F = 1,\, m_F = -1 \,\rangle \;\rightarrow\; |\, F = 2,\, m_F = -1 \,\rangle$ and 521 μs on the $|\, F = 1,\, m_F = -1 \,\rangle \;\rightarrow\; |\, F = 2,\, m_F = 0 \,\rangle$ transitions, respectively. This results in an identical spatial transfer profile or point spread function for both pulses. The shape of the dip in the measured density profile therefore corresponds to the PSF of eq. 4.3 convolved with itself. The full width, half maximum size (FWHM) size of the feature as obtained by fitting a gaussian to the data is 2.3 kHz. This corresponds to a spatial FWHM of 1.3μm for the measured dip and a 0.9 μm FWHM of the assumed gaussian PSF. The measured curve also agrees well with the shape calculated directly from the pulse parameters shown in red, which corresponds to a 0.83 μm FWHM of the point spread function.

4.5.3 The influence of the external confinement on the Mott insulator

As discussed in section 2.3.5, the shell structure of the Mott insulator in a trap is a result of its incompressibility and the confining potential of the trap. Due to the incompressibility, the density can only increase in steps which correspond to the edges of the shells. The distance between two steps and therefore the size and geometry of the shells depend on the gap energy and the gradient in the local chemical potential $\mu(\boldsymbol{r})$. Decreasing the strength of the confinement with otherwise unchanged parameters results in a slower variation on μ, which in turn causes larger shell sizes. It is important to note, however, that the density inside the shells does not change upon such decompression. The density in the center of the trap would change during compression and decompression for a classical gas or for a superfluid state. In the insulating state it can only change by introducing or removing additional shells with internally constant density in the center. Therefore, an important difference between these states arises when the confinement is such that only one MI shell exists: In this case, the density of the MI state can not be lowered, and the cloud does not expand, even if the confinement (and therefore the equivalent to the thermodynamic pressure) is reduced. The volume of the Mott insulating state thus increases upon deconfinement, until the cloud consists of only one shell. At this point its volume stays constant, even on further deconfinement.

In the optical lattice trap, the confinement strength is determined by the sum of the magnetic and the optical potentials. It is characterized by the trap frequencies for the harmonic oscillator, since the atoms are close to the minimum of the potential, where it can typically be well described by a parabolic shape. The attractive optical lattice potential strongly dominates the overall confinement even below the SF to MI transition. However, the confining force of the lattice potential created by red-detuned light can not be changed without modifying the lattice depth. An additional degree of freedom is therefore required to do this, which can be added in the form of an additional optical potential. To this end, a blue detuned (wavelength 765 nm) beam with the same beam geometry as the lattice beam on the x-axis is used. It is not retro-reflected and therefore provides a pure repulsive potential which counteracts the confinement in the radial directions due to the red beams.

The effect of such a deconfining potential is shown in figure 4.7. By varying the blue beam power, the confinement of the atom cloud can be within $\approx 55 - 70\,\mathrm{Hz}$ while maintaining otherwise identical lattice parameters. This changes the trap frequencies from $\approx 2\pi \times 73\,\mathrm{Hz}$ to $\approx 2\pi \times 57\,\mathrm{Hz}$ along the y- and z-axis, leading to an increase of the cloud diameter from $28 \pm 0.4\,\mu$m to $33.1 \pm 0.5\,\mu$m. This is a change of by $18.2 \pm 2.4\%$, consistent with the expectation for a multi-shell Mott insulator which will be derived in the following. It should be noted that, instead of creating the compressed Mott insulator first and then applying the deconfinement, the system was brought into the final state directly from the superfluid. In this way, it is much easier to fulfill the adiabaticity condition during the lattice changes, and the order of the

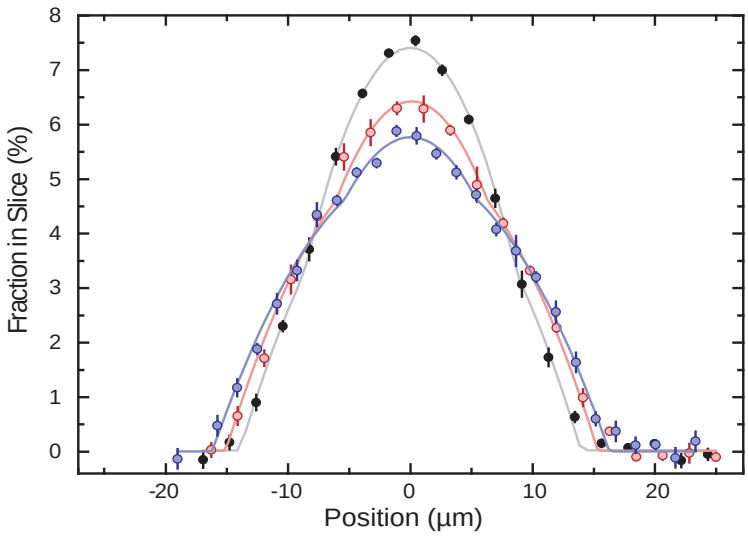

Figure 4.7: Mott insulator density profiles for different external confinement strengths, but otherwise similar trapping and probing parameters. Black data points correspond to a combined magnetic and optical trap potential of $2\pi \times (73 \pm 3)$ Hz along the y- and z-axis. Red and blue circles denote trap frequencies of $2\pi \times (63 \pm 4)$ Hz and $2\pi \times (57 \pm 4)$ Hz, respectively. Along the x-axis, the trap potential is not reduced. Lines show the results of fits with a Mott shell structure distribution.

sequence has no effect on the final distribution expected by theory. The lattice ramps used have been optimized numerically to achieve very good adiabaticity in the lattice manipulations and are relatively long (320 ms for the full sequence).

The blue detuned beam does not influence the confinement along its longitudinal directions, resulting in a non-isotropic decompression. Let us first consider the case of an incompressible cloud such as the single-shell Mott insulator. It can change its shape when it is subjected to a change of the confining potential as long as the overall volume is constant. In three dimensions, the gas will deform in such a way that it expands in the directions in which deconfinement is applied, and contracts along those directions with constant confining potential in order to keep the volume constant. This is why an expansion along the y-direction would be expected even in the case of a fully incompressible ensemble. The radii along the three dimensions can be easily calculated from the volume V of the single shell due to the condition that the chemical potential μ at the borders of the cloud has to be 0. The volume is given as

$$V = \frac{4}{3}\pi \bar{r}^3 = N \cdot a_{lat}^3$$

where a_{lat} is the lattice spacing, and $\bar{r} = (r_x r_y r_z)^{1/3}$ the average of the three cloud radii.

The on-site chemical potential

$$\mu(x,y,z) = \mu_0 - \frac{1}{2} m_{Rb}(\omega_x^2 x^2 + \omega_y^2 y^2 + \omega_z^2 z^2)$$

vanishes at the outer edge of the cloud. This yields

$$r_{x,y,z} = \sqrt{2\frac{\mu_0}{m_{Rb}\omega_{x,y,z}^2}} \text{ and } \mu_0 = \frac{m_{Rb}\bar{\omega}^2}{2} a_{lat}^2 \sqrt[3]{\frac{3N}{4\pi}}^2,$$

with $\bar{\omega} = \sqrt[3]{\omega_x\omega_y\omega_z}$

The slicing method determines the cloud size along the y-axis. Originally the confinement is approximately isotropic: $\omega_x = \omega_y = \omega_z$. Applying the deconfining potential reduces $\omega_y' = \omega_z'$ simultaneously by a factor α while keeping ω_x' constant. This leads to a scaling of the radius r_y as

$$r_y \propto \frac{\bar{\omega}}{\omega_y} = \sqrt[3]{\frac{\omega_x\omega_z}{\omega_y^2}} = \alpha^{-1/3}$$

In contrast, the total atom number in the superfluid (as well as the Mott insulator in the limit of high average occupation number and therefore a large number of shells), is determined by integrating the Thomas-Fermi distribution eq. 2.24 in the anisotropic harmonic confinement, which yields

$$N = \frac{4}{15}\frac{\pi m_{Rb}}{U a_{lat}^3}\bar{\omega}^2\bar{r}^5,$$

with $\bar{r} = \sqrt[3]{r_x r_y r_z}$ the geometric average of the Thomas-Fermi radii. The chemical potential in the center is

$$\mu_0 = \frac{1}{2} m\omega_j^2 r_j^2$$

with $j = \{x,y,z\}$. Under the same scaling of the trap frequencies as before, these relations lead to a scaling of

$$r_y \propto \alpha^{-3/5}.$$

Therefore, the formation of a single-shell Mott insulator can be identified by detecting the change in the vertical deconfinement response. Using the deconfining beam to reduce the radial trap frequencies by a 67% for example results in doubling the vertical size of a superfluid, whereas the single shell Mott insulator expands by only 45%. However, for the experimental configuration used, due to technical limitations arising with the blue beam setup such a large deconfinement could not be achieved with the required stability within reasonable effort. The combination of the two potentials along the same axis is very suceptible to fluctuations for large deconfinements

as one beam almost completely compensates the confinement from the other. Due to the stability limits, in the regime of low atom numbers and strong deconfinement the fluctuations of the confinement and position were large and made a reliable determination of the position of the shell boundaries difficult. Determining the shell geometry by probing the site occupation numbers directly proved to be more practical.

4.6 Site occupation number-dependent probing

The identification of constant density Mott shells depends on the identification of the shell boundaries. When using only density profiles, this in turn requires the identification of the kinks which appear in the density profile. These can be very weak even for ideal Mott states, making a clear identification difficult. A much better way to analyse the in-trap configuration is therefore to independently map the distributions of lattice sites with a specific occupation number. In this way, it can be directly determined whether the areas with different on-site occupations are separated or overlap.

This capability can be added to the slicing method by combining it with a number-state selective process. The approach pursued here is to transfer the slected slice into the $| F = 1, m_F = 0 \rangle$ state and to subsequently enable all atom pairs to undergo spin-changing collisions. The parameters are chosen as in section 4.1 such that the pairs among the transferred atoms change their state from $| m_F = 0, m_F = 0 \rangle$ to $| m_F = 1, m_F = -1 \rangle$. The otherwise unoccupied state $| F = 1, m_F = 1 \rangle$ therefore now directly reflects the amount of pairs in the selected slice.

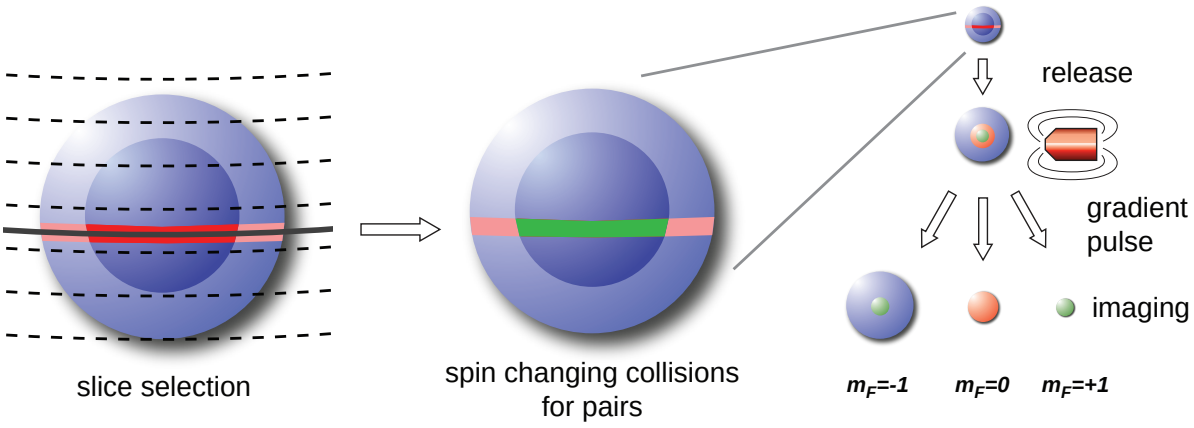

Figure 4.8: Illustration of the number state selective profiling technique. First one slice is transferred from $m_F = -1$ (blue) to $m_F = 0$ (red). Pairs in $m_F = 0$ then undergo a resonant collision into the $m_f = -1$ and $m_F = +1$ states (green). These three m_F-states are separated by a magnetic gradient on release, and imaged as separate clouds.

The typical parameters used for this extended process are slightly different from the usual ones, as the further subdivision of the transferred slice population and the additional experimental steps required reduce the signal-to-noise ratio. This will be discussed in more detail in section 4.6.1. Also, parallel probing of different locations in the cloud is no longer possible, leaving less points available for averaging. Taking this into account, the slicing π-pulse length is chosen as $150\,\mu s$. The pulse transfers the atoms from $|F = 1, m_F = -1\rangle$ to $|F = 2, m_F = 0\rangle$. A second π-pulse, which is resonant at the same position, is then applied to bring all atoms from $|F = 2, m_F = 0\rangle$ to $|F = 1, m_F = 0\rangle$ within $5.6\,\mu$s. This second pulse is applied with much higher coupling strength, leading to the short pulse time and a correspondingly large transfer profile in space. In addition to that, the $|\ F = 2,\ m_F = 0\ \rangle$ to $|\ F = 1,\ m_F = 0\ \rangle$ transition is much less magnetic field dependent than the slicing transition. Together, this ensures that all atoms which were addressed by the slicing pulse are also transferred back to the $F = 1$ hyperfine manifold by the second pulse.

The magnetic gradient field is then switched off completely, and a homogeneous offset field of 1.2 G remains. We then use the microwave dressing technique outlined in section 3.3.2 to switch on the coherent collisional coupling for 15 ms, which corresponds to one half oscillation. By this, pairs of atoms are transferred from the $|\ m_F = 0,\ m_F = 0\ \rangle$ to the $|\ m_F = 1,\ m_F = -1\ \rangle$ state. After this, the lattice is switched off, and the same ballistic expansion and imaging sequence with a 3.5 ms Stern-Gerlach pulse as in section 4.3 is used.

The population numbers $N_{m_F=-1}$, $N_{m_F=0}$ and $N_{m_F=+1}$ for the three m_F-states now encode the slice information in a different way than before. The reconstruction of the density distribution will be discussed in more detail in section 4.6.1. An approximation is the following: $N_{m_F=+1}$ contains one atom from each pair in the probed region, the other atom of each pair is counted by $N_{m_F=-1}$ together with all atoms outside of the slice. No spin-changing collision occur in sites with only one single atom transferred to the $m_F = 0$, and these are therefore counted in $N_{m_F=0}$.

4.6.1 Reconstruction and resolution of number-state distributions

By reconstruction from the above numbers the overall atom number N_{tot} as well as the total number of atoms in the slice region N_{slice} and the population in doubly occupied sites inside the slice N_2 are obtained. In order to discuss the resolution and detection limit of the number-state selective slicing method, the reconstruction process has to be looked at in more detail.

The counting technique yields the Zeeman state populations $N_{m_F=-1}$, $N_{m_F=0}$ and $N_{m_F=+1}$. After the slicing and the transfer pulse, the situation is still fairly simple: all the atoms of the slice are in the $m_F = 0$ state, whereas all other atoms are still in $m_F = -1$. However, the sequence which follows and allows for the number-state selective spin-changing collisions considerably complicates the situation.

Background calibration

One immediate effect, which is not number-state dependent is the following: During the switch-off of the magnetic trap, there is a finite probability for each atom to make a transition between two m_F states which differ by one quantum of angular momentum. This cannot be avoided for our setup, and is independently measured by calibration experiments, where combinations of the $m_F = -1$ and the $m_F = 0$ state are occupied and no spin-changing collisions take place. The transfer probabilites obtained from these calibrations are then used to compensate the effect in the measurements.

Resolution and slice transfer profile

The shape of the point spread function for single atoms was already discussed in section 4.5.2. For atom pairs, this shape changes due to the fact that a pair is only detected if both its members are transferred to the $|\, F = 1, m_F = 0 \,\rangle$ state, where they can undergo spin-changing collisions. The spin-dependent collisions are sensitive to *transferred* pairs only, not to doubly-occupied sites in general. Therefore, the probability distribution of detecting an atom pair is actually the squared single-particle distribution. This distribution is narrower in frequency space which means that, for pairs, a higher resolution is achieved with the same transfer pulse length. The FWHM of the central peak is narrower by almost 30%. When choosing the step size for the profiling scan, this is taken into account, which results in significant oversampling of the single atom signal profile.

As a consequence of the more narrow detection region for atom pairs, the detected atom numbers for the same over density are different for the two cases of pairs and single atoms. In order to be able to combine both numbers, this reduction is compensated. The ratio of the integrals of both point spread functions is 0.61. The measured number of pairs is therefore divided by this number in order to allow direct comparison to the overall number of atoms in the slice.

The pair detection could be improved if the PSF were made rectangular in such a way that it contains only the values 0 and 1. In that case, the probability of transferring only one atom out of a pair would be very small, and the point spread functions for both single atoms and pairs would have the same shape. The transfer pulse could be optimized in this regard by either using shaped pulses or multi-pulse sequences. These techniques are very common in classical nuclear magnetic resonance measurements to increase either spectral sensitivity or spatial resolution.

Another obvious way of removing this particular effect would involve initiating the spin-changing collisions before the slicing sequence. In this case the PSF for the two number states would be the same, and less corrections would be required. However, this would require switching the magnetic gradient fields off completely for the spin-changing collisions, and on again later as the gradient for the slicing pulse. The long

settling times however as well as the introduction of much more background due to the repeated magnetic field switching events make this approach less appealing.

Offset correction and data reconstruction

Due to the processes explained above, the three populations obtained from counting the atoms in the three final hyperfine states do not correspond directly to the quantities of interest. The relevant numbers are the atom numbers in the selected slices, separated for singly and doubly occupied sites.

The relation is still quite simple for the $m_F = 1$ state, which can only be populated by atoms undergoing a spin-changing collision from $m_F = 0$ to $m_F = 1$. However, only one atom of the pair ends up in this state, whereas the other is transferred back to $m_F = -1$. In addition to that, the pair transfer efficiency is 0.61 for the pulse shapes used compared to the single atom transfer. Therefore, the population in $m_F = 1$ is only 31% of the quantity of interest, the population of pairs inside the selected slice.

In contrast to this, $N_{m_F=-1}$ contains all atoms which were outside the selected slice, as well as an additional fraction of the atoms which were on the inside. This latter fraction contains two parts: One is due to atoms which were transferred back from the $m_F = 0$ to the $m_F = -1$ state during spin-changing collisions and the other due to atoms from doubly occupied sites in which only one atom of the pair was transferred to $m_F = 0$ by the slicing sequence. $N_{m_F=0}$ consists of the atoms in the slice from sites with single occupation as well as those of doubly occupied sites in the slice where the pair was not fully transferred.

In order to obtain the in-trap occupation numbers, these known transformation effects have to be taken into account. In addition, the effects of all unintended population transfers, generated mostly during the trap field switching, have to be reverted. This is done quite literally by combining them in a transformation matrix M which predicts the outcome of the "distorted" measurement from the original set of populations in the Zeeman states.

$$\begin{pmatrix} N'_{m_F=1} \\ N'_{m_F=0} \\ N'_{m_F=-1} \end{pmatrix} = \begin{pmatrix} 1 & P_{0,1} & P_{-1,1} \\ 0 & 1-P_{0,1} & P_{-1,0} \\ 0 & 0 & 1-P_{-1,0}-P_{-1,1} \end{pmatrix} \cdot \begin{pmatrix} N_{m_F=1} \\ N_{m_F=0} \\ N_{m_F=-1} \end{pmatrix} \tag{4.4}$$

Here, P_{m_1,m_2} denotes the probability of transferring an atom from $\mid F = 1,\, m_F = m_1 \rangle$ to $\mid F = 1,\, m_F = m_2 \rangle$, with typical values of $P_{-1,0} \approx 0.03$, $P_{0,+1} \approx 0.03$ and $P_{-1,+1} \approx 0.003$. These values are determined with an independent calibration measurement.

This matrix is then inverted and the resulting calibration matrix used to calculate the actual populations in the Zeeman states as produced by the slicing and exchange processes without distortions. From these populations, the populations $(N_{tot}, N_{slice}, N_2)$

are then determined:

$$\begin{aligned} N_{tot} &= N_{m_F=-1} + N_{m_F=0} + N_{m_F=1} \\ N_{slice} &= N_{m_F=0} + 2N_{m_F=1} \\ N_2 &= 2N_{m_F=1}/0.31 \end{aligned}$$

Averaging and Statistics

The averaging procedure is similar to the one described in section 4.4. After removing those images for which the atom number lies outside the targeted range, typically 2 to 5 images can be averaged per slicing frequency. If at the end of the data-taking run less than two valid data points in the chosen atom number range were recorded for any given slicing frequency, those slices are measured again until enough valid data is taken.

The error bars are determined independently for each curve in the same way as presented in section 4.4. It is worthwhile to note that due to the transformations required to calculate the slice atom fractions from the m_F state populations, the error bars for the derived numbers differ significantly from each other. Since only about one third of the atoms from doubly occupied sites in the slice is detected, this quantity has the highest fluctuations due to counting errors and consequently the largest error bars. Somewhat counter intuitively, the difference signal $N_{tot} - N_2$ typically has the smallest error bars. This is due to the fact that this quantity almost directly corresponds to the $m_F = 0$ population, which requires only a small correction and therefore does not accumulate errors from more than one source. Clearly, the signal to noise ratio for this measurements is lowest for the N_2 signal. The slice width and sampling step size is therefore optimized for this quantity, resulting in significantly wider slices and accordingly shorter pulses than for the experiment without number state selectivity.

4.6.2 Results

To display the resulting profiles, the averaged data is plotted against position as in the single-particle case. In order to visualize the different number state distributions, the density of singly occupied sites is of interest, as it is expected to display the characteristic plateau of the truncated parabola as soon as a central doubly-occupied core forms. For the typical atom numbers and trap parameters, only an $n = 1$ and an $n = 2$ shell is expected. In that case the $n = 1$ density can be displayed by subtracting the $n = 2$ atom density from the total atom density. Atoms on triply occupied sites undergo only weak spin exchange for the parameters chosen, and these atoms therefore appear mostly together with the single atoms.

In figure 4.9, the resulting number-state selective density profiles are shown. The measured curves are fitted with a model assuming three shells with a perfect shell

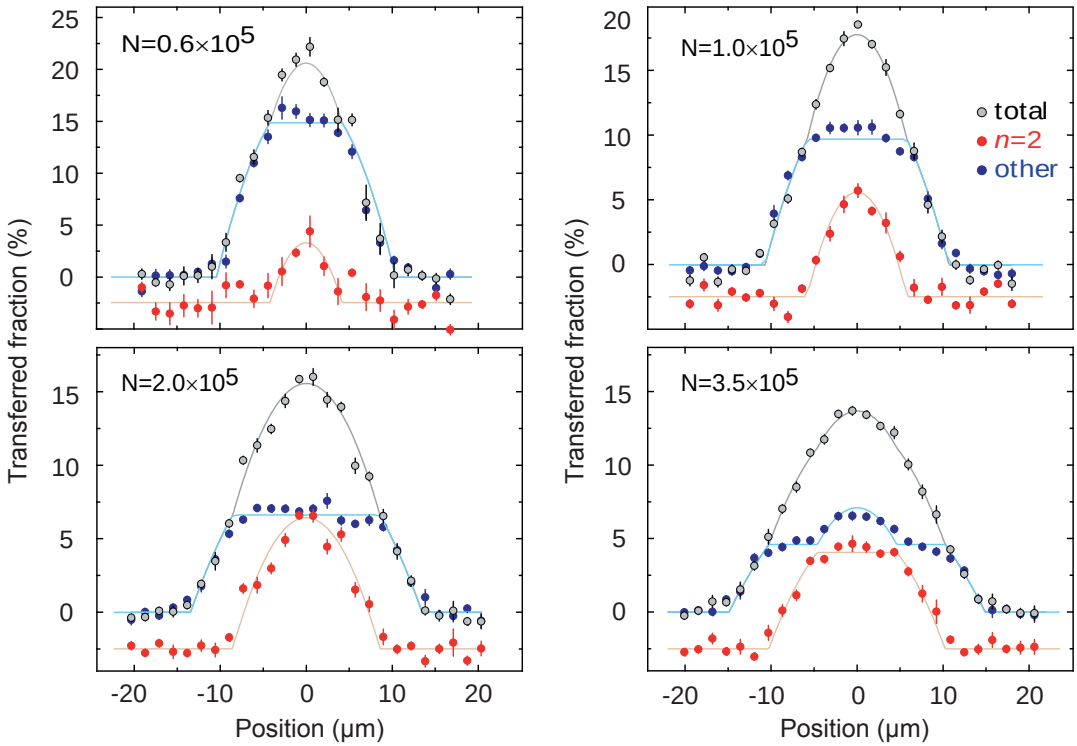

Figure 4.9: Number state resolved density profiles of the atom cloud for different total atom numbers: Grey points are the total density distribution and red points the distribution of doubly occupied sites. Blue points are the fraction of atoms from sites with occupations other than $n = 2$. The lines are fits with density profiles calculated using a perfect Mott shell structure. The atom pair signal is offset for clarity. The central core of doubly occupied sites is visible as a separate distribution of sites with $n = 2$ which is smaller than the overall radius. The density of singly occupied sites vanishes in this shell, resulting in a plateau in the integrated density profile for $n = 1$. For large atom numbers, a third shell with $n = 3$ appears in the center of the $n = 2$ shell, leading to a plateau structure of the $n = 2$ profile as well.

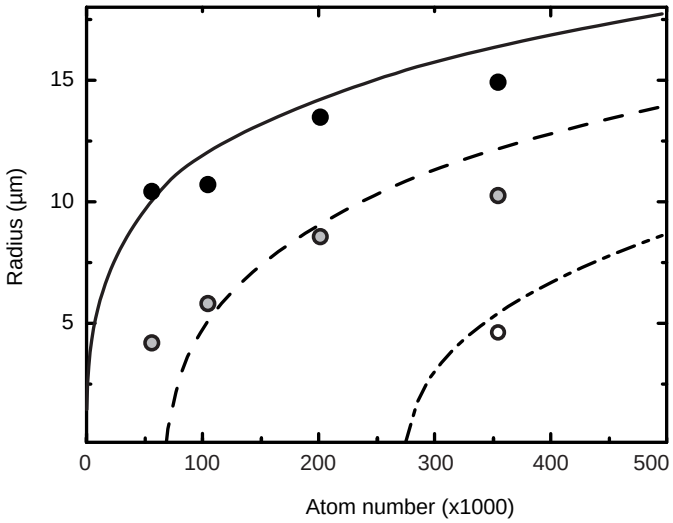

Figure 4.10: Fitted radii of the Mott shells for different atom numbers and a lattice depth of 22 E_r. The solid, gray and hollow data points denote the radii of the shells with single, double and triple occupation, respectively. The solid, dashed and dashed dotted lines are calculations of these first three Mott shell radii for zero temperature and zero tunnelling.

structure ($T = 0$ equivalent) and the shell radii as independent fit parameters. For very low atom numbers, only a very weak central $n = 2$ shell is visible, most of the cloud consists of singly occupied sites. For increasing atom number, the inner shell radius, and with it the size of the plateau in the single-atom signal, increases much faster than the outer shell radius. Above the threshold for the formation of a third, triply occupied shell in the center, the $n = 2$ shell profile develops a plateau structure and the additional structure on top of the $n = 1$-plateau indicates the presence of the new shell.

The signatures of the Mott shells in the trap are the parabola shapes of the $n = 1$ and $n = 2$ profiles with sharp edges and the flat top structure characteristic for a hollow shell. With increasing temperature $T > 0.2U$, these edges wash out, as shown in section 2.4. The fitted radii of the shells are plotted in figure 4.10 against atom number. They are compared with the calculated values for the $T = 0$, $J = 0$ idealized case without any free parameters. Qualitatively, the data agrees well with the predicted shape. The measured radii are generally somewhat smaller than expected. It appears therefore that the trap confinement along the vertical axis was larger than expected, reducing all measured radii and shifting the $n = 2$-shell formation threshold toward smaller atom numbers.

The density profiling process always takes place in a deep lattice, since tunneling has to be suppressed on the timescale required for the transfer pulses and the

spin-changing collisions. It is therefore not possible to obtain number-state selective density profiles in a lattice with strong tunnel coupling being present. However, the density profiles in this regime can be obtained if the tunneling is suppressed quickly by ramping up the lattice to a large barrier depth faster than atom redistribution can occur. In this way, the density profiles for the superfluid regime can be probed. Figure 4.11 shows several profiles in between the fully superfluid and the fully Mott insulating regime.

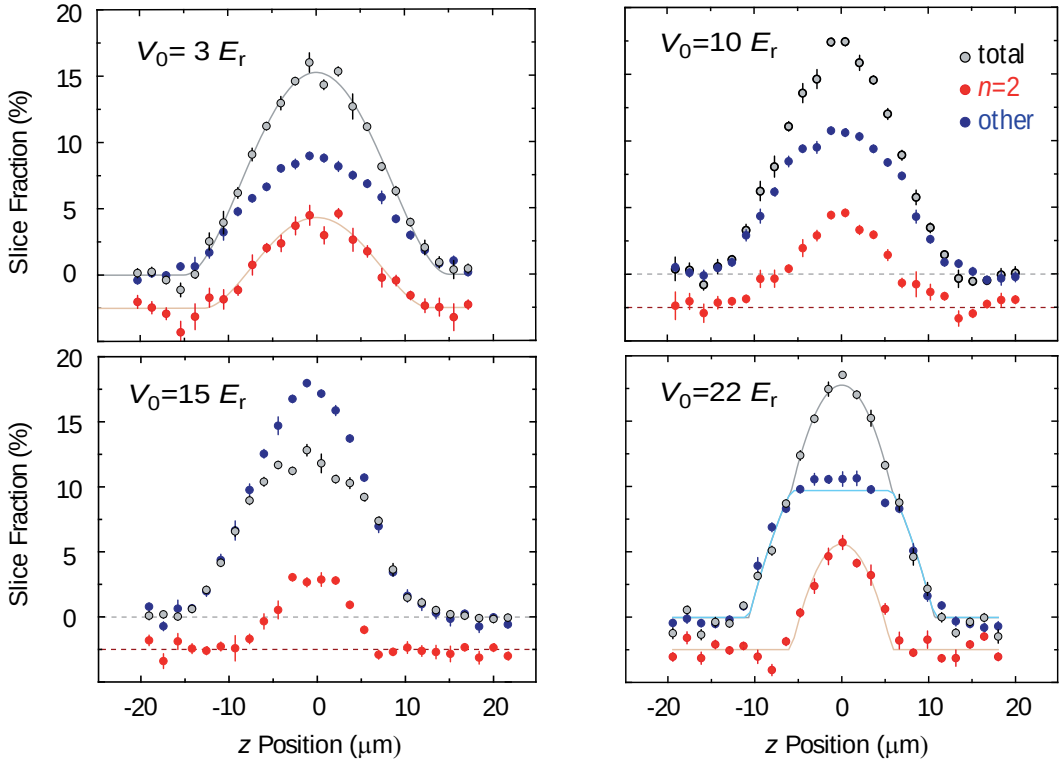

Figure 4.11: Number state selective density profiles of the atom cloud for different lattice depths V_0 and approximately 1.0×10^5 atoms. In the superfluid regime at low lattice depths, the data is well described by the Thomas-Fermi distribution. For the density chosen, doubly occupied sites are less likely then singly occupied ones, but can appear in all parts of the cloud. For high lattice depths, the cloud is separated into two shells and no doubly occupied sites occur in the outer region.

The first profile was taken at a lattice depth of $3\,E_r$, where $J/U \approx 0.8$. Correspondingly, the total density distribution is expected to be a Thomas-Fermi profile. The data shows a smooth density profile both for the $n = 1$ and the $n = 2$ component in this limit. It can be well described with the profiles expected from a Thomas-Fermi distribution (see section 2.3.4). With increasing lattice depth and therefore increasingly dominating interactions, the curves change toward the profiles that are expected for a Mott insulator with two shells. For the parameters chosen, the global density redis-

tribution occurs relatively early, already significantly below the Mott-insulator transition expected at $\approx 13\,E_R$. Above a lattice depth of approximately $10\,E_R$, the most pronounced changes of the profiles are at the edges of the shells. As far as the absolute width of the distribution in space is concerned, this is easy to understand. The ramping up of the lattice beams also increases the confinement of the cloud due to the attractive potential created by the gaussian beams. The trap frequency for our parameters changes from approximately 15 Hz to 80 Hz from the configuration without lattice to the full lattice potential with a depth of $40\,E_R$. Since the increase in pressure in the gas due to the increasing interaction is not large enough to counter this completely, the overall size of the cloud decreases. The above mentioned behavior, however, is also visible when this is accounted for.

In order to describe the transition in a more quantitative way, we define a quantity which describes the redistribution as the system undergoes the transition. An obvious feature which distinguishes the Thomas-Fermi distribution from the Mott insulator structure is the occurrence of doubly occupied sites everywhere in the cloud, all the way up to its outer edge. In the insulating case, atom pairs can only occur within the inner shell, which has a significantly smaller radius than the overall cloud. A straightforward parameter for the distributions shown therefore is the relative size of the two distributions obtained for singly- and doubly occupied sites.

In general, this choice is not as straightforward - it has the inherent problem, that the radius of the distributions for a given occupation number n always decreases with n, even for a thermal or superfluid ensemble. This is due to the fact that the site occupations are governed by Poisson statistics, for which the probability of a given site occupation is nonlinear in the density. In the outer regions of the cloud where the density is low, the occurrence of multiply occupied sites might always be possible, but can be very unlikely, yielding effectively smaller radii than the overall size. In the special case of average per-site densities only slightly larger than one, however, the method is feasible, as in this limit the sizes of the distributions for $n = 2$ is expected to be almost identical to the overall cloud size unless number squeezing occurs. It is therefore possible to use the ratio of the radii for distributions of both analyzed number states to characterize the transition from the superfluid to the Mott insulator, by choosing a low average occupation number. The resulting low atom numbers finally are the reason why the high resolution and signal to noise ratio is required.

In order to determine the radii, the integrated Thomas-Fermi profile is used as a fitting function. This choice is somewhat arbitrary, since no simple fit function models the profiles in both limiting regimes as well as the transition region. A model-independent approach such as using the root mean square (RMS) radius of the distribution was attempted first, but was abandoned as it was too unstable against the fluctuations of the signal around the baseline in the outer parts of each scan.

The evolution of the relative shell sizes is shown in figure 4.12. During the transition from the SF to the deep Mott insulating phase, a pronounced drop from ≈ 0.9 to ≈ 0.65 occurs. The theory estimates for the two limiting cases yield an expected

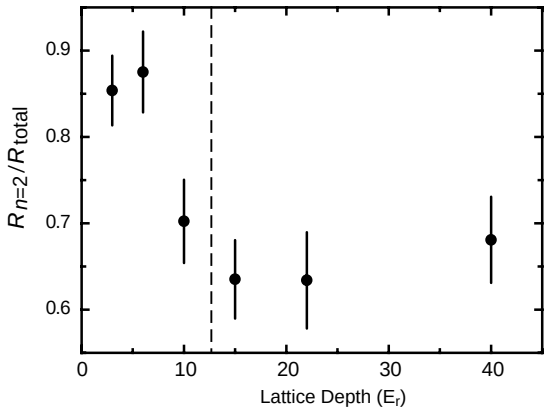

Figure 4.12: Evolution of the ratio $R_{n=2}/R_{n=1}$ through the superfluid to Mott-insulator transition for $N_{\text{total}} = (1.0 \pm 0.1) \times 10^5$ atoms. The drop in the ratio os due to the formation of a distinct inner shell with doubly occupied lattice sites. The dashed line marks the lattice depth at which the SF to MI transition is expected for an average site occupation of 1.

ratio of 0.99 for the superfluid in the $3\,E_{\text{R}}$ lattice depth configuration and 0.45 for a Mott insulator with that particular atom number, negligible tunneling and zero temperature. The deviation for the Mott insulating case is significantly larger than the error bars, which are derived from the fit uncertainties. However, the predicted value in this case depends strongly on the atom number and the strength of the external confinement. An increase of either of them would increase the ratio of sizes. Very high temperatures would have the same effect, but the shape of the profiles rules out a large enough temperature to explain the measured ratio. In fact, provided the interaction energy constant is known well enough, the determination of the atom number and the total confinement by measuring the shell radii is probably a more direct and more precise measurement of both parameters than the usual calibrations.

5 Characterizing quantum states using quantum noise correlation analysis

The workhorse among the detection methods used in the field of cold atoms today is the optical imaging technique [44], usually by absorption of resonant light. When applied in the time-of-flight (TOF) method described in chapter 3.2, imaging corresponds to measuring phase correlations (first-order correlations) between lattice sites, and one effectively measures the free-space momentum distribution of the ensemble. Properties which are related to phase correlations appear as spatial structures after the TOF period and can usually be measured very well with this kind of imaging technique. For example, the global phase coherence of a BEC in a lattice can be easily identified by the interference pattern. When the phase is constant throughout the cloud, the momentum distribution is given by the Fourier transform of the original density distribution (See section 3.2.1).

In the strongly correlated regime however, where particles are fully localized, there is no first-order correlation (phase relation) between different lattice sites. In this case, all interference terms vanish on average, apart from small contributions due to weak short range correlations [84, 85]. The time-of-flight distribution is then given only by the on-site properties of the atoms in the lattice, as all atoms from each site are released fully independently of all other sites. But even despite the independent release, the Hanbury Brown-Twiss effect (for bosons) [39, 134] causes spatial correlations of the atoms after a time-of-flight period [40, 135–137]. These second-order correlations arise due to the quantum statistics of the particles and build up when the system transitions to the strongly correlated regime, while the first-order correlations vanish. They reflect the spatial distribution of the atoms inside the lattice and can be detected in the atom shot noise of the 2D density distribution measured by absorption imaging.

As discussed in section 3.2.1, the overall shape of the expanded wave functions during ballistic time of flight is given by the expanded Wannier function of the lowest Bloch band, which is the on-site wave function for almost all experiments with strongly correlated systems in lattices (see section 2.3.1). Figure 5.1 shows an atom cloud after time-of-flight expansion from the Mott insulating state. The shape is given by the Wannier function in momentum space, an almost perfect gaussian without significant visible features. The only significant deviations are the statistical fluctuations of the data around the expected fitted curve.

For suitable parameters, the noise on images of the atom clouds is dominated by the atom shot noise, the deviation of the measured column density at a given pixel

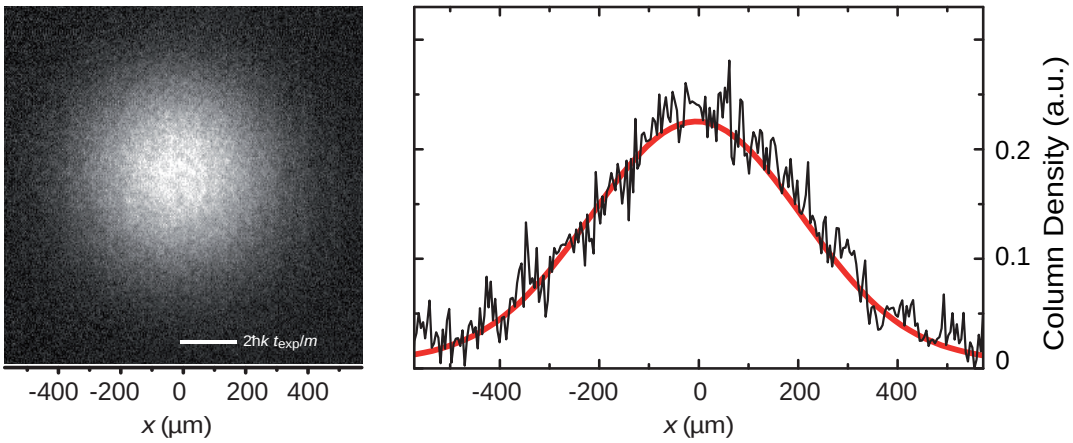

Figure 5.1: Atoms released from a Mott insulator (lattice depth $55\,E_R$) show a featureless gaussian distribution in momentum space. The noise seen on top of this shape is dominated by the atom shot noise in this image. A total of 5×10^5 atoms are in the cloud, which corresponds to a central density of 32 atoms per pixel. Taking a profile through the center of the cloud clearly shows these fluctuations around the gaussian curve fitted through the averaged profile. For perfect optical illumination and imaging these fluctuations would have an RMS width of $\sqrt{32} = 5.6$.

from the expectation value due to the discreteness of the atoms. The noise itself is Poisson-distributed, and is, for an individual pixel, completely random. The point-to-point correlations in the shot noise however encode two-body quantum correlations between the atoms, which are influenced by the structure of the cloud before the release. It was therefore proposed to use the shot noise correlations for the analysis of otherwise inaccessible in-trap properties of strongly correlated cold atom systems [40]. In this chapter, the origin of these shot noise quantum correlations and the application of the method will be shown.

5.1 Spatial correlations in two-particle measurements

The detection probability of a single particle in a given point in space in quantum mechanics is given by the absolute square of the spatial wave function of the atom at this point. This appears especially obvious if the particles in the experiment do not interact and are introduced individually - which requires that the full quantum mechanical state of all particles involved is separable into a product of single-particle states. In this case, the time evolution for all particles is independent, and, for indistinguishable particles, the detection probability of a particle at a given location is the sum of the detection probabilities of all particles.

Even in this very simple situation, surprising consequences arise when simultaneous detection of particles is possible, for example by using two separate detectors. Of course the above argument still holds for the measurements of each of the detectors when analyzed independently. However, it does not automatically imply that the outcomes of those measurements have to be completely independent. Instead correlations can and do occur between two separate but simultaneous measurements. In quantum mechanical terms this combined measurement not only probes the single-particle wave functions, but also the multi-particle states. Therefore, the full many-body state has to be taken into account in order to predict the outcome of the overall experiment including both detectors.

One well known example of such a correlation is the so-called Hong-Ou-Mandel effect [138]. This refers to the vanishing probability that two independent photons, which arrive simultaneously on the two input ports of a four-way beam splitter, will leave the splitter separately via separate output ports. The reason for this is the destructive interference between two possible two-photon paths, which occurs if the two photons – and therefore the two paths – are indistinguishable.

A more general effect of this type is the Hanbury Brown-Twiss effect [39, 134]. Originally formulated for classical electromagnetic fields, it states that for bosonic particles emanating from independent sources and arriving at two detectors, the probability of simultaneous detection of both atoms is not just the product of the single atom detection probabilities at the two positions. Instead, it also depends on the relative position of the two detectors.

This can be illustrated in a simple Gedankenexperiment. We assume that two bosonic particles are released by two completely independent sources, denoted $S1$ and $S2$ in figure 5.2. Two detectors A and B at two independent locations in space are used to probe the presence of an atom after some time of propagation. In the following, we analyze the case where one particle was detected at each detector location. In order to predict the probability of this event, the probability amplitudes of all possibly *two-particle* trajectories have to be summed. For two sources and two atoms, two combinations of single-particle trajectories are available: $S1 \rightarrow A$, $S2 \rightarrow B$ and $S1 \rightarrow B$, $S2 \rightarrow A$. The simultaneous detection probability for distinguishable particles would be the sum of the probabilities of both two-particle trajectories. As in the indistinguishable case the quantum mechanical probability amplitudes are summed as opposed to the individual probabilities, they can interfere constructively or destructively, depending on the relative phase. This phase typically depends on the relative path lengths of the two possible two-particle trajectories, therefore the combined detection probability can be reduced or enhanced for different relative positions of the two detectors. The result is the sinusoidal modulation shown in figure 5.2b. For distinguishable particles, the probabilities of both paths are summed, therefore the relative phase does not enter. In contrast to this, for indistinguishable fermionic particles an additional phase factor of -1 is introduced between the two possible path combinations. This is due to the antisymmetric fermionic wave function, since

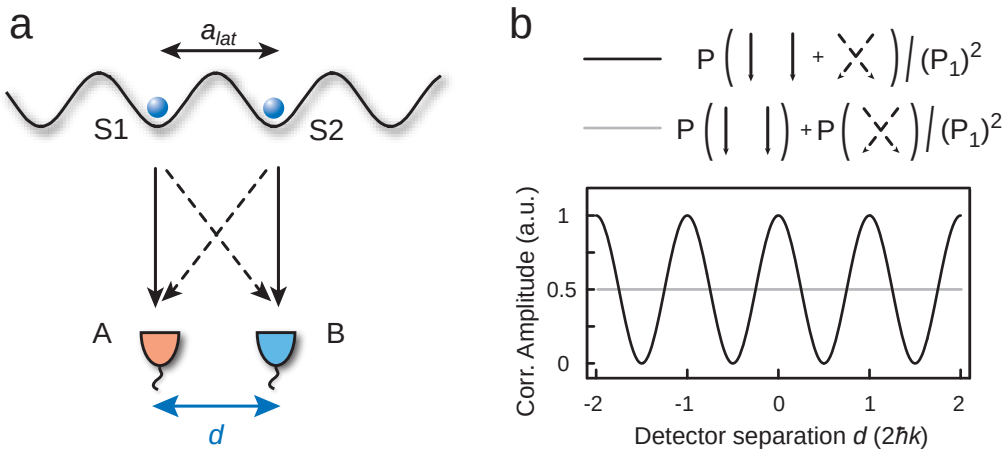

Figure 5.2: Origin of Hanbury Brown-Twiss correlations in atoms released from an optical lattice. **a)** Two lattice sites act as sources for one atom each. These atoms are detected simultaneously by two independent detectors after a time-of-flight period. For this outcome of the experiment, two different paths of the atom pair are possible. **b)** The interference of these paths leads to a joint detection probability which is modulated with the detector distance d (black curve). For distinguishable particles, the probabilities for both paths have to be added, leading to no interference (grey curve). Both curves are normalized by the squared probability P_1 of each detector for the detection of any of the two atoms released.

the two paths are related by a two-particle exchange. The probability amplitudes are therefore effectively subtracted, leading to a correlation function which is inverted compared to the bosonic case.

5.1.1 Correlated detection of bosons released from an optical lattice

When releasing atoms from an optical lattice in the deep Mott insulating regime, the individual sites can be viewed as independent sources. In this regime the occupation number on each site is fixed, there is no coherence and therefore no defined relative phase exists between particles on different lattice sites.

The degree of correlation between the measurements at two positions x_1 and x_2 in terms of the atom density operator $\hat{n}(\boldsymbol{x})$ is given by the quantity

$$G(\boldsymbol{x}_1, \boldsymbol{x}_2) = \frac{\langle \hat{n}(\boldsymbol{x}_1)\hat{n}(\boldsymbol{x}_2)\rangle}{\langle \hat{n}(\boldsymbol{x}_1)\rangle \langle \hat{n}(\boldsymbol{x}_2)\rangle}. \tag{5.1}$$

For very low densities $\langle \hat{n}(\boldsymbol{x}_1)\rangle \ll 1$, this is the probability of joint detection of atoms at both locations normalized by the probability of simultaneous detection in the uncorrelated case. The latter is given by the product of the overall probabilities of detecting an atom at the two detector positions. If G is larger than one, the probability

of simultaneous detection at the two detector locations is enhanced over the classical case. If it is smaller than one, this probability is reduced, the measurements at the two locations are anticorrelated.

In the following we will calculate the correlation factor for two detectors for independent atoms released simultaneously from separate sites of an optical lattice. Between release and detection, a time of flight period of length t is assumed.

The density operator for the detected number of atoms

$$\hat{n}(\boldsymbol{x},t) = \langle \Psi(t)|\hat{a}^\dagger(\boldsymbol{x})\hat{a}(\boldsymbol{x})|\Psi(t)\rangle$$

at position $\boldsymbol{x}$ for the system at time t after release was calculated in section 3.2.1 (eq. 3.4):

$$\hat{n}(\boldsymbol{x},t) = \sum_{j,k} W^*(\boldsymbol{x}-\boldsymbol{x}_j)W(\boldsymbol{x}-\boldsymbol{x}_k)e^{\frac{i\hbar t_{exp}}{2m\sigma_0^2\sigma(t_{exp})^2}(2\boldsymbol{x}(\boldsymbol{x}_j-\boldsymbol{x}_k)+\boldsymbol{x}_k^2-\boldsymbol{x}_j^2)}\hat{a}_j^\dagger\hat{a}_k \tag{5.2}$$

With $W(\boldsymbol{x},t)$ being the Wannier envelope of the wave function of an atom released from a deep lattice site. As the Mott insulator is always released from a very deep lattice, it can be well approximated by a gaussian. It has the initial width σ_0 in the trap and the expanded width $\sigma(t)$ at time t.

The correlated density operator, which correlates positions $\boldsymbol{x}_1$ and $\boldsymbol{x}_2$ is therefore

$$\hat{n}(\boldsymbol{x}_1,t)\hat{n}(\boldsymbol{x}_2,t) = \sum_{j,k,l,m} W^*(\boldsymbol{x}_1-\boldsymbol{x}_j)W(\boldsymbol{x}_1-\boldsymbol{x}_k)W^*(\boldsymbol{x}_2-\boldsymbol{x}_l)W(\boldsymbol{x}_2-\boldsymbol{x}_m)\cdot \tag{5.3}$$
$$e^{\frac{i\hbar t_{exp}}{2m\sigma_0^2\sigma(t_{exp})^2}(2\boldsymbol{x}_1(\boldsymbol{x}_j-\boldsymbol{x}_k)+\boldsymbol{x}_k^2-\boldsymbol{x}_j^2)+(2\boldsymbol{x}_2(\boldsymbol{x}_l-\boldsymbol{x}_m)+\boldsymbol{x}_m^2-\boldsymbol{x}_l^2)}\hat{a}_j^\dagger\hat{a}_k\hat{a}_l^\dagger\hat{a}_m$$

For simplicity, we make some of the same approximations as in section 3.2.1: We assume that t_{exp} is long enough such the expanded wave function size $\sigma(t)$ is much larger than both the on-site wave function size σ_0 (typically by a factor of 10^3) and the overall size of the in-trap distribution, and thus all $|\boldsymbol{x}_j|$. As $W(\boldsymbol{x},t)$ is smooth on the scale of $\sigma(t)$, we can substitute $W(\boldsymbol{x}+\boldsymbol{x}_j,t)$ with $W(\boldsymbol{x},t)$ in the envelope part of the function. Furthermore, $\sigma(\boldsymbol{x},t)$ can then be replaced by $t\hbar/(\sigma_0 m)$. This yields

$$\hat{n}(\boldsymbol{x}_1,t)\hat{n}(\boldsymbol{x}_2,t) =$$
$$\sum_{j,k,l,m} |W(\boldsymbol{x}_1)|^2|W(\boldsymbol{x}_2)|^2 e^{\frac{im}{2\hbar t}(2\boldsymbol{x}_1(\boldsymbol{x}_j-\boldsymbol{x}_k)+\boldsymbol{x}_k^2-\boldsymbol{x}_j^2)+(2\boldsymbol{x}_2(\boldsymbol{x}_l-\boldsymbol{x}_m)+\boldsymbol{x}_m^2-\boldsymbol{x}_l^2)}\hat{a}_j^\dagger\hat{a}_k\hat{a}_l^\dagger\hat{a}_m. \tag{5.4}$$

It should be noted that the third approximation made for the calculation of the interference pattern in section 3.2.1 is not necessary, the $\boldsymbol{x}_j$-terms are not neglected here. This means that, in contrast to the density distribution calculated earlier, the

results of this calculation will be correct even on scales smaller than the size of the initial density distribution[1].

The properties of the in-trap quantum state are probed by the term

$$\hat{a}_j^\dagger \hat{a}_k \hat{a}_l^\dagger \hat{a}_m$$

which in normal ordering yields

$$\hat{a}_j^\dagger (\hat{a}_l^\dagger \hat{a}_k + \delta_{lk}) \hat{a}_m \tag{5.5}$$

The delta term will lead to a peak at the $\boldsymbol{x} = 0$-position of the correlation function. For now it will be neglected, as we are interested in the other terms which contain the spatial ordering information. In principle the central peak contains useful information about the point spread function of the imaging system and about the overall noise of the system.

For a Mott insulator of filling n_j at site j, we have $\hat{a}_j^\dagger \hat{a}_k = \delta_{jk} n_j$, and the expression evaluates as

$$\hat{a}_j^\dagger \hat{a}_l^\dagger \hat{a}_k \hat{a}_m = \delta_{jk}\delta_{lm} n_j n_l + \delta_{jm}\delta_{lk} n_j n_l + \delta_{jk}\delta_{jl}\delta_{jm}(n_j(n_j-1) - 2n_j^2) \tag{5.6}$$

The third term of this sum will also be neglected, as the triple-δ inserted in eq. 5.4 creates only a small constant offset of order $1/\sum_j n_j$ to the overall signal and does not contain spatial information.

The contribution from the first term to the correlation operator eq. 5.3 is

$$\begin{aligned}
&\sum_{j,l} |W(\boldsymbol{x}_1)|^2 |W(\boldsymbol{x}_2)|^2 e^{\frac{im}{2\hbar t}(2\boldsymbol{x}_1(\boldsymbol{x}_j - \boldsymbol{x}_j) + \boldsymbol{x}_j^2 - \boldsymbol{x}_j^2) + (2\boldsymbol{x}_2(\boldsymbol{x}_l - \boldsymbol{x}_l) + \boldsymbol{x}_l^2 - \boldsymbol{x}_l^2)} n_j n_l = \\
&\sum_j |W(\boldsymbol{x}_1)|^2 n_j \cdot \sum_l |W(\boldsymbol{x}_2)|^2 n_l = \\
&|W(\boldsymbol{x}_1)|^2 |W(\boldsymbol{x}_2)|^2 N_{tot}^2.
\end{aligned} \tag{5.7}$$

This function has a smooth gaussian shape and is identical to the product of two expanded density distributions $\langle \hat{n}(x_1, t)\rangle \langle \hat{n}(x_2, t)\rangle$ as derived for the Mott insulator in section 3.2.1. It is therefore also identical with the denominator of eq. 5.1.

It is the second term which contains the structure information. It contributes to the

[1] In fact, none of the approximations made here are necessary; the end result is the same apart from minimal rescaling and adjusting of the global envelope. With the approximations, however, the calculation is much more compact.

correlation operator as

$$\sum_{j,l} |W(\boldsymbol{x}_1)|^2 |W(\boldsymbol{x}_2)|^2 \cdot e^{\frac{im}{2\hbar t}(2\boldsymbol{x}_1(\boldsymbol{x}_j-\boldsymbol{x}_l)+\boldsymbol{x}_l^2-\boldsymbol{x}_j^2)+(2\boldsymbol{x}_2(\boldsymbol{x}_l-\boldsymbol{x}_j)+\boldsymbol{x}_j^2-\boldsymbol{x}_l^2)} n_j n_l =$$

$$\sum_{j,l} |W(\boldsymbol{x}_1)|^2 |W(\boldsymbol{x}_2)|^2 \cdot e^{\frac{im}{\hbar t}(\boldsymbol{x}_2-\boldsymbol{x}_1)(\boldsymbol{x}_l-\boldsymbol{x}_j)} n_j n_l =$$

$$\sum_{j,l} |W(\bar{\boldsymbol{x}}-\boldsymbol{d}/2)|^2 |W(\bar{\boldsymbol{x}}+\boldsymbol{d}/2)|^2 \cdot e^{\frac{im}{\hbar t}(\boldsymbol{x}_l-\boldsymbol{x}_j)\cdot\boldsymbol{d}} n_j n_l. \tag{5.8}$$

This structure term only depends on the distance $\boldsymbol{d} = \boldsymbol{x}_2 - \boldsymbol{x}_1$, and not on the center coordinate $\bar{\boldsymbol{x}} = (\boldsymbol{x}_2 + \boldsymbol{x}_1)/2$ of the pair. Also, in the actual application described in this chapter, $\boldsymbol{x}_1$ and $\boldsymbol{x}_2$ are two- or three-dimensional vectors. $G(\boldsymbol{x}_1, \boldsymbol{x}_2)$ is then a four- or six-dimensional function. We will therefore define a new observable which is projected to the relevant subspace of $\boldsymbol{d}$ by integrating over $\bar{\boldsymbol{x}}$. This subspace then conveniently has the same dimensionality as the data.

Correlation Observable

From the above conclusions, we define as a practical observable for the correlations the quantity

$$C(\boldsymbol{d}) = \frac{\int \langle \hat{n}(\bar{\boldsymbol{x}}-\boldsymbol{d}/2)\hat{n}(\bar{\boldsymbol{x}}+\boldsymbol{d}/2)\rangle d\bar{\boldsymbol{x}}}{\int \langle \hat{n}(\bar{\boldsymbol{x}}-\boldsymbol{d}/2)\rangle\langle \hat{n}(\bar{\boldsymbol{x}}+\boldsymbol{d}/2)\rangle d\bar{\boldsymbol{x}}} - 1. \tag{5.9}$$

It is obtained by applying the same transformation and integration to the numerator and denominator of the original normalized correlation operator eq. 5.1 separately. This observable then has a simple structure: It is determined by computing the averaged autocorrelation function of the density distribution and normalizing it with the autocorrelation function of the average density distribution.

Inserting the two contributions to the numerator, eq. 5.7 and eq. 5.8 as well as the denominator, which is also given by eq. 5.7, we obtain for the Mott insulator

$$\begin{aligned} C(\boldsymbol{d}) &= \frac{\int |W(\bar{\boldsymbol{x}}-\boldsymbol{d}/2)|^2 |W(\bar{\boldsymbol{x}}+\boldsymbol{d}/2)|^2 (N_{tot}^2 + \sum_{j,l} e^{\frac{im}{\hbar t}(\boldsymbol{x}_l-\boldsymbol{x}_j)\cdot\boldsymbol{d}} n_j n_l) d\bar{\boldsymbol{x}}}{\int |W(\bar{\boldsymbol{x}}-\boldsymbol{d}/2)|^2 |W(\bar{\boldsymbol{x}}+\boldsymbol{d}/2)|^2 N_{tot}^2 d\bar{\boldsymbol{x}}} - 1 \\ &= \frac{1}{N_{tot}^2} \sum_{j,l} e^{\frac{im}{\hbar t}(\boldsymbol{x}_l-\boldsymbol{x}_j)\cdot\boldsymbol{d}} n_j n_l. \end{aligned} \tag{5.10}$$

For the optical lattice, the positions of the sites $\boldsymbol{x}_j$ are spaced in a regular array. Assuming that the lattice axes are mutually orthogonal and the spacing of the sites is given by a_{lat} in all three directions, the expression is easily recognized as the absolute square of a Fourier sum:

$$C(\boldsymbol{d}) = \frac{1}{N_{tot}^2} \sum_l e^{\frac{im}{\hbar t}\boldsymbol{x}_l\boldsymbol{d}} n_l \cdot \sum_j e^{-\frac{im}{\hbar t}\boldsymbol{x}_j\boldsymbol{d}} n_j = \frac{1}{N_{tot}^2} \left| \sum_{q_1,q_2,q_3} e^{-\frac{ima_{lat}}{\hbar t}(q_1 d_1 + q_2 d_2 + q_3 d_3)} n_{q_1,q_2,q_3} \right|^2$$

Here, d_i are the components of the vector $\boldsymbol{d}$, and n_{q_1,q_2,q_3} is the occupation of the lattice site at the position $\boldsymbol{x} = (x_1, x_2, x_3) = a_{lat} \cdot (q_1, q_2, q_3)$ The Fourier coefficients are the site occupation numbers n_{q_1,q_2,q_3}.

The periodicity l of the Fourier sum in each of the axes can be evaluated from the prefactor in the exponent

$$l = 2\pi \cdot \frac{\hbar t}{m a_{lat}} = \frac{2\hbar k_{lat}}{m} t. \tag{5.11}$$

In the limit of long expansion times, which is often assumed, the measured density distribution in $\boldsymbol{x}$ is equivalent to the momentum distribution in $\boldsymbol{p} = \boldsymbol{x}/t \cdot m$. In that case, the length l corresponds to the momentum $2\hbar k_{lat}$. Here k_{lat} is the wave vector of the lattice light. The periodicity of the function therefore has the same structure as the reciprocal lattice of the trapping potential.

The correlation pattern is very closely related to the one obtained for the momentum distribution (the *first* order correlation function) of the superfluid phase, derived in section 3.2.1. In that case, we obtained the modulus of the Fourier transform of the global wave function in the lattice. Here, the *second* order correlation function in the Mott insulator case yields the modulus of the Fourier sum of the density distribution (here equivalent to the square of the wave function). For homogeneous densities, there are only two significant differences: Due to the normalization in the definition of C, the correlation pattern is not multiplied by an envelope function. Instead, the visibility of the signal is limited for increasing coordinates $|\boldsymbol{d}|$ by the increase of the noise level. Also, the resolution of the correlation pattern is not limited by the initial size of the distribution. The features observed in the correlations after time of flight expansion can therefore be much smaller than the size of the distribution before the expansion.

A well-known property of the Fourier sum is that the integral over one full period of its absolute square can be evaluated as the sum of squared Fourier coefficients multiplied by the volume of the Fourier interval. For three dimensions, we therefore have as the integrated signal

$$S = \int C(\boldsymbol{d}) d\boldsymbol{d} = \frac{l^3}{N_{tot}^2} \cdot \sum_j n_j^2. \tag{5.12}$$

For a constant occupation n in each of the N_s occupied sites, the integrated signal therefore is

$$S = l^3 \frac{n}{N_{tot}} = l^3 \frac{1}{N_s}. \tag{5.13}$$

It scales as $1/N_s$ if additional sites, and therefore atoms, are added to the distribution. Similarly, for a fixed total atom number N_{tot} which is homogeneously spread out over N_s sites, the signal is decreased as $\bar{n} = N_{tot}/N_s$ when the number of sites is increased.

However, care must be taken with this interpretation, as the derivation of the signal assumes integer site occupations.

Another straightforward property of $C(\boldsymbol{d})$ is the fact that $C(0)$ is always 1 (In the fermionic case, it is -1). Since the function is periodic, this also applies to all other nodes of the reciprocal lattice. Therefore, as the averaged amplitude S/l^3 is usually smaller than 1, there will be a peak of height 1 at each site of the reciprocal lattice. Due to this fixed height of the peaks the previously discussed decrease in the integrated signal with increasing N_s is therefore due to a reduction of the peak width.

Homogeneous density distribution

To illustrate the characteristic properties of this function, let us analyze the very simplified case for a 1D chain of N_s sites occupied by one atom each. These sites are spaced by the distance a, and are located between $x = a$ and $x = N_s \cdot a$:

$$C_{1D}(d) = \sum_{k=1}^{N_s} \sum_{j=1}^{N_s} e^{i\frac{m}{\hbar t} dka} e^{-i\frac{m}{\hbar t} dja} = \frac{\sin(\pi N_s d/l)^2}{\sin(\pi d/l)^2}.$$

The shape of this function is shown in figure 5.3 for $N_s = 2$ and $N_s = 6$. For two atoms, a sinusoidal function emerges. For increasing N_s, it converges to a train of delta functions at each of the maxima of the fundamental sinusoidal function. These are located at the positions where the denominator vanishes, at integer values of d/l. This corresponds to the reciprocal lattice sites of the assumed lattice potential. To off-

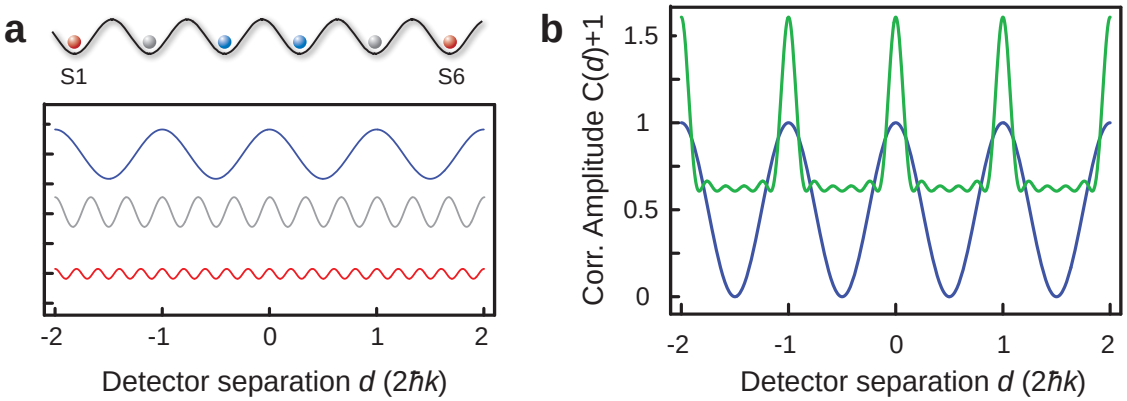

Figure 5.3: a) Contributions to the correlation signal from atom pairs separated by one, three and five lattice spacings (blue, gray and red). The amplitudes reflect the number of pairs with a given distance within a string of six atoms. b) Expected total correlation signal for a chain of two (blue) and six (green) filled sites in a 1D lattice.

set the curves against each other in figure 5.3b (as well as in figure 5.2), the triple-δ

term of eq. 5.6 was included in in the calculation. This leads to a downward shift by $1/N_s$ of the joint detection probability compared of the product of two independent single-particle detection probabilities at both locations. This can be understood from the overall reduction of the probability for detecting a second atom during joint measurement with a low total number of atoms. As one atom was already detected at another position, the number of particles which can hit the second detector is reduced.

The integral of the signal (without the offset) is

$$\int_0^l \frac{\sin(\pi N_s d/l)^2}{\sin(\pi d/l)^2} dd = l/N_s,$$

as expected. As the peak height quickly converges to 1, this means that the peak width scales as l/N_s. This behavior is characteristic for the Fourier transform which relates the correlation signal to the initial distribution. It therefore also holds in more than one dimension, where the peak widths along each of the axes scale with the size of the initial distribution along those directions.

Atom-atom correlations from the released superfluid ensemble

A superfluid state which is fully coherent exhibits a completely different signal than the Mott insulator. As far as the original HBT experiment for photons is concerned, this corresponds to using a coherent as opposed to a classical light source[2]. The significance was not immediately realized, but the issue was eventually resolved in that one of the decisive properties of coherent radiation is the *absence* of second order correlations between the photons [139]. This also applies to the correlations between atoms. The second-order correlations are suppressed with the occurrence of first-order coherence when the ensemble undergoes the transition from a thermal gas to a Bose-Einstein condensate, which can be detected by measuring collision rates [140] or by directly detecting particle-particle correlations with an appropriate single-particle sensitive detector array [141, 142].

A similar suppression can be expected when examining the noise correlations arising from a superfluid released from the lattice in the same way as the Mott insulator discussed before. In this case, we have $\hat{a}_j|\Psi\rangle = \alpha_j|\Psi\rangle$ with $|\alpha_j| = \sqrt{\langle n_j \rangle}$ and a phase factor which can be assumed to be 1 in the ground state. Instead of eq. 5.6, we therefore have

$$\langle \hat{a}_j^\dagger (\hat{a}_l^\dagger \hat{a}_k) \hat{a}_m \rangle = \sqrt{n_j n_l n_k n_m} = \langle \hat{a}_j^\dagger \hat{a}_k \rangle \langle \hat{a}_l^\dagger \hat{a}_m \rangle \tag{5.14}$$

The sum can then be factorized into two parts for $\boldsymbol{x}_1$ and $\boldsymbol{x}_2$ and we have

$$\langle \hat{n}(\boldsymbol{x}_1) \hat{n}(\boldsymbol{x}_2) \rangle = \langle \hat{n}(\boldsymbol{x}_1) \rangle \langle \hat{n}(\boldsymbol{x}_2) \rangle. \tag{5.15}$$

[2] In the original publications on noise correlations in the optical domain [39, 134] Hanbury Brown and Twiss demonstrate the effect for "coherent beams of light". This however refers to the spatial coherence, not the phase coherence of the radiation.

Therefore, any spatial pattern is removed by the normalization in the operator 5.1 and the correlation function is flat in the superfluid case.

However, in the type of experiment presented here it is difficult to observe this flat correlation function. The reason is that the cancellation due to the normalization does not always work perfectly, due to fluctuations between the individual images. For example, the peaks of the superfluid pattern can vary in position slightly between images, due to very small distortions of the overall phase. The analysis algorithm, which will be discussed in the following, would pick up these deviations as a correlation signal. Since the interference patterns of the superfluid have such a similar structure to the expected correlation pattern, this could in theory even result in spurious correlation peaks.

To rule out fluctuations of a very small superfluid fraction as the source of the observed correlation patterns in the Mott regime, a modified analysis was conducted which excluded those regions of each image in which the superfluid peaks are expected. This resulted in no significant change of the signal, indicating that no significant residual peaks are present. Also, it since became possible to observe the correlations with polarized fermions in a lattice, where no phase coherence can occur [143].

Recently, the exclusion method has been taken even further to make it possible to observe noise correlations in the explicit presence of a superfluid fraction [144]. This allows to analyze the noise correlations even within the crossover from the Mott insulator to the superfluid.

5.1.2 Prediction of the detected signal

In order to make a quantitative prediction for the absolute signal including the spherical shell structure of the Mott insulator, the Fourier sum is evaluated numerically. The algorithm takes an arbitrary 3D atom distribution in the lattice and calculates the corresponding normalized 3D correlation function $C(\boldsymbol{d})$, eq. 5.9. Using fast Fourier transformations, this can be done efficiently for any density distribution in the trap even for large atom numbers. It should however be kept in mind that this still assumes Fock states as the source of atoms before release – all atoms have to be fully localized. In-trap first order correlations such as those of atoms which are delocalized over lattice sites can not be calculated in this fashion, as equation 5.6 does not hold in that case.

The discussion so far was assuming point-like and perfect detectors with full 3D resolution. In the experiment, however, this is not the case. The detection does not yield the exact 3D position of all atoms in the cloud. Instead, integrated column densities are recorded by the CCD camera.

The effective geometry of the "detectors" represented by each pixel is illustrated in figure 5.4. It is characterized by a point spread function (PSF) with an effective length L given by the overall extent of the cloud and a radius R which characterizes

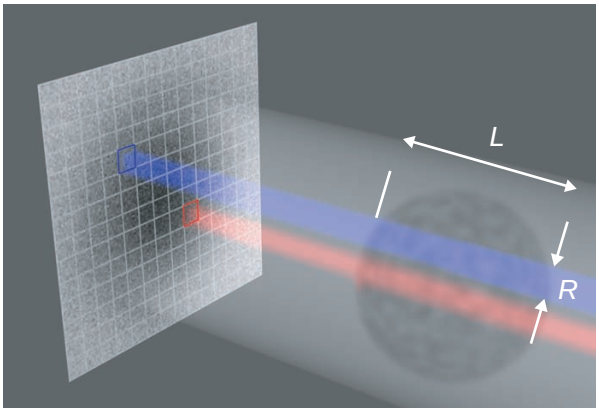

Figure 5.4: Schematic of the effective detectors geometry when using CCD images. Each pixel corresponds to one detector. The correlations are formed between two of these pixels, which sample different parts of the cloud. The detection volume of each of these extends along all light rays of the illumination beam which end on this pixel. Close to the imaging plane, the detector can therefore be effectively approximated as a volume which encompasses the full size of the atom cloud L in the z-direction. In the transverse direction it is given by the inverse point spread function of this pixel in the object plane, characterized in size by a radius R.

the resolution of the imaging system[3]. The volume given by R and L is much more coarse than the extension of the correlation features in $G(\boldsymbol{x}_1, \boldsymbol{x}_2)$ for typical cloud parameters. This results in a smoothing effect, which greatly reduces the amplitude of the peaks observed, which would otherwise be 1.

To correctly take a finite detection volume into account, the density operator has to be convolved with the effective detector response function. In the case discussed here this means convolving the 3D density distribution of the expanded cloud $n(\boldsymbol{x})$ (eq. 5.2) with the 3D point spread function (PSF) of the imaging system:

$$n_{CCD}(\boldsymbol{x}) = \int PSF(\boldsymbol{x}' - \boldsymbol{x}) n(\boldsymbol{x}') d\boldsymbol{x}'$$

Inserting this into the normalized autocorrelation observable eq. 5.1 yields

$$\begin{aligned} C'(\boldsymbol{d}) &= \frac{\int\int\int \langle PSF(\boldsymbol{x}' - \bar{\boldsymbol{x}} + \boldsymbol{d}/2) n(\boldsymbol{x}') PSF(\boldsymbol{x}'' - \bar{\boldsymbol{x}} - \boldsymbol{d}) n(\boldsymbol{x}'') \rangle d\boldsymbol{x}' \boldsymbol{x}'' d\bar{\boldsymbol{x}}}{\int\int \langle PSF(\boldsymbol{x}' - \bar{\boldsymbol{x}} + \boldsymbol{d}/2) n(\boldsymbol{x}') d\boldsymbol{x}' \rangle \int \langle PSF(\boldsymbol{x}'' - \bar{\boldsymbol{x}} - \boldsymbol{d}) n(\boldsymbol{x}'') \rangle d\boldsymbol{x}'' d\bar{\boldsymbol{x}}} - 1 \\ &\approx \int\int PSF(\boldsymbol{x}'' - \boldsymbol{x}') PSF(\boldsymbol{x}' - \boldsymbol{d}) C(\boldsymbol{x}'') d\boldsymbol{x}'' d\boldsymbol{x}' \\ &= PSF \otimes PSF \otimes C(\boldsymbol{d}) \end{aligned}$$

with the convolution operator $\otimes$. The main assumption made in the derivation of the second line is that the point spread function in the lateral directions is much smaller

[3]For an optical imaging resolution better than the CCD pixel size, the detector cross section would be given by the shape of the CCD pixel, and would be quadratic

than the extent of the Wannier function after expansion. This is always true for an imaging system with enough resolution to take meaningful images of the expanded atom cloud. Furthermore, it is assumed that the width of the Wannier function after expansion is equal or larger than l, which is the case for the experiments presented.

In order to determine the expected signal that is obtained with the real imaging system as the detector array, the signal obtained thus far is therefore integrated along the z axis and convolved twice with the lateral point spread function of the imaging system. This reduces the signal in the correlation peaks by the ratio in volume between the 3D PSF and the 3D volume of the peaks, resulting in typical values of 10^{-4} to 10^{-3}.

5.1.3 Extracting the noise correlations from CCD images

The data from the CCD camera[4] is first processed in the normal way described in section 3.2: The dark image is subtracted and each image of the atom cloud is divided by the reference image. The logarithm is taken to obtain optical densities, and the resulting images stored as an individual file.

For the analysis, a large set (typically 50-100) of such processed images is taken under identical conditions. For each of these images the 2D correlation function is calculated before the results for all images are averaged. Finally this average is normalized with the autocorrelation of the mean density. In the following all steps of the analysis are described in detail.

Postselection of Images

Before quantitative analysis, the images are typically selected according to specific parameters. This serves to ensure that their differences are only caused by the shot noise fluctuations, and not by other distortions. The main criterion for the selection apart from image distortions is typically the atom number, which fluctuates from shot to shot. For this, the atom number on each image is determined by integrating over the distribution. All images with an atom population outside a specified interval (for example $\pm 5\%$ around the target value) are removed from further analysis.

In the next step, all images are typically screened for obvious imaging problems. One common defect is the appearance of significant interference fringes not canceled by the image normalization. This is usually due to laser frequency fluctuations during the imaging sequence. The other relevant screening criterion is the visibility of readout noise produced by the electronics of the AP1E camera, which is sometimes strong enough to be visible even without further processing. These effects will be discussed in more detail in section 5.1.4.

[4] Apogee AP1E, with Kodak KAF-401E CCD chip, unless specified otherwise

Normalizing

The first step in the analysis of the remaining image files is the removal of any residual offset. The offset is determined by averaging a rectangular region without atoms, normally the region adjacent to the left of the region of interest which contains all atoms. For the following calculations, only this region of interest is used in order to speed up the calculations.

Usually, the image is then normalized to a fixed atom number by integrating over the region of interest and dividing each pixel by the value obtained. By this, a constant offset to the correlation function due to the fluctuating atom number is avoided (discussed in detail in section 5.1.4).

Calculating the autocorrelation function

To determine the numerator of the correlation observable eq. 5.9, the autocorrelation function of each image *img* is evaluated as

$$ac(\boldsymbol{d}) = \int img(\boldsymbol{x} - \boldsymbol{d}/2) \cdot img(\boldsymbol{x} + \boldsymbol{d}/2) d\boldsymbol{x}.$$

With the convolution operator $\otimes$, this can be written as

$$ac(\boldsymbol{d}) = img(\boldsymbol{x}) \otimes_{\boldsymbol{d}} img(-\boldsymbol{x}).$$

Fourier transforming both sides

$$F(ac) = \mathrm{F}(img) \cdot \mathrm{F}(img)^*$$

leads to

$$ac = \mathrm{F}^{-1}(|\mathrm{F}(img)|^2),$$

where F is the Fourier transformation operator and the asterisk denotes the complex conjugate. The autocorrelation function can therefore be expressed and evaluated with two Fourier transformations (a consequence of the Wiener-Khinchin Theorem, see e.g. [145]). This offers a large gain in speed over the direct calculation of the autocorrelation integral.

The Fourier transform itself is calculated using a fast Fourier Transfor (FFT) algorithm[5] on the image, and the modulus square of each Fourier coefficient is calculated. After this, an inverse Fourier transform is applied to obtain the single image autocorrelation function. All single image autocorrelation functions are then averaged to obtain the numerator of the correlation function (eq. 5.9).

[5] using the FFTW3 library for C++, http://www.fftw.org

Normalization of the correlation signal

All normalized images are also averaged, and the autocorrelation function of this average is computed to normalize the correlation pattern. This corresponds to determining the denominator in equation 5.9. It represents an approximation to the noise correlation signal of fully uncorrelated measurements for example from two separate runs of the experiment. Dividing the averaged autocorrelation functions by this and subtracting 1 yields the normalized 2D autocorrelation function $C_{exp}(\boldsymbol{d})$.

Resulting noise correlation data of the 3D Mott insulator

Figure 5.5 shows the normalized 2D correlation image resulting from this analysis sequence. For this experiment, 43 images were taken, one of which is shown in figure 5.1 (page 84). The atom number in the trap was $5.1 \pm 0.8 \times 10^5$, and the lattice was ramped to 50 and 55 E_R along the x and y direction, respectively. In the z direction (integration direction), the lattice depth was 40 E_R, and the time of flight used was 22 ms. The 2D correlation spectrum shows the expected regular array of peaks with

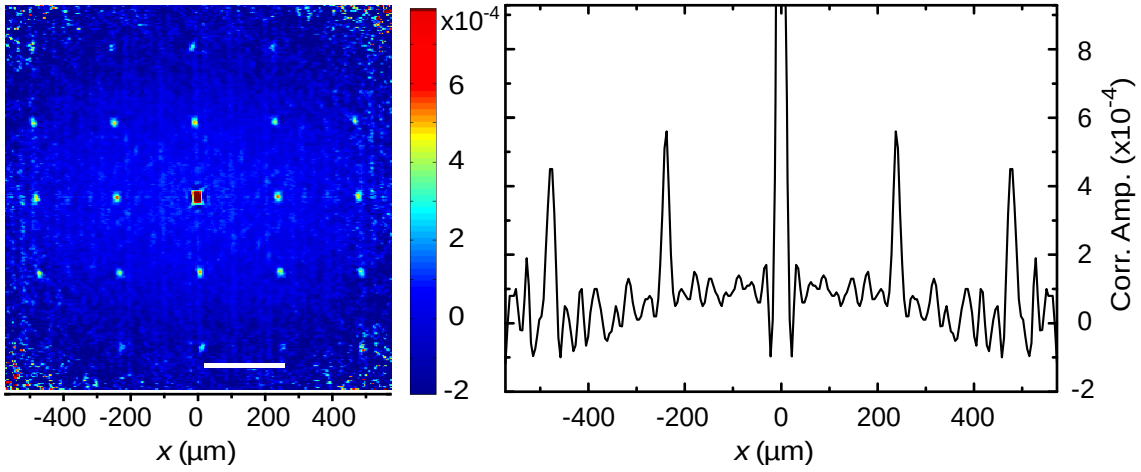

Figure 5.5: Normalized Spatial noise correlation signal. The left panel shows the 2D distribution of the correlations in th x-y-plane. The white bar denotes the $2\hbar k_{lat}$ lattice momentum scale for the 840 nm lattice. In the right panel, a profile along the direction of the horizontal lattice beam is shown. It is aligned with the (clipped) central peak and shows the regular array of sharp maxima with an amplitude of $5 \times 10^{-}4$.

an amplitude of 5×10^{-4} on a noise floor which is smaller than 5×10^{-5}. The only filtering which has been applied is a weak smoothing by convolution with a horizontal binomial filter. The background is dominated by a vertical stripe pattern caused by weak, fluctuating interference fringes within the illumination beam and a smooth

offset modulation. The latter is the result of fluctuations of the cloud width, and both effects and the filtering will be discussed in more detail in the following section.

The width of the correlation peaks is dominated by the imaging system resolution and the application of the smoothing filter, resulting in a measured resolution smaller than 9 μm RMS in both axes. This is significantly smaller than the initial size of the cloud, which in the configuration described has a radius of $\approx$ 15 μm. The central peak, which is determined by the autocorrelation signal of all noise sources - both quantum and technical - is prominently visible. The photon shot noise component and the thermal noise of the readout electronics are all contained in the central pixel, whereas the component which is created by the overall atom shot noise is convolved by the point spread function of the imaging system in the same manner as the correlations from quantum statistics. The aberrations of the relatively simple imaging system used are therefore readily visible in the shape of this peak, which, apart from the central pixel, is theoretically only given by the point spread function convoluted with itself. All other peaks have the same shape, but as their amplitude is much lower, no significant details are visible. For the quantitative analysis discussed later in this chapter, the detailed shape is ignored and approximated as gaussian.

5.1.4 Image artifacts and filtering

The noise correlation interferometry method relies on the analysis of deviations of a single measurement from its quantum mechanical expectation value. Many sources can lead to such fluctuations. The deviations which contain the signal are the shot noise fluctuations of the atom numbers counted on each pixel. Other deviations of similar or larger strength therefore have to be either avoided or rejected in the analysis process, unless their contributions to the autocorrelation function average to zero. The latter applies for example to the photon shot noise, which only contributes to the central pixel and otherwise averages out. In the implementation used here, the average of many measurements is used instead of the real quantum mechanical expectation value. This has the advantage that deviations from the expectation value which are the same for all images are not detected in the correlation analysis. This is for example the case with strong inhomogeneities in the illumination beam.

Only distortions which change between images can create undesired contributions to the signal. Still, several significant sources of such fluctuations are present and have to be addressed independently.

Trap and Cloud size Fluctuations

Another source of spatially correlated fluctuations between images arise from changes of the overall gaussian shape of the cloud. These can be introduced by shot to shot variations of the experimental parameters. A fluctuating cloud position along the horizontal axis, for example, causes variations which are anticorrelated between the

left and the right part of the cloud: A cloud shifted to the right always leads to an increase in the density on the right and a decrease on the left simultaneously. This results in a negative correlation on all length scales equal or larger than the cloud size. On distances smaller than the smallest feature size of the image (in this case the cloud size), the correlations have to be positive, yielding a broad maximum around the zero.

Similarly, a fluctuating cloud radius creates a positive correlation at small radii, and negative values, corresponding to the correlation between the center and the outer parts of the cloud, at a scale given by the cloud radius. At larger scales, contributions from correlations between opposite fringes of the cloud are dominant, leading to a positive contribution. Cloud radius fluctuations can be caused by variations in the lattice depth and strongly fluctuating atom numbers. In the latter case, the radius of the cloud can be influenced by the atom-number dependent mean-field interaction within the cloud during the initial stage of the expansion.

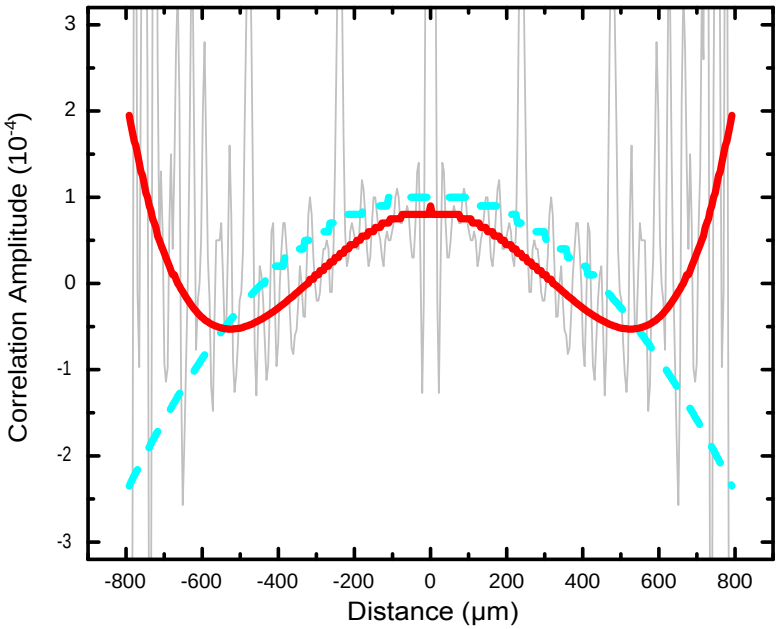

Figure 5.6: Signature of the fluctuations of cloud size and position on the noise correlation signal. The red curve shows the effect of a 0.5% fluctuation in the cloud width; the blue curve that of a $\pm 2.2\,\mu$m fluctuation in the cloud position. Both of these have been determined from computer-generated randomized datasets. The grey curve is the experimental data from figure 5.5 plotted for comparison. The discrete steps in the synthetic data curves are due to the quantization of the image files (16 bit, corresponding to 10^{-5}), which is not well averaged for small displacements.

In figure 5.6, the signal from a real measurement including the background is compared to the expected backgrounds for a fluctuating cloud size and fluctuating cloud

position. The expected background signals have been calculated using computer-generated sets of test images containing a perfectly gaussian shaped cloud without any noise. Each set contained 100 images, with the parameters chosen for the gaussian analog to those obtained from the real measurements. For the first set (red line), the width of the cloud was randomly varied by $\pm 0.5\%$ (RMS), corresponding to a 1% trap depth fluctuation or drift. For the second set (blue dashed line), the cloud position was varied by $\pm 2\,\mu$m (RMS). The gray curve shows a measurement result for comparison, using the same data as in figure 5.5.

According to this comparison, the dominating contribution to the background seems to be the cloud size fluctuation. At the same time, it shows that the shot-to-shot reproducibility of the cloud position in the 3D Mott insulating case is significantly better than $\pm 2\,\mu$m, an important prerequisite for the high spatial resolution analysis technique described in chapter 4.

Another strong effect of macroscopic fluctuations is due to the shot to shot variation of the atom number of typically $\pm 5\%$. This leads to uniformly positive density correlations between all parts of the cloud, and therefore to an overall positive offset. The effect is reduced by strong selection of images according to their atom number, and can be further compensated by normalizing all images prior to analysis. For this, the overall atom number is determined from the image by integration. The measured column density at each position is then divided by the total number of atoms. Analyzing a set of images normalized in this way typically results in a complete suppression of the offset.

Camera readout noise

One type of noise created in the imaging system is a very high frequency spatial modulation of the images. Often it is strong enough to be seen on single images. Even if this is not the case the pattern still appears in the averaged autocorrelation function. The modulation is always oriented along the horizontal direction, and the wavelength is two pixels. The phase of this pattern sometimes jumps by 180 degrees. Due to the structure it appears very clear that it is a result of electronic interference or crosstalk within the CCD camera, in the analog-to-digital converter card or, most likely, in the cable connecting the two. It is also observed that a much stronger pattern of very similar structure appears on the images if the cables from two cameras are close together and both devices are read out simultaneously.

Due to its simple structure, this kind of noise can be efficiently filtered by smoothing with a horizontal binomial filter with a width of 3 pixels. For this, the image is convolved with the smoothing mask $1/4[1\ 2\ 1]$. This filter is used on all correlation images obtained with the Apogee AP1E camera system as well as before any quantitative analysis of images.

Optical Interference fringes

The second main source of technical noise in the imaging system also creates a fluctuating horizontal modulation, but with a much longer wavelength. It appears to be created by interference of the imaging light within the camera due to reflections between the chip and the camera entrance window. This is consistent with the pattern's dependence on the angle in which the camera is positioned.

Since the camera tilt is such that the pattern is almost exactly vertical, it can be filtered without too much impact to the signal by applying a vertical high pass. This second filtering stage removes all Fourier components of the image with a wavelength longer than 20% of the height of the image. It applies a gaussian function centered at the vertical spatial frequency $k_y = 0$ and with an RMS width of 5, implemented by multiplying the fourier-transformed image with $1 - \exp(1/2 \cdot k_y^2/5^2)$.

5.1.5 Fitting

For a quantitative comparison of the signal with the prediction, one-dimensional profiles are extracted through the nine central peaks of each correlation image. The profiles are taken along the directions of the lattice momentum vectors and intersect at the positions denoted by multiples $2\hbar\boldsymbol{k}_{\{x,y\}}$ of either lattice axis (see figure 5.7). These positions were calibrated by fitting the positions of the correlation peaks for the largest available expansion times (22 msec).

The pixel values of the profiled points are then used to fit gaussian functions to the peaks. This is done with four of the nine most central peaks. These are located at -45°, 0°, +45° and +90° from the vertical. The other four are redundant because the autocorrelation function is invariant under inversion. Before fitting these peaks, a smooth background (approximated by two gaussians of large width) is fitted to the areas of the curve outside of the regions which contain the peaks and then subtracted from the profile. This is required to remove the effects of cloud parameter fluctuations discussed above. The high-pass filter removes most of this curvature, so the residual curvature fitted by this background function is usually small.

The procedure yields the pixel coordinate of the peak position along the profile direction, the peak height and the peak width. The high pass filter in the second filtering stage does produce typical high-pass artifacts. This means that sharp features such as the observed peaks produce an undershoot at the edges and all offsets are removed. Since the very non-isotropic high pass filter is effectively applied along each column of the y-axis independently, each column is offset to an average value of 0. This shows up as vertical "grooves" – columns with a negative offset aligned with the positive peaks. Because of this, the absolute peak height is reduced by a very small amount, on the order of $1/N_s$ of the total peak height.

Due to the constant offset over the column, this does not affect the peak heights relative to the background as determined by fitting cloud profiles along the y-axis.

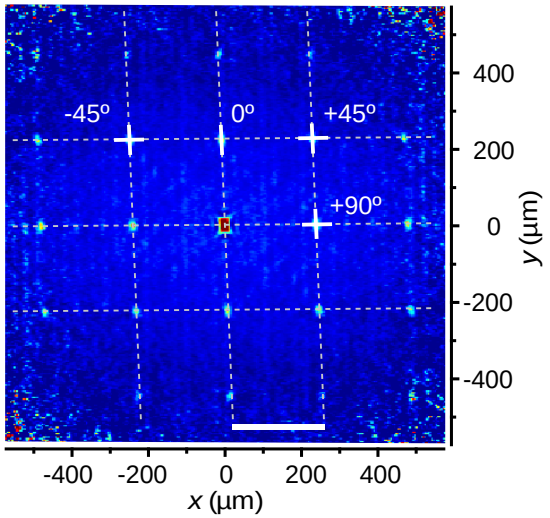

Figure 5.7: Geometry of the profiles extracted from the correlation images for fitting the peak parameters. The white bar shows the $2\hbar k_{lat} \times t/m$ lattice momentum scale for the 840 nm lattice. Due to symmetry, only the peaks at the -45°, 0°, +45° and +90° positions from the vertical are independent. The central peak is dominated by technical noise and is therefore not included in the quantitative analysis. Due to the default high-pass filtering, the horizontal profile of the 0° peak is also affected by the central peak and therefore ignored.

For all x-axis profiles but the ones at $x = 0$, the reduction is typically 1%, which is below the error of the measurement.

For the central column (x=0), the effect is significantly larger, because the central autocorrelation peak is much higher due to the contributions from the atomic shot noise and the imaging noise. Therefore, the offset imparted to these rows of the image is much bigger. This effect is strongly visible in the images shown in section 5.3 (page 107). For the vertical profile, this does not matter, as the offset is subtracted as a constant. But for the horizontal profile through the 180 degree peak, the offset can not be compensated and therefore the peak is significantly reduced. For this reason this horizontal profile is not included in the analysis, as shown in 5.7.

As the imaging resolution is no fundamental property of the physics involved and can even change[6], the correlation amplitude obtained by the fit is not used directly as the correlation signal. Instead, it is multiplied by the area of the peak as given by the product of the two widths of the gaussians along the x and y imaging axes. This quantity therefore has the unit μm^2. The final correlation signal (or correlation strength) plotted in the subsequent graphs is the average of the signals obtained for each of the available peaks in the 2D correlation function.

[6]Specifically, the resolution can vary for different expansion times, since the camera setup has to be modified and realigned to achieve some of the long expansion times used

5.2 Experimental results and comparison with theory

Correlation signal dependence on effective detector size

As outlined in the derivation of the signal, the amplitude of the correlation signal is expected to be 1 for a perfect, point-like detector. It is due to the non-negligible size of the detector volume that the actual amplitude observed is reduced to the 10^{-4} level. This ratio is given by the relative size of the detector volume vs. the volume defined by the width of the correlation peaks, as long as this width is smaller than the detector resolution. In momentum space, the volume is given as a constant fraction of the Brillouin zone volume in 3D (see eq. 5.12). The Brillouin zone in real space expands as l increases with increasing expansion time. On the other hand, the detector area in the x-y-plane is fixed by the camera resolution and does not depend on the Brillouin zone size. In contrast, the z-direction of the cloud is always integrated completely, resulting in an effective detector extent given by the expanded cloud size, which increases linearly with the expansion time.

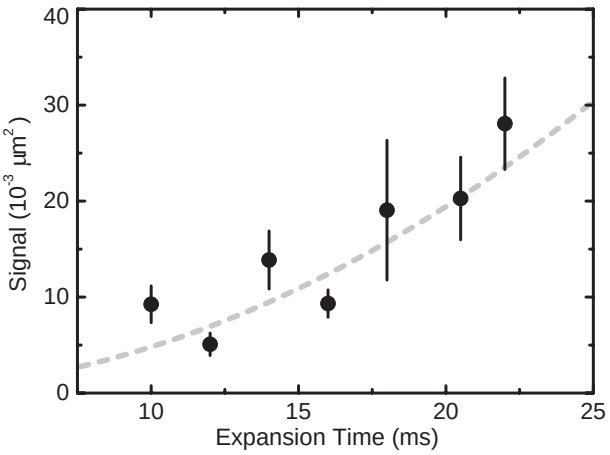

Figure 5.8: Height of the detected peaks vs. the expansion time. The momentum resolution for increasing ballistic expansion times improves, therefore the reduction of the peak height due to the finite resolution is reduced. Grey dashed line is a parabola fitted to the data points.

This means that during ballistic expansion, when the volume of the Brillouin zone increases as t_{exp}^3 in the expansion time, the detector volume only scales as t_{exp}. The result is an increase of the signal as t_{exp}^2. This is shown in figure 5.8. For the large atom numbers used in this measurement ($\approx 4 \times 10^5$), the width of the correlation peaks is on the order of 2% of the Brillouin zone size, and therefore significantly smaller than the optical resolution even for the longest expansion times of $t_{exp} = 22\,\text{ms}$. Both the signal and the correlation amplitude itself therefore scale quadratically with the

expansion time.

Due to this quadratic increase of the signal, long expansion times are desired for the noise correlation measurements as long as the atom density does not become excessively low compared to other noise sources. Most of the data with large atom numbers was therefore taken with $t_{exp} = 22\,\mathrm{ms}$. This is the longest expansion time that could be achieved without major changes to the camera setup used.

Correlation strength dependence on atom number and shell structure

A similar mechanism determines the strength of the signal with respect to the overall atom number in the Mott insulator prior to release. As discussed in section 5.1.1, the width of the correlation peaks scales as $1/N_s$, where N_s is the number of sites occupied along this direction. Therefore, when assuming constant density, the 3D volume of each peak should scale proportional to $1/N_s^3 \propto 1/N_{tot}$, where N_{tot} is the total atom number.

Figure 5.9 shows the atom number dependency of the measured correlation amplitude. Here, the atom number was varied strongly, by changing both the MOT loading times and the radiofrequency evaporation sequence. The expansion time used is 16 ms for all measurements.

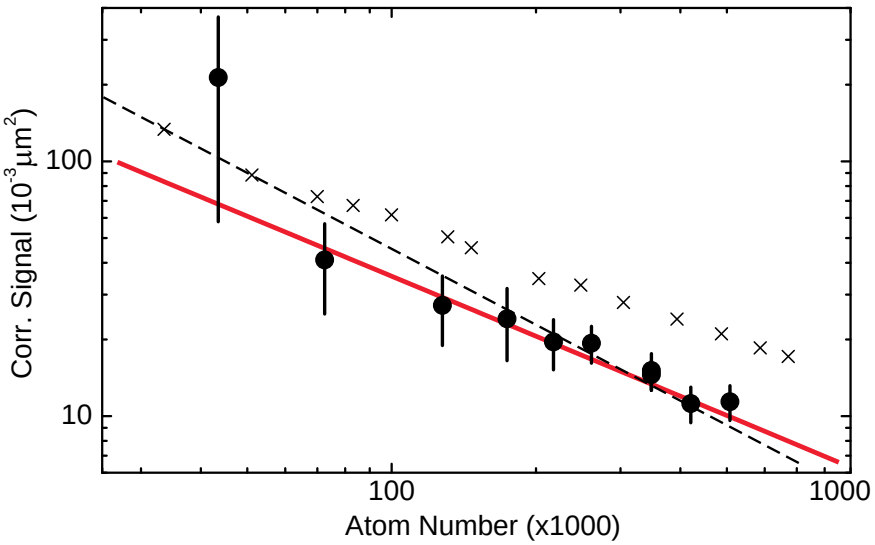

Figure 5.9: Strength of correlation signal vs. Atom number. The red line is a power law fit to the data. Dashed line and crosses indicate the theoretically predicted signal strength for various atom numbers calculated without free parameters, assuming constant density $n = 1$ (dashed line) and including the actual shell structure (crosses), respectively.

One striking feature of this graph is the fact that the slope in the log-log-plot does not correspond to the N_{tot}^{-1} behavior derived above for constant density (plotted as

dashed line for $n = 1$). This is due to the fact that for most atom numbers shown in the graph, the density in the cloud is actually not constant but consists of several Mott shells as explained in section 2.3.5. This leads to an increase in average site occupation with increasing atom number. The cloud size N_s therefore does not scale as $N_{tot}^{1/3}$, but with an even lower power.

The expected signal including the shell structure is shown as black crosses. It is calculated from first principles as outlined in section 5.1.2 for a Mott insulator structure modeled with negligible temperature and tunneling. These values deviate from the $n = 1$ line for atom numbers where more than one shell is expected. The successive formation of the Mott shells furthermore leads to a less smooth increase of the average density than for compressible gases. We also observe that the measured data is consistently reduced by $\approx 40\%$ from the expected values, but otherwise shows a very similar slope in the doubly logarithmic plot. Fitting a power law behaviour to the measured data shown results in an exponent of -0.78 ± 0.15, whereas the analog fit to the expected values yields a slope of $N^{-0.64}$. The shape of the signal is therefore reasonably consistent with the expectations apart from the overall reduction. The reason for this deviation is not known. It is too large to be fully explained by the uncertainty of the atom number calibration, the largest systematic uncertainty in this measurement. Some additional effects must therefore be present, especially since the measurements reported in [144] show a similar ratio between expected and observed signal. Deviations from the perfectly number-squeezed in-trap atom distribution due to thermal excitations, residual tunneling and distortions due to a not perfectly adiabatic lattice loading sequence could contribute. Another neglected effect is caused by atom-atom collisions in the cloud during the ballistic expansion. Any such collision can remove the correlation of the two participating atoms with the rest of the population. This would then reduce the detected amount of correlations caused by the Mott insulator structure. This seems to be supported by the measurements using fermionic ^{40}K in an otherwise comparable configuration [143]. For spin-polarized fermions, no collisions occur during the expansion, and the data obtained in that case is in agreement with the full expected signal (although a reduction can not be fully excluded).

5.3 Detection of density wave structures in the lattice

The noise correlation method determines the Fourier-transformed autocorrelation function of the atom distribution in the lattice potential. In the experiments shown so far, the structure of this distribution was simply given by the structure of the underlying potential. Apart from an overall large-scale density distribution, each site of the lattice is occupied by the same number of atoms, and the periodicity of the atom distribution is just the periodicity of the potential itself. For more complex quantum states, this is not necessarily the case. Many of those states are characterized by the

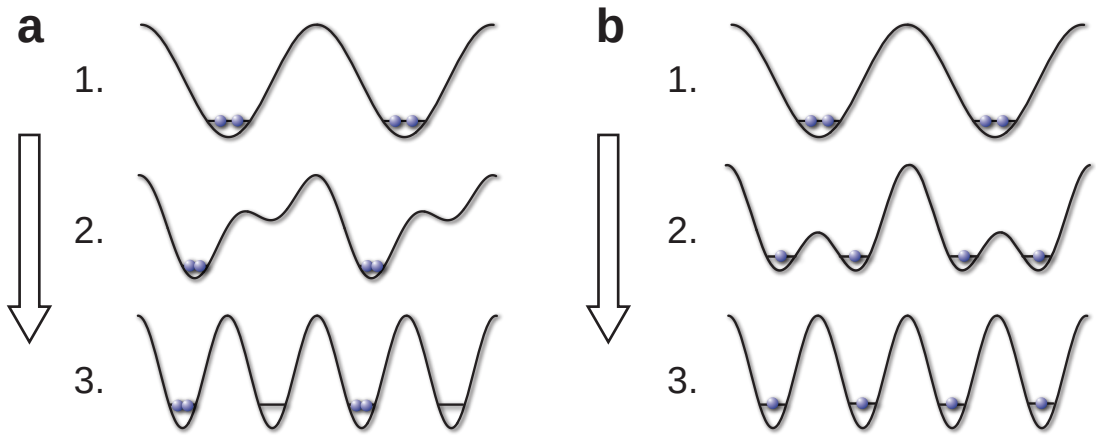

Figure 5.10: Illustration of the patterned loading sequence along the x-axis. **a** Only every second site is populated with atoms by applying an energy bias during the splitting (2.) of the initial superlattice (1.). **b** The lattice is filled homogeneously if no bias is applied. The final lattice configuration (3.) of for both cases is identical, a deep 765 nm lattice which suppresses all tunneling.

appearance of additional correlations between neighboring lattice sites which create a superstructure with a periodicity which is larger than that of the underlying lattice. A prominent example is the antiferromagnetic (or Néel) order for spin-1/2 systems, in which the spin state of the particles alternates between adjacent lattice sites. Another example is the density wave, which is characterized by a periodic modulation of the on-site occupation with a longer wavelength than the lattice spacings.

For bosons with strongly repulsive nearest-neighbor interactions, such a density wave structure would actually be present in the ground state of the many-body system. In that case, it is energetically favorable for the atoms to be separated from their nearest neighbors by an empty site, leading to a checkerboard-type pattern (see e.g. [146, 147]).

To demonstrate the signature of such a structure in the noise correlations, it is artificially created in the following with the help of the superlattice potential described in chapter 6. A superstructure can be created in this way even though nearest-neighbor interactions are negligibly small for the atomic species used. The loading procedure is very similar to the one used to prepare the initial state of the pair tunneling experiment used in section 6.6.3 and the patterned loading experiments described in [148]. It is illustrated in figure 5.10a. The atoms are first loaded into a potential with long periodicity ("long lattice"), and then transferred into a configuration in which the spacing between the lattice sites is half the periodicity of the initial lattice ("short lattice"). The phase between the two potentials is chosen such that all atoms from one superlattice site are transferred to one minimum of the short lattice potential, leaving every second site of that lattice empty. For comparison, a slightly modified transfer

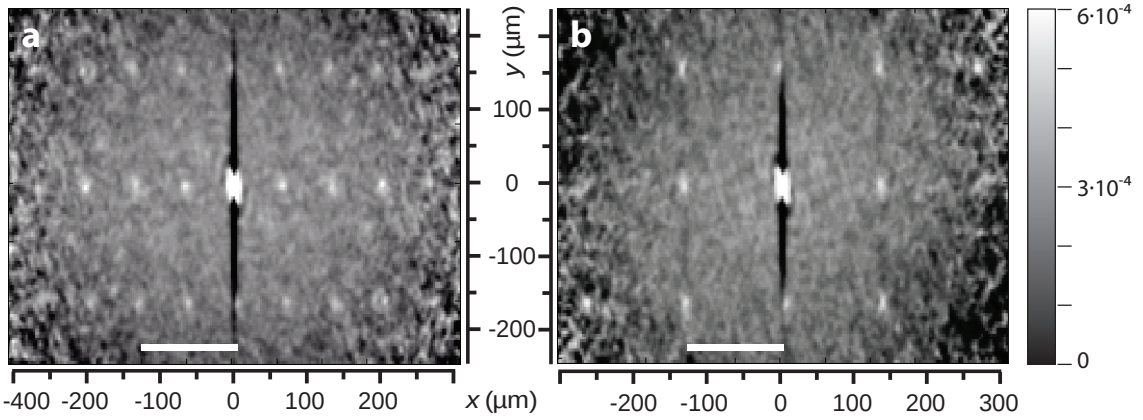

Figure 5.11: Detection of density wave structures in the atom distribution. In **a**, every second site of the lattice is empty, creating a density wave–type superstructure with a wavelength of 2 lattice sites. This structure appears in the correlation signal in the form of additional peaks along the x-axis spaced by $l_x/2$. In **b**, the lattice has been loaded with a uniform density, showing the normal peak pattern with spacing l_x. The lattice potential configuration in the final state is identical in **a** and **b**. White bars denote the characteristic lattice momentum scale of the final state x-axis lattice $l_x = 2\hbar k_{lat,x}$.

sequence is used, which creates the same global density distribution, but with the atoms evenly distributed over all short lattice sites (figure 5.10b).

The final configuration of the lattice potential is the same in both cases: The y- and z-axis are 420 nm-periodic, whereas the x-axis has a periodicity of 382.5 nm. With evenly distributed atoms, correlation peaks are therefore expected at positions corresponding to multiples of the doubled recoil momenta scales $l_{x,y} = 2\hbar k_{x,y}/m \times t$ of the 840 nm light along the y-axis and 765 nm along the x-axis, respectively. This is the case in figure 5.11b. The signature of a density wave, a periodic modulation of the density with a wave vector k_{DW}, is the appearance of additional correlation peaks at multiples of $\hbar k_{DW}$ as well as the sums and differences of these and the fundamental lattice vectors. The periodicity of the artificially prepared density wave in this experiment is twice that of the lattice potential and oriented along the x axis. Therefore the additional peaks in figure 5.11a have a spacing of $l_x/2$ from and appear between the original peaks along the x direction. The periodicity along the other direction is unchanged. For this experiment 86 images were analyzed, which were taken by an Andor Ixon DV 885 camera.

In principle, this experiment can be conducted with any superlattice-type potential: The factor of two in periodicity between the underlying lattice and the superlattice is not required, any other periodic potential can be used. All of these will create a modulated density distribution of the lattice which will generate correlation peaks at the corresponding lattice momenta and all combinations thereof. The noise correlation spectrum will then show the 2D Fourier spectrum of the autocorrelation function of

the density distribution. This of course also holds for non-periodic density distributions. Their signal is, however, not characterized by periodic structure of sharp peaks, and could therefore be much harder to observe against the noise background. For the large family of strongly correlated quantum states with periodic superstructure in the lattice, however, the noise correlation method appears as a powerful detection method.

6 Observation of tunneling processes in two-well potentials

6.1 The double well system

This chapter focuses on the tunneling processes in the strongly interacting regime. These are studied with experiments conducted in a conceptually very simple setup: A trap with only two minima, coupled by a tunnel junction, and filled with a maximum of two atoms which influence each other by repulsive interaction as shown in figure 6.1. It is the most simple system which contains all of the ingredients of the standard Bose-Hubbard model – an interaction energy U and a tunnel coupling J, and possibly a potential gradient, given by an energy bias Δ between the two sites.

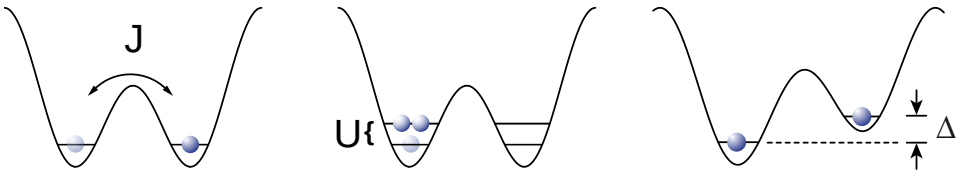

Figure 6.1: A double well potential for atoms is characterized by three parameters in close analogy to the Hubbard model. The two sides are coupled by an interaction matrix element J, and adding an atom to an occupied site raises the energy of the state by the interaction energy U. An external potential gradient is defined by the bias energy Δ.

This model system can be seen as the a maximal simplification of two very different physical systems. For one, it can be viewed as the minimal fraction of a lattice potential, containing only two of the lattice wells of the macroscopic system.

Alternatively, it can be viewed as the ultimate miniaturization of a superconducting Josephson junction, where the two conductors coupled by the junction are so small that the repulsive interaction of the particles within them is comparable to the strength of the tunnel coupling. At that point, the system can no longer be described in terms of two coherent fields and a quantized model has to be used.

In this chapter, both aspects are explored experimentally with respect to the dynamics of the particles in such systems. Due to the overall simplicity of the two atom– and two well–configuration, it is possible to directly study complex tunneling phenomena, which can otherwise only be observed indirectly.

6.1.1 The double well potential as a miniaturized Josephson junction

A system of two sites connected by a tunnel junction was first studied extensively in the context of superconductors, after Brian D. Josephson first predicted its properties using a description with two macroscopic quantum fields[149]. In a Josephson Junction two superconductors are coupled by an insulator which is thin enough to allow for the Cooper-paired electrons to tunnel. The system is then described in terms of the voltage resulting from the population difference of Cooper pairs on either side of the junction and the phase relation between these two superconductors [150]. Here, the quantized nature of the fields does not play a role.

For high atom numbers and weak atom-atom interactions a double well system can be described in the same way as a superconducting Josephson junction. The macroscopic matter wave field then has the same description as the macroscopic wave function in a superconductor, and, correspondingly, the same phenomena such as Josephson oscillations and self-trapping can be observed [16].

Tunneling processes for very small conductors with low numbers of charge carriers which interact strongly can not be described in terms of continuous Fermi seas or, for Cooper pairs, in terms of Josephson-type coherent fields. Instead, a quantized Josephson description has to be used. Such systems have first been studied for solid state quantum dot devices in the context of electronic transport through a junction [151, 152]. Since in the presence of strong interactions this transport is strongly nonlinear, they are described as transistors. Devices which are based on the tunneling of individual electrons were named single electron transistors (SET)[153, 154], whereas configurations in which individual Cooper pairs tunnel are named Bloch transistors [155–158].

The concept of these devices is very similar to a microscopic field effect transistor (FET). In such a device, electrons pass through a region with a variable potential, which can be modified by an external gate voltage. If a FET would be scaled down indefinitely, eventually the interaction of a single charge in the gate electrode with the individual electrons passing through the transistor can significantly influence the conductivity. A typical configuration is shown in figure 6.2.

To reach this regime, a very small isolated conductor or quantum dot forms a "charge island" which is connected to two or more electrodes via tunnel junctions. These two electrodes are the equivalent of the source and drain gates of a FET, and can add and remove electrons from the island. The voltage of the island can be externally biased with respect to the voltages on the two electrodes. The capacity C of the island to the electrodes is small enough that the presence of a single electron increases its voltage by $V_t = e/C$ which is larger than the thermal energy $k_B T$ and the kinetic energy J given by the tunnel coupling. Therefore, if the voltage drop V_s over the source junction is smaller than V_t, no other charge can tunnel to the island while it is "occupied" by an electron. Below this threshold voltage V_t, the conductivity of the device therefore breaks down due to the interaction of two individual

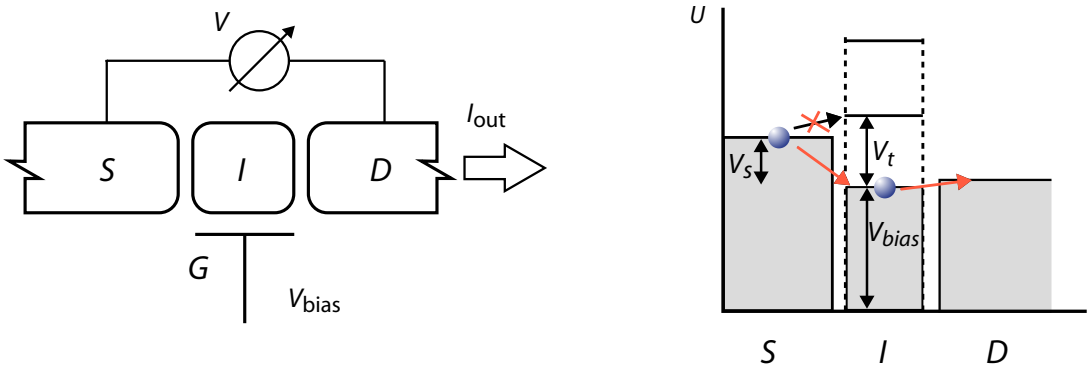

Figure 6.2: Quantum dot cotunneling: A single atom transistor consists of an island I connected to two electrodes S and D (source and drain) via tunnel junctions. The electric potential of the island can be biased by an additional gate capacitor G. If the island is occupied by an electron, its Fermi level is raised by V_t, the charging energy of the island with one elementary charge. This blocks tunneling of a second electron (black arrow) if $V_s < V_t$. The second-order process (red arrows), which consists of two simultaneous electron tunnel events, is still possible.

electrons. This effect is called "Coulomb blockade". Since V_s can be controlled externally by charging and capacitive biasing of the island, this device effectively forms a transistor [153, 159].

However, current can still flow through the device in the Coulomb blockade regime. This requires a two-step tunneling process called "macroscopic quantum tunneling" or "cotunneling", via a virtual intermediate state. This cotunneling motion was first observed for systems of coupled quantum dots by spectroscopy (see e.g. [160, 161]).

Another important second-order tunnel effect, where particles with different spin are exchanged via a tunnel junction, can be directly observed in double quantum dots on pairs of electrons [162, 163].

6.1.2 The double well potential as a minimized optical lattice

Since a two well system as illustrated in figure 6.1 is the most simple configuration described by the same hamiltonian as a lattice, it can be seen as a prototype system for an extended lattice. This holds both for weakly interacting systems with large atom numbers and for strongly correlated systems.

In the limit of large atom numbers, where the double well is a direct analog to the Josephson junction, bosons in optical lattices can also be described by an array of Josephson junctions [4, 164–166]. For low occupation numbers such as those found in 3D optical lattice experiments in the strongly correlated regime, the matter wave fields are intrinsically quantized, and the natural way to describe these systems is the

quantized Hubbard or Bose-Hubbard hamiltonian. For the analysis of the underlying basic processes which govern the properties of the ensemble of atoms, it can be desirable to reduce the system to the most simple configuration which includes all important parameters. For investigating dynamical phenomena and complex tunnel couplings in a lattice potential this configuration is a double well occupied by two atoms. Here, the many-body aspect is removed from the model, since the system can only occupy a very limited number of states. In this way, the influence of the interaction on the tunneling process itself can be studied by directly observing the tunneling process, rather than analyzing the effect of interaction and tunneling on the ground state of a many-body system of atoms. This will be demonstrated in this chapter for two different tunnel processes.

In the typical strongly correlated regimes, first order tunneling is completely suppressed by the interactions. This can for example lead to atom pairs in the lattice which are bound, even though they interact repulsively and unoccupied neighboring lattice sites are available [167]. In this situation higher-order tunneling effects such as cotunneling, where two particles tunnel in a correlated way, are the dominant dynamical processes in the system and can define its properties.

An important aspect of higher-order tunneling arises with particles that have a spin degree of freedom. In that case, second-order tunneling between neighboring sites can lead to a spin exchange even though there is no significant wave function overlap of the atoms. Such superexchange type processes are a mechanism for effective spin-dependent next neighbor interactions which can give rise to magnetic phases in real materials and are a possible source for quantum magnetism with atoms in lattice potentials [41, 168–170].

6.1.3 Double well potentials for atoms

Double-well potentials for neutral atoms can be created by very different means. The experiments initially focused on the Josephson regime, studying systems of two coherent fields. The first one certainly is the landmark experiment demonstrating the interference pattern of two independently created condensates [7]. Here, the repulsive potential from a blue-detuned light sheet was used in order to split a magnetic trap to create a potential with two minima which supported one condensate each. In this case, the barrier was very wide, and there was negligible tunnel coupling.

Another method of "splitting" a magnetic trapping potential was demonstrated recently, which exploits the strong curvature of the field lines in magnetic microtraps. This curvature results in a strongly inhomogeneous coupling to the different polarization components of a radiofrequency field. For the typical microtrap geometry, an elongated potential along the trapping wire can be split by a central barrier along the long axis. This barrier is produced by the shift of the atomic levels due to the strong and localized coupling to the radiofrequency field [171, 172]. These barriers are also wide in the sense that the single particle matrix element J is negligible for all reason-

able trap configurations. However, due to bosonic enhancement tunnel coupling can be possible for large well occupations. Very recently, evidence for tunneling-induced effects such as number squeezing and the coupling of the phases between the wells have been reported [173, 174].

A two-well potential with a thinner barrier and thus stronger tunnel coupling can be realized if the well is produced by an antinode of a standing-wave potential. This was realized in [16], where a standing wave was combined with a very narrow dipole trap, which contained only two periods of the standing wave. In this way, only two minima of the standing wave are global minima, and they are coupled by tunneling through the central barrier.

Coherent oscillations of individual atoms between two potential wells were first observed by Haycock et al. using a spin dependent lattice [175]. Here, the two periodic potentials for the two spin states are displaced to each other, and coupling between the potential minima is mediated by microwave transitions between the spin states. By measuring the overall magnetization, the relative population of the two sides can be determined, allowing for the observation of coherent population oscillations.

In a purely spin-independent double well potential, tunneling of individual atoms was realized with a cold argon 40 beam which traversed a double well standing wave. Here, coherent tunneling shows in the oscillation of the relative phases between the wave functions in the two sites of the double wells [176].

For the experiments described in section 6.6, both a strong tunnel coupling and a very strong on-site interaction between the atoms is required. The coupling parameter J and the interaction energy U should be the two dominant energy scales present in the experiment. Their characteristic time scales h/J and h/U should be much shorter than a typical experiment duration. For given and fixed collisional properties of the atoms, a large interaction energy requires strong confinement of the atoms to the trap sites. This can be achieved by an additional strong confinement also along the axes which are perpendicular to the double well axis. This is realized by adding additional deep standing waves on these axes, which effectively create a two-dimensional array of one-dimensional superlattice potentials. If tunneling between the double wells of the superlattice is suppressed, a three-dimensional lattice of double-wells is formed, where only the two sites of each individual double well are coupled exactly as illustrated earlier in figure 6.1.

Such a configuration is possible by using cross-interferences between two optical standing waves in one plane. If the polarizations of the two beams are chosen such that two orthogonal beams can interfere, a pattern with a two times larger periodicity can be created [177]. In such a potential both a strong tunnel coupling and a strong on-site interaction can be achieved [178, 179]. In addition, it can be strongly spin-sensitive, enabling individual addressing of the two wells [180, 181].

6.2 Realization of the double well lattice

The double wells for the experiments described here are created by a two-color standing wave using two independent laser beams. This type of setup was chosen for its robustness in terms of the stability of the resulting potential. The two standing wave potentials differ in periodicity by exactly a factor of two. The longer wavelength one ("long" or "red" potential) is created by light at 1530 nm, the other ("short" or "blue" potential) by a 765 nm standing wave. Therefore, by choosing the potential maxima of the long standing wave to coincide with maxima of the blue potential, a symmetric double well configuration arises as shown in figure 6.3. Here, each minimum of the red fundamental lattice – which is typically deep enough to suppress any significant tunneling between its wells – is split by the blue potential to form two wells separated by a potential barrier created by the short standing wave. Therefore, the 765 nm laser is also referred to as barrier laser, and the 1530 nm potential as the fundamental lattice in the following.

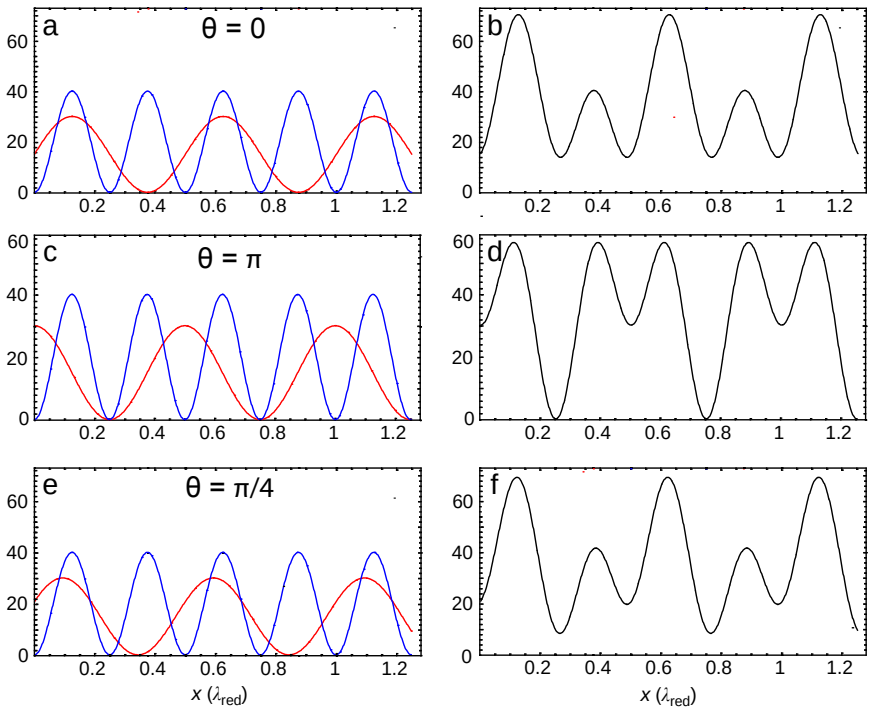

Figure 6.3: Creation of a periodic double well potential from two independent sinusoidal potentials: A long (red curves) and a short (blue curves) standing wave potential are superimposed with a controllable phase Θ. This phase can change the potential from a symmetric double well (a,b) to an antisymmetric single well configuration (c,d). For small phase angles (e,f), a double well potential with an energy offset between the two minima is produced.

The setup is capable of producing two fully independent standing waves, as long

as the red wavelength is almost exactly twice that of the blue laser. Both potential depths can be chosen independently and can be varied dynamically. Also, the relative phase of the two sinusoidal potentials can be freely controlled during the experiment. Therefore, any potential which can be constructed of two such standing waves can be created, and dynamically changed into any other potential configuration. Three typical configurations with both standing waves active are shown in figure 6.3. They are characterized by the relative phase Θ of the two potentials. The standard is the symmetric configuration with $\Theta = 0$ – a double well where both localized states have the same energy, the energy offset Δ is 0.

In the antisymmetric configuration with $\Theta = \pi$, one well is very deep, while the other is elevated. This leads to maximal confinement in the bottom well, resulting in very high collision rates. Due to the symmetry of the configuration, the tunnel coupling is actually homogeneous in this case. The tunneling rate is the same between all neighboring sites, which only differ by an energy offset. Technically, it is therefore not a double-well potential.

If a detuning of the two ground states of the wells is desired, a finite phase Θ is chosen, leading to a tilted double well potential. Here, the right well is biased by an energy offset Δ with respect to the left well.

Controlling the relative phase

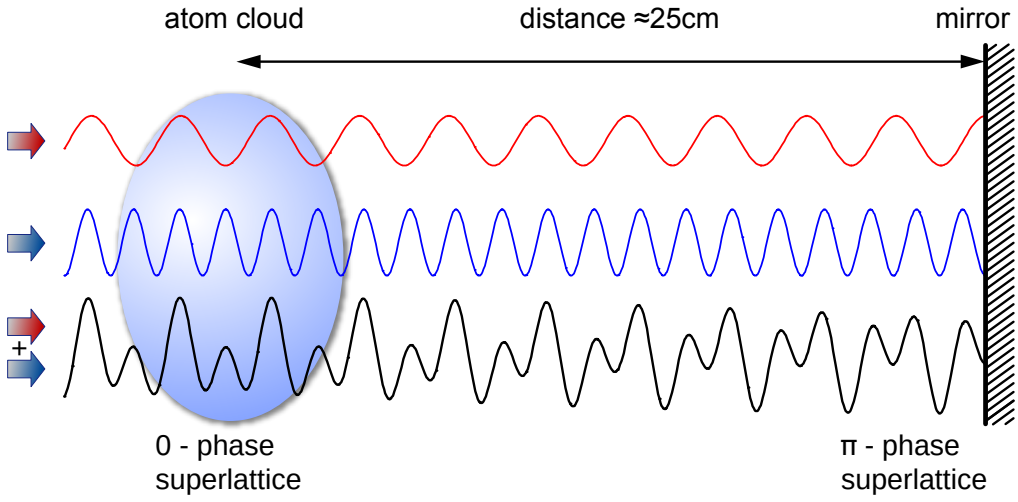

Figure 6.4: Setting the phase of the superlattice at the atom position by applying a detuning to the red laser. Both standing waves have a node in the mirror plane. This results in an antisymmetric double well configuration with $\Theta = \pi$. By applying a small relative detuning to the standing wave, a total phase slip of π can be realized between the mirror position and the atoms ($\approx 25\,\mathrm{cm}$) to create a symmetric potential.

The two standing waves are produced by two independent laser sources with a 765 nm and 1530 nm wavelength, respectively, which are superimposed on a bichromatic mirror and reflected by the same retroreflector. Using a common retroreflector sets the relative phase of the sinusoidal potentials created, as the mirror fixes the node position of both standing waves. This enforces a potential maximum from the red, and a potential minimum from the blue detuned beam in the mirror plane, resulting in a $\Theta = \pi$ antisymmetric potential configuration.

By slightly detuning the red wavelength λ_{red} from the reference $2 \cdot \lambda_{blue}$, however, the relative phase between the two sinusoidal potentials changes along the standing wave axis as the distance from the mirror increases. This is illustrated in figure 6.4. The phase slip per short lattice period (765 nm/2) along this axis is $2\pi\frac{\delta}{f_{blue}}$, where δ is the detuning of the red light from the reference frequency, which is given by 1/2 the blue laser frequency f_{blue}.

The phase slips of all standing wave periods between the mirror and the atom position add up, leading to a total phase slip of

$$\Theta = 2\pi\frac{\delta}{f_{blue}} \cdot \frac{L}{\lambda_{blue}/2} = 4\pi \cdot \frac{\delta L}{c} \tag{6.1}$$

with L the distance between mirror and the atom position and c the speed of light.

Therefore, the tuning range of Θ depends on the tuning range of the laser and the optical path length between the atoms and the retroreflector. In order to be able to compensate for drifts of approximately $\pm\pi$ in either direction and still have a phase tuning range of 2π available, an overall tuning range of approximately 4π is desired. Since the tuning range of the laser was determined to be larger than 0.5 GHz, $L \approx$ 25 cm was chosen.

Controlling frequency and amplitude of the lattice light

The two laser beams required for the double well potential are created by two independent laser sources. The 1530 nm light is produced by an erbium fiber laser which can be frequency tuned by a fiber-stretching piezo attached to the fiber cavity. The 765 nm light for the blue lattice is created by a titanium-sapphire (Ti:Sapph) laser running at 765 nm, which is frequency stabilized by locking it to a temperature-controlled reference cavity.

The setup for generating the superlattice light is shown in figure 6.5. Two independent fibers are used to guide the two lattice beams to the experiment. They are superimposed on a dichroic mirror shortly before the glass cell of the apparatus. The powers of the beams are controlled using AOMs with variable radiofrequency power before the fiber couplings. The intensity of each beam is independently stabilized by feeding back the signal from a photodiode behind the fiber to the radiofrequency generator. In order to set the detuning δ, the 1530 nm laser is frequency-locked to the

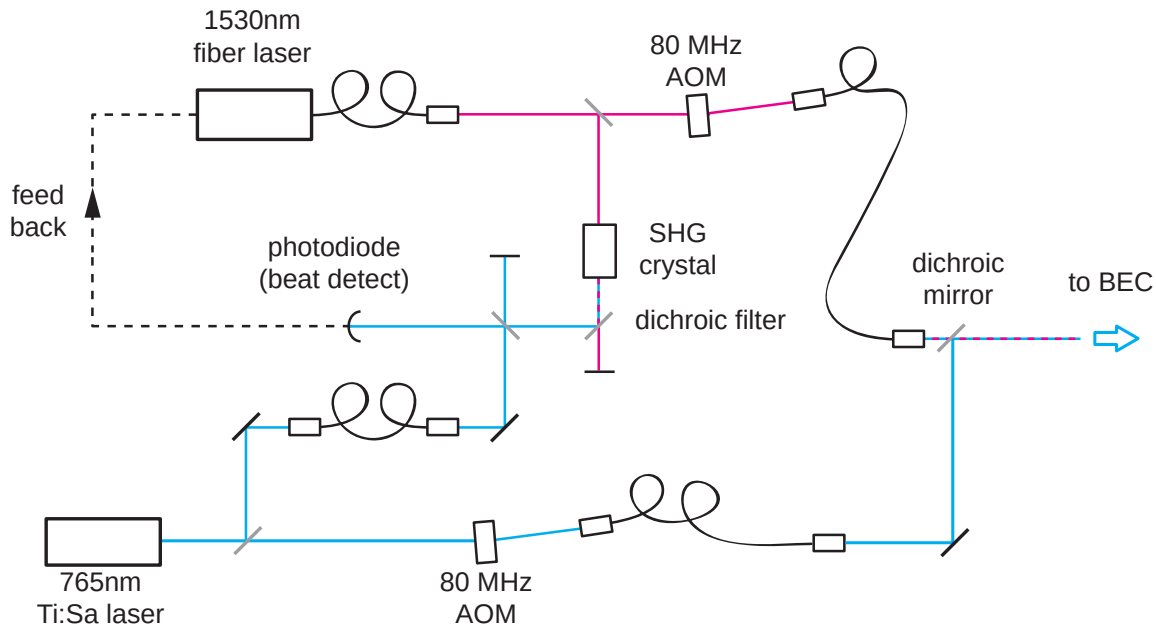

Figure 6.5: Laser setup for generating the two light frequencies used to create the double well lattice. The long wavelength lattice is produced by a 1530 nm fiber laser, the short wavelength lattice by a stabilized Titanium-Sapphire laser at 765 nm. A part of the long wavelength light is frequency doubled in order to obtain a beat signal with the 765 nm light.

765 nm light. For this, a small amount of the light from the laser is frequency-doubled in a periodically poled lithium niobate (PPLN) crystal. The doubled light is then superimposed on a fast photodiode together with a reference beam from the Ti:Sapph laser. The beat signal recorded from this photodiode due to the interference of the two beams is $2 \cdot f_{red} - f_{blue} = 2 \cdot \delta$. The radiofrequency signal from the photodiode is then electronically mixed with a reference signal from a voltage-controlled oscillator (VCO) which generates a variable frequency f_{VCO}. The lower sideband of the resulting signal then has the frequency $2 \cdot \delta - f_{VCO}$. This frequency is actively stabilized to a fixed value of approximately 160 MHz using a delay line-based frequency offset locking scheme [182]. For the feedback, the error signal is used to control the fiber-stretching cavity piezo of the 1530 nm fiber laser with a bandwidth of approximately 3 kHz and 0 V to 40 V range.

The desired offset frequency δ is chosen by varying the frequency of the VCO, which is computer controlled and can be programmed for arbitrary phase ramps during the experiment cycle. The VCO used (Mini Circuits POS2120W) has a frequency range of 1060 MHz to 2120 MHz, leading to frequency offsets δ of the red light in a range between 580 MHz and 1180 GHz. When locked, the residual frequency fluctuations of the laser are smaller than 100 kHz. In typical operation, the energy offset Δ between two wells in the symmetric configuration in the center of the trap can be kept

below $h{\cdot}200\,\mathrm{Hz}$ in this way. More locking bandwidth and faster response to phase changes could in principle be obtained by using the frequency shifting capabilities of an AOM in one of the beams.

6.3 Superlattice band structure

The superlattice band structure can be calculated in the same way as the one of the underlying sinusoidal red lattice by taking the additional Fourier components of the barrier lattice potential into account [70, 71]. This leads to deformations and shifts compared to the fundamental lattice band structure. In the following, we will discuss the symmetric case, as this is the regime where most of the dynamical effects investigated in the experiments take place. It is important to note that the natural unit of energy for band structure calculations is the recoil energy E_R corresponding to the underlying periodicity – therefore the natural unit of energy in the following is the recoil energy of scattering a 1530 nm photon,

$$E_{R(red)} = h^2/(2m\lambda_{red}^2) \approx h \cdot 980\,\mathrm{Hz},$$

which is used as E_R unless otherwise noted. The more intuitive scale for experiments confined to a single double well structure, however, is the recoil energy of the barrier lattice light. This corresponds to interpreting the double well as an optical lattice with only two sites formed by 765 nm light. In this way, the double well experiments are directly comparable to the bulk lattice experiments described, especially since the bulk laser wavelengths used (typically 840 nm) are similar to that of the blue laser. Therefore, in some cases energies will be given explicitly in units of the blue light recoil energy $E_{R(blue)} = E_R(765\,nm) \approx h \times 3919\,\mathrm{Hz}$.

Low superlattice depth

Figure 6.6 shows the band structures for different fundamental and barrier lattice depths. As discussed in section 2.3.1, the width of each band, defined by the maximal energy difference within that band, determines the tunnel coupling between lattice sites, as given by the *overall periodicity*. This means that in the context of a superlattice, the bandwidth gives the tunneling strength from one double well to the next. Correspondingly, the Wannier functions associated with each band are functions which are localized to one double well structure, not necessarily to an individual well inside it. In this case, the tunneling barrier is the potential maximum separating two neighboring double well structures. As for the sinusoidal lattice (see section 2.3.1), the tunnel matrix element to the next superlattice site J_{ext} is connected to the band width $E_{max} - E_{min} = 4J_{ext}$.

In comparison with the simple sinusoidal red lattice, the introduction of the blue lattice in the symmetric configuration leads to a reduction of the bandwidth and to a

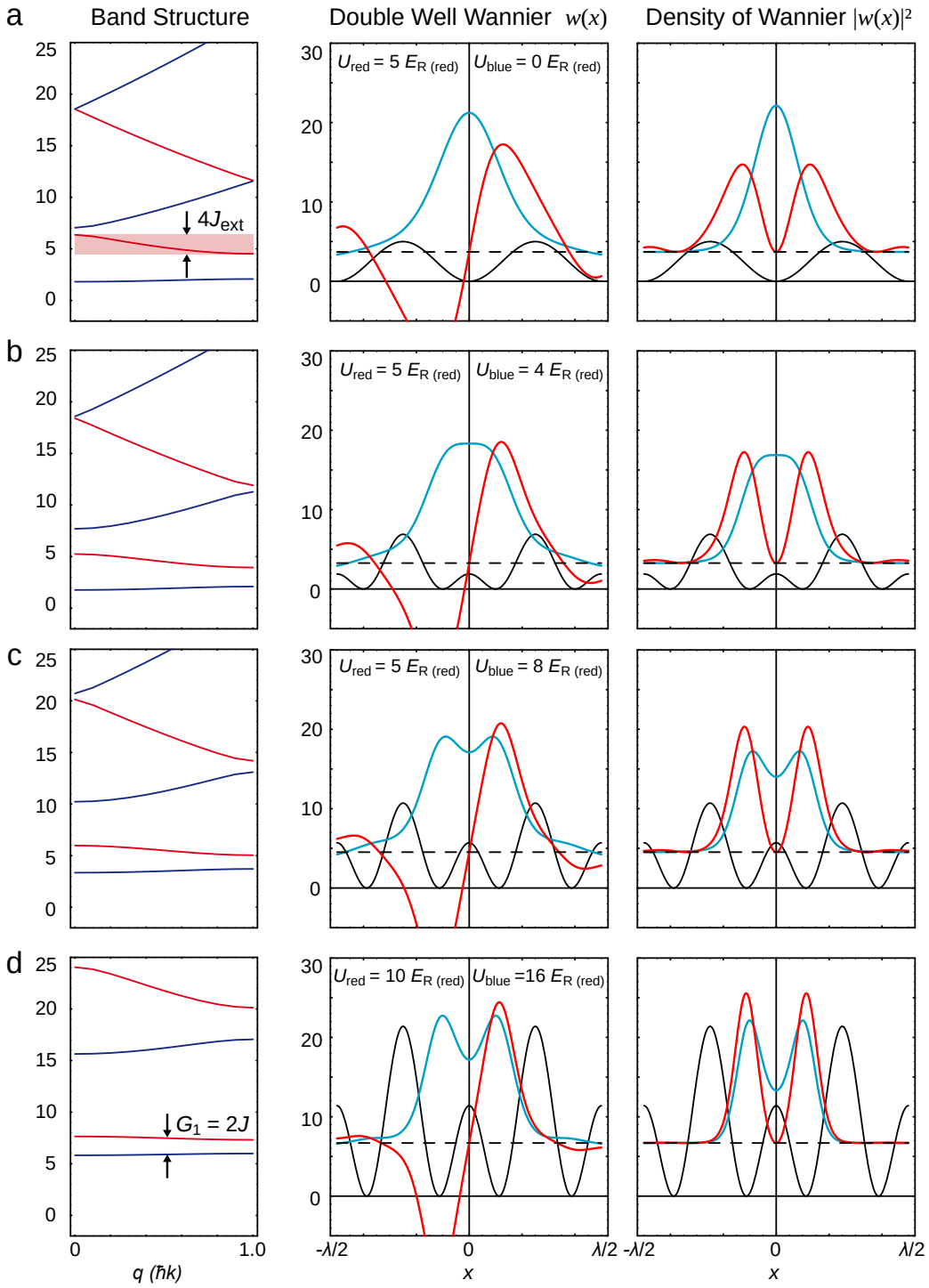

Figure 6.6: Band structure of shallow superlattices. The band structure (first column) of the fundamental lattice (a) is modified by the addition of the blue potential (b-d). Pairs of bands separated by a reduced gap G form, representing a symmetric (blue) and an antisymmetric (red) wave Wannier function. The wave functions are shown in the second column, and their probability densities in the third. For increasing depths, they converge to a symmetric and an antisymmetric superposition of a localized peak in each of the wells.

pairing of bands, where each pair consists of a lower energy symmetric band and a higher energy antisymmetric band.

Deep superlattice

The experiments described in this chapter are conducted mostly in the regime where the atoms in the lowest Bloch band are localized both to one specific double well structure and to the two single wells inside this structure. For this, the bands occupied have to be lower in energy than both the inter-double well barriers and the tunneling barrier separating the two wells inside. For symmetric double well configurations the corresponding Wannier functions are, just like in an ordinary lattice, alternatingly symmetric and antisymmetric in structure with respect to the center of the double well.

Increasing the strength of the red lattice to achieve confinement to the double well results in flatter bands as shown in figure 6.7, indicating a lower tunneling strength between neighboring double wells. In most experiments, the tunneling between neighboring double well structures is suppressed on all relevant timescales, the bandwidth can be neglected and the bands can be treated as levels. After making this approximation, the levels can be treated as two states in the local potential created by a single double well structure. Increasing the depth of the blue lattice potential and thus raising the barrier separating the two wells leads to a reduction of the separation of the levels of each pair. In the limit of very deep potentials, where the energy gap between the two can be neglected and the two wells can approximated by parabolic potentials, these two levels correspond to the symmetric and antisymmetric superpositions $|+\rangle$ and $|-\rangle$ of a particle fully delocalized over both wells. We can therefore reconstruct the two wave functions localized in the left and in the right well as

$$\begin{aligned} |L\rangle &= \frac{1}{\sqrt{2}}(|+\rangle - |-\rangle) \\ |R\rangle &= \frac{1}{\sqrt{2}}(|+\rangle + |-\rangle). \end{aligned} \tag{6.2}$$

This construction can be used with any band pair. Using it with the nth band pair constructs the nth harmonic oscillator levels of the left and right well, respectively, within the harmonic oscillator approximation for very deep potentials.

The energies of the two states $|+\rangle$ and $|-\rangle$ differ by the band gap G_n of the nth band pair. Preparing the state $|L\rangle = \frac{1}{\sqrt{2}}(|+\rangle - |-\rangle)$ therefore leads to a coherent evolution:

$$\Psi(t) = \frac{1}{\sqrt{2}}\left(|+\rangle - \mathrm{e}^{i(G_n)/\hbar t}|-\rangle\right) \tag{6.3}$$

It corresponds to a tunneling oscillation between the two wells as will be outlined in section 6.5.1. The ad hoc construction of the two states $|L\rangle$ and $|R\rangle$ is also a meaningful operation when the potentials are not assumed to be very deep. It corresponds

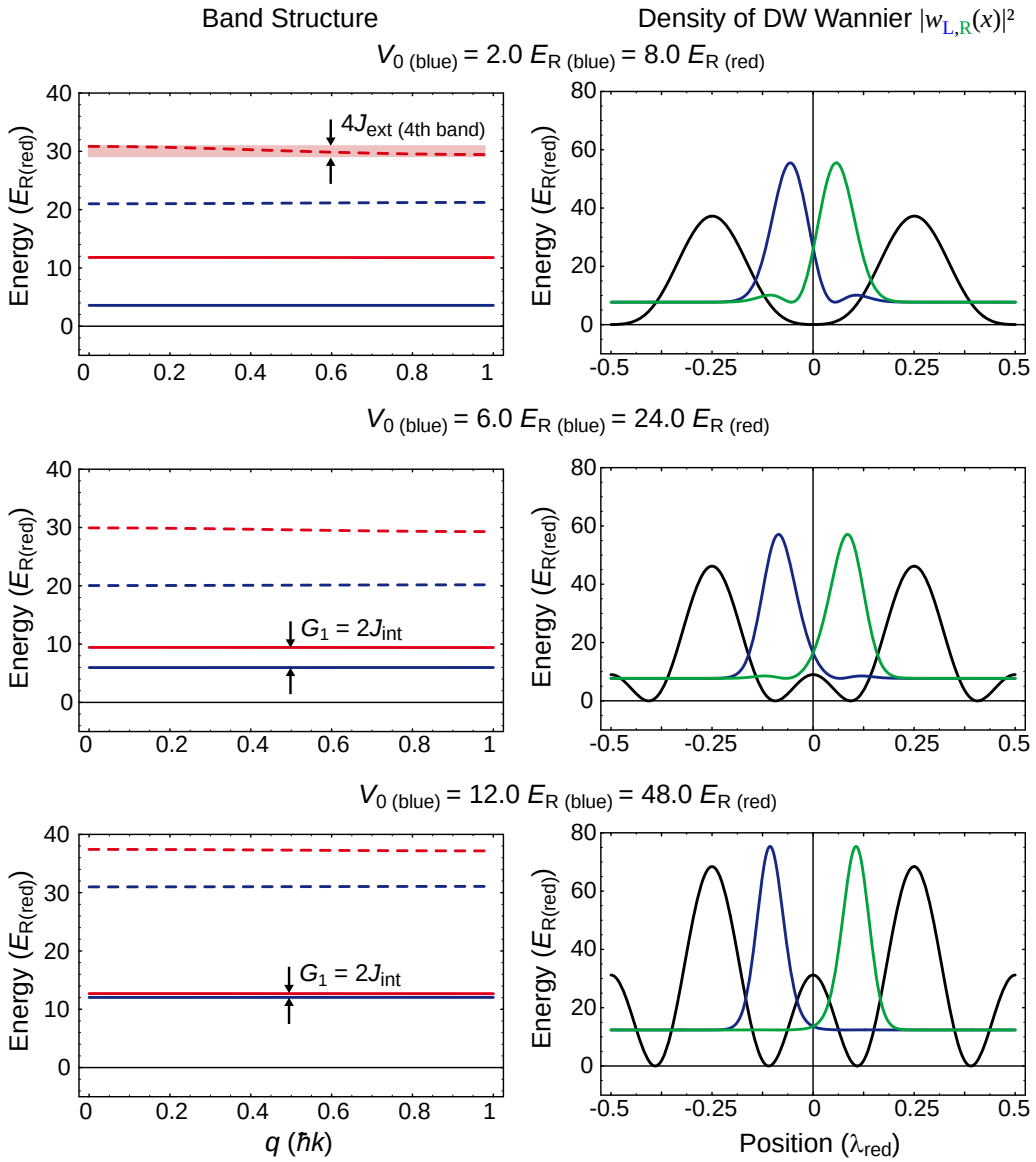

Figure 6.7: On-site wave functions and band structure in the double well lattice for a deep ($V_{0(red)} = 37.2\,E_R$) fundamental lattice and increasing barrier height. In the limit of strongly localized on-site wave functions, the energy bands become paired. The width of each band (the difference between highest and lowest energy in quasimomentum space) determines the tunneling rate between double wells. The tunnel coupling between the two sites of an individual double well is given by the gap G between the two bands of a pair. The wave functions shown on the right correspond to the lowest band pair. Their plots are shifted upwards by the average of the two band energies in order to visualize the relation between these ground state energies and the height of the tunnel barrier.

to the construction of the Wannier function equivalent for the individual sites within each superlattice cell when combining the two bands of each pair. In analogy to real Wannier functions, we define these site Wannier functions as maximally localized to one particular well and construct them in the same way as the Wannier functions of a periodic lattice:

$$w_{\text{well: } l,n,m}(x) = \sum_j \mathrm{e}^{i\pi j \cdot m} w_{\text{fund:}l,2\cdot n+j-1}$$

Here, j can have the values 0 and 1 for the two bands of each pair. $w_{well,l,n,m}$ is the wave function corresponding to the nth band pair localized at the lth double well on side m. A value of $m = 0$ corresponds to the right site, $m = 1$ to the left site. It is constructed from the superlattice Wannier functions $w_{\text{fund: } l,b}$ in band b localized on double well l. The experiments in this chapter can usually be described in terms of a single double well and therefore $l \equiv 1$. The two relevant single-site wave functions for the configurations used are $w_L(x) = w_{\text{well: } 1,1,1}(x)$ with the atom localized on the left, and $w_R(x) = w_{\text{well: } 1,1,0}(x)$ which is maximally localized in the right well.

Figure 6.7 shows this construction and the resulting wave functions in a deep superlattice. In the lowest bands of the lattice potential, tunneling is almost completely suppressed and the bands can be approximated as levels. Also, the wave functions are localized to a single well very strongly, even for significant gaps between the two bands of the pair.

6.4 BEC in the superlattice

In analogy to the experiments with a BEC in a normal 3D optical lattice, we load a Bose-Einstein condensate with approximately $1 \cdot 10^5$ atoms into a weak superlattice potential. For this, all lattice axis are ramped up within 160 ms without leaving the 3D superfluid regime. This means that all lattice potentials are weaker than $3\,E_r$, allowing for strong tunneling along all lattice directions. In this situation, all atoms are fully delocalized, and the phase of the matter wave is constant over the cloud. The density distribution is given by the Thomas-Fermi distribution for a constant chemical potential μ, as illustrated in 6.8. The lattice is then switched off instantaneously and the atom distribution undergoes a free expansion. The images shown in figure 6.8 are taken after a time of flight period $t_{exp} = 15\,\text{ms}$, and reflect the in-trap momentum distribution. Due to the constant phase of the matter wave in the trap, this approximately corresponds to the Fourier transform of the density distribution (see section 3.2.1).

In the case of a symmetric double well (fig. 6.8c), the wells have equal atom population. Also, the distance between the two wells separated by the internal barrier is almost the same as the one between wells separated by the higher inter-double well barrier. Therefore, the density distribution is an almost exactly periodic peak structure with the same periodicity as the blue lattice. The resulting momentum distribu-

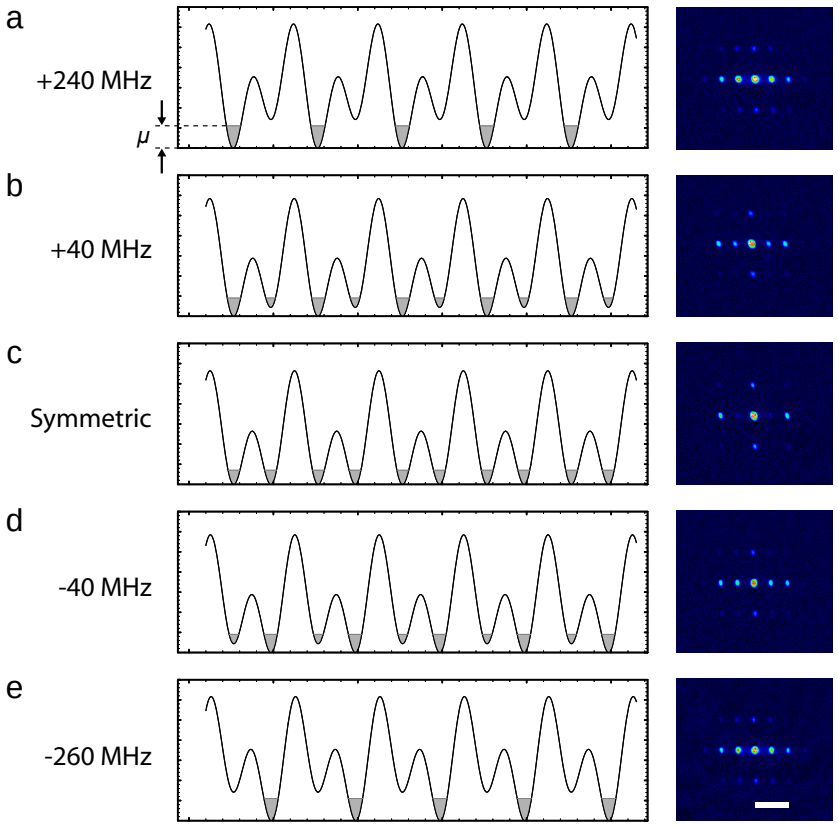

Figure 6.8: Superfluid in a 3D lattice formed by a superlattice along the horizontal axis and simple sinusoidal lattices along the two other directions. All lattice depths are very low ($< 4\,E_R$) such that tunneling through all barriers is possible and all atoms are fully delocalized. In this regime the atoms distribute according to the Thomas-Fermi distribution and the phase is constant over the entire cloud (left column). Therefore, the density distribution measured after 15 ms time-of-flight expansion (right column) corresponds approximately to the Fourier transform of the density distribution in the trap (filled areas in left column). The length of the white bar $l = 2\hbar k_{blue}/m \cdot t_{exp} = 184\,\mu$m shows the blue lattice momentum scale.

tion visible in the time-of-flight image therefore is a peak structure with a periodicity according to $l_{blue} = 2\hbar k_{blue} \cdot t_{exp}/m$. The extent of the pattern is limited by the extent of the gaussian momentum space Wannier function on each site, therefore the periodic pattern is bounded by a gaussian envelope.

This periodicity is not conserved when the double wells are configured in an asymmetric way by changing the superlattice phase Θ via the frequency offset δ of the red laser (figs. 6.8b,d). The periodicity of the density distribution is now given by the periodicity of the fundamental lattice. This results in the appearance of additional components in the momentum distribution and the resulting pattern consists of peaks at positions $n \cdot l_{red} \approx n \cdot l_{blue}/2$. The relative heights of the peaks depend on the relative occupation of the left and the right wells inside each double well.

When the asymmetry is large enough such that all atoms are contained on the same side of their respective double well (figs. 6.8a,e), the density again has a periodic structure made up of identical density peaks, where the spacing is now that of the red lattice. Further increase of the asymmetry does not change the momentum space distribution, as the structure of the resulting density distribution is not significantly modified.

6.5 Bose-Hubbard model for the double well

In the regime of tight confinement, the two-well system can be described using the Bose-Hubbard formalism in the same way as for atoms in a regular optical lattice. Since effectively only two spatial modes are involved when the tunneling coupling through the long standing wave is suppressed, we refer to the Hamiltonian as the two-mode Bose-Hubbard hamiltonian.

The alternative point of view, interpreting the two wells as the two sides of a Josephson junction, leads to the same description. The original Josephson junction model assumes wave functions with well-defined phase on either side of the well and therefore requires a description in coherent states [149]. For systems with low occupation numbers of the wells and no coupling to particle reservoirs, the quantized nature of the wave functions has to be taken into account. Such quantized Josephson junctions follow the same description as the Bose-Hubbard model reduced to two sites:

The corresponding hamiltonian can be written as

$$H = -J\left(\hat{a}_L^\dagger \hat{a}_R + \hat{a}_R^\dagger \hat{a}_L\right) - \frac{1}{2}\Delta(\hat{n}_L - \hat{n}_R) + \frac{1}{2}U(\hat{n}_L(\hat{n}_L - 1) + \hat{n}_R(\hat{n}_R - 1)) \qquad (6.4)$$

which is the usual Bose-Hubbard hamiltonian (equation 2.19) adapted for the special case of two sites L and R coupled by one junction with the tunneling matrix element J. The interaction energy between two atoms is again denoted by U and the external potential term is expressed in terms of the energy bias Δ. This denotes the

offset from the lowest energy state of the left site L to the right site R. It is alternatively called "tilt", as it is analogous to an external potential energy gradient such as the one arising from tilting the overall trap geometry with respect to gravitation.

The operators $\hat{a}_i^\dagger$, $\hat{a}_i$ and $\hat{n}_i$ denote the usual creation, annihilation and number operators applied to site i. Equation 6.4 therefore describes a two-well system with arbitrary occupation on each side of the barrier. Since in the following we will be only interested in the cases involving one or two atoms in total, it can be easily written explicitly in matrix form.

6.5.1 Single particle hamiltonian

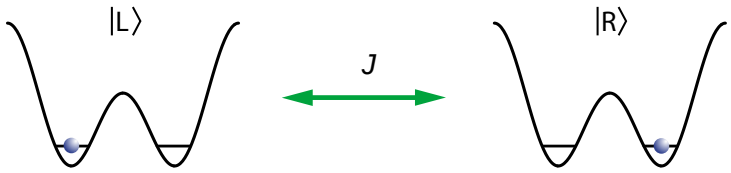

Figure 6.9: A single atom in a symmetric double well corresponds to a symmetric two-level system. When initially prepared on either side, an atom will undergo a resonant tunneling oscillation between the two wells.

Let us first consider the single-atom case. Using the lowest energy states $|L\rangle$ and $|R\rangle$ localized on each side of the well as eigenstates, the hamiltonian can be written in matrix form:

$$H_1 = \begin{pmatrix} -\frac{1}{2}\Delta & -J \\ -J & \frac{1}{2}\Delta \end{pmatrix} \tag{6.5}$$

This hamiltonian can be easily solved for $\Delta = 0$ and has the eigenstates

$$\begin{aligned} |+\rangle &= \frac{1}{\sqrt{2}}(|R\rangle + |L\rangle) \\ |-\rangle &= \frac{1}{\sqrt{2}}(|R\rangle - |L\rangle) \end{aligned} \tag{6.6}$$

with the corresponding eigenvalues $E_+ = -J$ and $E_- = J$.

Preparing the atom on the left site corresponds to preparing the state $|L\rangle = \frac{1}{\sqrt{2}}(|+\rangle - |-\rangle)$, with a subsequent time evolution of

$$|\Psi(t)\rangle = \frac{1}{\sqrt{2}}\left(|+\rangle - e^{i(E_+ - E_-)/\hbar}|-\rangle\right). \tag{6.7}$$

The resulting expectation values for the occupation of the left and the right side are

$$\begin{aligned}\langle\hat{n}_L(t)\rangle &= \langle\Psi(t)|\hat{n}_L|\Psi(t)\rangle = \cos^2(Jt/\hbar) = \frac{1}{2} + \frac{1}{2}\cos(2Jt/\hbar) \\ \langle\hat{n}_R(t)\rangle &= \langle\Psi(t)|\hat{n}_R|\Psi(t)\rangle = \sin^2(Jt/\hbar) = \frac{1}{2} - \frac{1}{2}\cos(2Jt/\hbar).\end{aligned} \tag{6.8}$$

This describes the tunnel coupling-induced coherent oscillation of the initially localized atom between the left and the right well with a frequency of $2J/h$ shown in figure 6.9. By comparing equations 6.7 and 6.3 we can therefore conclude that the tunnel coupling between the ground states of the two wells is given by $J = \frac{1}{2}G_1$, where G_1 is the band gap of the lowest band pair.

6.5.2 Two particle hamiltonian

In the general case, the system with two particles is obtained by squaring the Hilbert space for a single particle, resulting in four states $|LL\rangle$, $|LR\rangle$, $|RL\rangle$ and $|RR\rangle$. However, for indistinguishable bosons, all states have to be symmetrized. Symmetrizing $|LR\rangle$ and $|RL\rangle$ yields the state $|SS\rangle = \frac{1}{\sqrt{2}}(|LR\rangle + |RL\rangle)$ and its orthogonal $|AA\rangle = \frac{1}{\sqrt{2}}(|LR\rangle - |RL\rangle)$. Since $|AA\rangle$ is antisymmetric, it can not exist for indistinguishable bosons and we are left with three states. Writing the hamiltonian in matrix form for these three states $|LL\rangle$, $|SS\rangle$ and $|RR\rangle$ yields:

$$H_2 = \begin{pmatrix} U-\Delta & -\sqrt{2}J & 0 \\ -\sqrt{2}J & 0 & -\sqrt{2}J \\ 0 & -\sqrt{2}J & U+\Delta \end{pmatrix} \tag{6.9}$$

Solving the matrix yields the three eigenvalues

$$\begin{aligned}E_1 &= U \\ E_2 &= \frac{1}{2}U(1 - \sqrt{1 + 16J^2/U^2}) \\ E_3 &= \frac{1}{2}U(1 + \sqrt{1 + 16J^2/U^2})\end{aligned} \tag{6.10}$$

corresponding to the (not normalized) eigenvectors

$$\begin{aligned}|1\rangle &= (1, 0, -1) \\ |2\rangle &= (\frac{\sqrt{2}J}{E_3}, 1, \frac{\sqrt{2}J}{E_3}) \\ |3\rangle &= (\frac{\sqrt{2}J}{E_2}, 1, \frac{\sqrt{2}J}{E_2}).\end{aligned} \tag{6.11}$$

In the strongly interacting limit $J \ll U$, the eigensystem splits into two subsystems. Two of the states, $|1\rangle$ and $|3\rangle$ have eigenenergies $E_1 = U$ and

$$E_3 \xrightarrow{J/U \to 0} U + 4\frac{J^2}{U},$$

converging to U for $J/U \ll 1$.

The two eigenstates in this limit converge to

$$\begin{aligned} |1\rangle \quad &\equiv \quad |--\rangle = \frac{1}{\sqrt{2}}(|LL\rangle - |RR\rangle) \\ |3\rangle \quad &\xrightarrow{J/U \to 0} \quad |++\rangle = \frac{1}{\sqrt{2}}(|LL\rangle + |RR\rangle) \end{aligned} \tag{6.12}$$

for which the probability to find an unpaired atom in a well is always 0 in the limit of $J = 0$. The eigenenergy E_2, however, converges to 0 as

$$E_2 \xrightarrow{J/U \to 0} -4\frac{J^2}{U}.$$

The corresponding eigenstate $|2\rangle$ converges to the state $|SS\rangle$ in this regime. In this state, one atom is localized on each side of the barrier.

Since $|S\rangle$ has a coupling strength J to all other states in the hamiltonian H_2 (eqn. 6.9), it is intuitively clear that coupling between these two subspaces will be suppressed as J becomes much smaller than the energy gap U between the two. This means that the first order tunneling process of a single atom out of a pair as illustrated in figure 6.10 does not occur. Therefore, an atom pair will never separate, and the system will always stay in the subspace of states with paired atoms. The suppression of the separation of these "repulsively bound pairs" can be detected by probing the pair fraction, as well as their specific single-particle momentum distribution in that situation [167].

Within this subspace of atom pairs the structure of the two eigenstate limits $|++\rangle$ and $|--\rangle$ as defined in eqn 6.12 is the same as the structure of the two single-particle eigenstates and $|+\rangle$ and $|-\rangle$ (eqn. 6.6). In this limit, the two atoms will thus behave like one particle and tunnel as a pair between the two wells. The tunnel frequency is therefore given by $\omega = \Delta E/\hbar$, with ΔE the energy difference between the two respective eigenvalues, in the same ways as for single atoms. For the two states $|++\rangle$ and $|--\rangle$ this energy difference is $4 \cdot J^2/U$. In the limit of small J/U, therefore, the atom pairs tunnel like one particle with an effective coupling strength of $J_{(2)} = 2J^2/U$. This pair tunnel process is a second order process from $|LL\rangle$ to $|RR\rangle$ via a virtual (detuned) intermediate level $|SS\rangle$ as shown in figure 6.10.

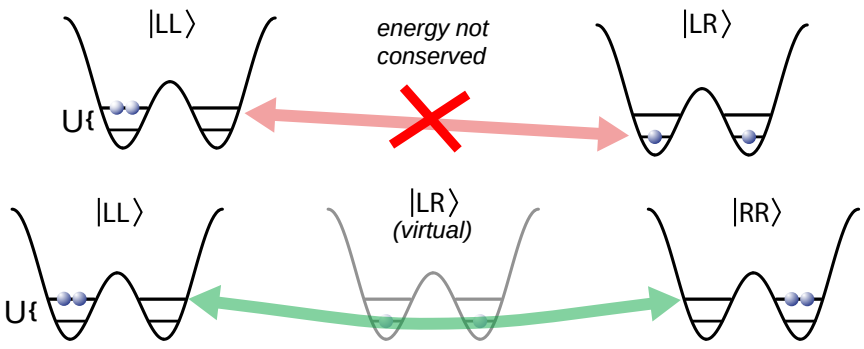

Figure 6.10: In the strongly interacting regime ($J \ll U$), two atoms localized in the left well can not separate. The first-order tunnel process with coupling strength J is energy detuned by the interaction energy U, and is therefore suppressed. The only other resonant level is $|RR\rangle$, with both atoms localized on the right side. It can only be reached in a second-order tunnel process via virtual occupation of $|LR\rangle$. This combined process has an effective tunnel coupling $2J^2/U$

6.6 Experimental sequence

For the observation of pair tunneling, the desired initial state of the atom ensemble in the lattice is such that each double well is occupied by two atoms, which are both fully localized on the same side of the barrier. This state is prepared using a very high barrier, such that the tunneling process can later be initiated by lowering the barrier in a controlled way. After an evolution period with constant parameters ("hold time"), the final state is read out. The experiment is repeated with different hold time times in order to record the dynamical evolution.

6.6.1 Lattice loading

The lattice potential is filled with atoms in a way which is very similar to the sequence used for the creation of a Mott insulator described in the previous chapters: After preparation of a BEC with the desired number of atoms (typically $8 \cdot 10^4$), the lattice potential is slowly ramped up to load the BEC into the optical lattice. For the experiment described in this section, the four standing waves which create the superlattice are ramped up simultaneously with an s-shaped ramp of 160 ms length. In the final configuration of this ramp the 765 nm lattice potential is 10 E_R deep, whereas the other three standing waves are set to a depth of 40 E_R(where $E_R$is the recoil energy corresponding to the respective wavelength). This suppresses tunneling in the two transverse directions and between the double-wells, but not between the two sites of each individual double-well.

The ground state ($T = 0$) configuration for an atom cloud in this potential com-

bined with the harmonic trap would consist of an inner core of doubly occupied double-wells surrounded by a shell of double-well potentials occupied by only one atom each. However, due to the cloud geometry and the smaller energy gaps during the ramp as compared to the "simple" 3D lattice used for Mott insulator experiments, we do not expect to reach such a shell structure. Nonetheless, the potential does still favor the $n = 2$ occupation of the double well over $n = 1$. Typically more than 60% of all atoms are in doubly occupied DW sites and less than 40% occupy their double well alone. The doubly occupied state is depicted as the initial state in figure 6.11.

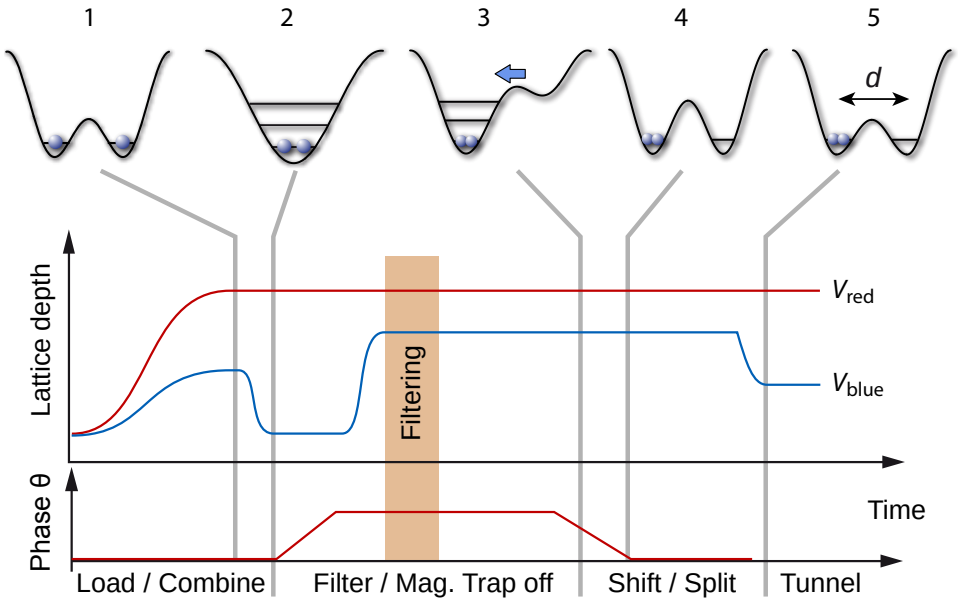

Figure 6.11: Sequence for the preparation of atom pairs on the left side of the double well potential. The graphs show the evolution of the red and blue lattice depths as well as the red lattice phase during the preparation. After the ramp-up into the initial configuration, the most probable state is the one with a single atom in each well (1). By adiabatically ramping the barrier height to zero, both atoms are brought together in a single site (2). The superlattice phase is shifted by π and the barrier is ramped up in the antisymmetric configuration. This puts both atoms into one common minimum of the blue lattice, which is then shifted to the left relative to the red lattice (3). After this shift, the potential is again a symmetric superlattice configuration with both atoms localized in the left well (4). By reducing the barrier height, the tunneling process is initiated (5). To achieve an ensemble without atom pairs, a filtering sequence can be inserted (see text).

6.6.2 Filtering

It is possible to significantly reduce the fraction of singly occupied sites further by using ramps which are better optimized toward achieving $n = 2$ occupation of double wells. Creating atom pairs out of a Mott insulator with constant $n = 1$ by combining two neighboring but initially completely independent lattice sites in a similar way as the "constructed pair" technique discussed in [179], for example, yields an improved pair fraction. However, this does still not reduce the single-particle fraction far enough that its contribution to the measured signal can be neglected. Therefore, a filtering approach was taken in order to separate the contributions from the singly- and doubly-occupied fractions. In the approach taken, first the total signal containing both components is taken for a given data point. The experiment is then repeated with a "filtering sequence" inserted after the initial loading. This sequence is designed to remove both atoms of each atom pair from the trap. This measurement then yields the single atom signal, and by subtracting it from the total signal, the contribution from the doubly occupied sites can be deduced.

The filtering sequence is applied after the two wells of each double well site are merged into a single site by ramping the barrier laser to zero, combining the pair in one well (state (2) in figure 6.11). The superlattice phase is then turned by 180 degrees to align the minima of the red and the blue potential. Subsequently the blue lattice is ramped up to a high power of $\approx 40\ E_{\mathrm{R}}$to achieve a strong confinement of the pair and therefore a high rate of collisions. A 10 ms microwave adiabatic rapid passage then transfers the atoms from the $|\, F = 1,\, m_F = -1 \,\rangle$ state to $|\, F = 2,\, m_F = 0 \,\rangle$. In this state, spin relaxation collisions are strongly enhanced[114, 117, 183]. These collisions release an energy of $h \cdot 6.8\,\mathrm{GHz}$ per pair, which removes both atoms very efficiently from the trap. After a 40 ms hold time in this state, a second adiabatic rapid passage transfers the remaining atoms back to the original hyperfine state.

When the filtering sequence is not activated, the lattice potential manipulations are still being applied, but the microwave pulse driving the state transfer to $F = 2$ is not activated. At the end of this sequence therefore both atom pairs and single atoms are tightly confined by the 765 nm lattice in the single well configuration.

6.6.3 Initial state preparation: patterned loading

To achieve the desired double-well setup, the 1530 nm standing wave is shifted back to the right by 180 degrees without reducing either of the potentials before the shift. Since the confinement of the short standing wave is much stronger than that of the 1530 nm potential, the barrier moves the atoms to the left relative to the long wavelength potential (depicted in inset 3 of figure 6.11). The result is a double-well potential with high barrier and with all atoms within the double well loaded in the left node of the 765 nm standing wave (inset 4). Now the tunneling dynamics can be initiated by rapidly reducing the height of the central barrier (inset 5 of figure 6.11), which is

achieved by reducing the blue lattice potential in a 200 μs exponential ramp.

6.6.4 Final state readout

After an arbitrary evolution time, the resulting state in the double well has to be analyzed. Considering as one example the case of a single atom, the complete quantum state is characterized by the occupation probability of either site (since this defines the occupation probability of the other site) and the phase relation between the wave functions on the left and on the right site:

$$|\Psi(t)\rangle = \sqrt{n_L}|L\rangle + e^{i\varphi}\sqrt{1-n_L}|R\rangle$$

Since they are conjugate variables, they cannot be measured at the same time (although in principle it would be possible to measure the phase in one part of the lattice and the occupation numbers in another), therefore two separate methods are employed.

Phase and visibility measurement

In order to measure the phase relation between the left an the right mode, the atoms from both sides of the barrier have to be brought to interference. This fortunately is very easy and can be achieved by simply releasing the atoms from the trap. The wave functions, which are strongly localized initially in their respective well, will expand quickly and overlap. This is the matter wave analog to the well known double-slit experiment for light, with the slit separation corresponding to the distance d of the two potential well minima. After expansion, the resulting density distribution is a double-slit interference pattern with a gaussian envelope as shown in figure 6.12. Since there is no fixed phase relation between separate double wells, the only interference is between the atoms from the two sites of each individual double well, and the density distribution is modulated with a sinusoidal pattern. The shape and size of the envelope is given by the expansion of the wave function from a single site in the same way as discussed in section 3.2.1. For the double well potential, the single-site Wannier function is again close to a gaussian, especially in the strong barrier limit.

The images of the double slit pattern are integrated perpendicularly to the double well axis. The resulting profile is then fitted with the function

$$DS(x) = A \cdot (1 + V \cdot \cos(k \cdot x + \theta))\, e^{-(x^2 - x_0^2)/W^2}. \tag{6.13}$$

The amplitude A, the center x_0 and the width W define the gaussian envelope, whereas the periodicity k, the visibility V and the phase θ characterize the interference pattern.

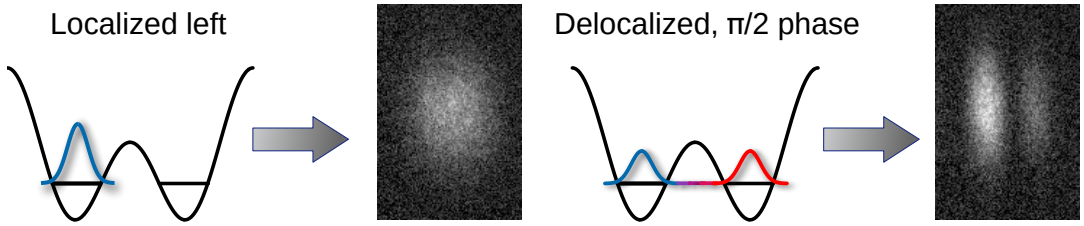

Figure 6.12: Observation of the double slit interference pattern of the cloud after release from the double well trap and ballistic expansion yields the phase relation between the two wells. As the two wave functions emanating from the two wells overlap, an interference pattern arises if there is a defined phase between the wells. The visibility of the pattern yields the degree of localization of the atoms, the phase of the pattern yields the phase difference between the wave functions in the two wells.

Atom Position Measurement

The other accessible observable is the occupation of the left and right wells, respectively. Since in the experiment always a large ensemble is measured, this is expressed in terms of the expectation values as the overall imbalance $x = (\langle \hat{n}_R \rangle - \langle \hat{n}_L \rangle)/(\langle \hat{n}_R \rangle + \langle \hat{n}_L \rangle)$ of the ensemble.

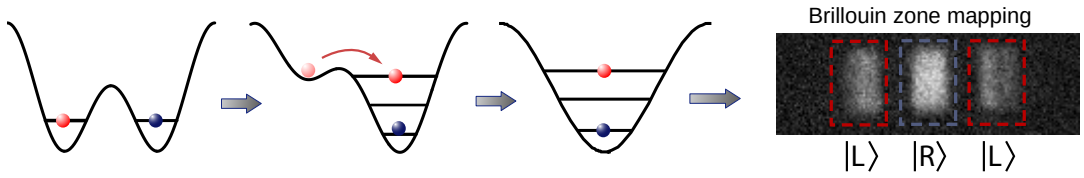

Figure 6.13: Measurement of the occupation of the left and the right well. By dynamically tilting to the right with strong tunnel coupling, the population in the lowest vibrational level of the left well is transferred to an excited level on the right. After removing the blue potential completely, the populations of the left and right well have been mapped to two different bands in the remaining lattice. Using Brillouin zone mapping and time of flight expansion, they can be separated and then counted independently.

In order to measure the average occupation on either side of the barrier, a band mapping method is employed which was named "dumping" in ref [179]. It is illustrated in figure 6.13, and is applied after all tunneling dynamics is frozen out by raising the barrier to $V_{blue} > 40\,E_R$ in $200\,\mu$s. After this, the double well is strongly biased, and tunneling is enabled again by ramping down the barrier laser in to 0

in 400 μs. During this ramp, the bias results in crossings of the lowest vibrational state in the left well with the excited vibrational states on the right side of the barrier. Since those levels are coupled by tunneling, this results in an adiabatic rapid passage which transfers all atoms from the left side to the excited states of the right well. After the barrier laser has been ramped down completely, the remaining potential is the sinusoidal fundamental lattice. A subsequent band mapping ramp (exponentially reducing the power of the long lattice to 0 in 1 ms) maps the different excited levels (or bands) into separate Brillouin zones of the free space momenta [102, 103]. After a time of flight expansion, these Brillouin zones are well separated. This allows for a separate determination of N_R, the number of atoms in the lowest band, which were originally on the right, and the number of atoms in the excited bands N_L, which originated from the left side of their respective double wells (see fig. 6.13). From these, the population imbalance

$$x = \frac{N_R - N_L}{N_R + N_L} \tag{6.14}$$

is computed. On the scale of a single double well, this quantity can be viewed as the center of mass position of the atoms with respect to the center of the double well potential, given in units of half the double well separation d. Here, $x = -1$ and $x = +1$ denote that all atoms are localized in the left well and the right well, respectively, whereas for $x = 0$ both sides have the same average occupation.

Efficiency and calibration of position measurement

In addition to the two bands used by the dumping technique, a small but visible population of atoms in other bands is observed. Especially in the cases where the occupation is larger than one and all atoms are on the side which is dumped to the higher-lying band, some atoms are detected in different excited bands than the one that was addressed, or in bands which are excited perpendicularly to the double well axis. We also expect other effects such as collisions during the TOF expansion period to limit the overall efficiency of the dumping process. We observe a 80% to 90% fraction when preparing all atoms on the left or on the right side and directly applying the dumping sequence without a tunnel coupling period.

By direct band-mapping without dumping we verify that no excited bands are populated during the state preparation sequence. It is therefore concluded that the dominating effect of the deviations from 100% occupation which we measure originates from the dumping and band mapping procedure itself rather than the state preparation method which seems to be robust. We therefore use a calibration method in order to take this into account.

For this, one dumping sequence is measured for each of the four possible combinations of preparation methods: Atoms on the left vs. atoms prepared in the right well, and filtering sequence activated vs. filtering sequence not activated.

The atoms in each of the bands are then counted with fairly tight counting regions, which means that some atoms close to the boundary of their Brillouin zone are discarded. In turn, this excludes most of the atoms in bands populated from collisions. Normalizing each count by the total atom number N_T yields four pairs $\{\bar{N}_L, \bar{N}_R\}$, where each number is between 0 and 1. The two pairs with the filtering sequence activated together form the matrix

$$T_S = \begin{pmatrix} \bar{N}_L^L & \bar{N}_R^L \\ \bar{N}_L^R & \bar{N}_R^R \end{pmatrix}$$

which gives the linear transformation which connects the occupation numbers $\{N \cdot \langle n_L \rangle, N \cdot \langle n_R \rangle\}$ inside the trap to the measured quantities N_L and N_R. In the ideal case for perfect dumping and mapping, this would be an identity matrix. By inverting the actual matrix and applying the inverse to the measurement results, the in-trap occupation numbers are reconstructed.

This procedure is applied to the single-atom signal and the total atom signal individually. While it is not a rigid calibration scheme in the case of strong corrections, it is nonetheless very accurate as long as the efficiencies of the raw measurements are not far lower than 100%.

6.6.5 Time evolution in weakly interacting regime

The time evolution of the double well system in a weakly interacting case is shown in figure 6.14. Here, the measurements are shown as dots, whereas the lines are fits to the theory as described in section 6.7 and 6.8. The measurements start at the end of the 200 μs barrier reduction ramp. As tunneling starts already during this ramp, there is an effective time offset of $\approx 70\ \mu s$, which is determined by a fit.

For single atoms, the position measurements show a clear sinusoidal tunneling motion between the two wells. After a tunneling time of $\approx$ 75 μs the atom is fully delocalized between the two wells, which is shown by a maximum of the interference fringe visibility. The phase (black dots) is alternating between the values $\pm\pi/2$, abruptly reversing its sign whenever the direction of the tunneling process reverses.

The population imbalance signal for two atoms initially in the left well is shown as red dots in the second panel. Here, both first order and second order tunneling is possible and the resulting "beat" signal in the position measurement has several frequency components. In this configuration, the two processes are of similar strength and can not be distinguished.

6.6.6 Time evolution in the strongly interacting regime

When the system is brought into the strongly interacting regime by increasing the barrier height and reducing the tunnel coupling such that $J \ll U$, the behavior is markedly changed compared to the weakly interacting case. In this regime, the first

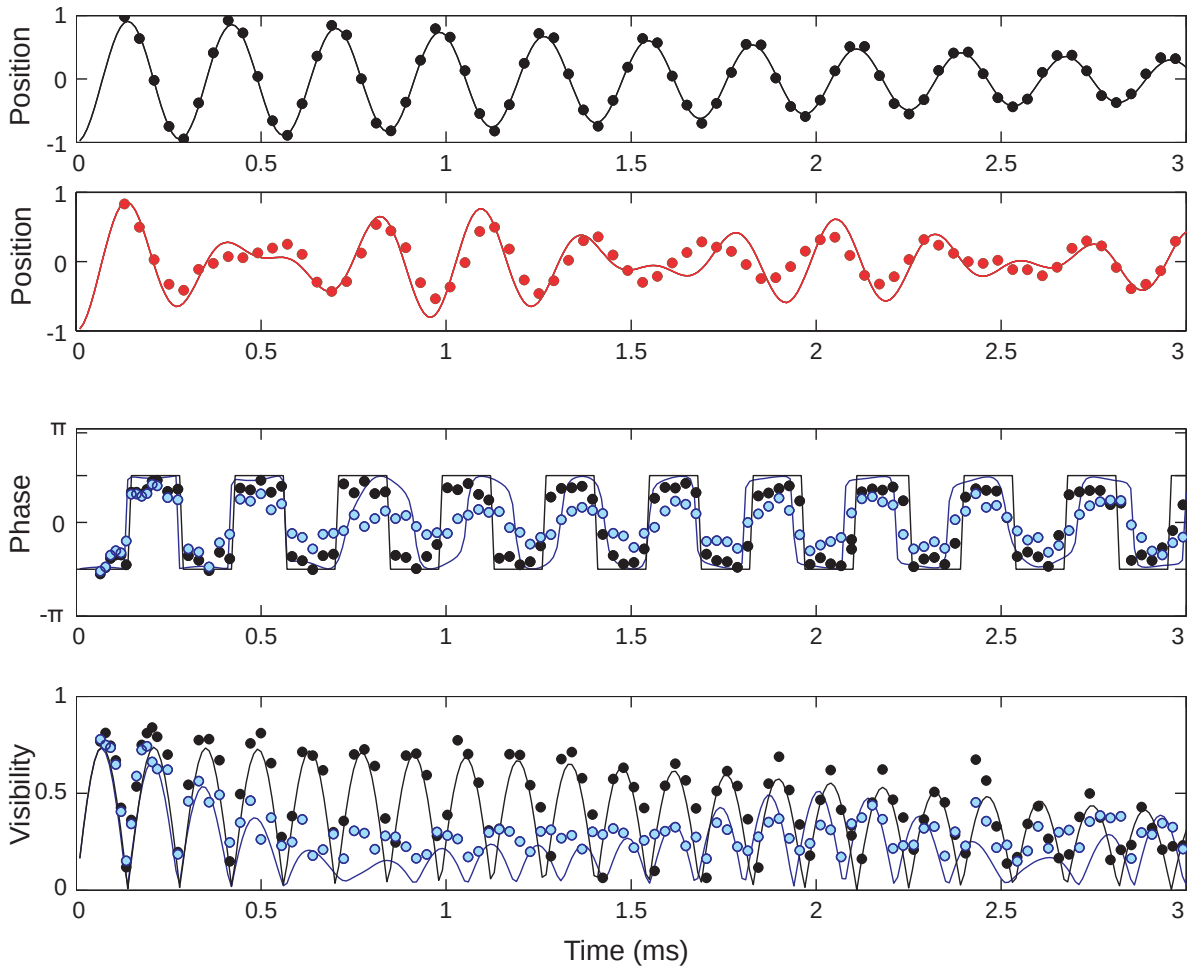

Figure 6.14: Signature for tunneling of single atoms and atom pairs in the weakly interacting regime (J/U=1.5). The black dots denote the single atom position, phase and visibility data. The red dots show the position signal from doubly occupied potentials, blue hollow dots the coherence information (phase / visibility) for the total population. Particles are initially localized on the left (position -1). Individual atoms coherently oscillate between the left and the right well. The relative phase between the two sites is constant during the tunneling process, but jumps between the two possible values $\pm\pi/2$ whenever the particle reverses direction. The single particle signal shows a single tunneling component whereas for two atoms several frequency components are present in the dynamical evolution. The solid lines are fits to the datasets as described in section 6.8.

and second-order tunnel processes are very different and can be distinguished. Figure 6.15 shows data taken for a ratio of $J/U \approx 0.2$.

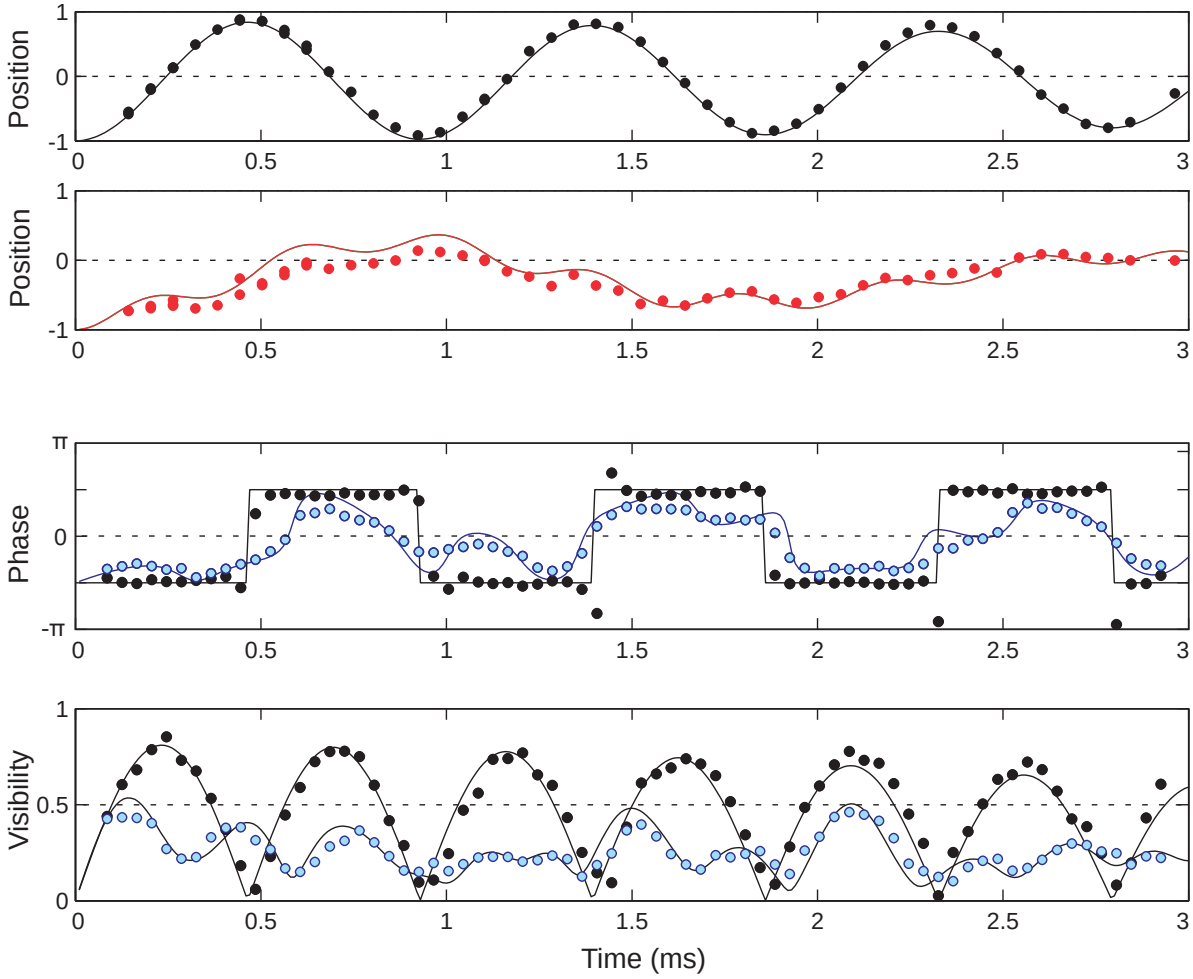

Figure 6.15: Pair tunneling in the strongly correlated regime using the same symbols and fit functions as fig. 6.14. Here, first-order tunneling is suppressed and shifted to a detuned frequency of $U/h \approx 2.5\,\mathrm{kHz}$. The dominant dynamical process is now second-order or pair tunneling. It is visible as the dominant slow oscillation in the second panel with frequency $4J^2/hU \approx 550\,Hz$.

The single atom signal still shows a perfect sinusoidal signal, since the atom-atom interaction does not have an effect. The only difference is the slower oscillation frequency due to the reduction of the tunnel coupling parameter J. For atom pairs, however, the first-order process is now strongly detuned, resulting in a strong suppression and an increase in frequency. In contrast, the second-order process is still resonant: Therefore, the average position signal for pairs (red dots in figure 6.15) now

shows two distinct components: The dominating process is a slow oscillation with a period of 1.8 ms due to the still resonant second-order tunneling. A fast oscillation with a small amplitude and a period of 400 μs shows the residual first-order process.

Despite the second-order process being in resonance for $\Delta = 0$, in our experimental setup the average oscillation amplitude does not reach 1, since $\Delta \approx 0$ is only realized in the center of the trap, even in configurations with an average Δ of 0. This will be explained in more detail in the following section. The visibility signal for the pairs is strongly reduced as well, since the TOF double slit pattern measures the average *single particle* phase. A delocalized pair ($|LL\rangle + |RR\rangle$) itself however does not contribute to this observable, as it would only show a double slit interference pattern if the distribution of center of mass positions of each pair could be probed after expansion. The only sources of single-particle interference in the two-particle case are therefore from superpositions of the states $|LL\rangle$ and $|LR\rangle$ as well as from superpositions of $|LR\rangle$ and $|RR\rangle$. Since for small J/U the population of the state $|LR\rangle$ is suppressed, the interference visibility of the pair fraction is reduced and the total visibility shown as blue hollow dots is caused to a large degree by the single-particle sites.

6.7 Modeling of overall system

The time evolution for single atoms and atom pairs in one single double well can be easily computed using the hamiltonians 6.5 and 6.9 and their respective solutions described in section 6.5. The actual measurement, however, is done with a large ensemble of on the order of 10^5 individual double well potentials. Even with all of those initialized in the same way and the tunneling being initiated at the same time, their time evolutions are not completely identical. First of all, some atoms are in double wells with occupancy of $n = 2$ (typically 60%) while others are in singly occupied sites, as outlined in section 6.6.1. Furthermore, the overall system is not completely homogeneous, especially due to the confining potential and the gaussian intensity profile of the lattice laser beams. Therefore, the parameters which govern the dynamical behavior are not the same for each double well. In the following, we will discuss the main deviations and how they are taken into account in order to calculate the observed averaged dynamical evolution of the overall ensemble.

The interaction energy U depends on the confinement of the atoms at their respective site of the double well. As such, it is reduced when the lattice laser intensities are reduced. Due to the gaussian shape of the lattice beams, this reduces the interaction energy for double wells far away from the center of the trap. For deep lattices, however, U depends only weakly on each of the standing wave intensities. For a typical cloud radius of 30 μm and typical beam waists of 130 μm, the change of U on the edge of the cloud as compared to the trap center is in the percent range. Compared to the other inhomogeneities this has only weak consequences for the shape of the observed signal and is therefore neglected.

A more significant effect is the inhomogeneity of the tunneling parameter J, which can have a larger relative change over the cloud as it typically depends exponentially on the depth of the barrier, and also strongly on the long lattice potential. This effect leads to a dephasing of the tunneling for sites situated at different distances perpendicularly to the double well axis, where both the long lattice and the short lattice fall off due to their gaussian envelope. A reduction of the barrier lattice depth obviously leads to an increased tunnel coupling between the wells. A reduction of the long lattice strength, however, reduces the confinement within the overall double well along the superlattice direction. Because of this, the two potential minima and therefore the atoms move further apart, leading to a decrease in the tunneling rate. For the parameters used in the experiment, this effect significantly reduces the impact of the blue lattice depth reduction. As a result, there is only in a weak increase of the tunnel coupling for sites far away from the center of the superlattice beams. The effect of the inhomogeneity of J on the overall signal was determined by a calculation which also includes the inhomogeneity of Δ which will be discussed next. The J-inhomogeneity leads to a slow dephasing of the individual sites and therefore a dampening of the total signal. Compared to the dephasing from the inhomogeneous Δ it is only significant for certain parameters in the weak barrier limit.

The atom ensemble is confined by the magnetic trap as well as the global confinement produced by the gaussian shapes of the lattice laser beams. Approximated as a parabolic potential close to the center of the trap, it has a total trap frequency of $\omega_{trap} \approx 2\pi \cdot 80\,\mathrm{Hz}$. Therefore, there is a potential gradient present for all atoms which are located away from the trap center along the double well axis, as illustrated in figure 6.16. Adding this gradient to the double well potential results in an effective

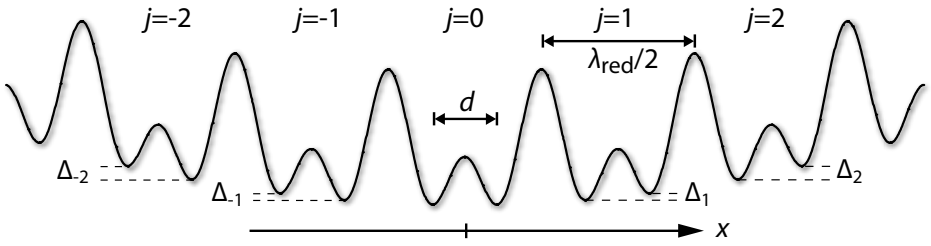

Figure 6.16: Detuning of double wells which are not in the center of the trap. The harmonic confinement along the x-axis leads to a local bias Δ_j at site j, which increases with the distance from the trap center.

bias $\Delta \neq 0$ for these sites. This bias is the same for all sites within one x-y-plane of the lattice which is perpendicular to the double well axis. With the two sites of the jth double well located at the positions $x_{j,L}$ and $x_{j,R}$ separated by the distance d, the

energy difference Δ_j between them can be calculated as

$$\begin{aligned}\Delta_j &= \frac{1}{2}m\omega_{trap}^2\left(x_{j,R}^2 - x_{j,L}^2\right)\\ &= \frac{1}{2}m\omega_{trap}^2\left((j\cdot\lambda_{red}/2 + d/2)^2 - (j\cdot\lambda_{red}/2 - d/2)^2\right)\\ &= \frac{1}{2}m\omega_{trap}^2\left(j\cdot\lambda_{red}/2\cdot d\right).\end{aligned} \tag{6.15}$$

For typical values such as $j = 25$ and $d = 765\,\mathrm{nm}/2$, Δ_j can be up to $h\cdot 400\,\mathrm{Hz}$ at the edge of the cloud. This is a very significant effect especially in the strongly correlated limit where the tunnel coupling J is low and the second-order tunnel rate even lower. It therefore has to be included in order to predict the overall signal of the ensemble.

In addition to the parameter inhomogeneities discussed, the aforementioned separation of the atom population into the two sub-ensembles occupying sites with $n = 2$ or $n = 1$ has to be taken into account. Therefore, for the modeling, a three-dimensional distribution of atoms in the trap is assumed, which consists of an inner core of double wells with occupation $n = 2$ and a radius R_2 along the x-axis surrounded by an outer shell of singly occupied double wells and outer radius R_1 along x. This corresponds to assuming $T = 0$ after the initial ramp up of the lattice. Such an assumption is not very realistic for our chosen ramp speeds and lattice parameters, but it is observed that the result does not depend strongly on details of the density distribution such as sharp shell boundaries. Assuming a thermal Bose gas with a temperature $T \approx U$ yields very similar results.

From this, the number of singly and doubly occupied double wells is determined separately for each layer of the lattice along the superlattice direction. Furthermore, the local Δ within the layer is calculated. The time evolution for each of these two ensembles and for each of the layers is calculated independently. The measurement results of all layers are then averaged in order to yield the overall expectation values for the single atom signal, the atom pair signal, and the total signal which includes both.

The time evolution for each layer is calculated using the solutions of the Hamiltonians eq. 6.5 and eq. 6.9 with the bias parameter Δ set according to the position of the layer. Additionally, it is necessary to use a modified tunnel coupling J' for the two atom case which differs from the bare J by up to 10%. This difference results from higher-order couplings which are neglected in the simple Bose Hubbard model, but can be approximated by number-state dependent corrections to the tunneling and interaction strength. These effects will be discussed in more detail in section 6.9.

6.8 Fitting the model to the data

While in principle all parameters of the system are known or can be determined by independent reference measurements, it turns out that the observation of the tunnel-

ing dynamics allows for a more precise derivation of most of the system parameters than the calibration measurements. For example, the particular measurement used for calibrating the lattice depth[1], as employed here had an absolute accuracy of about 2%. At the highest short lattice depths used, this leads to an uncertainty of 15% in the bare tunneling rate J. In contrast, J can be determined from the data to better than 5% for long measurement series.

As a consequence, it was decided to use the ensemble model as a fit function to the data. The algorithm uses both the imbalance data from a given run and the phase/visibility dataset to compute a total fit error value which is then minimized with respect to seven fit parameters:

- J, the bare tunnel matrix element
- U, the interaction energy
- J', the modified tunneling rate for atom pairs in a double well
- Δ_0, the bias energy in the center of the trap
- ω_x, the overall confinement frequency along the double well axis
- R_2, the inner shell radius
- V_{max}, the maximum two-slit interference fringe visibility
- t_0, the time offset due to the barrier ramp-down

The parameter V_{max} is necessary because the observed visibility for the phase and visibility measurement is always lower than one. Partly this is due to the fact that the visibility is fitted with a two-slit pattern which assumes a gaussian envelope. The correct Wannier function for finite tunneling has a momentum distribution which differs slightly from a gaussian, resulting in a lower measured contrast. Other factors such as the small angle mismatch between the vertical axis of the camera and the vertical lattice beam can also reduce the fringe contrast due to the integration. For the sequence presented here, we typically observe a maximum visibility which is slightly lower than 80%.

Within the described model, which assumes a harmonic confinement, a spherical shell structure and neglects inhomogeneities other than those in Δ, the description in terms of two shell radii and the harmonic confinement frequency is redundant. This is due to the fact that effectively only the ratio of the two populations enters. As long as the radii are much larger than the lattice spacing (and therefore the distribution is

[1]The lattice depth was calibrated by determining the resonance frequency for parametric excitation. For this, the lattice depth is modulated with a small amplitude at a frequency corresponding to the energy difference between the first and the third band. The 2% limit results from the particular parameters chosen for the resonance scan.

well approximated by an integral), the change to the distribution due to an increase in the trap frequency, for example, can also be obtained by increasing both shell radii by the same relative amount. It was therefore chosen to keep the outer radius R_1 of the assumed shell structure constant at a value of 30 sites, which corresponds to the expected radius for the atom number chosen. Only R_2 and ω_{trap} are then determined by the fit.

Since several dephasing processes are neglected which all lead to a faster loss of the total signal, the damping rate is always underestimated. Within the model used for fitting, the confining force acts as the only source of dephasing between the individual double-wells, and is therefore the only source of damping of the overall signal. When fitting this simplified model to the data, the fit tends to accommodate the non-included sources of damping by assuming a larger confinement than the one that is actually present in the experiment. This overestimation can be as large as 200%. The predicted damping constant of the simplified model has an especially large deviation for low barrier depths. This is expected due to the increased importance of higher bands for the Wannier functions due to the reduced band separation, adding an additional dephasing mechanism. Also, the inhomgeneity of J over the ensemble due to the gaussian beam shape has the strongest effect in this parameter regime. The effect is most pronounced for the position measurement, and we therefore include an empirically determined additional damping term into the model, for wich we find a time constant of 3.5 ms . This modification is not used for the phase and visibility datasets.

To initiate the tunneling, the barrier height is reduced as quickly as possible. It can not be switched instantaneously to the desired value, as this would be non-adiabatic with respect to the trap frequencies and induce band excitations. Experimentally a time of 200 μs was found to be slow enough to reliably avoid band excitations when ramping to the desired value with an s-shape function. A consequence of this is that the tunneling process starts even before the end of the ramp-down. Therefore, the fit function contains a time offset t_0 to account for this difference. This offset is typically $t_0 = 70\,\mu s$, which corresponds to the expected value obtained from numerically integrating the time evolution during this barrier ramp within the Bose-Hubbard hamiltonian with dynamically changing parameters. This time offset enters twice in the position measurements, as the tunneling can continue in the beginning of the ramp-up for the suppression of the tunneling at the end of the experiment. This ramp is the inverse of the one used for initiation of the tunnel process.

Although the fit algorithm can use an error function which takes both the position and the coherence signal into account, typically only the coherence data is taken, as it yields more information (phase and visibility as opposed to position only) per single run of the experiment. For the typical parameters of the experiment, the resulting datasets contain enough information to obtain all fit parameters of the model.

In figure 6.17, the main fit parameters for the data taken are shown and compared to the theoretical predictions of the standard two-site Bose-Hubbard model. The val-

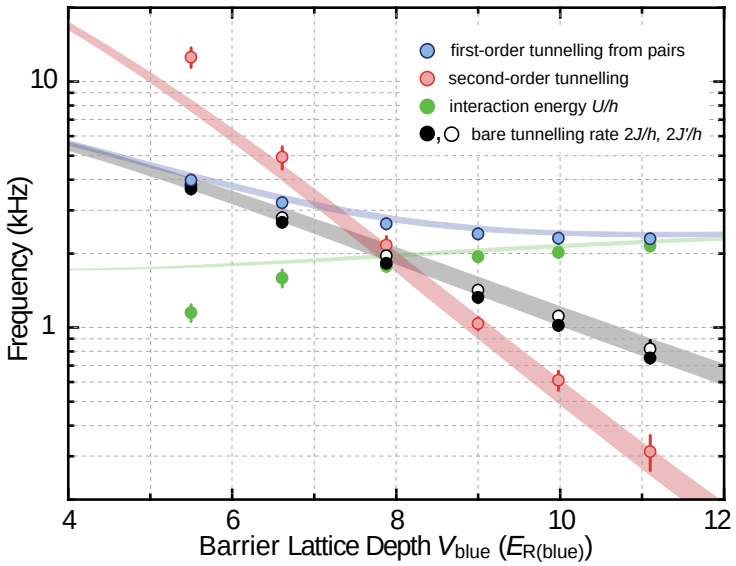

Figure 6.17: Bose-Hubbard parameters extracted from measured data by fitting the theory for the ensemble. Energies are plotted in kHz against the short lattice depth V_{blue}. The frequencies which correspond to the coupling matrix elements for single atoms, J and J' are plotted as black dots and circles and the interaction energy U as green filled circles. The second-order tunneling frequency determined from these values is shown as red dots, and the frequency of the detuned first-order process for pairs is plotted as blue dots, which approaches U (green filled circles) for $J/U \rightarrow 0$. Shaded regions denote the theoretical predictions for each of these values.

ues for J and U are determined from band structure calculation. The width of the bars denotes the systematic uncertainty due to the 2% uncertainty of the lattice depth calibration. There is an overall good agreement between the measured values and those calculated from band structure. The measured single particle tunnel coupling is typically 5% lower than the predicted one, which is slightly larger than explained by deviations due to the lattice calibration.

However, there is a bias toward measuring lower tunnel couplings due to the same simplifications in the model which were already discussed with respect to the damping processes: The only damping mechanism which the model does include originates from the detuning of the tunneling between the two wells (inhomogeneous Δ) and the resulting inhomogeneous *increase* in tunneling frequency which leads to a dephasing of the oscillations. This mechanism therefore always increases the average tunneling frequency compared to the trap center. As some of the real damping mechanisms are not necessarily associated with an average increase in frequency, the oscillations calculated by the model are incorrectly accelerated by several percent. In order to fit this oscillation frequency to the measured data, the fit procedure for the

model therefore yields a correspondingly lower tunnel matrix. This leads to a small expected negative offset in J compared to the band structure results.

6.9 Deviations from the standard Bose-Hubbard model

When fitting the model both for ensembles of singly- and doubly occupied double-wells, it is observed that the Bose-Hubbard model parameters obtained for these two cases differ slightly. For the two particle case, the tunnel coupling has to be replaced by an effective tunnel coupling J', which deviates from J by 3-10%. This deviation

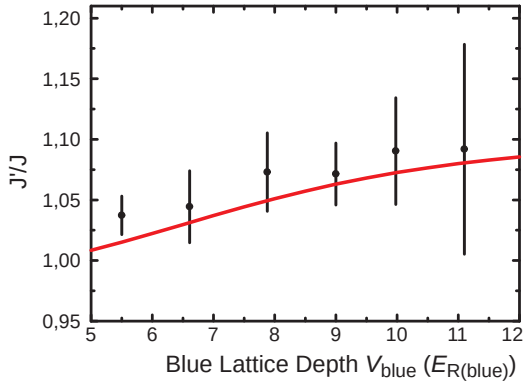

Figure 6.18: Comparison of the coupling matrix elements J and J' for single atoms and atom pairs, respectively. The data shows a significant difference between the two parameters. The red line corresponds to the prediction of an extended Bose-Hubbard model which takes some higher-order coupling terms into account.

originates from two approximations which are made in the determination of the parameters for the Bose Hubbard model. Firstly, modifications to the single particle wave functions due to the interaction with a second atom are neglected. For higher occupation numbers, these effects are stronger and interaction-induced modifications of the wave function have to be taken into account even in deep lattices [184]. The shift in interaction energy for larger site occupation numbers can also be measured spectroscopically [73]. For most experiments with low occupation numbers in 3D optical lattices, the unperturbed single-particle wave functions are a good approximation. Interactions do however create corrections to the relevant overlap integrals on the percent level [74], especially for strong orthogonal confinement at low superlattice depths. These have to be taken into account by including contributions from higher bands.

The on-site interactions effect the observed tunneling rates, as the modified wave functions also have a modified overlap with the neighboring sites, thus changing the

tunnel matrix element. An order-of-magnitude estimate was made by slightly varying the parameters which define the shape of the double well Wannier functions in order to minimize the overall energy for two interacting atoms. Due to the somewhat arbitrary parametrization of the wave functions this was not expected to give a very precise result, but the ansatz did yield an up to 5% change in the tunnel matrix element.

The second approximation is made by the Bose Hubbard hamiltonian [4] as used here (Eq. 6.4). This simplified model does not contain all possible higher-order coupling terms between the two modes. All contributions from first order operators are included – the symmetrized coupling term $\hat{a}_L^\dagger \hat{a}_R + \hat{a}_R^\dagger \hat{a}_L$ and the bias energy term $\hat{n} = \hat{a}_j^\dagger \hat{a}_j$ with (j = L,R). In contrast, only one of the possible second-order terms is considered: The on-site interaction term $\hat{n}_j(\hat{n}_j - 1)$, for j = L,R. All other terms are small compared to this one and are neglected in the standard Bose-Hubbard model. They can, however, be detected due to the possibility of directly comparing two tunneling frequencies measured with high precision in the measurements described above.

The most prominent of the neglected second-order terms is the direct nearest neighbor interaction [3]. It is sometimes included into the model, usually by assuming some direct long-range interaction mechanism such as dipole-dipole interactions. For the two well system it has the form

$$V\hat{n}_L\hat{n}_R = U_2\hat{a}_L^\dagger a_L a_R^\dagger a_R,$$

where U_2 is the nearest neighbor interaction strength. Without considering additional long-range interaction mechanisms, it is determined by the overlap of the density distributions of the two wells:

$$U_2 = \frac{4\pi\hbar^2 a_s}{m} \int w_L^*(\vec{x}) w_L(\vec{x}) w_R^*(\vec{x}) w_R(\vec{x}) d\vec{x}$$

Other neglected contributions are $\hat{a}_L^\dagger a_L a_L^\dagger a_R$, which describes a combination of tunneling and interaction ("interaction-driven tunneling") and $\hat{a}_L^\dagger a_R a_L^\dagger a_R$, the direct second-order tunneling term.

For specific initial conditions such as the ones in this experiment, these contributions can be included as an extension to the two-site Bose-Hubbard hamiltonian 6.4 in the form of corrections to the tunneling and interaction parameters U and J [185, 186]. In the limit of large barrier heights, these corrections are the dominant deviation from the unmodified two well Bose-Hubbard model. Specifically, it is the interaction-driven tunneling which provides the main contribution U_3, resulting in a correction to the pair tunneling dynamics as

$$J'_{(2)} = \frac{2(J + U_3)^2}{U}.$$

This correction can be absorbed into the tunnel coupling J, resulting in the modified coupling J' in the case of an atom pair being prepared. For the second-order tunneling process which leads to superexchange [185] of two neighboring atoms, it is the nearest neighbor wave function overlap U_2 which provides the dominant correction. It should be emphasized that the corrections are determined from the first band pair alone without any contribution from higher bands. Of course, all of these models approximate the time-dependent Schrödinger equation, which, if used directly, allows one to obtain the exact dynamics.

Figure 6.18 shows the ratio of the bare single-particle tunnel matrix element J to the effective single-particle tunnel coupling J' for the case of the double well being occupied by two atoms. The red line denotes the expected ratio for the extended Bose-Hubbard model obtained by taking the corrections due to higher-order coupling terms into account, without any contributions due to higher bands. With these modifications, the measurement is consistent with the model to within the error bars.

6.10 Conditional tunneling

The suppression of the first order tunneling for a double well with occupation $n = 2$ is due to the energy mismatch between the initial state and the final state of the process. For the symmetric configuration with both atoms initially in the left well, this mismatch is equal to the interaction energy U. However, by biasing the double well in such a way that the potential energy of atoms is reduced in the left well and increased in the right well, the mismatch can be reduced below the coupling strength J, and even completely canceled for $\Delta = U$, bringing the first order process into resonance. Figure 6.19 shows the tunneling dynamics for two different values of the bias energy Δ and otherwise identical preparation ($V_{red} = 10\,E_{R(red)}$, $V_{blue} = 12\,E_{R(blue)}$). In both cases the position signal for single atoms and atom pairs is shown. For the symmetric double-well, tunneling of single atoms is resonant, and atom pairs predominantly tunnel in second order as a pair. As described before, the first-order process is seen as a strongly suppressed oscillation. The single atom tunneling period is approximately 1.1 ms for a single atom.

If the bias energy is adjusted to coincide with the interaction energy U, however, tunneling is strongly suppressed for single atoms, since this process now is detuned by $\Delta \equiv U = 0.73\,E_{R(blue)}$. The second order tunnel process is fully suppressed, as it is detuned by $2 \cdot \Delta$. In contrast, the first order pair-breaking tunnel process is now in resonance. It can be visualized as one atom of the pair staying in the original well with the other undergoing a periodic tunneling motion. It should therefore show a center-of-mass oscillation amplitude half as large as that of the single atom resonance in the symmetric potential. At the same time, the tunneling rate is enhanced due to the bosonic statistics in the presence of the second atom, which should reduce the periodicity by a factor of $\sqrt{2}$. Indeed, this process is observed as an oscillation with

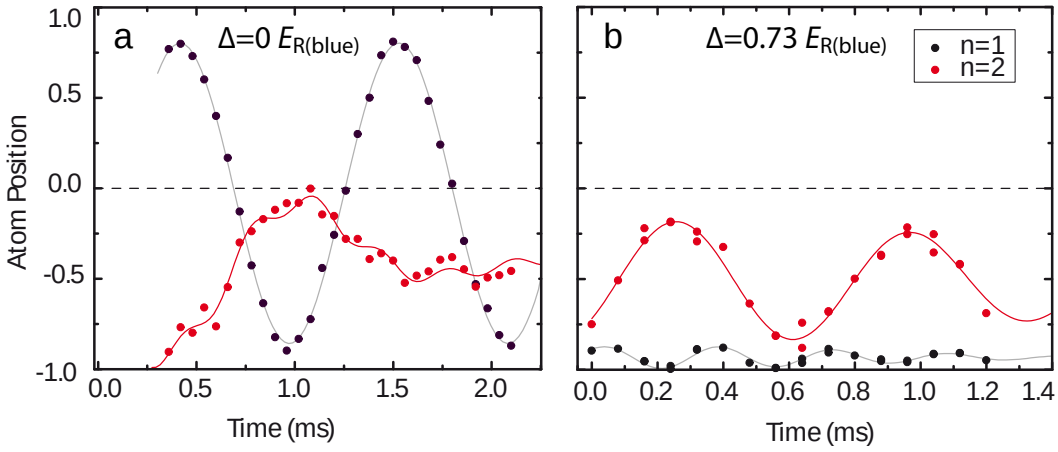

Figure 6.19: Effect of an energy bias $\Delta \neq 0$ on the tunneling of single atoms (black dots) and atom pairs (red dots). In both cases, atoms are prepared on the left side of the double well in the strongly interacting regime ($V_{red} = 10\,E_{(R(red)}$, $V_{blue} = 12\,E_{R(blue)}$). In **a**, the energy bias $\Delta = 0$, leading to resonant second order tunneling for pairs and single atoms, but suppressed first order tunneling for a single atom out of a pair. In **b**, a bias of $\Delta = U = 0.73\,E_{R(blue)}$ offsets the effect of the interaction energy, enabling resonant tunneling of a single atom from the pair, with all other tunneling processes being suppressed.

an amplitude of 0.32 and a period of 0.7 ms.

The resonances can be mapped by taking the tunneling signals for the same initial state with different bias configurations. To extract the tunnel oscillation periodicities and amplitudes, the obtained traces are fitted with a fit function consisting of two independently damped sinusoidal functions:

$$x(t) = A_0 + \sum_{j=\{1,2\}} A_j \cdot e^{-t^2/T_j^2} \cdot \cos(\omega_1(x - t_j)) \tag{6.16}$$

Figure 6.20 shows the amplitudes and the tunneling periods of the individual processes against the bias energy. The error bars shown are derived from the fit uncertainty. As the fit function only delivers the parameters for each frequency component regardless of the underlying process, they have to be assigned to the first-order and second-order type manually in the atom pair case.

The resulting curves allow the identification of a single resonance for $n = 1$ occupation, and two clearly distinct peaks for the $n = 2$ case. Here, the second-order tunneling resonance can be found for $\Delta = 0$, whereas the second frequency component shows a peak around a value of 0.78(2) $E_{R(blue)}$, corresponding to the interaction energy U for this lattice configuration. At this bias energy, the tunneling therefore depends on the presence of a second atom in the initial well. This second atom effectively switches the tunneling of the first in a very similar way as the electrons

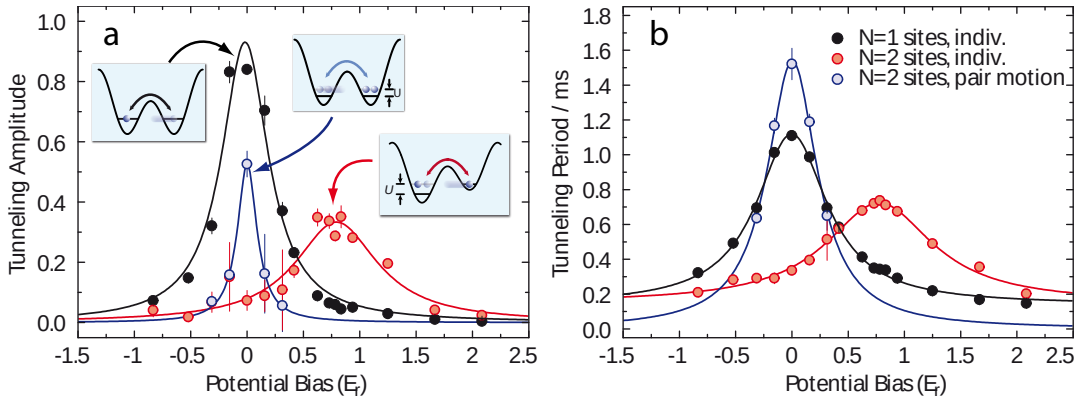

Figure 6.20: Amplitudes (a) and periods (b) of the different tunneling processes plotted against bias energy. The insets schematically show the respective tunneling processes. Black data points denote the tunneling of solitary atoms, whereas red symbols correspond to the tunneling of a single atom out of a pair. The simultaneous tunneling of the pair is shown as blue hollow circles. Tunneling of pairs and of a solitary atom is resonant for the unbiased configuration. The pair breaking tunnel process of a single atom is resonant when the bias Δ compensates the pair interaction energy U.

influence each other in single electron transistors using semiconductor quantum dots or metallic islands.

Due to the conditional behavior this process can therefore be used as a two-particle operator to create entanglement - for example if applied between two adjacent double wells. In that case, tunneling would only take place if the right site of the left double well and the left site of the right one are occupied simultaneously. Processes of this kind can therefore create entanglement along a chain of double wells, yielding entanglement between many sites simultaneously.

7 Outlook

In this thesis several new methods for manipulating and probing correlated quantum states of atoms in optical lattices were described. The motivation for these developments is to facilitate or enable novel experiments with such states. This final chapter will summarize the main results and give an outlook on some of the possible applications and extensions.

7.1 Probing the density distribution and number statistics of Mott shells

A method to determine the overall density distribution and to demonstrate the existence of the Mott insulator Shell structure was presented in chapter 4. For this, the spin state of atoms in a very localized region of space is selectively modified, and the number of atoms in that region determined. This allows for an integrated density profile with a better linear resolution than achieved so far by direct optical imaging of the atoms in the lattice potential. Using this method, it is possible to show the existence of the Mott shell structure with sharp boundaries separating the shells. As one consequence, this yields some insight into the temperature of the system in the lattice, in a regime of very low temperatures $k_B T \ll U$ where temperature measurements are notoriously difficult. As the Mott shell structure is strongly affected by thermal excitations, analyzing it allows us to give a upper bound of $k_B T_{max} \approx 0.2\,U$ for the temperature of the ensemble inside the lattice potential.

Another obvious application of the slicing technique would be the combination with a high resolution imaging system in order to generate two-dimensional images of the individual slices. In this way, it would be possible to directly determine the 3D distribution in the trap, without having to resort to reconstruction techniques. By selectively imaging specific number states, the number state distribution could thus be determined with 3D resolution. Together with the spatially varying chemical potential, a whole line of the Bose-Hubbard phase diagram could be measured at the same time in the trap.

Addressing atoms with high resolution at specific positions along one of the lattice axes has of course more applications than imaging alone. It can also be used for manipulating the quantum gas in the trap, while simultaneously providing a spin-sensitive readout with the same spatial resolution along the same axis. This method has been proposed as an addressing technique for quantum information purposes. For this, a chain of atoms or molecules is placed in a magnetic (or electric in the case

of dipolar molecules) field gradient. A large enough spacing and a strong enough gradient provided, the internal state of each atom can then be addressed individually, providing an important prerequisite for quantum computing [130, 131]. In the optical lattice, this method could be used to address atoms in 1D chains of sites to create arbitrary initial states.

Combining tunneling along the detection axis and a spin degree of freedom also creates an interesting system for studying dynamical effects in Luttinger liquids such as spin-charge separation [187–189]. For this, the equilibrium state could be locally perturbed by microwave addressing. The propagation of the the perturbation along the tunneling axis could then be observed by repeatedly measuring the density profiles in each of the spin states [190].

7.2 Noise correlation interferometry

In chapter 5, using the Hanbury Brown-Twiss effect as a probe for a strongly correlated quantum gas is demonstrated. By analyzing the correlations in the quantum noise of the expanded atom cloud, it is possible to determine the spatial correlations of the cloud inside the lattice. This is possible even though the average density distribution, without noise, does not yield any information other than on the on-site wave function on each lattice site.

By observing an artificially prepared charge density wave, it is shown that the method is able to pick up non-trivial order in the optical lattice. This capability is a crucial requirement in the current quest for the realization of quantum states with complex order in optical lattices.

Another important step for the application of the noise correlation analysis was the recent demonstration of anticorrelations for spin-polarized fermions in the lattice [143] and for a bulk gas [191]. In the lattice, the fermionic band insulator state has the same spatial structure as the bosonic Mott insulator. However, in this case the Fermi statistics leads to peaks of reduced correlations (anticorrelations) as opposed to the increased correlations of bosons.

With the recent experimental progress in cooling fermions far below the degeneracy temperature and loading them into lattice potentials [37, 38], the demonstration of antiferromagnetic ordering of fermionic atoms in a lattice also seems within reach. This state would not have any signature in the momentum distribution of the atoms, but could be identified by quantum noise interferometry due to the doubling of the lattice unit cell.

Ground states with the same Néel-type order could also be created with bosons through non-local interactions such as those in the recently demonstrated dipolar quantum gases [147, 192–196] or by using specially tailored spin-exchange interactions in spin-dependent lattices [197] or superlattices [198].

7.3 Optical superlattices

In chapter 6 the creation of a lattice of double well potentials was demonstrated. In this array of double wells, it is possible to observe tunneling of single atoms and to show the crossover from independent tunneling to correlated tunneling of interacting atom pairs. In the strongly correlated regime, atom pairs can not be broken up by single atom tunneling events, even though the interaction is repulsive, and it was shown that the pair then tunnels as a whole in a second order process. Furthermore, it was demonstrated that first-order tunneling of one atom of a pair can be resonantly controlled in an "atom transitor"–type setup.

These experiments show the capabilities of the double well lattice potential, which is the starting point for a whole range of possible experiments.

Demonstration of spin-exchange interactions in the double well

The obvious next step from the experiments with higher order tunnel processes presented here is the introduction of the spin degree of freedom, since second order tunnel coupling between neighboring sites is an important process for mediating spin-dependent next-neighbor interactions, which could lead to quantum magnetism in the lattice [41].

With two different spins, the underlying exchange process of the two spins can be directly observed by preparing a defined spin configuration and letting it evolve under the corresponding two species Hubbard hamiltonian. This is possible by first using the controlled spin-changing collisions discussed in section 3.3 to create a "spin-triplet" state in a single well. An ordered spin state can be engineered in each double well by adiabatically separating the two spins to the left and the right well in a controlled way. First-order tunneling in this case is suppressed due to the on-site interaction, as both sites are occupied with one atom. "Simultaneous" tunneling, leading to an exchange of the spins in a second order tunnel process, is however possible. Since the two-color double well potential is completely spin-independent, the two possible spin-ordered states are fully degenerate. This makes it possible to observe spin superexchange interactions between the two sites even at the very low second order coupling strengths. In this way, the spin-exchange interaction between neighboring lattice sites could already be observed directly [185]. In addition, the sign of this coupling can be inverted by using a strong double well bias [185, 198]. This realizes an effective antiferromagnetic coupling for bosons.

Entanglement and spin chain preparation

The single-site triplet state can also be transformed to a delocalized triplet by splitting the site into a two-well potential. External field gradients then allow for the coupling between this triplet and the corresponding spin singlet, the dynamics of which can

be observed directly. These states are otherwise very robust to decoherence, making the system an interesting resource for quantum information [199] or precision measurements [200].

In the quantum information context, the spin superexchange process between neighboring sites of a spin chain can be used as a quantum gate. It implements a $\sqrt{swap}$-gate between neighboring qubits in a chain. This was originally proposed by [162] for quantum computers implemented as chains of quantum dots. Another possibility to implement such a gate is the controlled on-site exchange process which can be achieved by dynamically combining two neighboring wells [181, 201].

Using similar operations with appropriately tuned interactions it should also be possible to entangle neighboring spins in an array of atoms, thereby creating entangled spin chains similar to cluster states [202], or the resonating valence bond states of condensed matter physics [203, 204]. Such cluster states in chains of spins are another approach for implementing quantum information processing in the so-called one-way quantum computer [205, 206].

Quantum ladders and coupled 1D gases

In the experiments presented in this thesis, the superlattice is used to create two separated wells which each hold one spatial mode, without any additional spatial degree of freedom. All tunneling perpendicular to the double well axis is fully suppressed. If, in contrast to this, tunnel coupling along one of these axes is enabled, a quantum ladder system emerges. Here, two strings of lattice sites run in parallel and are coupled at each site by a lateral tunnel junction. Even though such systems still have a 1D structure, they can have very different properties [207, 208]. One prominent example is the gapped ground state with properties analog to a superconductor if fermions are loaded into the ladder potential [207, 209].

2D superlattices

A fascinating regime can also be reached by creating a 2D superlattice, where two lattice axes have superlattice periodicity. This produces a 2D array of weakly coupled quadratic "plaquettes" of four lattice sites each. These four sites are connected by strong tunneling links in a closed square. Such plaquettes would also enable the preparation of resonating valence bond (RVB) states known from solid state physics as well as allow the existence and observation of novel, higher order tunneling modes [210]. In a plaquette filled with four atoms, a ring-exchange process is possible, where the whole quantum state is rotated by 90 degrees. This tunneling process has been studied previously in the context of superfluidity and quantum hall effects in fermionic systems [211, 212] while also giving rise to novel quantum phases for bosons [213]. In the strongly correlated regime with strong interactions, where the first-order tunneling is suppressed, this process could be observable if it is possible

to also selectively suppress the second order tunnel coupling without influencing the ring exchange. For an initial geometry with alternating up and down spins around the ring, this could be achieved by applying a magnetic field gradient along one diagonal of the square. This would lift the spin exchange degeneracy, but not detune the ring exchange from resonance, which could then be the dominant tunneling process.

7.4 Conclusion

With the current progress on the experimental cold atom physics, ideas and concepts waiting to be realized with ultracold atoms in optical lattices are created at an even higher pace. Their number is rising with every new method or quantum phase which is discovered. In the span of only a few years, ultracold quantum gases have evolved from a spectacularly clean system capable of implementing fundamental effects of quantum mechanics, to an extremely flexible model system for fundamental condensed matter physics. With the new methods and implementations which are becoming available now, cold atoms in optical potentials are starting to be applied to the investigation of current topics in condensed matter physics. In addition, condensed matter systems could be realized with ultracold atoms which have no current equivalent in "real" solid state physics yet. But apart from the demonstration aspect for systems which are considered understood, it now also seems realistic that ultracold atoms can soon help in solving significant challenges in fields such as superconductivity or magnetism, thus making real contributions to condensed matter physics.

.

Bibliography

[1] D. Jaksch, C. Bruder, J. I. Cirac, C. W. Gardiner, and P. Zoller. *Cold Bosonic Atoms in Optical Lattices*. Phys. Rev. Lett. **81**, 3108–3111 (1998).

[2] M. Greiner, O. Mandel, T. Esslinger, T. W. Hänsch, and I. Bloch. *Quantum phase transition from a superfluid to a Mott insulator in a gas of ultracold atoms*. Nature **415**, 39–44 (2002).

[3] J. Hubbard. *Electron correlation in narrow energy bands*. Proc. Roy. Soc. **A276**, 238–257 (1963).

[4] M. P. A. Fisher, P. B. Weichman, G. Grinstein, and D. S. Fisher. *Boson localization and the superfluid-insulator transition*. Physical Review B **40**, 546–570 (1989).

[5] M. Anderson, J. Ensher, M. Matthews, C. E. Wieman, and E. A. Cornell. *Observation of Bose-Einstein Condensation in a Dilute Atomic Vapor*. Science **269**, 198 (1995).

[6] K. B. Davis, M. O. Mewes, M. R. Andrews, N. J. van Druten, D. S. Durfee, D. M. Kurn, and W. Ketterle. *Bose-Einstein Condensation in a Gas of Sodium Atoms*. Phys. Rev. Lett. **75**, 3969–3973 (1995).

[7] M. R. Andrews, C. G. Townsend, H.-J. Miesner, D. S. Durfee, D. M. Kurn, and W. Ketterle. *Observation of Interference Between Two Bose Condensates*. Science **275**, 637–641 (1997).

[8] M.-O. Mewes, M. R. Andrews, D. M. Kurn, D. S. Durfee, C. G. Townsend, and W. Ketterle. *Output Coupler for Bose-Einstein Condensed Atoms*. Phys. Rev. Lett. **78**, 582–585 (1997).

[9] B. P. Anderson and M. A. Kasevich. *Macroscopic Quantum Interference from Atomic Tunnel Arrays*. Science **282**, 1686–1689 (1998).

[10] E. W. Hagley, L. Deng, M. Kozuma, J. Wen, K. Helmerson, S. L. Rolston, and W. D. Phillips. *A Well-Collimated Quasi-Continuous Atom Laser*. Science **283**, 1706–1709 (1999).

[11] I. Bloch, T. W. Hänsch, and T. Esslinger. *Atom Laser with a cw Output Coupler*. Phys. Rev. Lett. **82**, 3008–3011 (1999).

[12] M. R. Matthews, B. P. Anderson, P. C. Haljan, D. S. Hall, C. E. Wieman, and E. A. Cornell. *Vortices in a Bose-Einstein Condensate*. Phys. Rev. Lett. **83**, 2498–2501 (1999).

[13] K. W. Madison, F. Chevy, W. Wohlleben, and J. Dalibard. *Vortex Formation in a Stirred Bose-Einstein Condensate*. Phys. Rev. Lett. **84**, 806–809 (2000).

[14] K. W. Madison, F. Chevy, W. Wohlleben, and J. Dalibard. *Vortices in a stirred Bose-Einstein condensate*. Journal of Modern Optics **47**, 2715–2723 (2000).

[15] J. R. Abo-Shaeer, C. Raman, J. M. Vogels, and W. Ketterle. *Observation of Vortex Lattices in Bose-Einstein Condensates*. Science **292**, 476–479 (2001).

[16] M. Albiez, R. Gati, J. Fölling, S. Hunsmann, M. Cristiani, and M. K. Oberthaler. *Direct Observation of Tunneling and Nonlinear Self-Trapping in a Single Bosonic Josephson Junction*. Physical Review Letters **95**, 010402 (2005).

[17] S. Levy, E. Lahoud, I. Shomroni, and J. Steinhauer. *The a.c. and d.c. Josephson effects in a Bose-Einstein condensate*. Nature **449**, 579–583 (2007).

[18] I. Bloch, J. Dalibard, and W. Zwerger. *Many-Body Physics with Ultracold Gases*. ArXiv e-prints **704** (2007). URL `http://arxiv.org/abs/0704.3011`. To be published in Rev. Mod. Phys.

[19] E. Tiesinga, A. J. Moerdijk, B. J. Verhaar, and H. T. C. Stoof. *Conditions for Bose-Einstein condensation in magnetically trapped atomic cesium*. Phys. Rev. A **46**, R1167–R1170 (1992).

[20] E. Tiesinga, B. J. Verhaar, and H. T. C. Stoof. *Threshold and resonance phenomena in ultracold ground-state collisions*. Phys. Rev. A **47**, 4114–4122 (1993).

[21] S. L. Cornish, N. R. Claussen, J. L. Roberts, E. A. Cornell, and C. E. Wieman. *Stable Rb-85 Bose-Einstein condensates with widely tunable interactions*. Phys. Rev. Lett. **85**, 1795–1798 (2000).

[22] K. M. O'Hara, S. L. Hemmer, M. E. Gehm, S. R. Granade, and J. E. Thomas. *Observation of a Strongly Interacting Degenerate Fermi Gas of Atoms*. Science **298**, 2179–2182 (2002).

[23] M. Bartenstein, A. Altmeyer, S. Riedl, S. Jochim, C. Chin, J. H. Denschlag, and R. Grimm. *Crossover from a Molecular Bose-Einstein Condensate to a Degenerate Fermi Gas*. Phys. Rev. Lett. **92**, 120401 (2004).

[24] T. Bourdel, L. Khaykovich, J. Cubizolles, J. Zhang, F. Chevy, M. Teichmann, L. Tarruell, S. J. J. M. F. Kokkelmans, and C. Salomon. *Experimental Study of the BEC-BCS Crossover Region in Lithium 6*. Phys. Rev. Lett. **93**, 050401 (2004).

[25] C. A. Regal, M. Greiner, and D. S. Jin. *Observation of Resonance Condensation of Fermionic Atom Pairs*. Phys. Rev. Lett. **92**, 040403 (2004).

[26] M. W. Zwierlein, C. A. Stan, C. H. Schunck, S. M. F. Raupach, A. J. Kerman, and W. Ketterle. *Condensation of Pairs of Fermionic Atoms near a Feshbach Resonance*. Phys. Rev. Lett. **92**, 120403 (2004).

[27] Y. Castin and J. Dalibard. *Quantization of Atomic Motion in Optical Molasses*. Europhysics Letters (EPL) **14**, 761–766 (1991). URL `http://stacks.iop.org/0295-5075/14/761`.

[28] A. Hemmerich and T. W. Hänsch. *Two-dimesional atomic crystal bound by light*. Phys. Rev. Lett. **70**, 410–413 (1993).

[29] M. Weidemüller, A. Hemmerich, A. Görlitz, T. Esslinger, and T. W. Hänsch. *Bragg Diffraction in an Atomic Lattice Bound by Light*. Phys. Rev. Lett. **75**, 4583–4586 (1995).

[30] M. Ben Dahan, E. Peik, J. Reichel, Y. Castin, and C. Salomon. *Bloch Oscillations of Atoms in an Optical Potential*. Phys. Rev. Lett. **76**, 4508–4511 (1996).

[31] S. R. Wilkinson, C. F. Bharucha, K. W. Madison, Q. Niu, and M. G. Raizen. *Observation of Atomic Wannier-Stark Ladders in an Accelerating Optical Potential*. Phys. Rev. Lett. **76**, 4512–4515 (1996).

[32] C. Orzel, A. K. Tuchman, M. L. Fenselau, M. Yasuda, and M. A. Kasevich. *Squeezed states in a Bose-Einstein condensate*. Science **291**, 2386–2389 (2001).

[33] T. Stöferle, H. Moritz, C. Schori, M. Köhl, and T. Esslinger. *Transition form a strongly interacting 1D superfluid to a Mott insulator*. Phys. Rev. Lett. **92**, 130403 (2004).

[34] M. Köhl, H. Moritz, T. Stöferle, C. Schori, and T. Esslinger. *Superfluid to Mott insulator transition in one, two, and three dimensions*. Journal of Low Temperature Physics **138**, 635–644 (2005).

[35] B. Paredes, A. Widera, V. Murg, O. Mandel, S. Fölling, I. Cirac, G. V. Shlyapnikov, T. W. Hänsch, and I. Bloch. *Tonks-Girardeau gas of ultracold atoms in an optical lattice*. Nature **429**, 277–281 (2004).

[36] T. Kinoshita, T. Wenger, and D. S. Weiss. *Observation of a One-Dimensional Tonks-Girardeau Gas*. Science **305**, 1125–1128 (2004).

[37] M. Köhl, H. Moritz, T. Stöferle, K. Günter, and T. Esslinger. *Fermionic atoms in a three dimensional optical lattice: Observing Fermi-surfaces, dynamics and interactions*. Phys. Rev. Lett. **94**, 080403 (2005).

[38] J. K. Chin, D. E. Miller, Y. Liu, C. Stan, W. Setiawan, C. Sanner, K. Xu, and W. Ketterle. *Evidence for superfluidity of ultracold fermions in an optical lattice*. Nature **443**, 961–964 (2006).

[39] R. H. Brown and R. Q. Twiss. *Correlation between photons in two coherent beams of light*. Nature **177**, 27–29 (1956).

[40] E. Altman, E. Demler, and M. D. Lukin. *Probing many-body states of ultracold atoms via noise correlations*. Phys. Rev. A **70**, 013603 (2004).

[41] L.-M. Duan, E. Demler, and M. D. Lukin. *Controlling Spin Exchange Interactions of Ultracold Atoms in Optical Lattices*. Phys. Rev. Lett. **91**, 090402 (2003).

[42] F. Dalfovo, S. Giorgini, L. P. Pitaevskii, and S. Stringari. *Theory of Bose-Einstein condensation in trapped gases*. Rev. Mod. Phys. **71**, 463 (1999).

[43] C. Pethick and H. Smith. *Bose-Einstein Condensation in Dilute Gases*. Cambridge University Press, Cambridge (2001).

[44] W. Ketterle, D. Durfee, and D. Stamper-Kurn. *Making, probing and understanding Bose-Einstein condensates*. In M. Inguscio, S. Stringari, and C. Wieman, editors, *In Bose-Einstein condensation in atomic gases, Proceedings of the International School of Physics "Enrico Fermi"*, pages 67–176. IOS Press, Amsterdam (1999).

[45] A. J. Leggett. *Bose-Einstein condensation in atomic gases: some fundamental concepts*. Rev. Mod. Phys. **73**, 307–356 (2001).

[46] I. Bloch. *Ultracold Quantum Gases in Optical Lattices*. Nature Physics **1**, 23–30 (2005).

[47] O. Morsch and M. Oberthaler. *Dynamics of Bose-Einstein condensates in optical lattices*. Reviews of Modern Physics **78**, 179 (2006).

[48] M. Lewenstein, A. Sanpera, V. Ahufinger, B. Damski, A. Sen, and U. Sen. *Ultracold atomic gases in optical lattices: mimicking condensed matter physics and beyond*. Advances in Physics **56**, 243–379 (2007).

[49] A. Einstein. *Quantentheorie des einatomingen idealen Gases*. Sitzungsber. Preuss. Akad. Wiss., phys.-math. Klasse **23**, 1–14 (1925).

[50] S. N. Bose. *Plancks Gesetz und Lichtquantenhypothese*. Zeitschrift für Physik **26**, 178–181 (1924).

[51] O. Penrose and L. Onsager. *Bose-Einstein Condensation and Liquid Helium*. Phys. Rev. **104**, 576–584 (1956).

[52] J. Weiner, V. S. Bagnato, S. Zilio, and P. S. Julienne. *Experiments and theory in cold and ultracold collisions*. Rev. Mod. Phys. **71**, 1–85 (1999).

[53] J. Dalibard. *Collisional dynamics of ultra-cold atomic gases*. In M. Inguscio, S. Stringari, and C. E. Wieman, editors, *Proceedings of the International School of Physics Enrico Fermi, Course CXL: Bose – Einstein condensation in gases, Varenna 1998*. IOS Press (1999).

[54] E. P. Gross. *Structure of a quantized vortex in boson systems*. Nuovo Cimento **20**, 454–477 (1961).

[55] L. P. Pitaevskii. *Vortex lines in an imperfect Bose gas*. Sov. Phys. JETP **13**, 451–454 (1961).

[56] D. A. Butts and D. S. Rokhsar. *Predicted signatures of rotating Bose-Einstein condensates*. Nature **397**, 327 (1999).

[57] W. Zhang, D. F. Walls, and B. C. Sanders. *Atomic soliton in a traveling wave laser beam*. Phys. Rev. Lett. **72**, 60–63 (1994).

[58] P. A. Ruprecht, M. J. Holland, K. Burnett, and M. Edwards. *Time-dependent solution of the nonlinear Schrödinger equation for Bose-condensed trapped neutral atoms*. Phys. Rev. A **51**, 4704–4711 (1995).

[59] G. Baym and C. J. Pethick. *Ground-State Properties of Magnetically Trapped Bose-Condensed Rubidium Gas*. Phys. Rev. Lett. **76**, 6–9 (1996).

[60] L. H. Thomas. *The calculation of atomic fields*. Proc. Cambridge Phil. Soc. **23**, 542–8 (1927).

[61] E. Fermi. *Eine statistische Methode zur Bestimmung einiger Eigenschaften des Atoms und ihre Anwendung auf die Theorie des periodischen Systems der Elemente*. Zeitschrift für Physik A **48**, 73–79 (1928).

[62] N. Bogoliubov. *On the theory of superfluidity*. J. Phys. **11**, 23 (1947).

[63] E. Timmermans, P. Tommasini, and K. Huang. *Variational Thomas-Fermi theory of a nonuniform Bose condensate at zero temperature*. Phys. Rev. A **55**, 3645–3657 (1997).

[64] E. A. Donley, N. R. Claussen, S. L. Cornish, J. L. Roberts, E. A. Cornell, and C. E. Wieman. *Dynamics of collapsing and exploding Bose-Einstein condensates*. Nature **412**, 295–299 (2001).

[65] P. O. Fedichev, M. W. Reynolds, and G. V. Shlyapnikov. *Three-Body Recombination of Ultracold Atoms to a Weakly Bound s Level*. Phys. Rev. Lett. **77**, 2921–2924 (1996).

[66] M. W. Jack and M. Yamashita. *Signatures of the quantum fluctuations of cold atoms in an optical lattice in the three-body loss rate*. Phys. Rev. A **67**, 033605 (2003).

[67] K. Petsas, A. Coates, and G. Grynberg. *Crystallography of optical lattices*. Phys. Rev. A **50**, 5173–5189 (1994).

[68] R. Grimm, M. Weidemüller, and Y. Ovchinnikov. *Optical dipole traps for neutral atoms*. Adv. At. Mol. Opt. Phys. **42**, 95 (2000).

[69] H. Metcalf and P. van der Straten. *Laser Cooling and Trapping*. Springer, New York (1999).

[70] N. Ashcroft and N. Mermin. *Solid State Physics*. Harcourt Brace College Publishers, Fort Worth (1976).

[71] C. Kittel. *Introduction to solid state physics*. Wiley, Philadelphia (2004).

[72] D. Jaksch. *Bose-Einstein Condensation and Applications*. PhD thesis, Leopold-Franzens-Universität Innsbruck, Austria (1999). URL `http://www2.arcs.ac.at/dissdb/rn034177`.

[73] G. Campbell, J. Mun, M. Boyd, P. Medley, A. E. Leanhardt, L. Marcassa, D. Pritchard, and W. Ketterle. *Imaging the Mott Insulator Shells by Using Atomic Clock Shifts*. Science **313**, 649–652 (2006).

[74] T. Busch, B. Englert, K. Rzążewski, and M. Wilkens. *Two Cold Atoms in a Harmonic Trap*. Foundations of Physics **28**, 549–559 (1998).

[75] B. Sun, W. X. Zhang, S. Yi, M. S. Chapman, and L. You. *Dipolar Effect in Coherent Spin Mixing of Two Atoms in a Single Optical Lattice Site*. Phys. Rev. Lett. **97**, 123201 (2006).

[76] J. H. Mentink. *Interacting Atoms in Optical Lattices*. Master's thesis, Eindhoven University of Technology (2006).

[77] R. J. Glauber. *Coherent and Incoherent States of the Radiation Field*. Phys. Rev. **131**, 2766–2788 (1963).

[78] K. Sheshadri, H. R. Krishnamurthy, R. Pandit, and T. V. Ramakrishnan. *Superfluid and insulating phases in an interacting-boson model: mean-field theory and the RPA*. Europhys. Lett. **22**, 257–263 (1993).

[79] J. K. Freericks and H. Monien. *Phase diagram of the Bose-Hubbard Model*. Europhys. Lett. **26**, 545–550 (1994). ISSN 0295-5075.

[80] D. van Oosten, P. van der Straten, and H. Stoof. *Quantum phases in an optical lattice*. Phys. Rev. A **63**, 053601 (2001).

[81] B. Capogrosso-Sansone, N. V. Prokof'ev, and B. V. Svistunov. *Phase diagram and thermodynamics of the three-dimensional Bose-Hubbard model*. Physical Review B (Condensed Matter and Materials Physics) **75**, 134302 (2007).

[82] N. Elstner and H. Monien. *Dynamics and thermodynamics of the Bose-Hubbard model*. Phys. Rev. B **59**, 12184–12187 (1999).

[83] S. Sachdev. *Quantum Phase Transitions*. Cambridge University Press, Cambridge (1999).

[84] F. Gerbier, A. Widera, S. Fölling, O. Mandel, T. Gericke, and I. Bloch. *Phase Coherence of an Atomic Mott Insulator*. Phys. Rev. Lett. **95**, 050404 (2005).

[85] F. Gerbier, A. Widera, S. Fölling, O. Mandel, T. Gericke, and I. Bloch. *Interference pattern and visibility of a Mott insulator*. Phys. Rev. A **72**, 053606 (2005).

[86] F. Gerbier. *Boson Mott Insulators at Finite Temperatures*. Phys. Rev. Lett. **99**, 120405 (2007).

[87] S. Fölling, A. Widera, T. Müller, F. Gerbier, and I. Bloch. *Formation of Spatial Shell Structure in the Superfluid to Mott Insulator Transition*. Phys. Rev. Lett. **97**, 060403 (2006).

[88] F. Gerbier, S. Fölling, A. Widera, O. Mandel, and I. Bloch. *Probing Number Squeezing of Ultracold Atoms across the Superfluid-Mott Insulator Transition*. Phys. Rev. Lett. **96**, 090401 (2006).

[89] M. Greiner. *Magnetischer Transfer von Atomen - Ein Weg zur einfachen Bose-Einstein-Kondensation*. Diploma thesis, Ludwig-Maximilians-Universität München (2000).

[90] M. Greiner, I. Bloch, T. W. Hänsch, and T. Esslinger. *Magnetic transport of trapped cold atoms over a large distance*. Phys. Rev. A **63**, 031401/1–4 (2001).

[91] I. Bloch, M. Greiner, O. Mandel, T. W. Hänsch, and T. Esslinger. *Sympathetic cooling of 85Rb and 87Rb*. Phys. Rev. A **64**, 021402/1–4 (2001).

[92] M. Greiner. *Ultracold quantum gases in three-dimensional optical lattice potentials*. PhD thesis, Ludwig-Maximilians-Universität München (2003). URL `http://edoc.ub.uni-muenchen.de/968/`.

[93] O. Mandel. *Entanglement with quantum gates in an optical lattice*. PhD thesis, Ludwig-Maximilians-Universität München (2005). URL `http://edoc.ub.uni-muenchen.de/archive/00003568/`.

[94] A. Widera. *Constructing Correlated Spin States with Neutral Atoms in Optical Lattices*. PhD thesis, Johannes Gutenberg-Universität Mainz (2007).

[95] E. L. Raab, M. Prentiss, A. Cable, S. Chu, and D. E. Pritchard. *Trapping of Neutral Sodium Atoms with Radiation Pressure*. Phys. Rev. Lett. **59**, 2631–2634 (1987).

[96] S. Chu, J. E. Bjorkholm, A. Ashkin, and A. Cable. *Experimental Observation of Optically Trapped Atoms*. Phys. Rev. Lett. **57**, 314–317 (1986).

[97] A. L. Migdall, J. V. Prodan, W. D. Phillips, T. H. Bergeman, and H. J. Metcalf. *First Observation of Magnetically Trapped Neutral Atoms*. Phys. Rev. Lett. **54**, 2596–2599 (1985).

[98] W. Petrich, M. H. Anderson, J. R. Ensher, and E. A. Cornell. *Stable, Tightly Confining Magnetic Trap for Evaporative Cooling of Neutral Atoms*. Phys. Rev. Lett. **74**, 3352–3355 (1995).

[99] T. Esslinger, I. Bloch, and T. W. Hänsch. *Bose-Einstein Condensation in a Quadrupole-Ioffe-Configuration Trap*. Phys. Rev. A **58**, R2664–R2667 (1998).

[100] V. A. Kashurnikov, N. V. Prokof'ev, and B. Svistunov. *Revealing the superfluid-Mott insulator transition in an optical lattice*. Phys. Rev. A **66**, 031601(R) (2002).

[101] F. Gerbier, S. Foelling, A. Widera, and I. Bloch. *Visibility of a Bose-condensed gas released from an optical lattice at finite temperatures*. ArXiv Condensed Matter e-prints (2007). URL `http://arxiv.org/abs/cond-mat/0701420`.

[102] A. Kastberg, W. D. Phillips, S. L. Rolston, R. J. C. Spreeuw, and P. S. Jessen. *Adiabatic Cooling of Cesium to 700 nK in an Optical Lattice*. Phys. Rev. Lett. **74**, 1542–1545 (1995).

[103] M. Greiner, I. Bloch, O. Mandel, T. W. Hänsch, and T. Esslinger. *Exploring Phase Coherence in a 2D Lattice of Bose-Einstein Condensates*. Phys. Rev. Lett. **87**, 160405 (2001).

[104] J. Hecker Denschlag, J. E. Simsarian, H. Häffner, C. McKenzie, A. Browaeys, D. Cho, K. Helmerson, S. L. Rolston, and W. D. Phillips. *A Bose-Einstein condensate in an optical lattice* . J. Phys. B **35**, 3095–3110 (2002).

[105] T. Müller, S. Fölling, A. Widera, and I. Bloch. *State Preparation and Dynamics of Ultracold Atoms in Higher Lattice Orbitals*. Phys. Rev. Lett. **99**, 200405 (2007).

[106] O. Mandel, M. Greiner, A. Widera, T. Rom, T. W. Hänsch, and I. Bloch. *Controlled Collisions for Multiparticle Entanglement of Optically Trapped Atoms*. Nature **425**, 937 (2003).

[107] A. Widera, O. Mandel, M. Greiner, S. Kreim, T. W. Hänsch, and I. Bloch. *Entanglement Interferometry for Precision Measurement of Atomic Scattering Properties*. Phys. Rev. Lett. **92**, 160406–1–4 (2004).

[108] T. Rom, T. Best, O. Mandel, A. Widera, M. Greiner, T. W. Hänsch, and I. Bloch. *State Selective Production of Molecules in Optical Lattices*. Phys. Rev. Lett. **93**, 073002 (2004).

[109] K. Winkler, G. Thalhammer, M. Theis, H. Ritsch, R. Grimm, and J. H. Denschlag. *Atom-Molecule Dark States in a Bose-Einstein Condensate*. Phys. Rev. Lett. **95**, 063202 (2005).

[110] T. Stöferle, H. Moritz, K. Günter, M. Köhl, and T. Esslinger. *Molecules of Fermionic Atoms in an Optical Lattice*. Phys. Rev. Lett. **96**, 030401 (2006).

[111] G. Thalhammer, K. Winkler, F. Lang, S. Schmid, R. Grimm, and J. H. Denschlag. *Long-Lived Feshbach Molecules in a Three-Dimensional Optical Lattice*. Phys. Rev. Lett. **96**, 050402 (2006).

[112] T. Volz, N. Syassen, D. M. Bauer, E. Hansis, S. Dürr, and G. Rempe. *Preparation of a quantum state with one molecule at each site of an optical lattice*. Nature Physics **2**, 692–695 (2006).

[113] C. Ospelkaus, S. Ospelkaus, L. Humbert, P. Ernst, K. Sengstock, and K. Bongs. *Ultracold Heteronuclear Molecules in a 3D Optical Lattice*. Phys. Rev. Lett. **97**, 120402 (2006).

[114] A. Widera, F. Gerbier, S. Fölling, T. Gericke, O. Mandel, and I. Bloch. *Coherent Collisional Spin Dynamics in Optical Lattices*. Phys. Rev. Lett. **95**, 190405 (2005).

[115] F. Gerbier, A. Widera, S. Fölling, O. Mandel, and I. Bloch. *Resonant control of spin dynamics in ultracold quantum gases by microwave dressing*. Phys. Rev. A **73**, 041602 (2006).

[116] A. Widera, F. Gerbier, S. Fölling, T. Gericke, O. Mandel, and I. Bloch. *Precision measurement of spin-dependent interaction strengths for spin-1 and spin-2 87Rb atoms*. New Journal of Physics **8**, 152 (2006).

[117] H. Schmaljohann, M. Erhard, J. Kronjäger, M. Kottke, S. van Staa, L. Cacciapuoti, J. J. Arlt, K. Bongs, and K. Sengstock. *Dynamics of $F = 2$ Spinor Bose-Einstein Condensates*. Phys. Rev. Lett. **92**, 040402 (2004).

[118] M.-S. Chang, C. D. Hamley, M. D. Barrett, J. A. Sauer, K. M. Fortier, W. Zhang, L. You, and M. S. Chapman. *Observation of Spinor Dynamics in Optically Trapped ^{87}Rb Bose-Einstein Condensates*. Phys. Rev. Lett. **92**, 140403 (2004).

[119] M.-S. Chang, Q. Qin, W. Zhang, L. You, and M. S. Chapman. *Coherent spinor dynamics in a spin-1 Bose condensate*. Nature Physics **1**, 111–116 (2005).

[120] N. Ramsey. *Molecular Beams*. Oxford University Press, London (1956).

[121] H. Pu and P. Meystre. *Creating Macroscopic Atomic Einstein-Podolsky-Rosen States from Bose-Einstein Condensates*. Phys. Rev. Lett. **85**, 3987–3990 (2000).

[122] L.-M. Duan, A. Sørensen, J. I. Cirac, and P. Zoller. *Squeezing and Entanglement of Atomic Beams*. Phys. Rev. Lett. **85**, 3991–3994 (2000).

[123] A. Sørensen, L.-M. Duan, J. I. Cirac, and P. Zoller. *Many-particle entanglement with Bose-Einstein condensates*. Nature **409**, 63–66 (2001).

[124] K. Burnett, M. Edwards, C. W. Clark, and M. Shotter. *The Bogoliubov approach to number squeezing of atoms in an optical lattice*. J. Phys. B **35**, 1671 (2002).

[125] M. Shotter. *The Bogoliubov approach to number squeezing of atoms in an optical lattice*. J. Phys. B **35**, 3019 (2002).

[126] R. Roth and K. Burnett. *Superfluidity and interference pattern of ultracold bosons in optical lattices*. Phys. Rev. A **67**, 031602 (2003).

[127] J. Garcia-Ripoll, J. Cirac, P. Zoller, C. Kollath, U. Schollwöck, and J. von Delft. *Variational ansatz for the superfluid Mott-insulator transition in optical lattices*. Opt. Exp. **12**, 42–54 (2004).

[128] L. I. Plimak, M. K. Olsen, and M. Fleischhauer. *Occupation number and fluctuations in the finite-temperature Bose-Hubbard model*. Phys. Rev. A **70**, 013611 (2004).

[129] B. Capogrosso-Sansone, E. Kozik, N. Prokof'ev, and B. Svistunov. *On-site number statistics of ultracold lattice bosons*. Phys. Rev. A **75**, 013619 (2007).

[130] F. Mintert and C. Wunderlich. *Ion-Trap Quantum Logic Using Long-Wavelength Radiation*. Phys. Rev. Lett. **87**, 257904 (2001).

[131] D. Schrader, I. Dotsenko, M. Khudaverdyan, Y. Miroshnychenko, A. Rauschenbeutel, and D. Meschede. *Neutral Atom Quantum Register*. Phys. Rev. Lett. **93**, 150501 (2004).

[132] H. Ott, E. de Mirandes, F. Ferlaino, G. Roati, V. Türck, G. Modugno, and M. Inguscio. *Radio Frequency Selective Addressing of Localized Atoms in a Periodic Potential*. Phys. Rev. Lett. **93**, 120407 (2004).

[133] T. Gericke, F. Gerbier, A. Widera, S. Fölling, O. Mandel, and I. Bloch. *Adiabatic loading of a Bose-Einstein condensate in a 3D optical lattice*. J. Mod. Opt. **54**, 735 (2007).

[134] R. H. Brown and R. Q. Twiss. *The question of correlation between photons in coherent light rays*. Nature **178**, 1447–1448 (1956).

[135] J. Grondalski, P. M. Alsing, and I. H. Deutsch. *Spatial correlation diagnostics for atoms in optical lattices*. Opt. Exp. **5**, 249–261 (1999).

[136] A. Kolovsky. *Interference of cold atoms released from an optical lattice*. Europhys. Lett. **68**, 330–336 (2004).

[137] R. Bach and K. Rzążewski. *Correlation functions of cold bosons in an optical lattice*. Phys. Rev. A **70**, 063622 (2004).

[138] C. K. Hong, Z. Y. Ou, and L. Mandel. *Measurement of subpicosecond time intervals between two photons by interference*. Phys. Rev. Lett. **59**, 2044–2046 (1987).

[139] R. J. Glauber. *Photon Correlations*. Phys. Rev. Lett. **10**, 84–86 (1963).

[140] E. A. Burt, R. W. Ghrist, C. J. Myatt, M. J. Holland, E. A. Cornell, and C. E. Wieman. *Coherence, Correlations, and Collisions: What One Learns about Bose-Einstein Condensates from Their Decay*. Phys. Rev. Lett. **79**, 337–340 (1997).

[141] M. Schellekens, R. Hoppeler, A. Perrin, J. V. Gomes, D. Boiron, A. Aspect, and C. I. Westbrook. *Hanbury Brown Twiss Effect for Ultracold Quantum Gases*. Science **310**, 648–651 (2005).

[142] J. V. Gomes, A. Perrin, M. Schellekens, D. Boiron, C. I. Westbrook, and M. Belsley. *Theory for a Hanbury Brown Twiss experiment with a ballistically expanding cloud of cold atoms*. Phys. Rev. A **74**, 053607 (2006).

[143] T. Rom, T. Best, D. van Oosten, U. Schneider, S. Fölling, B. Paredes, and I. Bloch. *Free fermion antibunching in a degenerate atomic Fermi gas released from an optical lattice*. Nature **444**, 733–736 (2006).

[144] I. B. Spielman, W. D. Phillips, and J. V. Porto. *Mott-Insulator Transition in a Two-Dimensional Atomic Bose Gas*. Phys. Rev. Lett. **98**, 080404 (2007).

[145] J. Goodman. *Statistical Optics*. Wiley, New York (1985).

[146] E. Demler and F. Zhou. *Spinor Bosonic Atoms in Optical Lattices: Symmetry Breaking and Fractionalization* (2002).

[147] K. Góral, L. Santos, and M. Lewenstein. *Quantum Phases of Dipolar Bosons in Optical Lattices*. Phys. Rev. Lett. **88**, 170406 (2002).

[148] S. Peil, J. Porto, B. Laburthe-Tolra, J. Obrecht, B. King, M. Subbotin, S. Rolston, and W. Phillips. *Patterned loading of a Bose-Einstein condensate into an optical lattice*. Phys. Rev. A **67**, – (2003).

[149] B. D. Josephson. *Possible new effects in superconductive tunnelling*. Physics Letters **1**, 251–253 (1962).

[150] K. Likharev. *Superconducting weak links*. Rev. Mod. Phys. **51**, 101–159 (1979).

[151] D. Averin. *Quantum Computing and Quantum Measurement with Mesoscopic Josephson Junctions*. Fortschr. Phys. **48**, 1055–1074 (2000).

[152] Y. Makhlin, G. Schön, and A. Shnirman. *Quantum-state engineering with Josephson-junction devices*. Rev. Mod. Phys. **73**, 357–400 (2001).

[153] D. V. Averin and K. K. Likharev. *Coulomb blockade of single-electron tunneling, and coherent oscillations in small tunnel junctions*. J. Low Temp. Phys. **62**, 345–373 (1986).

[154] T. A. Fulton and G. J. Dolan. *Observation of single-electron charging effects in small tunnel junctions*. Phys. Rev. Lett. **59**, 109–112 (1987).

[155] K. K. Likharev and A. B. Zorin. *Theory of the Bloch-wave oscillations in small Josephson junctions*. J. Low Temp. Phys. **59**, 347–382 (1985).

[156] T. A. Fulton, P. L. Gammel, D. J. Bishop, L. N. Dunkleberger, and G. J. Dolan. *Observation of combined Josephson and charging effects in small tunnel junction circuits*. Phys. Rev. Lett. **63**, 1307–1310 (1989).

[157] L. J. Geerligs, V. F. Anderegg, J. Romijn, and J. E. Mooij. *Single Cooper-pair tunneling in small-capacitance junctions*. Phys. Rev. Lett. **65**, 377–380 (1990).

[158] D. J. Flees, S. Han, and J. E. Lukens. *Interband Transitions and Band Gap Measurements in Bloch Transistors*. Phys. Rev. Lett. **78**, 4817–4820 (1997).

[159] L. Kouwenhoven, C. Marcus, P. McEuen, S. Tarucha, R. Westerelt, and N. Wingreen. *Electron Transport in Quantum Dots*. In L. Sohn, L. P. Kouwenhoven, and G. Schön, editors, *Mesoscopic Electron Transport*, pages 105–214. Kluwer, Dordrecht (1997).

[160] S. De Franceschi, S. Sasaki, J. M. Elzerman, W. G. van der Wiel, S. Tarucha, and L. P. Kouwenhoven. *Electron Cotunneling in a Semiconductor Quantum Dot*. Phys. Rev. Lett. **86**, 878–881 (2001).

[161] D. M. Zumbühl, C. M. Marcus, M. P. Hanson, and A. C. Gossard. *Cotunneling Spectroscopy in Few-Electron Quantum Dots*. Phys. Rev. Lett. **93**, 256801 (2004).

[162] D. Loss and D. P. Divincenzo. *Quantum computation with quantum dots*. Physical Review A **57**, 120–126 (1998).

[163] J. R. Petta, A. C. Johnson, J. M. Taylor, E. A. Laird, A. Yacoby, M. D. Lukin, C. M. Marcus, M. P. Hanson, and A. C. Gossard. *Coherent Manipulation of Coupled Electron Spins in Semiconductor Quantum Dots*. Science **309**, 2180–2184 (2005).

[164] E. Šimánek. *Instability of granular superconductivity*. Phys. Rev. B **22**, 459–462 (1980).

[165] S. Doniach. *Quantum fluctuations in two-dimensional superconductors*. Phys. Rev. B **24**, 5063–5070 (1981).

[166] M. P. A. Fisher and G. Grinstein. *Quantum critical phenomena in charged superconductors*. Phys. Rev. Lett. **60**, 208–211 (1988).

[167] K. Winkler, G. Thalhammer, F. Lang, R. Grimm, J. Hecker-Denschlag, A. Daley, A. Kantian, H. Büchler, and P. Zoller. *Repulsively bound atom pairs in an optical lattice*. Nature **441**, 853–856 (2006).

[168] A. Auerbach. *Interacting Electrons and Quantum Magnetism*. Springer, Berlin (1998).

[169] A. B. Kuklov and B. V. Svistunov. *Counterflow Superfluidity of Two-Species Ultracold Atoms in a Commensurate Optical Lattice*. Phys. Rev. Lett. **90**, 100401 (2003).

[170] E. Altman, W. Hofstetter, E. Demler, and M. Lukin. *Phase diagram of two-component bosons on an optical lattice*. New J. Phys. **5**, 113 (2003).

[171] T. Schumm, S. Hofferberth, S. Wildermuth, L. M. Andersson, S. Groth, I. Bar-Joseph, J. Schmiedmayer, and P. Krüger. *Matter-wave interferometry in a double well on an atom chip*. Nature Physics **1**, 57 (2005).

[172] I. Lesanovsky, T. Schumm, S. Hofferberth, L. M. Andersson, P. Krüger, and J. Schmiedmayer. *Adiabatic radio-frequency potentials for the coherent manipulation of matter waves*. Physical Review A **73**, 033619 (2006).

[173] S. Hofferberth, I. Lesanovsky, B. Fischer, T. Schumm, and J. Schmiedmayer. *Non-equilibrium coherence dynamics in one-dimensional Bose gases*. Nature **449**, 324–327 (2007).

[174] G.-B. Jo, Y. Shin, S. Will, T. A. Pasquini, M. Saba, W. Ketterle, D. E. Pritchard, M. Vengalattore, and M. Prentiss. *Long Phase Coherence Time and Number Squeezing of Two Bose-Einstein Condensates on an Atom Chip*. Phys. Rev. Lett. **98**, 030407 (2007).

[175] D. Haycock, P. Alsing, I. H. Deutsch, J. Grondalski, and P. Jessen. *Mesoscopic Quantum Coherence in an Optical Lattice*. Phys. Rev. Lett. **85**, 3365–3368 (2000).

[176] R. Ettig. *Beobachtung des Tunnelns massiver Teilchen in Doppeltopfpotentialen*. Diploma thesis, Ruprecht-Karls-Universität Heidelberg (2006). URL `http://www.kip.uni-heidelberg.de/Veroeffentlichungen/details.php?id=1740`. KIP-ID: HD-KIP 06-12.

[177] J. Sebby-Strabley, M. Anderlini, P. S. Jessen, and J. V. Porto. *Lattice of double wells for manipulating pairs of cold atoms*. Physical Review A **73**, 033605 (2006).

[178] M. Anderlini, J. Sebby-Strabley, J. Kruse, J. V. Porto, and W. D. Phillips. *Controlled atom dynamics in a double-well optical lattice*. J. Phys. B **39**, 199 (2006).

[179] J. Sebby-Strabley, B. L. Brown, M. Anderlini, P. J. Lee, W. D. Phillips, J. V. Porto, and P. R. Johnson. *Preparing and Probing Atomic Number States with an Atom Interferometer*. Phys. Rev. Lett. **98**, 200405 (2007).

[180] P. J. Lee, M. Anderlini, B. L. Brown, J. Sebby-Strabley, W. D. Phillips, and J. V. Porto. *Sublattice Addressing and Spin-Dependent Motion of Atoms in a Double-Well Lattice*. Phys. Rev. Lett. **99**, 020402 (2007).

[181] M. Anderlini, P. J. Lee, B. L. Brown, J. Sebby-Strabley, W. D. Phillips, and J. V. Porto. *Controlled exchange interaction between pairs of neutral atoms in an optical lattice*. Nature **448**, 452–456 (2007).

[182] U. Schünemann, H. Engler, R. Grimm, M. Weidemüller, and M. Zielonkowski. *Simple scheme for tunable frequency offset locking of two lasers*. Review of Scientific Instruments **70**, 242–243 (1999).

[183] C. Myatt, E. Burt, Ghrist, R.W., Cornell, E.A., and C. Wiemann. *Production of Two Overlapping Bose-Einstein Condensates by Sympathetic Cooling*. Phys. Rev. Lett. **78**, 586–589 (1997).

[184] D. van Oosten, P. van der Straten, and H. T. Stoof. *Mott insulators in an optical lattice with high filling factors*. Physical Review A **67**, 033606 (2003).

[185] S. Trotzky, P. Cheinet, S. Fölling, M. Feld, U. Schnorrberger, A. M. Rey, A. Polkovnikov, E. A. Demler, M. D. Lukin, and I. Bloch. *Time-Resolved Observation and Control of Superexchange Interactions with Ultracold Atoms in Optical Lattices*. Science **319**, 295–299 (2008).

[186] A. M. Rey, V. Gritsev, I. Bloch, E. Demler, and M. D. Lukin. *Preparation and Detection of Magnetic Quantum Phases in Optical Superlattices*. Phys. Rev. Lett. **99**, 140601 (2007).

[187] H. J. Schulz, G. Cuniberti, and P. Pieri. *Fermi liquids and Luttinger liquids*. In G. Morandi, P. Sodano, A. Tagliacozzo, and V. Tognetti, editors, *Field Theories*

for Low-Dimensional Condensed Matter Systems, volume 131 of *Springer Series in Solid-State Sciences*, pages 9–82. Springer (2000). ISBN 978-3-540-67177-0.

[188] A. Recati, P. O. Fedichev, W. Zwerger, and P. Zoller. *Spin-Charge Separation in Ultracold Quantum Gases*. Phys. Rev. Lett. **90**, 020401 (2003).

[189] O. M. Auslaender, H. Steinberg, A. Yacoby, Y. Tserkovnyak, B. I. Halperin, K. W. Baldwin, L. N. Pfeiffer, and K. W. West. *Spin-Charge Separation and Localization in One Dimension*. Science **308**, 88–92 (2005).

[190] C. Kollath, U. Schollwöck, and W. Zwerger. *Spin-Charge Separation in Cold Fermi Gases: A Real Time Analysis*. Phys. Rev. Lett. **95**, 176401 (2005).

[191] T. Jeltes, J. M. McNamara, W. Hogervorst, W. Vassen, V. Krachmalnicoff, M. Schellekens, A. Perrin, H. Chang, D. Boiron, A. Aspect, and C. I. Westbrook. *Comparison of the Hanbury Brown-Twiss effect for bosons and fermions*. Nature **445**, 402–405 (2007).

[192] L. Santos, G. V. Shlyapnikov, P. Zoller, and M. Lewenstein. *Bose-Einstein Condensation in Trapped Dipolar Gases*. Phys. Rev. Lett. **85**, 1791–1794 (2000).

[193] H. Pu, W. Zhang, and P. Meystre. *Ferromagnetism in a Lattice of Bose-Einstein Condensates*. Phys. Rev. Lett. **87**, 140405 (2001).

[194] W. Zhang, H. Pu, C. Search, and P. Meystre. *Spin Waves in a Bose-Einstein–Condensed Atomic Spin Chain*. Phys. Rev. Lett. **88**, 060401 (2002).

[195] J. Stuhler, A. Griesmaier, T. Koch, M. Fattori, T. Pfau, S. Giovanazzi, P. Pedri, and L. Santos. *Observation of Dipole-Dipole Interaction in a Degenerate Quantum Gas*. Phys. Rev. Lett. **95**, 150406 (2005).

[196] A. Griesmaier, J. Stuhler, T. Koch, M. Fattori, T. Pfau, and S. Giovanazzi. *Comparing Contact and Dipolar Interactions in a Bose-Einstein Condensate*. Phys. Rev. Lett. **97**, 250402 (2006).

[197] A. Sørensen and K. Mølmer. *Spin-Spin Interaction and Spin Squeezing in an Optical Lattice*. Phys. Rev. Lett. **83**, 2274–2277 (1999).

[198] A. M. Rey, V. Gritsev, I. Bloch, E. Demler, and M. D. Lukin. *Preparation and Detection of Magnetic Quantum Phases in Optical Superlattices*. Phys. Rev. Lett. **99**, 140601 (2007).

[199] C. Roos, G. Lancaster, R. M., H. Häffner, W. Hänsel, S. Gulde, C. Becher, J. Eschner, F. Schmidt-Kaler, and R. Blatt. *Bell States of Atoms with Ultralong Lifetimes and Their Tomographic State Analysis*. Phys. Rev. Lett. **92**, 220402 (2004).

[200] C. F. Roos, M. Chwalla, K. Kim, M. Riebe, and R. Blatt. *'Designer atoms' for quantum metrology*. Nature **443**, 316–319 (2006).

[201] D. Hayes, P. S. Julienne, and I. H. Deutsch. *Quantum Logic via the Exchange Blockade in Ultracold Collisions*. Phys. Rev. Lett. **98**, 070501 (2007).

[202] H. J. Briegel and R. Raussendorf. *Persistent entanglement in arrays of interacting particles*. Phys. Rev. Lett. **86**, 910–913 (2001).

[203] P. W. Anderson. *The resonating valence bond state in La_2CuO_4 and superconductivity*. Science **235**, 1196–1198 (1987).

[204] S. Trebst, U. Schollwöck, M. Troyer, and P. Zoller. *d-Wave Resonating Valence Bond States of Fermionic Atoms in Optical Lattices*. Phys. Rev. Lett. **96**, 250402 (2006).

[205] R. Raussendorf and H. J. Briegel. *A one-way quantum computer*. Phys. Rev. Lett. **86**, 5188–5191 (2001).

[206] R. Raussendorf, D. Browne, and H. Briegel. *Measurement-based quantum computation on cluster states*. Phys. Rev. A **68**, 022312 (2003).

[207] E. Dagotto and T. M. Rice. *Surprises on the Way from One- to Two-Dimensional Quantum Magnets: The Ladder Materials*. Science **271**, 618–623 (1996).

[208] T. Giamarchi. *Quantum physics in one dimension*, volume 121 of *The international series of monographs on physics*. Oxford University Press (2004). ISBN 0198525001.

[209] J. J. Garcia-Ripoll, M. A. Delgado, and J. I. Cirac. *Implementation of spin hamiltonians in optical lattices*. Phys. Rev. Lett. **93**, 250405 (2004).

[210] B. Paredes and I. Bloch. *Minimum instances of topological matter in an optical plaquette*. Phys. Rev. A **77**, 023603 (2008).

[211] D. J. Thouless. *Exchange in solid 3He and the Heisenberg Hamiltonian*. Proceedings of the Physical Society **86**, 893–904 (1965). URL `http://stacks.iop.org/0370-1328/86/893`.

[212] G. Misguich, C. Lhuillier, B. Bernu, and C. Waldtmann. *Spin-liquid phase of the multiple-spin exchange Hamiltonian on the triangular lattice*. Phys. Rev. B **60**, 1064–1074 (1999).

[213] A. Paramekanti, L. Balents, and M. P. A. Fisher. *Ring exchange, the exciton Bose liquid, and bosonization in two dimensions*. Phys. Rev. B **66**, 054526 (2002).